Non-equilibrium conditions at solid/liquid interfaces

Nazim Abdedou

Université de Lorraine
ECOLE DOCTORALE Chimie - Mécanique - Matériaux - Physique

THÈSE DE DOCTORAT

présentée et soutenue publiquement le 4 décembre 2023
pour l'obtention du titre de

Docteur de l'Université de Lorraine
Spécialité Sciences des Matériaux

par

Nazim Abdedou

Non-equilibrium conditions at solid/liquid interfaces

Composition du jury:

Silvère Akamatsu	INSP, Sorbonne Université-CNRS	Rapporteur
Florian Kargl	DLR, Institut für Materialphysik im Weltraum	Rapporteur
Nathalie Mangelinck-Noël	IM2NP, Aix Marseille Université-CNRS	Examinatrice
Noël Jakse	SIMAP, Université Grenoble Alpes-CNRS	Examinateur (Président)
Julien Zollinger	IJL, Université de Lorraine-CNRS	Co-directeur de thèse
Benoît Appolaire	IJL, Université de Lorraine-CNRS	Directeur de thèse

acknowledgements

First, I want to thank Florian Kargl and Silvère Akamatsu for agreeing to review my thesis, and the jury members Nathalie Mangelinck-Noel and Noël Jakse for examining my work.

My deepest gratitude goes to my advisors, Benoît Appolaire and Julien Zollinger. Working alongside them has been both a privilege and a source of immense learning. Their invaluable advice, unwavering patience, and ever-present sense of humor were the driving forces that kept the spark alive. Truly, I could not have asked for more fitting mentors.

I'd also like to extend my gratitude to Maike Becker and Florian Kargl for their guidance and support during our experiments at DLR. Likewise, Bernard Rouat deserves my heartfelt thanks for his assistance throughout the experimental process.

Massive thanks to my friends and office mates, Mathias Lamari and Ivan Cazic, for the endless laughs and unforgettable moments we've shared together. Big ups to Ilia Ushakov and Julien Banos, along with all the amazing friends and colleagues who made this journey incredible. Couldn't have asked for a better squad.

Lastly, my deepest appreciation is reserved for my family, whose unwavering support and sacrifices have been the true foundation of my achievements.

Sincerely,

Nazim

Table of content

Résumé étendu en français

Ces dernières années ont vu l'essor de procédés de fabrication et de traitement de pièces métalliques qui mettent en jeu d'une part des transformations de phase se déroulant dans des conditions extrêmes (par ex. la fabrication additive [1] ou la fusion sélective[2]), d'autre part des matériaux multiples dont l'assemblage peut s'avérer problématique. Parmi les phénomènes dont la compréhension freine l'avancée de ces procédés, les transformations de phase figurent en première place, puisque c'est la fusion, la solidification et les transformations de phase à l'état solide successives qui génèrent les microstructures, la composition des zones d'assemblage, et donc leurs propriétés. En effet, ces transformations qui sont habituellement contrôlées par la diffusion des éléments d'alliage, se déroulent dans des situations extrêmes. Lorsque les compositions des matériaux en contact sont très différentes et que l'histoire thermique est très rapide, les interfaces entre phases (solide/liquide et/ou solide/solide) sont le plus souvent hors équilibre. À l'heure actuelle, il est difficile de comprendre leur comportement, bien que ce soit essentiel pour étudier la formation des microstructures. Cela tient à la difficulté d'une part de concevoir et réaliser des expériences contrôlées, d'autre part de développer des modèles pertinents.

Dans ce travail, nous avons combiné différentes techniques complémentaires, tant expérimentales que de modélisation et de simulation, pour étudier ces interfaces lors des transformations de phase contrôlées par diffusion.

Expériences de fusion solutale

L'expérience menée par Dutta et Rettenmayr [3] constitue une référence dans les études de fusion solutale. Cependant, elle présente des limites, notamment des effets de convection significatifs dus à la taille de l'échantillon, la présence d'un léger gradient de température et un traitement simplifié des alliages. Des recherches ultérieures ont mis en évidence l'importance de la densité de la solution liquide et des gradients thermiques sur la fusion, soulignant la nécessité de concevoir de nouvelles expériences pour étudier la fusion solutale. Celles-ci devront minimiser l'impact de la convection, mieux contrôler la composition et mesurer en temps réel la vitesse du front de fusion, afin d'améliorer la compréhension de ce processus.

Une nouvelle étude menée par Deillon et al. [4] a proposé une méthode pour étudier la fusion solutale sans convection, en utilisant un système Cu-Ni. Ils ont conçu un système réduit pour minimiser les effets de convection, en utilisant des échantillons de petits cylindres concentriques chauffés à des températures de 1115 °C et 1145 °C. La position de l'interface a été suivie en temps réel par microscopie confocale. Les résultats ont révélé que l'interface solide-liquide était hors équilibre pendant toute la durée du processus de fusion solutale. Une analyse post-mortem a indiqué que la dissolution du Ni n'était pas toujours homogène et que des effets de convection persistaient le long de l'axe vertical de l'échantillon.

Face à ces résultats inattendus, une nouvelle approche faisant appel à la radiographie à rayons X a été proposée dans cette thèse. Cette méthode permet une analyse volumique de l'échantillon pendant la fusion. Pour minimiser les effets de convection, des échantillons minces ont été sélectionnés pour cette étude. Le système Au-Ag a été choisi pour cette expérience en raison de la similarité de son diagramme de phase avec celui du système Cu-Ni, et de la différence notable de densité entre l'or et l'argent, qui se traduit par un bon contraste en niveaux de gris sur les images, permettant de distinguer clairement les deux matériaux.
Les échantillons d'Ag et d'Au sont constitués de feuilles de 50 µm d'épaisseur. L'Ag est découpé en forme de disque et est placé au milieu de la feuille d'Au dans une cavité de la même taille, de manière à ce que l'argent liquide reste confiné par l'échantillon d'Au lorsque l'ensemble est chauffé à 1000 °C.
Les expériences ont été réalisées au Centre allemand pour l'aéronautique et l'astronautique (DLR) à Cologne dans l'équipe du professeur Kargl, en utilisant un four isotherme chauffé par résistance. Le thermocouple est placé dans la paroi du four afin d'éviter toute interférence avec le faisceau X incident. Le temps d'acquisition est de 1 FPS (1 image par seconde) avec une résolution d'image de $4 \times 4\,\mu m^2$ par pixel.
L'analyse d'images a été effectuée à l'aide du logiciel ImageJ pour suivre le mouvement de l'interface et le changement de composition à partir des images en niveaux de gris (Figure 1). Le suivi du mouvement de l'interface est réalisé par binarisation des images. Les intensités en niveaux de gris sont converties en concentrations grâce à la loi de Beer-Lambert:

$$I = I_0 \exp\left(-d \sum_i x_i \, \mu_{m,i} \, \rho_i(T) \right) D(E)$$

où I_0 est l'intensité initiale du faisceau incident en unités arbitraires, d (cm) l'épaisseur de l'échantillon, et $D(E)$ une correction reflétant l'efficacité quantique du détecteur. Chaque élément i de l'alliage est caractérisé par sa concentration x_i, sa densité $\rho_i(T)$ ($g\,cm^{-3}$) dépendant de la température, et son coefficient d'absorption massique $\mu_{m,i}$ ($cm^2\,g^{-1}$).

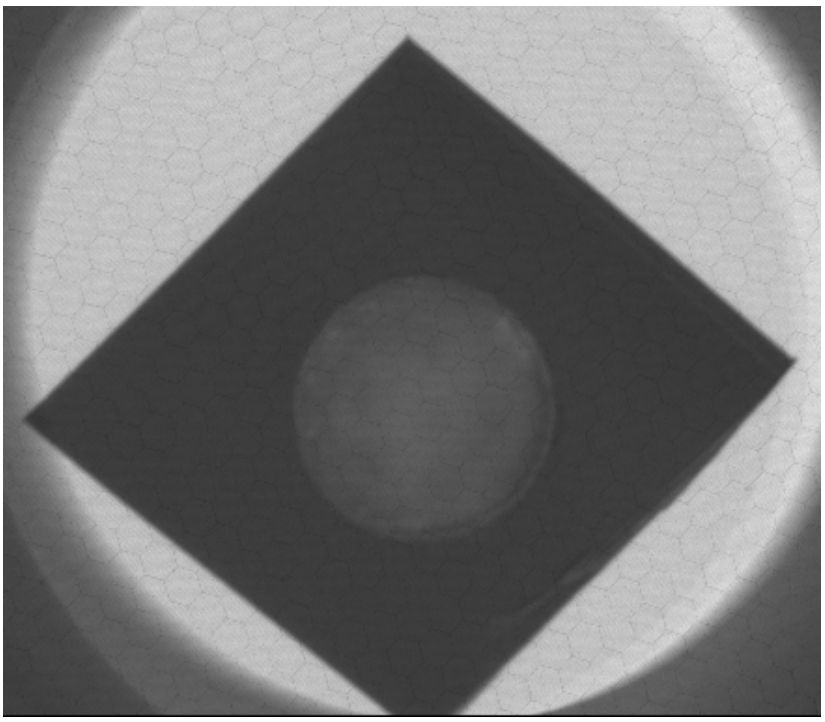

Figure 1 – Image en niveau de gris de l'échantillon Au-Ag lors d'une expérience de fusion solutale (le disque d'Ag est en phase liquide au centre de la feuille d'Au restant en phase solide).

Le profil de concentration d'Ag à 300 s est représenté sur la figure 2 à proximité de l'interface. Ce résultat a été obtenu en exploitant les niveaux de gris extraits d'un segment linéaire traversant les deux phases, avec l'interface solide-liquide au centre. Les niveaux de gris ont ensuite été convertis en concentrations via l'équation de Beer-Lambert.

L'analyse des profils de concentration du système Au-Ag révèle une situation similaire à celle observée dans le système Cu-Ni. En effet, l'interface est constamment en déséquilibre durant tout le processus de fusion solutale. Les analyses post-mortem des profils de concentration réalisées grâce à la technique EDX ont montré que l'Ag solidifié contient en moyenne 30% massique d'or dans toute la zone de liquide solidifié, ce qui est inférieur à la composition du liquidus, estimée à 34,5 % massique d'or à 1000 °C.

La figure 3 montre deux gradients distincts sur le profil de concentration. Ce phénomène pourrait révéler l'existence d'une interface où le coefficient de diffusion change lors de la transition entre les phases. Notamment, on observe un gradient beaucoup plus fort dans la phase solide sur la droite, traduisant une interdiffusion plus faible de l'argent et de l'or dans cette phase.

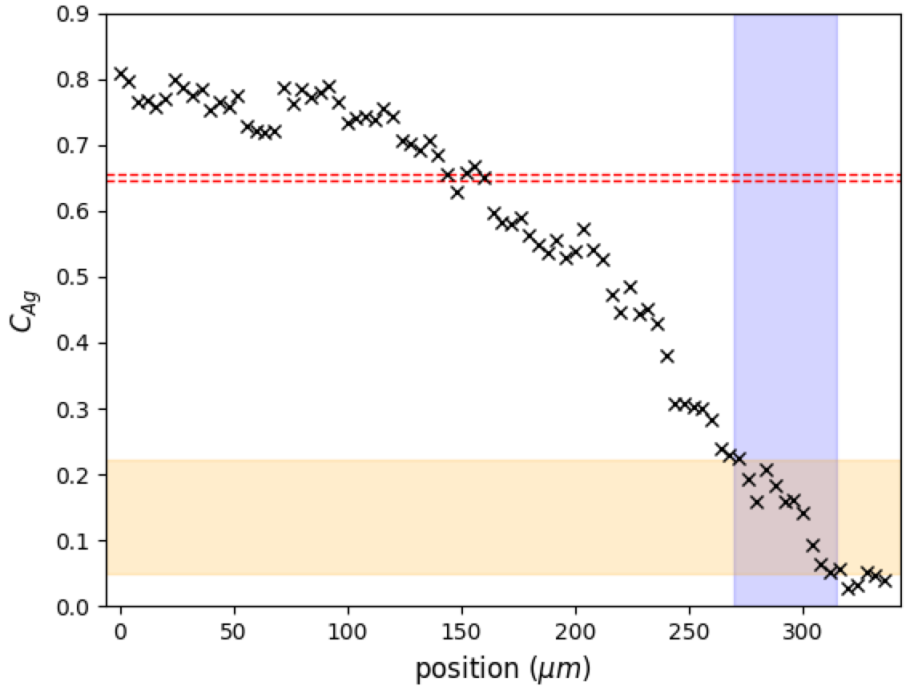

Figure 2 – Profils de concentration en Ag à proximité de l'interface solide-liquide Au-Ag à 300 s*, vers la fin de la fusion solutale. Les lignes pointillées rouges représentent la composition du liquidus (ligne supérieure) et du solidus (ligne inférieure).*

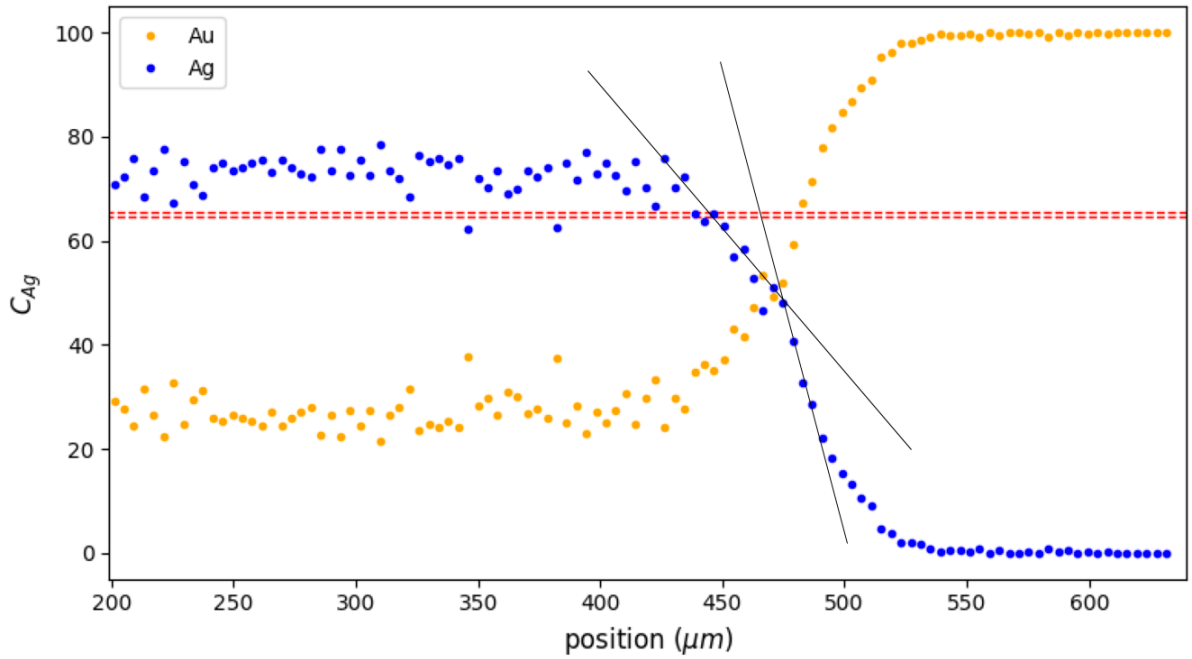

Figure 3 – Profil de concentration post-mortem dans la région interfaciale Au-Ag montrant deux pentes distinctes à l'interface.

Modèle thermodynamique

Nous avons introduit un nouveau modèle basé sur la thermodynamique des processus irréversibles. Ce modèle réussit à reproduire qualitativement les comportements observés lors des expériences de fusion solutale des systèmes Cu-Ni et Au-Ag.
Le développement de ce modèle repose sur l'application du deuxième principe de la thermodynamique. En examinant le cas de l'échange d'éléments d'alliage entre une phase liquide et une phase solide dans un mélange binaire de deux espèces A et B, le taux de production d'entropie peut être exprimé comme suit [5] :

$$T\,\dot{s}_{\mathrm{irr}} = I_{\mathrm{A}}(\mu^s_{\mathrm{A}} - \mu^l_{\mathrm{A}}) + I_{\mathrm{B}}(\mu^s_{\mathrm{B}} - \mu^l_{\mathrm{B}})$$

Les flux de matière sont supposés dépendre linéairement des forces motrices impliquées, donnant lieu aux expressions suivantes :

$$I_{\mathrm{A}} = L_{\mathrm{AA}}\,\Delta\mu_{\mathrm{A}} + L_{\mathrm{AB}}\,\Delta\mu_{\mathrm{B}}$$
$$I_{\mathrm{B}} = L_{\mathrm{BA}}\,\Delta\mu_{\mathrm{A}} + L_{\mathrm{BB}}\,\Delta\mu_{\mathrm{B}}$$

Pour assurer le respect du deuxième principe de la thermodynamique, à savoir une production d'entropie positive, la forme quadratique des coefficients cinétiques doit être définie et positive. De plus, les relations de réciprocité d'Onsager entre les termes croisés permettent d'établir les conditions d'existence des paramètres cinétiques [6]:

$$L_{\mathrm{AB}} = L_{\mathrm{BA}}$$
$$L_{ii} \geq 0$$
$$L_{\mathrm{AA}} \times L_{\mathrm{BB}} \geq L^2_{\mathrm{AB}}$$

En adjoignant aux expressions de flux interfaciaux, le bilan de soluté à l'interface, il est possible de déterminer l'évolution temporelle des concentrations et de la vitesse de l'interface. Les équations sont ensuite adimensionnées pour faire apparaître les nombres adimensionnels contrôlant le processus. Il s'agit essentiellement de rapports entre les temps caractéristiques de différents phénomènes qui interviennent, à savoir la migration de l'interface, les transferts élémentaires à travers elle, et la diffusion des espèces chimiques en volume.
En raison des difficultés rencontrées pour mesurer les paramètres cinétiques L^{ij}, le problème a été simplifié en faisant l'hypothèse que les mobilités dépendent des concentrations à l'interface de manière simple. Ainsi, dans le cas de la fusion solutale, une dépendance avec la concentration du solide a été considérée, contrairement à l'hypothèse habituelle pour les interfaces solide-liquide où la diffusion dépend uniquement du côté liquide.

La figure 4 illustre l'évolution au cours du temps des concentrations à l'interface du liquide (en rouge) et du solide (en noir) dans le système Cu-Ni. Les concentrations initiales du solide et du liquide sont respectivement $c^l_{\mathrm{Cu}} = 1$ et $c^s_{\mathrm{Cu}} = 0$. Les lignes en pointillés représentent les concentrations à l'équilibre vers lesquels le système tend aux temps longs en condition isotherme.
Un nombre de Péclet négatif (rapportant la vitesse de l'interface à la vitesse de diffusion du Cu dans le liqude) indique un processus de dissolution. Le liquide est initialement du cuivre pur, puis sa concentration diminue en dessous de la valeur d'équilibre à mesure que la transformation progresse. Avec le temps, les concentrations du solide et du liquide convergent et se stabilisent aux compositions d'équilibre.

Aux temps longs, l'interface cesse de se déplacer (le nombre de Péclet est nul, voir la Figure 5) alors que les concentrations à l'interface sont encore loin de l'équilibre. Le modèle reproduit ainsi qualitativement le comportement général observé lors des expériences de fusion solutale des systèmes Cu-Ni et Au-Ag.

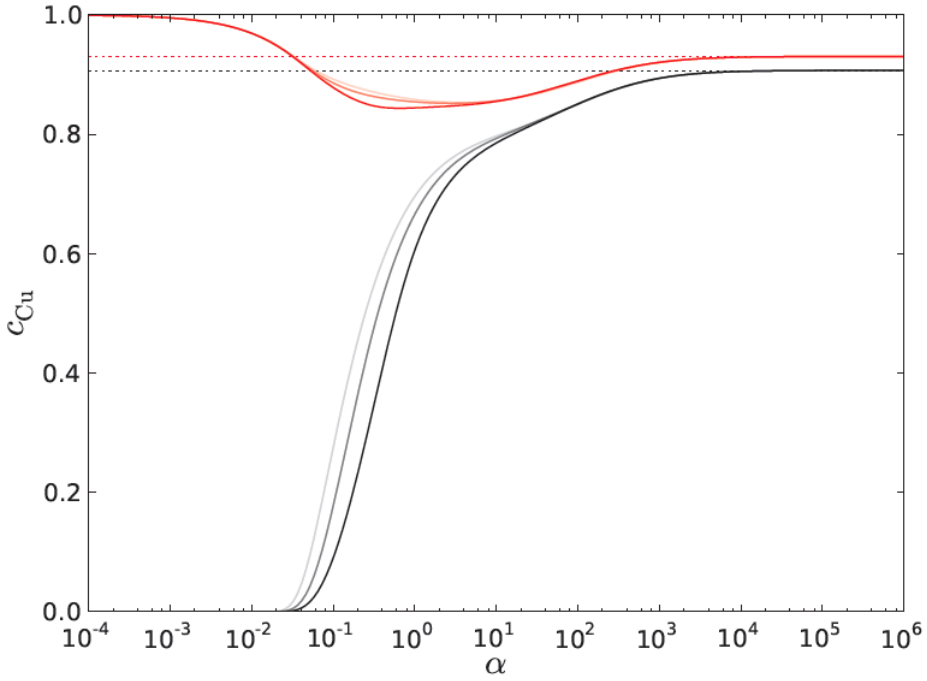

Figure 4 – Concentration en Cu du liquide (rouge) et du solide (noir) en fonction du paramètre adimensionnel α proportionnel à $\sqrt{t}$.

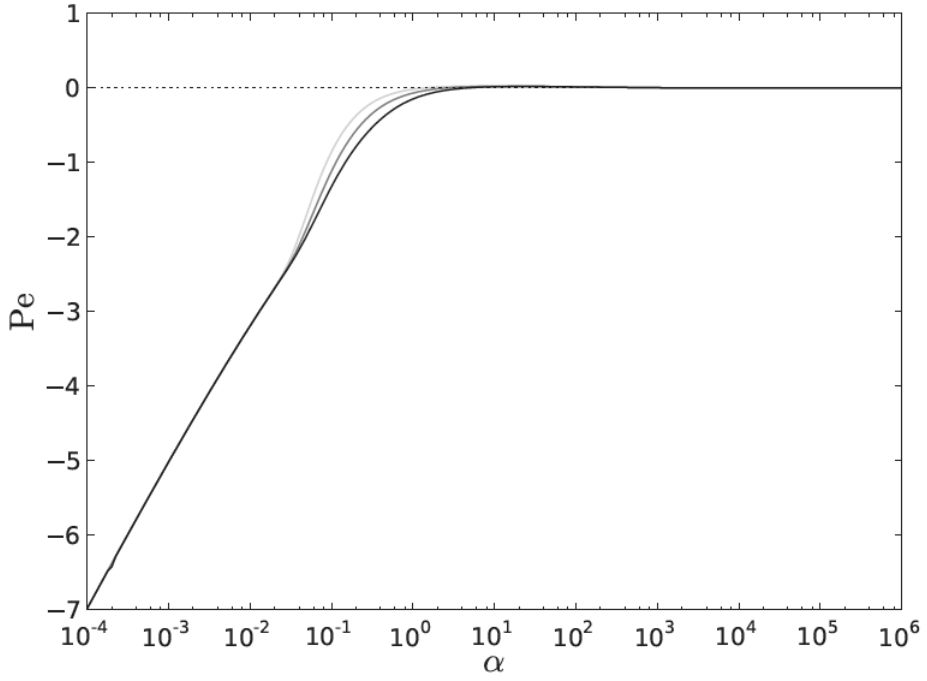

Figure 5 – Nombre de Péclet en fonction du paramètre adimensionnel α.

Dynamique moléculaire

La simulation en dynamique moléculaire se révèle extrêmement utile pour accéder à des mesures de certains paramètres à l'interface qui seraient impossibles à obtenir expérimentalement. Dans le but de déterminer les paramètres cinétiques du modèle thermodynamique, une simulation de fusion solutale en dynamique moléculaire a été réalisée sur une structure solide-liquide, avec le Ni à l'état solide et le Cu à l'état liquide.

Le logiciel LAMMPS (Large-scale Atomic/Molecular Massively Parallel Simulator) a été utilisé pour toutes les simulations en dynamique moléculaire. Une boîte de simulation quasi-2D solide-liquide contenant environ 400 000 atomes a été préparée en joignant une structure solide de Ni pur et une structure liquide de Cu pur. Les deux structures ont ensuite été portées à une température de 1400 K et une pression de 0 bars avec l'ensemble NPT pendant 100 ns avec un pas de temps de 1 fs, durant lesquels le processus de fusion solutale a été observé.

Les paramètres nécessaires pour le modèle thermodynamique de Lesoult ont été extraits de cette simulation, à savoir la vitesse de l'interface, la concentration à l'interface du côté liquide, les potentiels chimiques et le flux de Ni passant en phase liquide.
La vitesse d'interface est déterminée à partir de l'évolution de position d'interface en fonction du temps. Cette dernière a été déterminée à l'aide de la méthode PTM (Polyhedral Template Matching) mise en œuvre dans le logiciel de visualisation et d'analyse de données Ovito. La méthode PTM utilise des modèles atomiques tridimensionnels, appelés templates, qui représentent différentes structures cristallines possibles. La structure qui correspond le mieux à un atome et à ses voisins est celle qui minimise le RMSD (Root Mean Square Deviation). Cette technique a permis de délimiter et de positionner l'interface solide-liquide et d'en extraire les paramètres pertinents pour le modèle thermodynamique, telle que la vitesse d'interface et la concentration d'interface, illustrées sur la figure 7 et 8.

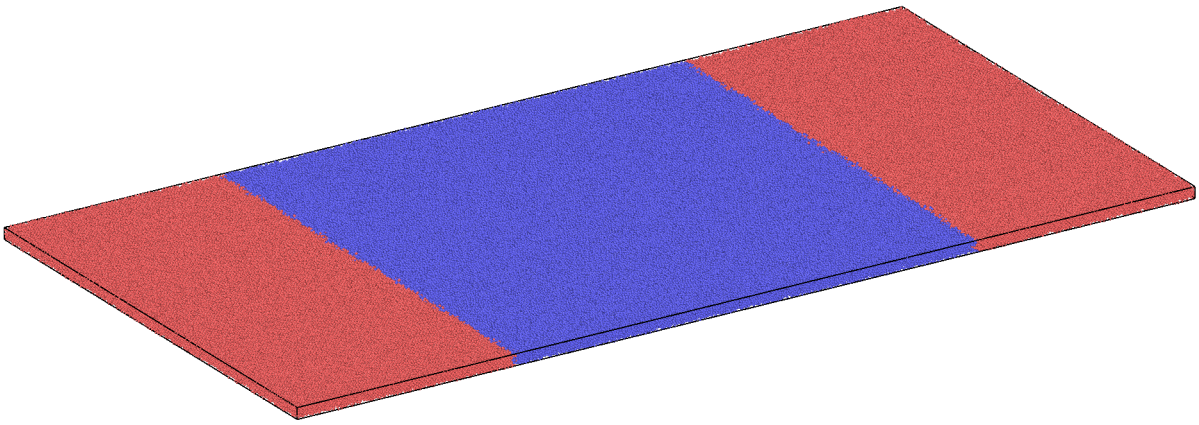

Figure 6 – Système étudié par dynamique moléculaire : Ni CFC (rouge) en contact avec Cu liquide (bleu) à 1100 °C.

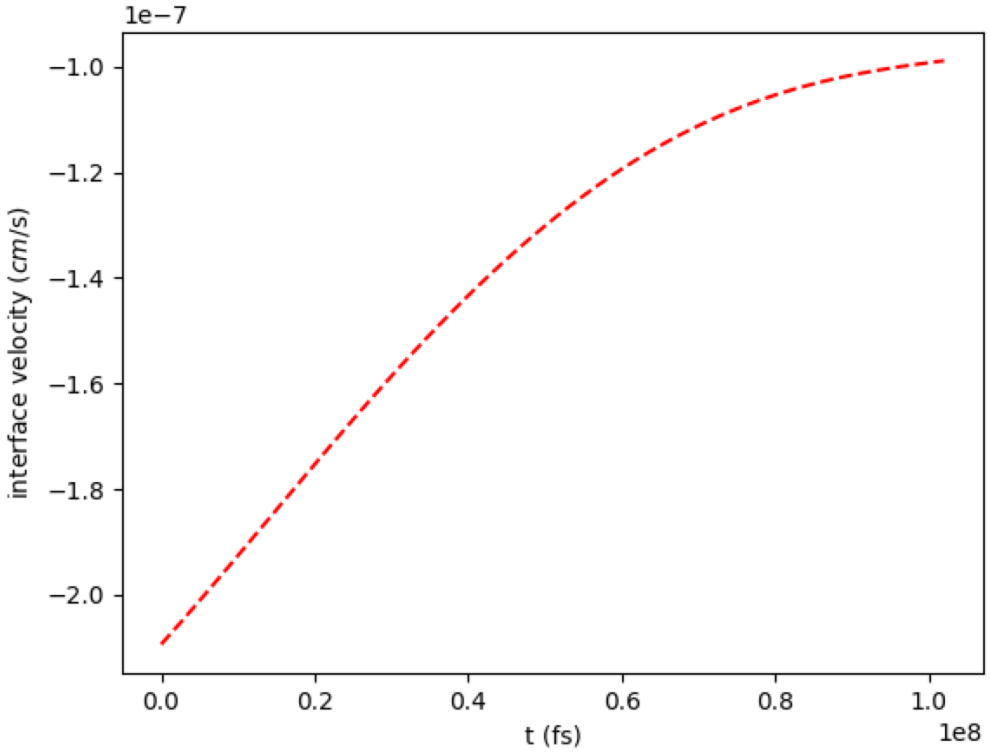

Figure 7 – Évolution de la vitesse d'interface lors de la fusion solutale du nickel dans le cuivre à 1115 °C *prédite par dynamique moléculaire.*

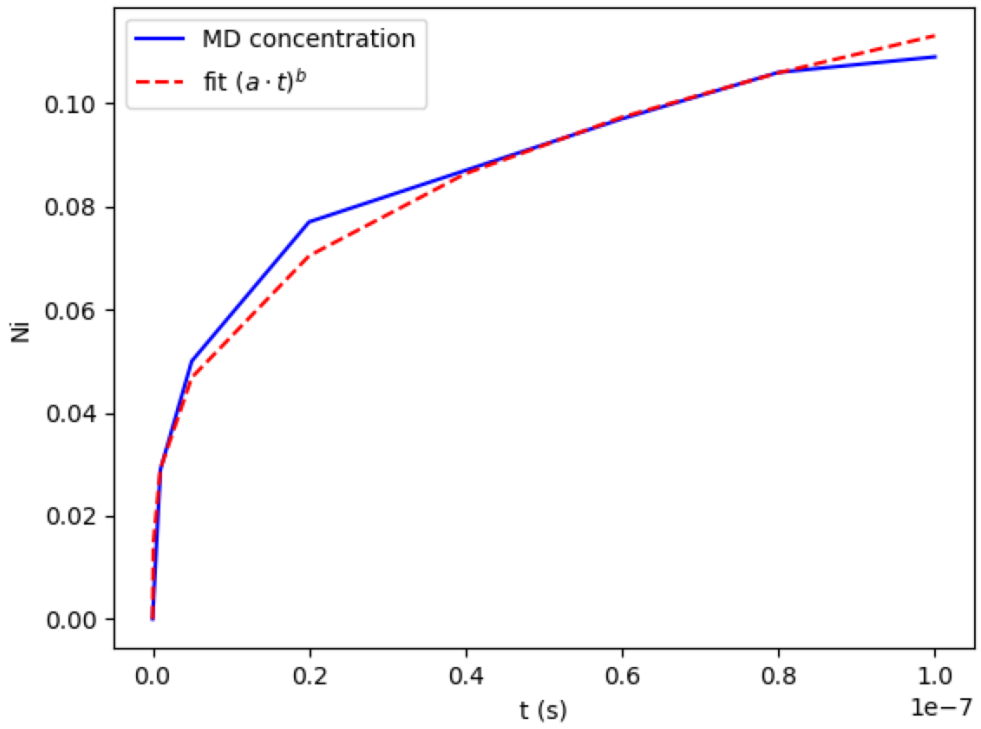

Figure 8 – Évolution au cours du temps de la concentration en Ni à l'interface du côté liquide, pendant la fusion solutale du Ni dans le Cu simulée par dynamique moléculaire.

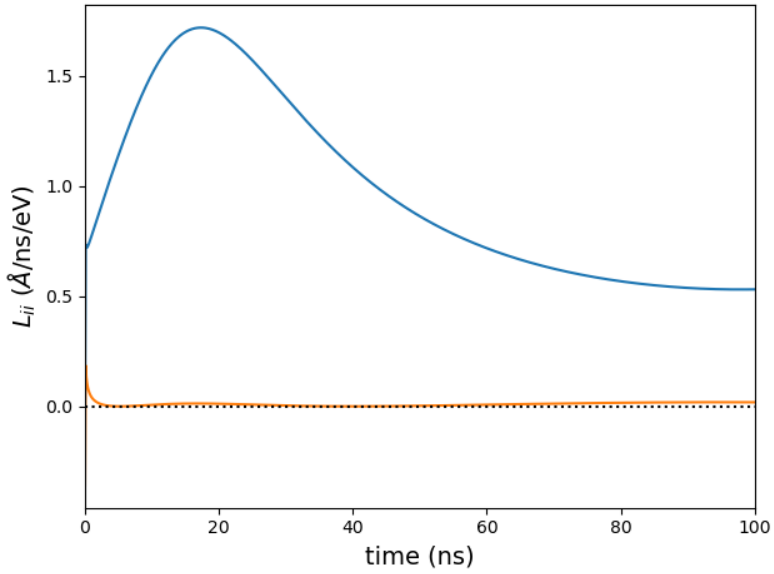

Figure 9 – Évolution des mobilités d'interface L_{NiNi} (bleu) et L_{CuCu} (orange) déduites d'une analyse des simulations de dynamique moléculaire.

Il n'existe pas de méthode directe pour obtenir le potentiel chimique en utilisant LAMMPS. La méthode la plus efficace pour déterminer le potentiel chimique en fonction de la concentration du soluté est l'intégration thermodynamique en utilisant la méthode atom/Swap, qui simule un comportement d'ensemble semi-grand canonique SGCMC. En imposant une différence de potentiel chimique donnée, la concentration se stabilise à une valeur d'équilibre correspondant à cette différence. Les courbes de potentiel chimique sont ajustées puis intégrées pour obtenir les courbes d'énergie de Gibbs pour la phase solide et la phase liquide.
Enfin, nous avons mis en œuvre un modèle à interface mobile contrôlée par la diffusion des éléments d'alliage dans le liquide. La calibration, puis la confrontation de résultats de ce modèle avec les évolutions prédites par la dynamique moléculaire nous ont permis de déduire le flux de Ni se dissolvant dans le liquide lors de la fusion solutale.

Une fois tous les paramètres nécessaires pour le modèle de Lesoult obtenus, deux scénarios ont été considérés pour l'estimation des paramètres d'Onsager. Dans le premier scénario, le terme croisé L_{NiCu} est négligé, ce qui mène à un problème car les conditions d'Onsager imposent que les paramètres cinétiques soient positifs alors que L_{CuCu} est négatif dans ce cas. Dans le second scénario, les termes croisés sont conservés en considérant le cas limite où $L^2_{\mathrm{NiCu}} = L_{\mathrm{NiNi}} \times L_{\mathrm{CuCu}}$. Les paramètres L_{ij} trouvés sont tous deux positifs et respectent les conditions d'Onsager, comme le montre la Figure 9. Les valeurs obtenues sont bien plus grandes que celles déduites de l'analyse des expériences de Deillon et coll. [4] à l'aide du modèle de Lesoult au chapitre précédent. Néanmoins, les paramètres utilisés dans l'étude préliminaires du modèle de Lesoult sont probablement trop éloignés de ceux nécessaires pour juger de la pertinence des mobilités interfaciales extraites de calculs de DM. Notamment, il semble important de prendre en compte un contraste important entre les mobilités diagonales du Ni et Cu, avec $L_{\mathrm{CuCu}} \ll L_{\mathrm{NiNi}}$. Outre ce contraste, les calculs de DM ont montré qu'il est

indispensable de prendre en compte les mobilités croisées, contrairement à ce que les calculs thermo-cinétiques suggéraient. Enfin, la prise en compte de la diffusion du Cu dans le Ni solide semble être un facteur important à prendre en compte, malheureusement hors de portée de calculs de DM.

Conclusion

Dans ce travail de thèse, nous avons étudié de manière approndie le phénomène de fusion solutale, en combinant études expérimentale, modélisation thermo-cinétique et simulations par dynamique moléculaire.
Nous avons retrouvé l'asymétrie intrinsèque entre la solidification et la fusion, remettant en question l'idée que la fusion est simplement l'inverse de la solidification. Contrairement à la solidification, la fusion présente des caractéristiques uniques, avec une interface restant hors équilibre sur des temps bien plus longs que ce qui est observé en solidification à des vitesses comparables.
Un nouveau modèle thermo-cinétique a été proposé pour reproduire ce comportement hors équilibre, montrant sa capacité à prédire l'évolution des concentrations d'interface sugérée par les expériences.
Enfin, les simulations de dynamique moléculaire se sont révélées un outil précieux pour étudier la fusion solutale de manière fine. En effet, elles nous ont permis de reproduire les premiers instants du processus et d'obtenir des valeurs de mobilités interfaciales, impossible à déterminer autrement.

Notre travail présente des perspectives ambitieuses pour réconcilier les mesures expérimentales, les résultats préliminaires du modèle thermo-cinétique de Lesoult et les simulations de dynamique moléculaire.

Tout d'abord, on peut envisager des expériences complémentaires pour étayer les résultats, d'une part sur le système Ni-Cu pour lequel il est possible de faire des calculs à l'échelle atomique grâce aux potentiels interatomiques empiriques, et d'autre part sur le système Au-Ag. Pour cela, on pourrait réaliser des expériences de radiographie à rayons X au synchrotron pour de meilleures résolutions en temps et en espace. À cet effet, il faudrait reprendre le principe du dispositif mince pour éviter les effets parasites de la convection et l'améliorer pour supprimer toute variation d'épaisseur. Des maintiens plus longs suivis de trempes seraient également nécessaires pour mesurer des profils de diffusion dans le solide et obtenir les diffusivités dans cette phase. Enfin, on pourrait envisager de réaliser des expériences à des températures différentes pour modifier l'espèce majoritaire dans le liquide à l'interface et voir quelle en est la conséquence sur le processus et sa cinétique.

Ensuite, il faudrait reprendre le modèle thermo-cinétique de Lesoult en le couplant au modèle de diffusion 1D pour s'affranchir des estimations grossières des termes de diffusion en volume. Il serait également utile d'intégrer la diffusion dans le solide, ainsi que les potentiels chimiques obtenus par intégration thermodynamique pour se placer dans les conditions les plus proches possibles des calculs de DM. On pourrait ainsi refaire des calculs utilisant les mobilités extraites de la DM, en tenant compte en particulier de leur fort contraste. Enfin, il paraît important d'étudier de manière extensive l'importance des mobilités croisées.

Enfin, on pourrait penser à réitérer l'analyse des calculs de DM pour extraire des mo-

bilités interfaciales dans le cas des autres boîtes investiguées dans le présent travail, et voir comment les mobilités interfaciales dépendent des diffusivités effectives en volume. La réalisation de simulations de dynamique moléculaire Ab initio sur le potentiel Ag-Au pour confirmer les résultats de DM sur le système Cu-Ni et les comparer aux expériences réalisées dans le cadre de cette thèse constituerait également une perspective intéressante.

Introduction

In recent years, additive manufacturing (AM) has been recognized as a promising approach for creating metallic components. Generally, AM processes utilize a precise blend of molten metallic powder, arranged layer by layer, allowing their subsequent solidification to form the final product in a near net shape. Consequently, the resulting microstructures and corresponding mechanical properties are heavily influenced by both the melting of the powder and the solidification of the added layers.

The range of materials utilized in transportation sectors, such as the automotive and aeronautical industries, has expanded significantly over recent decades. This is to leverage their individual benefits and capitalize on potential synergies. However, while integrating similar materials is well managed, the assembly of dissimilar materials presents an ongoing challenge, particularly when industrializing novel material combinations.

Among the different phenomena that should be better understood for improving the processes mentioned above, phase transformations are the main issue since the microstructures, the composition and the resulting mechanical properties are resulting from melting, solidification and solid state transformations. Indeed, these transformations that are usually diffusion controlled are occuring under extreme conditions. Hence, when the compositions of materials that come into contact are very different or when temperature history is very rapid, the interfaces between the different phases (liquid/solid and/or solid/solid) are most often strongly out-of-equilibrium.

The characteristics of a cast material are inherently tied to the microstructure development during the process of solidification, irrespective of the preceding phase of melting. Due to this understanding, there has been a limited emphasis placed on experimental or theoretical research into the thermodynamics and kinetics of melting. Traditionally, melting is regarded simply as inverse solidification.

However, in a myriad of technical applications, melting and solidification can occur concurrently. For instance, within the 'mushy zone', an intermediate region where the material is neither completely solid nor liquid,local remelting of partially solidified structures is a common occurrence. This phenomenon can also be observed during the process of joining dissimilar metals and alloys. The simultaneous occurrence of melting and solidification plays

a crucial role in shaping the final properties of the material, influencing its structure, integrity, and performance.

Historically, due to the perception of melting as the inverse process of solidification, both phase transformations have been treated with symmetry. The theoretical frameworks developed for understanding solidification have been analogously adapted for the study of melting. While this may provide adequate explanations for situations with low transformation rates, where local equilibrium at the interface holds and nucleation phenomena are negligible, it fails to address complexities arising from differences in the conditions required for solidification and melting.

Solidification invariably involves a degree of undercooling below the equilibrium melting temperature, which is an effect hard to circumvent. Conversely, for melting to occur, considerable experimental effort is required to induce superheating, whereby a metal is compelled to remain in a solid state above its natural melting point. Achieving superheating is even more challenging due to the lack of a nucleation barrier for liquid phases and the premelting effects that arise from the lower coordination number of surface atoms, which are less thermally stable. These factors contribute to the formation of thin liquid layers below the equilibrium melting temperature, further depressing the melting point.

Numerous aspects of asymmetry that separates melting from solidification were pointed out by Rettenmayr in his work [7, 8]. Pre-conditions for the migration of a solid-liquid interface are contingent on the direction of phase transformation. During the melting phase, atoms crossing the interface, that can be either rough or smooth, will invariably accommodate in the liquid phase. However, the same is not universally true for the process of solidification. In solidification, the interface is always rough, and atoms may encounter unfavorable sites and be repelled.

Furthermore, the dynamics of the melt structure diverge significantly from those of solidification. The higher diffusivity of the liquid phase contributes to its role as the rate-controlling phase for both melting and solidification, primarily due to its ability to accommodate any amount of solute rejected during the process of solidification. By contrast, during melting, the release of solute from the solid to balance the solute depletion in the newly formed liquid is unattainable.

Solute distribution at the solid-liquid interface plays a major role in controlling the rates of both solidification and melting processes, particularly when thermal effects are insignificant and when either the solid or liquid phase is not at the equilibrium composition at the interface. Melting, under these conditions, is often referred to as solutal melting. A common experimental configuration for solutal melting involves positioning a solid in contact with a solute-enriched liquid. The liquid's composition exceeds the equilibrium within its corresponding single-phase domain. Consequently, the dissolution of the solid occurs in an effort to guide the interface towards achieving equilibrium.

In the context of isothermal solidification, solute enrichment at the interface ensues as the solid forms with lower solute content. The surplus solute is absorbed by the liquid, halting solidification once the liquid reaches equilibrium at the interface. To resume the process, solute needs to be transported away from the interface. During solutal melting, the interface undergoes solute depletion and solute needs to be transported from the solid to the interface. However, due to the lower diffusivity of the solid and its usual solute depletion, this process is nearly impossible to achieve.

Unlike solidification, solutal melting of a solid with steep concentration gradients can lead to a considerable deviation of the interface from equilibrium, allowing for a broad spectrum of potential interfacial concentrations. When a solid with a low solute content dissolves, off-equilibrium interfacial concentrations may be sustained over extended periods, even at velocities lower than those projected by analogous rapid solidification theory [9]. This raises pertinent questions regarding the time span required to regain an equilibrium state.

Currently, the behavior of such interfaces is not thoroughly understood, despite its critical role in microstructure formation. This lack of understanding can be attributed to the difficulties inherent in designing and executing controlled experiments for these situations, coupled with the challenges in developing relevant theoretical models.

To address some of these scientific challenges presented by the processes outlined above, and to illuminate the nature of strongly out-of-equilibrium interfaces during diffusion-controlled phase transformations, this PhD research will adopt a multi-faceted approach. This research will encompass solutal melting experiments of binary systems, utilizing X-ray radiography for in-situ analysis of the process, and employing post-mortem characterization to discern chemical profiles across the interfaces. Furthermore, the development of a novel model based on irreversible thermodynamics will be pursued, with input data derived from molecular dynamics calculations. This integrated method aims to bring fresh insights into the complex and dynamic behaviors of out-of-equilibrium phase transformations, ultimately contributing to a more comprehensive understanding of the solutal melting process.

CHAPTER 1

Solutal melting experiment

1.1 Introduction

Melting processes have gained more attention since they have a direct impact on the properties of some large technical castings. An example can be direct-chill castings of aluminium where remelting can lead to inverse segregation and surface exudation [10]. Local remelting due to thermosolutal convection at the root of the secondary dendrite arms where they are generally thinner leads to detachment of dendrite arms and leading thus to dendrite fragmentation, which in turn is responsible for the columnar-to-equiaxed transition in most casting processes [11, 12] and freckle formation in directionally solidified nickel-base superalloys [13] or Sn-Bi alloys [14]. Thus, the importance of melting could no longer be ignored due to its undeniable influence on the solidified structures and its predominant effects on the newly developed processes such as additive manufacturing. In the latter case, each layer is partly remelted any time a new layer is build. This has led to an increasing interest for further developing the theoretical aspects of melting for both academic research purposes and industrial applications.

Solutal melting stands as one of the least understood melting process due to the difficulty of properly investigating diffusion at the scale of the interface, in addtions to the complex nature of the convection effects that can hardly be avoided in experiments. Some of the most popular solutal melting studies are presented in [15, 3, 16], where solid and liquid metals of composition both in their respective one-phase field in the phase diagram (non equilibirium state) were put into contact with one another (see illustration in figure 1.1). The interface velocity was deduced from the experiments.

In the dissolution experiment described in [15], Rettenmayr et al. reported a surprising result where low composition at a formerly melting interface was measured. The reliability of the measurement was however criticized in [17] due to: (i) the difficulty in determining the interface position precisely and (ii) in the averaging effects of the electron-matter interaction

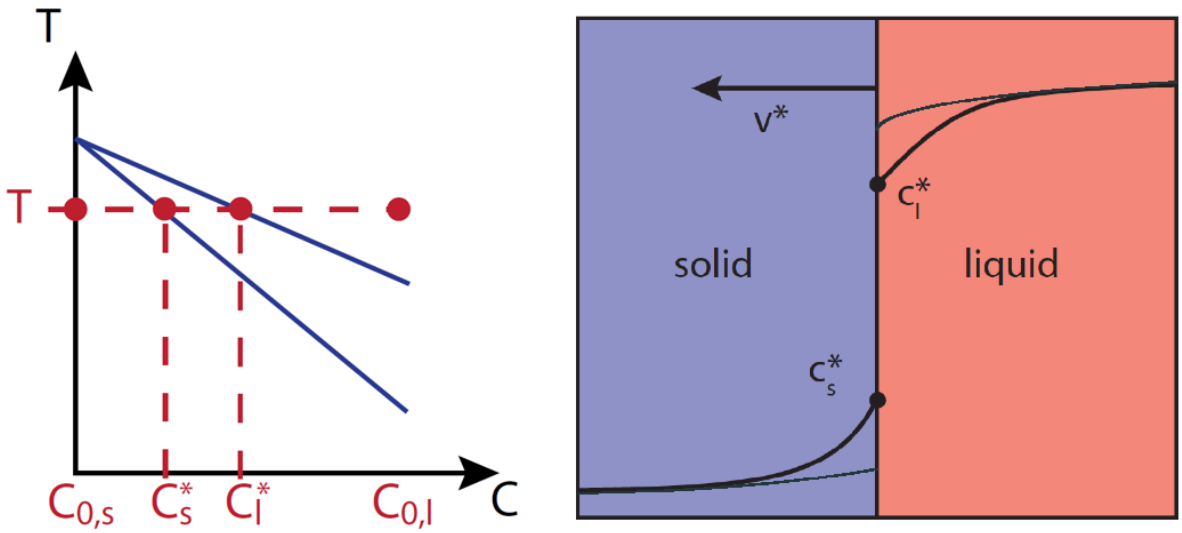

Figure 1.1 – Illustration of a fictitious solutal melting configuration at a set temperature T. The left side represents a phase diagram where the initial concentrations of solid and liquid are labeled as $C_{0,s}$ and $C_{0,l}$. A typical concentration profile for this situation is depicted in the right sketch, where, as the melting front advances in the direction of the solid phase, the concentration profile is expected to transition from the profile represented in the thin black line to the profile corresponding to equilibrium concentrations at the interface C_l^* and C_s^* represented by the thick black line.

volume of the energy dispersive X-ray spectroscopy (EDX) measurements. In addition, some diffusion may have occurred during the quench, inducing a bias in the analyzed results. In [16] the possibility of a composition of liquid near the interface below the equilibrium value of the solid, lying inside the one-phase field domain was raised by Rettenmayr et al. The authors assert from their EDX chemical measurements of concentrations in the solid at the position of a formerly remelting interface that even at low interface velocity, local thermodynamic equilibrium is not achieved in case of supersaturation in the liquid or solid depletion in the solid. The authors simulated the solid dissolution by 2-D numerical calculations by first assuming an equilibrium concentration, and found that the calculated velocity of melting was 50% of the observed velocity. The experimental front velocity results were well reproduced if non-equilibrium effects at the interface were assumed, *i.e.* by considering the solid phase interfacial compositions were different than those of the wide-spread use of local equilibrium assumption.

Hillert and Argen however argued in a subsequent discussion [18] that equilibrium is reached when diffusivity in the solid is high enough to form a pronounced concentration gradient in the solid phase, with the peak concentration at the equilibrium value. For this gradient to exist, the criterion $D/v > d$ must be satisfied with d the distance between atoms and D the diffusion coefficient of the solid, and judging by the measured velocity from the experiment, they concluded that a deviation from local equilibrium was unlikely as local equilibrium conditions were well established. Then Hillert and Rettenmayr in [9] as a reply to the discussion in [18] assumed a case of an equilibrium concentration at the liquid in contact with a solute depleted solid, and stated that melting is still expected to occur despite a supposedly available driving force for solidification due to different diffusivity in the two phases and enforces the

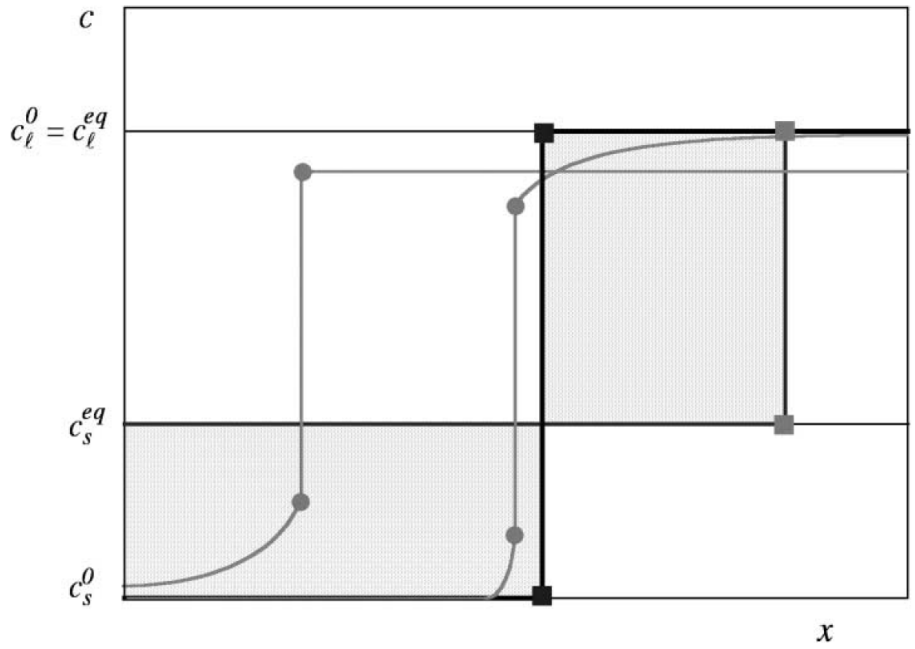

Figure 1.2 – Fictitious experiment presented by Rettenmayr and Hillert [9] where an initial liquid of c_l^{eq} and a solid of c_s^0 depicted by the black squares are brought into contact. The intermediate stages are represented by circles, and the final ones by gray squares.

asymmetry aspects between solidification and melting which is usually treated incorrectly as inverse solidification. Under these conditions, they arrive at the conclusion from solute balance calculation requirement that the interface concentration of the solid must be below the solidus value, and that the liquid at the interface must be below the liquidus composition inside the solid+liquid two-phase domain. This latter assertion was qualitatively confirmed in [17] from simulations based on thermodynamic extremal principle where the liquid phase at the interface can indeed move into the two-phase region for the case of high interface mobilities in the early stages of the transformation. A fictitious experiment is sketched by Rettenmayr and Hillert in figure 1.2 that summarizes solutal melting stages. The interface starts moving in the direction of melting in the early stages with an out-of-equilibrium interface concentration. Solidification stage begins when the interface is stable, and the system reaches local equilibrium when global equilibrium is attained.

The interface is therefore by no means limited by the concentrations in the range within the equilibrium values during melting as opposed to solidification. The wide variety of possible thermodynamic conditions at the interface cause the equilibrium to be lost more easily during melting. The melting/dissolution process is usually approached qualitatively since no consistent thermodynamic description has been worked-out in the literature. It was shown in [3, 19] that convection is a prominent mechanism controlling the melting rate. It can be either thermal due to temperature gradient or solutal due to density difference. An attempt to suppress the convection effects, solutal melting experiments are presented in the following section in the aim of gaining a better understanding of diffusion controlled dissolution.

1.2 Experimental study of solutal melting

Dutta and Rettenmayr's experiment has always been a reference for solutal melting studies. In their investigation on the kinetics of solute-driven remelting of what they assumed to be pure Al [3], they used a graphite sheet to isolate the liquid from the solid phase, allowing the experiment to start only when the graphite sheet was removed. This design provided better control over the initial conditions of the experiment. Additionally, the presence of intermetallics in the system enabled the researchers to visually track the melting front from post-mortem examinations.

However, the experiment had some drawbacks. The large sample size led to significant convection effects, which could affect the measured velocities. Moreover, the authors treated the Al-Fe and Al-Mg systems as binary alloys, despite their non-binary nature. The melting front velocity was determined through post-mortem measurements, which only provided an average value. Due to the presence of an Ar gas stream, a slight temperature gradient from the bottom to the top of the sample was observed, leading to variations in the melting front velocities across the sample height.

Interestingly, despite the temperature decrease from the bottom to the top of the sample, the melting front velocity was higher at the top. This phenomenon was attributed to gravity-induced segregation of Mg toward the top of the liquid, leading to thermosolutal convection due to the density difference between Mg and Al. Consequently, the variation in remelting velocity across the height of the sample was primarily driven by the change in supersaturation resulting from the segregation of Mg.

As previously established by Fang and Hellawell, who studied the influence of liquid solution density on the melting regime of crystals [19], the density of the liquid phase played a crucial role in determining the melting regime of the crystals. When a crystal was melted in a low-density liquid, the melting front was smooth, exhibiting a "diffusional melting" regime where heat was transported by diffusion through the liquid. Conversely, when the crystal was melted in a high-density liquid, the melting front was rough, displaying a "convective melting" regime in which heat was primarily transported by convection due to the density gradients in the liquid phase.

Further exploring the effects of thermal gradients on the dissolution process, Rajesh et al. investigated the dissolution process of GaSb into InSb melt [20]. They observed that when a small thermal gradient was applied to the sample, convection was induced in the liquid melt due to the density differences caused by the temperature difference, resulting in enhanced mass transfer and faster dissolution. They noted that even minor thermal gradients could lead to significant convective flow, which in turn affects the kinetics of melting and mass transfer rates.

In the light of the drawbacks observed in the aforementioned studies, it becomes imperative to design new experiments that compensate for these shortcomings while investigating solutal melting processes. The new experiments should aim to minimize the impact of convection, better control the system's composition, and provide real-time measurements of the melting front velocity. This would pave the way for a more comprehensive understanding of solutal melting and its underlying mechanisms.

1.3 Experimental study of Deillon et al.

Leveraging the insights gathered from the previous studies, a novel approach was developed to investigate solutal melting in a convection-free environment, ensuring that the kinetics were solely diffusion-controlled. This new approach, which focused on the Cu-Ni system, was carried out by L. Deillon et al. using laser scanning confocal microscopy.

1.3.1 Experimental set-up

In-situ experiments of solutal melting on the Cu-Ni system using laser scanning confocal microscopy were carried out by L.Deillon et al. [4] to characterize a tentative convection-free solutal melting, in which only diffusion-controlled kinetics are involved. To minimize gravity induced convection effects, they designed a system small enough to reduce their impact. Ni and Cu, which are adjacent in the periodic table, have similar densities and exhibit complete miscibility, as shown in the phase diagram in figure 1.3. The sample consists of two concentric cylinders cut into 1.5 mm thick slices using a precision saw. The inner one made of pur Cu has diameter of 2 mm and is fitted inside a hollow cylinder of pure Ni with an internal diameter of 2 mm and an outer diameter of 5 mm, as shown in figure 1.4.

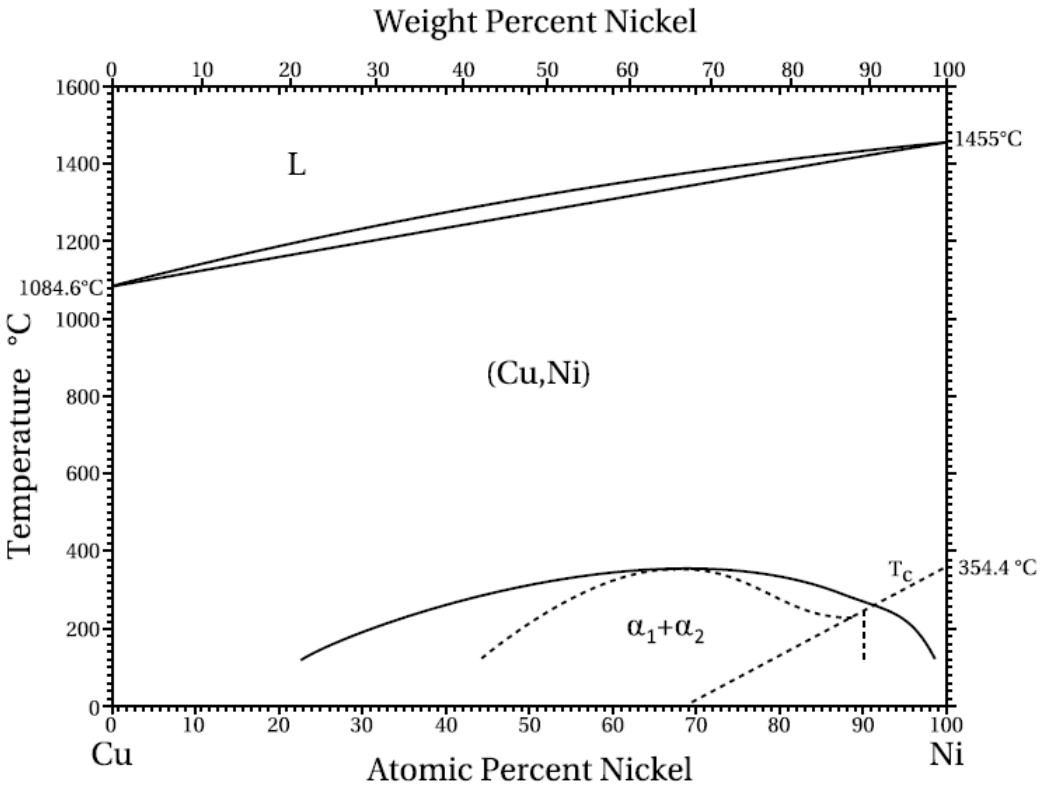

Figure 1.3 – Cu-Ni binary phase diagram [21].

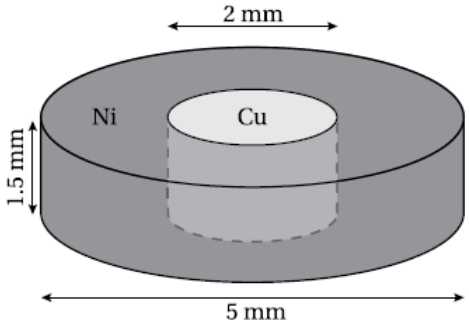

Figure 1.4 – Cu-Ni sample set-up.

The discs were placed in an alumina crucible, and heated from the sides and underneath to deliver the most possible homogeneous temperature, mitigating convection induced by thermal gradients. The experiments were conducted at 1115 °C and 1145 °C. The heating rate was 150 ℃/min up to 1055 ℃ (below the Cu melting point), followed by a temperature stabilization period of 3 min, then 100 ℃/min up to the aimed temperature. The confocal laser scanning microscope, with a spacial resolution of 0.62 µm and an acquisition frequency of 0.64 FPS (frame per second), enabled real-time tracking of interface velocity. Subsequent to the experiments, a post-mortem analysis was conducted using a scanning electron microscope (SEM) combined with energy dispersive X-ray spectroscopy (EDX) measurements on a vertical section of the sample along its diameter to verify whether the dissolution occured homogeneously throughout the height of the sample.

1.3.2 Results and discussion

During the experiment, three primary reactions took place: Cu melting, Ni dissolution, and resolidification during a 1-hour holding period. A solid layer, 20 µm thick, persisted above the melting Cu as a result of solid-state diffusion during heating, leading to a localized increase in the liquidus temperature. The complete melting of Cu is taken as the starting point for tracking the interface.

Dissolution velocities as function of time for both temperatures were plotted in figure 1.5. The velocities from experimental data were compared to the velocities calculated from mass balance by finite difference modeling, assuming equilibrium at the interface with zero diffusion in the solid phase:

$$v\,(c_s - c_l) = j^s - j^l \tag{1.1}$$

with $c_s = 0$ and $c_l = c_l^e$ the composition of the solid and liquid, and $j_s = 0$ and j_l their respective fluxes. The calculated velocities were observed to be lower than the experimental results, with the exception of the initial stage, and this discrepancy was more pronounced at higher temperatures. The dissolution started immediately after the liquid came into contact with the solid Ni during the heating step before reaching constant temperature, leading to an increase in velocity as the concentration gradient increases between the initial composition and the equilibrium point. The slight delay between the experimental data and the simulation can be attributed to the presence of the diffusion layer. Velocities initially increased for 20-30 seconds, reaching a peak of 0.6-0.8 $\mu m\,s^{-1}$ at 1115 °C and 4.8 $\mu m\,s^{-1}$ at 1145 °C, before

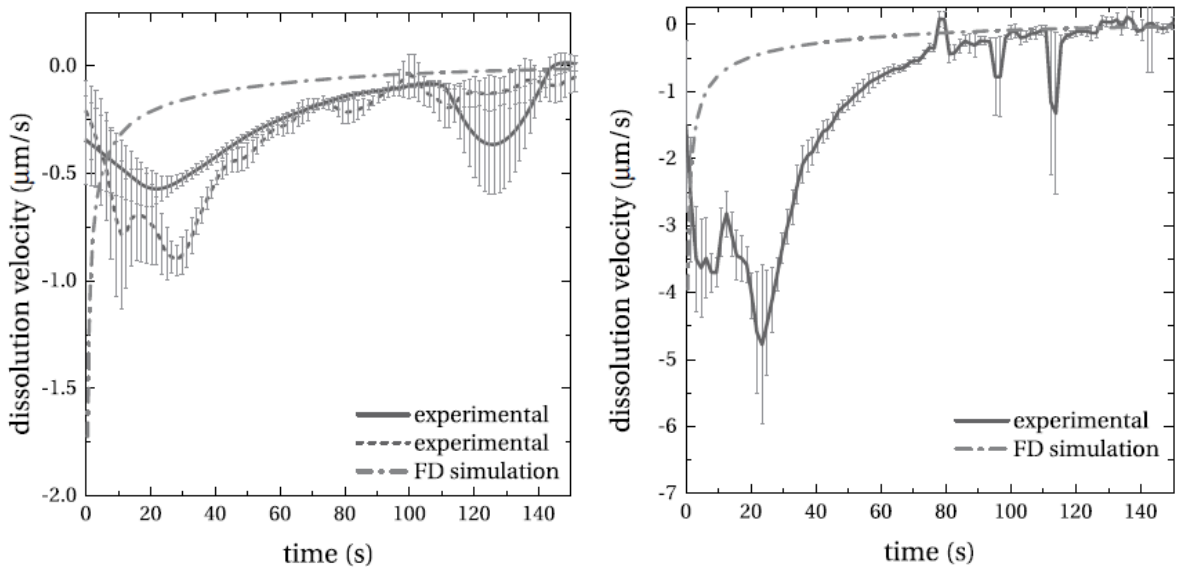

Figure 1.5 – Experimental and simulated dissolution velocity as function of time at 1115 °C *(left) and* 1145 °C *(right) [4]. Two experimental results are presented at* 1115 °C *to ensure reproducibility.*

beginning to decline. The dissolution process at both temperatures lasted for approximately 3 minutes and was followed by solidification during the temperature holding phase.

Post-mortem observation on the vertical section of the sample using an optical micrograph revealed that for the sample held at 1115 °C the Ni was dissolved homogeneously over the entire sample height, which rules out significant convection effects given the straight interface. On the other hand, the interface held at 1145 °C exhibited greater dissolution in the upper portion of the sample. Considering the increased density of the liquid at higher Ni content, solutal convection could potentially account for the curved interface, as the greater dissolution in the upper region might be due to a lower Ni content in the liquid. Furthermore, the authors also suggested the possibility of a solutal Marangoni effect, in which the liquid is drawn towards the interface as a result of the increased surface tension caused by the enriched liquid.

The expected dissolved thickness was calculated by simple Cu solute balance, assuming no diffusion in the solid:

$$\Delta r = r_0 \left(\sqrt{\frac{\rho_l^0}{\rho_l^e c_l^e}} - 1 \right) \tag{1.2}$$

with r_0 the initial radius, c_l^e equilibrium concentration, ρ_l^0 and ρ_l^e the densities of the pure liquid Cu and saturated liquid respectively.

For both temperatures, the experimentally observed dissolved thickness was significantly larger than the predictions from mass balance calculations. The dissolved thickness as function of time is reported in figure 1.7. At 1115 °C the experiment was repeated twice for the sake of reproducibility , which is why two curves are displayed in the left plot. The calculated thickness that should be dissolved based on equation 1.2 and accounting for an uncertainty of ±15 °C, ranged between 9 and 31 µm, which is lower than the experimental values of 40-50 µm. At 1145 °C the discrepancy was even more pronounced, with a calculated thickness

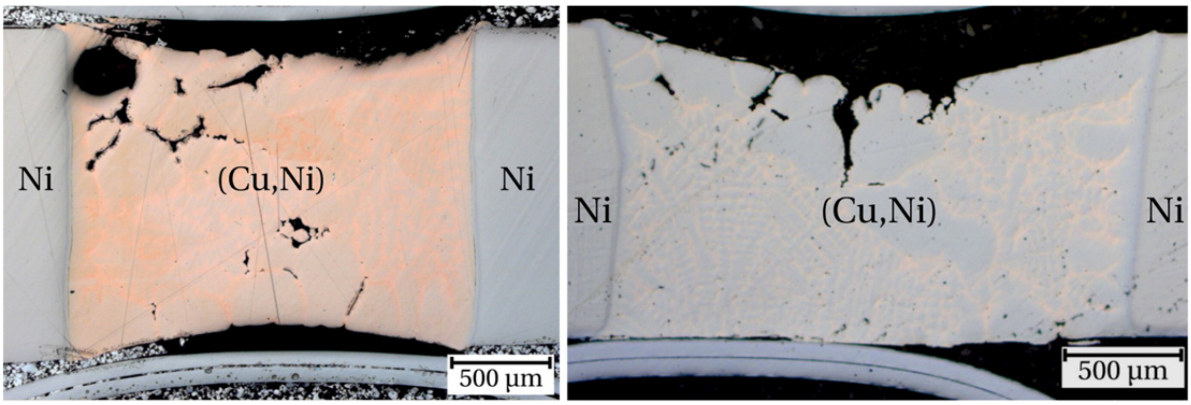

Figure 1.6 – Post-mortem optical micrograph image of the sample cross-section held at 1115 °C *(left) and* 1145 °C *(right) [4].*

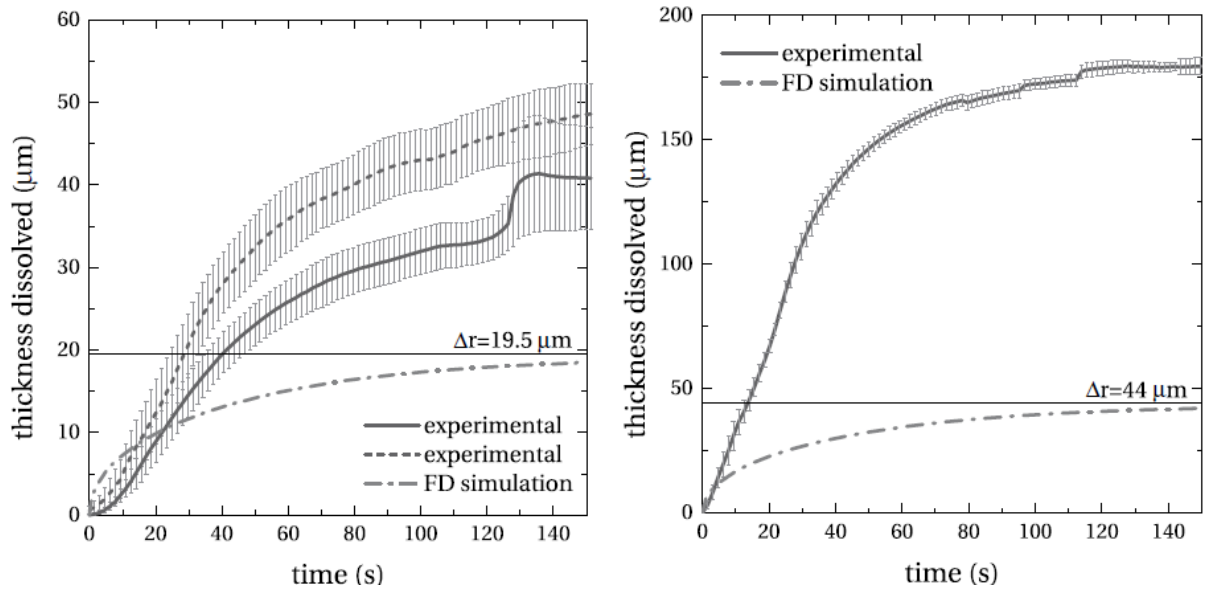

Figure 1.7 – Experimental and calculated thickness dissolved as function of time at 1115 °C *(left) and* 1145 °C *(right) [4].*

of 31-58 µm with ±15 °C uncertainty, while the experimental value reached 180 µm.
The EDX measurement revealed that the average concentration over the entire liquid area were found to be out-of-equilibrium, with 92.5 at.% at 1115 °C, and 81.7% at 1145 °C (versus 95.6 at.% and 89.8 at.% liquidus composition respectively), which still remains difficult to explain.

In light of the findings and limitations observed in the Cu-Ni experiment conducted by Deillon et al., an alternative solutal melting experiment will be introduced in the following section. This new approach aims to address and minimize some of the challenges encountered in the previous study, such as the formation of a diffusion layer during heating that hinders dissolution, concentration profiles derived from post-mortem analysis after a rapid cooling step, and results potentially influenced by thermal or solutal convection. By employing a

different investigation method and focusing on a different system, this alternative experiment seeks to validate the findings of the Cu-Ni study and confirm that the results are not exclusive to that particular methodology and sample set-up.

1.4 Experimental study of solutal melting

1.4.1 Experimental set-up

Following the unexpected and unprecedented behaviour revealed in the Cu-Ni solutal melting experiment where the interface is strongly out-of-equilibrium, a different experimental method is required in order to verify the reproducibility of these findings. X-ray radiography can address some of the problems faced in the previous Cu-Ni. In contrast to confocal microscopy, which only provides superficial information, X-ray radiography performs volume analysis of the sample by transmitting X-rays through it and collecting gray-level images from the detector on the opposite side during the process of solutal melting. This method requires working with samples thin enough to allow X-ray transmission, which in turn eliminates completely the convection effects observed in the Cu-Ni case. Additionally, the samples must exhibit a high enough contrast to distinguish between the two materials and phases. The contrast is associated with the materials' densities and absorption coefficients, meaning that a significant difference in X-ray absorption is necessary to discern variations in gray-levels. The differences in gray-levels can then be assigned to the material composition, allowing for in-situ monitoring of concentration profile evolution over time.

To identify a suitable system for the X-ray radiography experiment that can be compared with the Cu-Ni system, several binary phase diagrams were examined using different criteria. The primary criterion was to find a binary system with properties similar to those of the Cu-Ni system. The system is required to have a similar phase diagram in a portion or the entire range of temperatures, featuring only one liquid phase and one solid phase with a minimum solubility of 10% to ensure that both solid and liquid are out of equilibrium during the initial phase of solutal melting. The two elements should display a significant mass absorption contrast using X-ray radiography. Temperature ranges were chosen from 400 to 1000 ℃ to ensure that the diffusion is high enough. The 1000 ℃ limit is due to the furnace's limited capacity to ramp up any higher temperatures. Heavy elements that might act as a beam stop were excluded, as well as harmful elements such as Cd. Elements like Al that might form oxide layers at the interface which hinder diffusion and act as a barrier between solid and liquid were also excluded.

The system which corresponds best to the above mentioned criteria is the Au-Ag system. Its phase diagram, presented in figure 1.8 closely resembles the Cu-Ni system where both elements are totally miscible. The Ag melting point is 961 ℃. Although the temperature is at the upper end of the range that the furnace is able to handle, it can nevertheless still adequately perform the experiment. Furthermore, Ag and Au are directly above one another in the periodic table, suggesting that a noticeable mass absorption contrast could be expected in X-Ray radiography due to their density differences.

The Au and Ag foils are 50 µm thick with a purity of 99.95% for Au and 99.9% for Ag. The Ag foil is cut into a 3 mm diameter disc, and disposed in the center of a hollow Au foil as presented in figure 1.9 in a way that when the sample is heated up above Ag melting point,

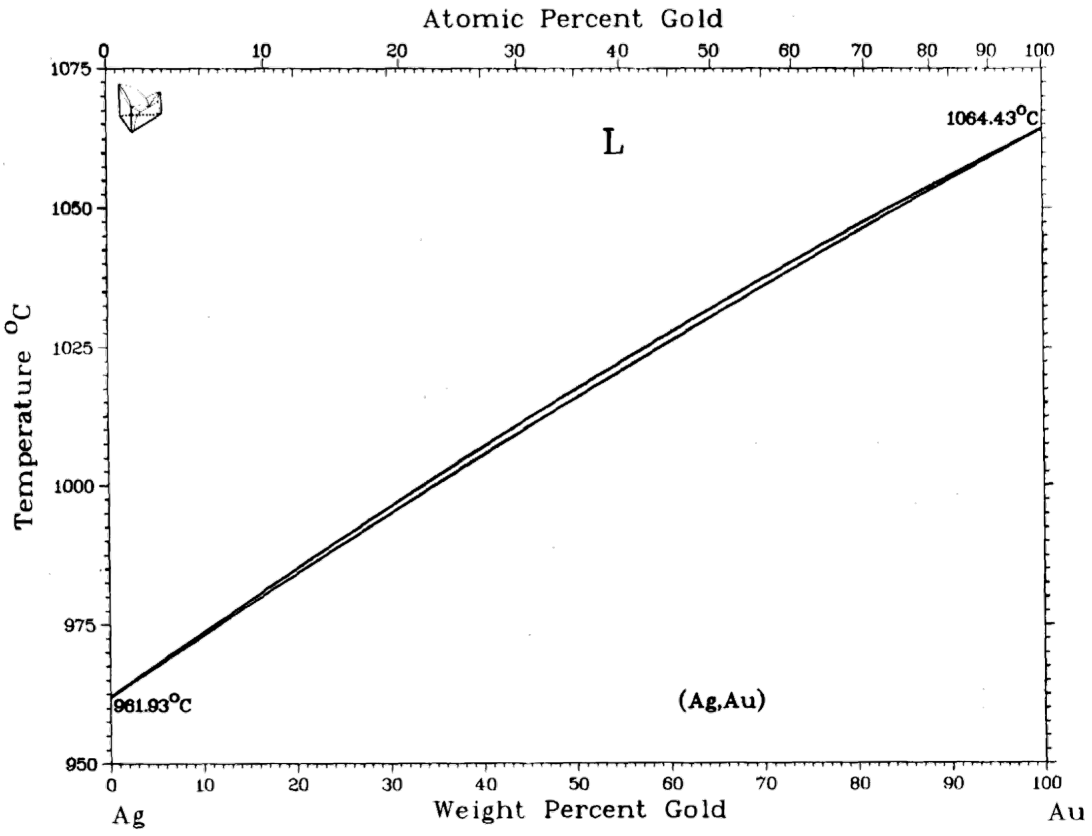

Figure 1.8 – Au-Ag binary phase diagram [22].

the liquid Ag remains contained within the the gold foil.

The experiment was realized at the Institute of Materials Physics in Space at the German Aerospace Center (DLR e. V.) in Cologne, Germany using the XRISE-PF facility [23] processing the sample in an isothermal furnace insert. The furnace was designed to deliver homogenous temperature distribution inside the sample and was initially developed to study equiaxed microstructure evolution and grain interaction [24]. The furnace body consists of boron nitride, an outer shell, and a piston. The boron nitride piston applies variable pressure on the sample by adapting the rods length that hold the furnace between two metal plates, to ensure uniform thickness at its molten state. The meander shaped graphite heater is 150 µm thick, wrapped around the furnace body to deliver heat uniformly. For temperature control, a thermocouple with a diameter of 0.5 mm situated inside the furnace wall is used, with its tip positioned at the height of the sample plane. Having the thermocouple inside the furnace wall avoids interference with both the X-ray beam path and the temperature field inside the sample. But as a result, the thermocouple is closer to the heater, which means that measured temperatures are higher than that of the sample. The furnace is wrapped in six sheets of 1.25 mm alumina paper at the sides, and graphite foam on top and bottom for heat insulation. This heat insulation allows the furnace to operate at 700 ℃ for several hours, and withstand short-term experiments up to 1100 ℃. For ground experiments, the furnace is water-cooled inside an aluminum cartridge, which can be vacuumed down to 10^{-3} mbar. The sample diameter is

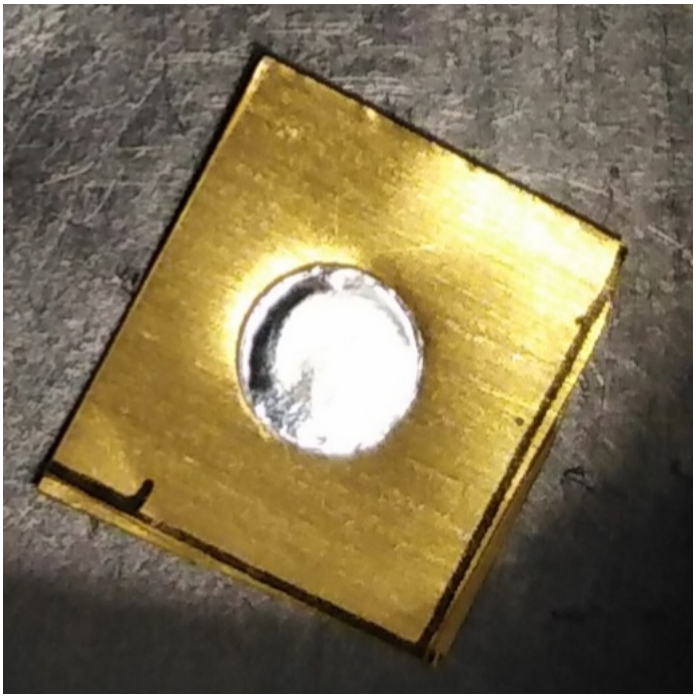

Figure 1.9 – Ag foil (gray) in the center of Au foil (yellow).

restricted to 18 mm and is positioned in the center of the furnace between the furnace body and the piston. To prevent direct contact between the liquid sample and the furnace environement, the sample is sandwiched between two 150 µm thin graphite foils that present good heat transfer to the sample. As schematic of the operating furnace is shown in figure 1.10. The X-ray beam passes through holes on the insulation material and furnace mounting then encouters, in top of the sample, 6 mm of boron nitride and two graphite foils. The boron nitride and graphite foils are transparent enough to leave the image quality undisturbed.

The X-ray source consists of a 5 µm thin tungsten layer on an aluminum target that generates a Bremsstrahlung spectrum with a Kα-line at around 69 keV. The X-ray source delivers a maximum acceleration voltage of 100 kV and an electron beam current of 200 µA. The voltage value determines the energy of the electrons hitting the target, and consequently the energy and the produced photons. The electron beam current determines the number of electrons hitting the target and the amount of photons produced by the tube. The higher the energy of the photons the less they interact with the sample, leading to a bright image and lower contrast. Additionally, an increase in operating power results in a larger spot size, which compromises the spatial resolution. Also, a sufficient photon quantity is needed for good signal to noise ratio. Therefore, an optimal value of the voltage and electron current is necessary for a good image quality. These parameters vary depending on the nature of the elements and the sample thickness. The operating source parameters for the Au-Ag experiment are 70 kV acceleration voltage and 134 µA electron beam current. A compromise between the spatial resolution and the field of view size is achieved by setting the proper source-to-sample and sample-to-detector distance. Due to the furnace geometry requirements, the source-to-detector distance is 150 mm and the source-to-sample distance is 66 mm. A cone-shaped

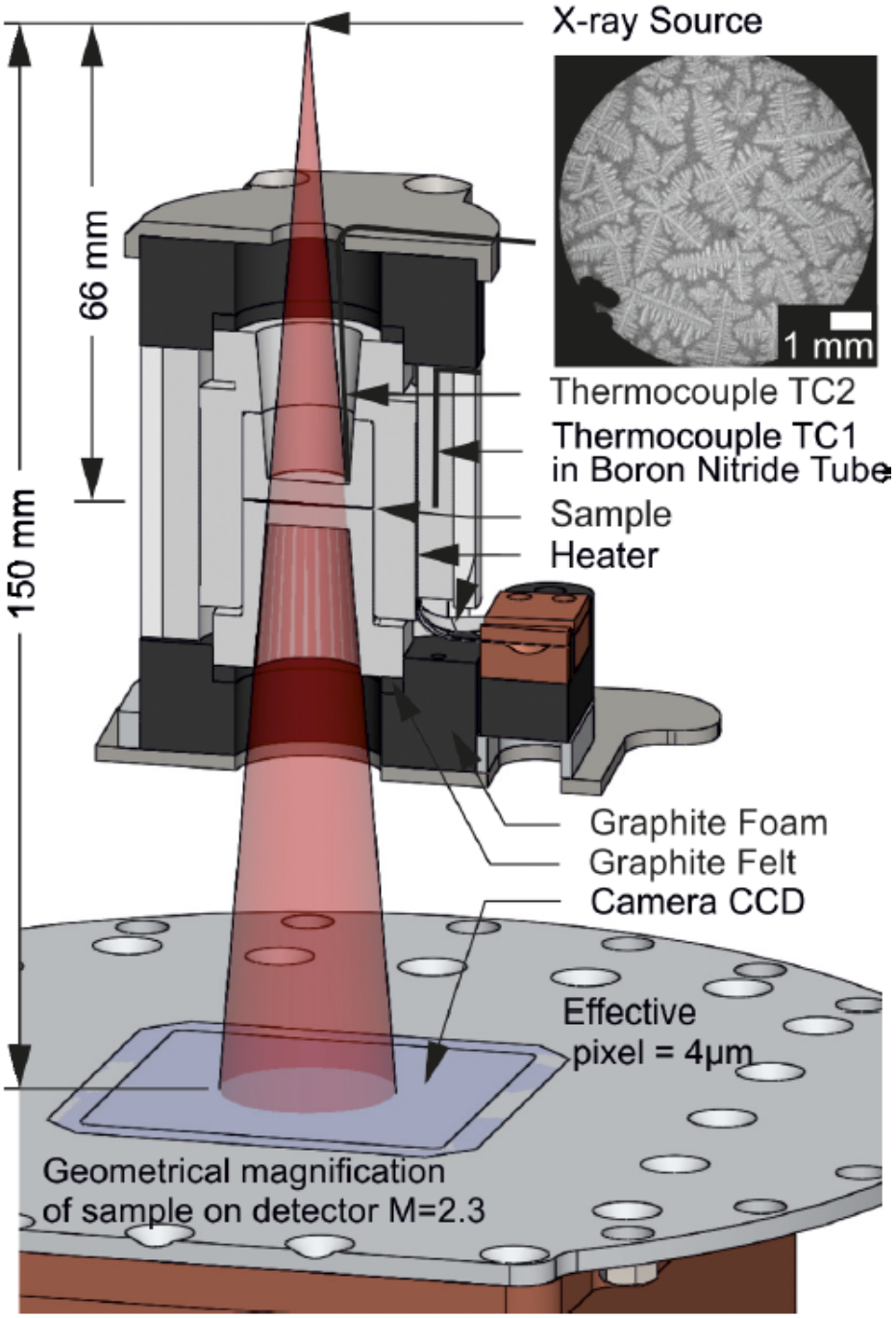

Figure 1.10 – Sketch of the X-ray imaging system showing the X-ray source to sample and to detector distance [24].

polychromatic X-ray beam goes through the sample and is collected by a detector which features a digital camera with a 24 mm $\times$ 36 mm active array CCD sensor and a structured CsI scintillator. These settings result in a sample magnification of 2.3 on the detector, a field of view of 10.5 mm, and an effective pixel size of 4 µm $\times$ 4 µm.

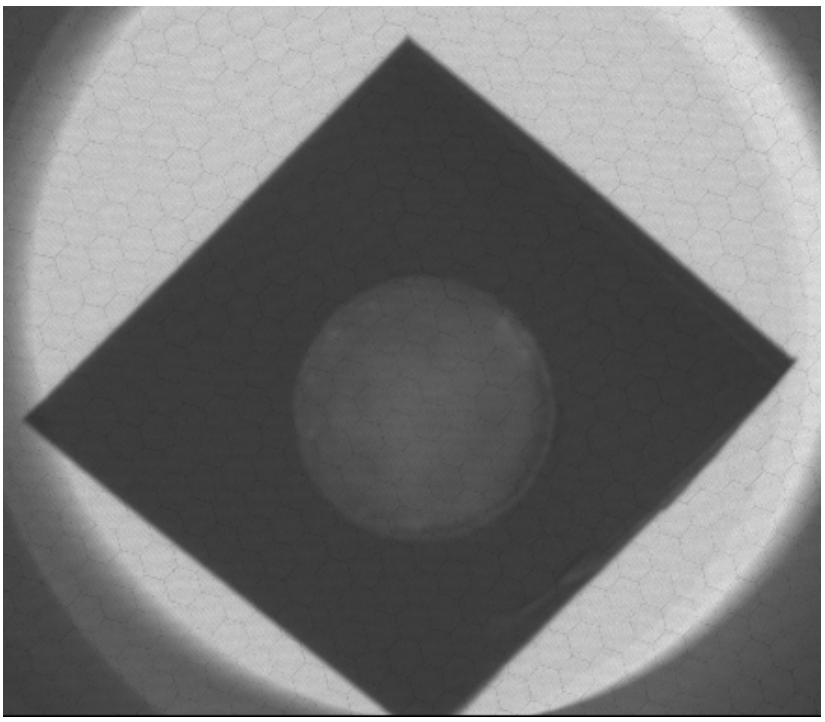

Figure 1.11 – Raw X-Ray image of a Au-Ag sample.

The resulting gray-level image is shown in figure 1.11. The Ag disc appears brighter due to lower absorption coefficient as compared to Au. The structured patterns correspond to the scintillator structure that are visible due to the chosen current and voltage parameters for this particular experiment. The Au-Ag solutal melting experiment was performed at 1000 °C with an image acquisition frequency of 1 FPS. Prior to ramping up the temperature, the furnace environment is vacuumed to at least 10^{-5} mbar using a secondary vacuum pump. The heating process goes through several steps before reaching the target temperature:

- Heating from room temperature to 300 °C in 16.6 min. This slow heating is chosen so that sufficient time is given to the pump to evacuate the various gases that evaporates as the temperature increases.
- Steady heating from 300 to 900 °C in 18.3 min. This corresponds to the furnace's maximum heating rate that ensures that the expected temperature calculated from the delivered power matches the furnace temperature measured by the thermocouple.
- Holding at 900 °C for 5 min to achieve thermal equilibrium since a minor lag subsists between the simulated temperature calculated from the delivered power and the real temperature measured by the thermocouple that might also be different from the sample's temperature since the thermocouple is positioned inside the furnace wall.
- Heating from 900 to 1000 °C in 6 min, with Ag melting occurring around the 4-minute mark at 966 °C, which is closely aligned with the the 961 °C melting point of pure Ag. The rapid heating rate of 16.6 °C/min also plays a role in delaying the onset of melting to higher temperatures.

- Holding at the target temperature of 1000 ℃ for 5 minutes, during which solutal melting is observed, followed by a free cooling process. This process took roughly 2 hours for the furnace to cool down to room temperature, featuring non-linear initial cooling rates.

The camera starts recording at around 950 ℃, prior to the melting point of Ag, up until the Ag solidifies during the free cooling step. The choice of operating at 1000 ℃ is to ensure both solid and liquid phases out-of-equilibrium during the dissolution process.

1.5 Data analysis

1.5.1 Image analysis

All image analysis were performed using ImageJ software to track the interface motion and composition changes from the gray-level images. The brightness and contrast were further enhanced to emphasize visually the contrast difference between the solid and liquid, making it easier to locate the interface. An example is presented in figure 1.12.

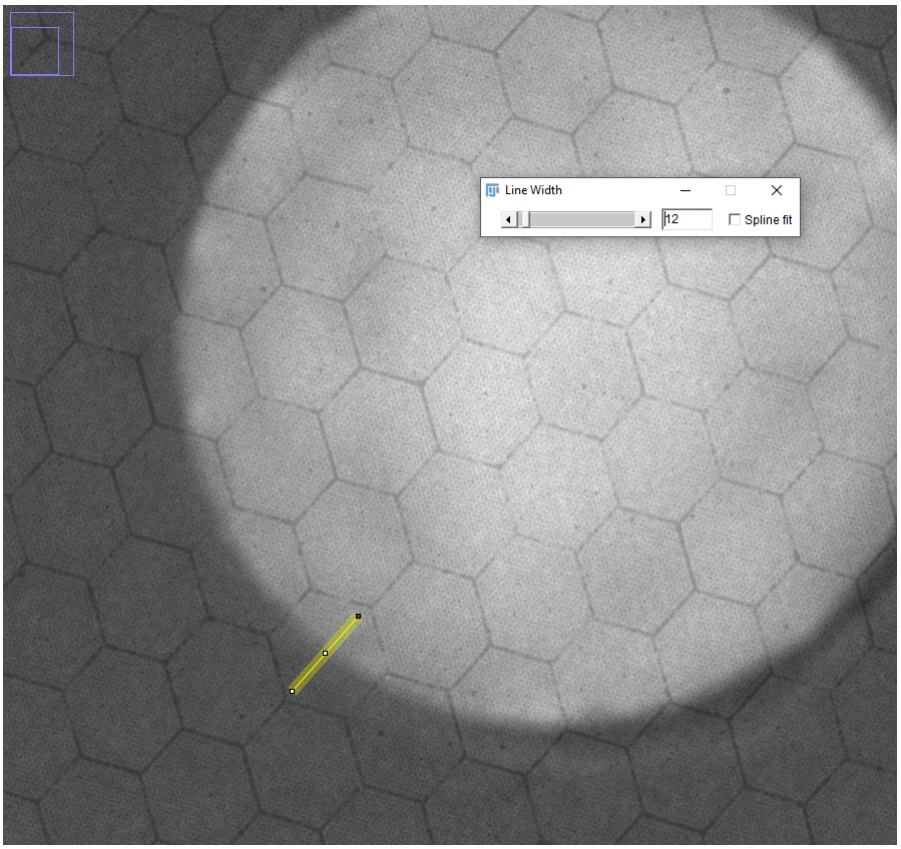

Figure 1.12 – Gray level image of a Au-Ag sample after brightness and contrast adjustments, with Ag being at liquid state. The yellow line represents the segment where the gray-level values were collected for plotting the concentration profile.

In the figure, some hexagons are visible and correspond to the detector patterns that tamper with the gray-level values of the images. One possible solution to get rid of the patterns was to substract a reference image of the detector from the sample images. However, this resulted in a very deteriorated image and the patterns were not entirely removed. Therefore, the images were kept unchanged and the gray-level measurements for calculating the concentration profiles were collected from a segment positioned in way that it did not cross the detector patterns as shown in figure 1.12. The width of the segment was set to 12 pixels, to get an averaged gray-level intensity at any given position. In addition to the detector patterns, another issue arouse that also interferes with the gray-level intensity. As it can be noticed from both figure 1.11 and 1.12, small gray-level variations are observed in the Ag sample before and after melting. These variations originate from an imperfect contact between the Ag and Au foil, leading a slightly deformed Ag foil as observed in figure 1.9, leading to small thickness variations in the sample post-melting which can be wrongly interpreted as a concentration variation since the gray-level intensity depends on both the nature of the element and its thickness.

The major problem that was encountered during the experiments was due to an imperfect contact with the graphite the shrinking of the Ag liquid phase right after melting due to wetting on the graphite substrate enclosing the Ag-Au sample. A particularly catastrophic example is shown in figure 1.13. The liquid Ag wets the graphite foils leading to an imperfect solid-liquid contact as the liquid phase thickness increase due to wetting, leading to strongly inhomogeneous grey level in the liquid phase. From all the experiment performed, only those leading to limited variation of gray-level after melting (see figure 1.12) were analyzed in this work.

1.5.2 Interface tracking

Tracking the interface motion is achieved through image binarization by choosing a threshold that results in a contour coinciding with the interface position after binarization. ImageJ has several implemented binarization methods for converting gray-level images into black and white [25]. Among the available methods, the Mean method, which uses the mean gray-levels as a threshold, provided the most suitable result that aligns well with the interface position. The interface is located after image binarization at the position where the ratio of black and white pixels (0 and 1 ratio) is closest to 50%. Figure 1.14 shows a zoom-in of a portion of the Ag-Au interfacial region before and after binarization. The segment where the binary values are collected is oriented to point towards the center of the Ag disc since the interface advances radially. The interface position is monitored using this procedure on the entire stack of images. By doing so, the interface position evolution over time can be plotted, and the interfacial velocity is extracted from the slope.

One can see from figure 1.14 that the interface position is determined with an uncertainty ranging from 3 to 4 pixels in average. Knowing that each pixel is a 4 µm$\times$4 µm square, this leads to an uncertainty of 4-12 µm on the interface position which is moderate considering that the dissolution is over a hundred microns as will be shown later on in the following section. Another consequence of the low image resolution is having a concentration averaged over 4 µm, which can be problematic in the vicinity of the interface where the concentration gradients are important.

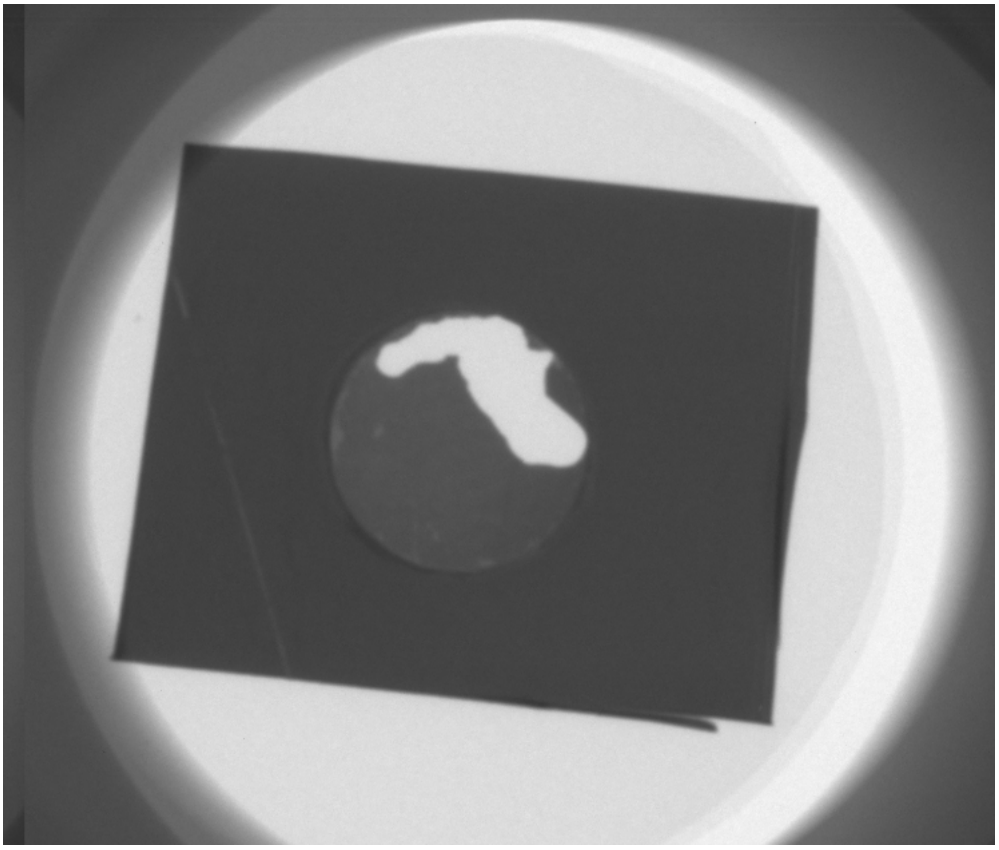

Figure 1.13 – Raw image of Au-Ag sample after melting, showing the liquid Ag retracted into itself leading to imperfect solid-liquid contact.

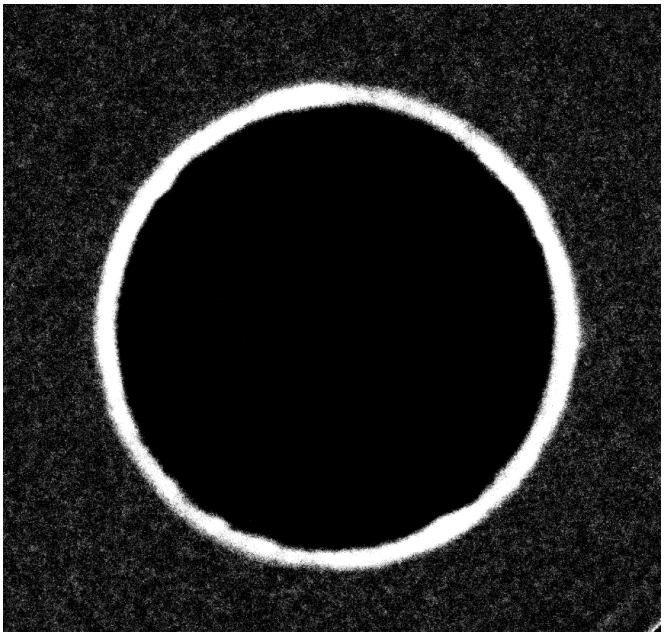

Figure 1.15 – Image of Au-Ag at the end of solutal melting, obtained by subtracting the first image taken right after the melting of Ag. The white area defines the distance traveled by the interface.

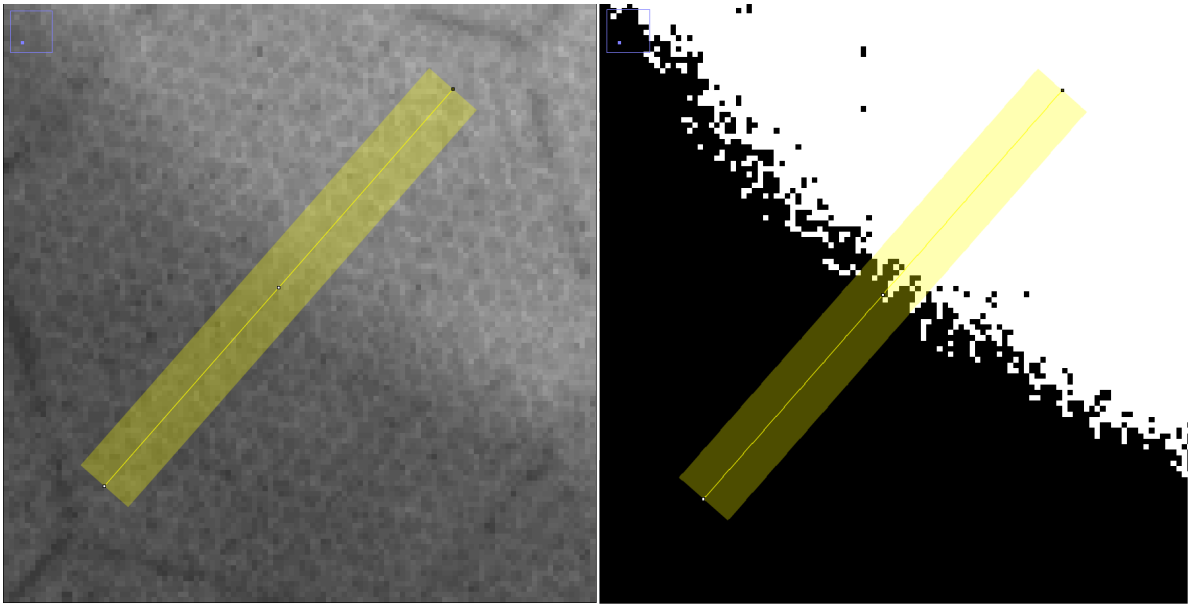

Figure 1.14 – Zoom-in at the interfacial region before (right) and after (left) binarization. The yellow segment is used to measure the gray-level for concentration calculations in the left image, and for interface position determination.

Binarization method turned out to be more efficient for tracking the interface and measuring its velocity. An alternative method could also be employed to observe the interface displacement, based on the image subtraction function available in ImageJ. This latter method relies on subtracting the stack of images by the first image where dissolution begins. The differences and changes of the images relative to the first image are highlighted using this method and the front displacement can thus be observed, defined by the white ring in figure 1.15 as it expands throughout time during dissolution. The radial expansion of the liquid at the expense of the solid phase is put in evidence, and the interface keeps its circular shape during the whole process. Using this method, the total interface displacement can be estimated by measuring the thickness of the white ring. Tracking the interface displacement however is not easily done, mainly due to the fact that differences between the first few images from the early stage of melting and the initial image are not very much pronounced, making it hard to define the boundaries of the white ring corresponding to the liquid front.

1.5.3 Composition determination

The concentrations can be derived from the gray-level values using Beer-Lambert's law, linking the concentration to the transmitted intensity that's attenuated as the X-rays pass through matter due to absorption or scattering, which depends on the material properties, the nature of the radiation, and the detector characteristics. The Beer-Lambert law for a monochromatic radiation connecting the gray-level intensity I to the concentration is expressed as the following:

$$I = I_0 \exp(-\mu d) \tag{1.3}$$

with I_0 the initial intensity of incident beam in arbitrary units, ranging from 0 to 255, reflecting the gray-level value. μ (cm^{-1}) is the mass absorption coefficient, and d (cm) the sample thickness.
The linear mass absorption can also be written as:

$$\mu = \mu_m \rho \tag{1.4}$$

μ ($cm^2\,g^{-1}$) is the mass absorption coefficient, ρ is the material density ($g\,cm^{-3}$).
This latter quantity is assumed to depend on the concentration of the elements following a simple mixture rule for a binary mixture:

$$\mu_m \rho = x_A \mu_{m,A} \rho_A + (1 - x_A) \mu_{m,B} \rho_B \tag{1.5}$$

where x_A is the concentration of the element A.
For a polychromatic X-ray source the intensity depends on the photon energy E (keV), the element fraction X_i, and the temperature T(K). Equation 1.3 becomes:

$$I = I_0 \exp\left(-d \sum_{i=1}^{n} x_i \mu_{m,i} \rho_i(T) \right) D(E) \tag{1.6}$$

where $D(E)$ is a correction reflecting the quantum efficiency of the detector, proportional to $\exp(\mu(E) d_{sc})$, where $\mu(E)$ is the linear absorption coefficient of the scintillator material and d_{sc} is the scintillator thickness. The scintillator presents a monotonic behaviour at X-ray energies above 17 keV and the intensity are assumed to be the same for each pixel due to the integral nature of the recorded intensities [26]. $D(E)$ is therefore neglected. The final Beer-lambert expression is given by the following equation:

$$I = I_0 \exp\left[-d \left(x_{Ag} \mu_{m,Ag} \rho_{Ag} + (1 - x_{Ag}) \mu_{m,Au} \rho_{Au} \right) \right] \tag{1.7}$$

From equation 1.7 the concentration is calculated as follow:

$$x_{Ag} = \frac{1/d \ln(I/I_0) + \mu_{m,Au} \rho_{Au}}{\mu_{m,Au} \rho_{Au} - \mu_{m,Ag} \rho_{Ag}} \tag{1.8}$$

Determining the composition in binary alloys in the case of a polychromatic light is not straight forward, mainly due to mass attenuation coefficient in Beer-Lambert's law of pure elements that are unknown since they vary as function of the photon energy. To overcome this problem, the mass absorption coefficients are callibrated from the gray-level value of the pure element taken separately. Since the gray intensities, the densities, and the concentrations are known, the mass absorptions can be deducted from equation 1.7.

1.6 Results and discussion

1.6.1 Interface position and velocity

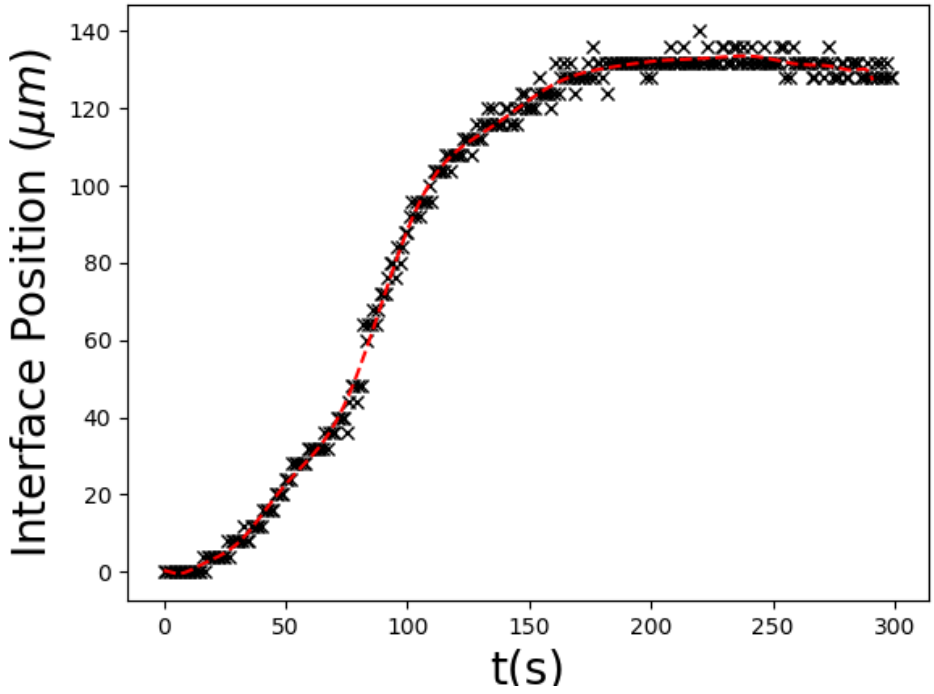

Figure 1.16 – Au-Ag interface position as function on time

The interface position was monitored using the binarization method as showcased in figure 1.14. The resulting interface position profile is plotted in figure 1.16. Since the recording started just prior to the melting of solid Ag, the initial position remains at zero for the first few seconds. After melting of the solid pure Ag, the interface starts moving in the direction of the solid Au for a duration of 150 s before stabilizing at a fixed position. This stage corresponds to solutal melting. Upon completion of the melting phase, solidification ensues, resulting in the interface position gradually shifting in the opposite direction during the final stage of the experiment. This movement was also directly observable in the gray-level images. Since isothermal solidification is driven only by diffusion in the solid phase, it is much slower than the solutal melting stage.

The interface velocity is derived from the slope of the position curve and is shown in Figure 1.16. Initially, the velocity is 0 when the interface remains motionless, and then it increases monotonically. This gradual velocity increase might be explained by the fact that right after melting at 961 ℃, the liquidus composition is 100% Ag. The temperature takes approximately a minute and half to reach the aimed temperature of 1000 ℃. As the temperature rises, the liquidus point changes accordingly and is further away from the composition of pure Ag. The supersaturation (given by the gap between the liquidus and the initial liq-

uid composition of Ag) increases, increasing thus the available driving force, which might explain the velocity increase.

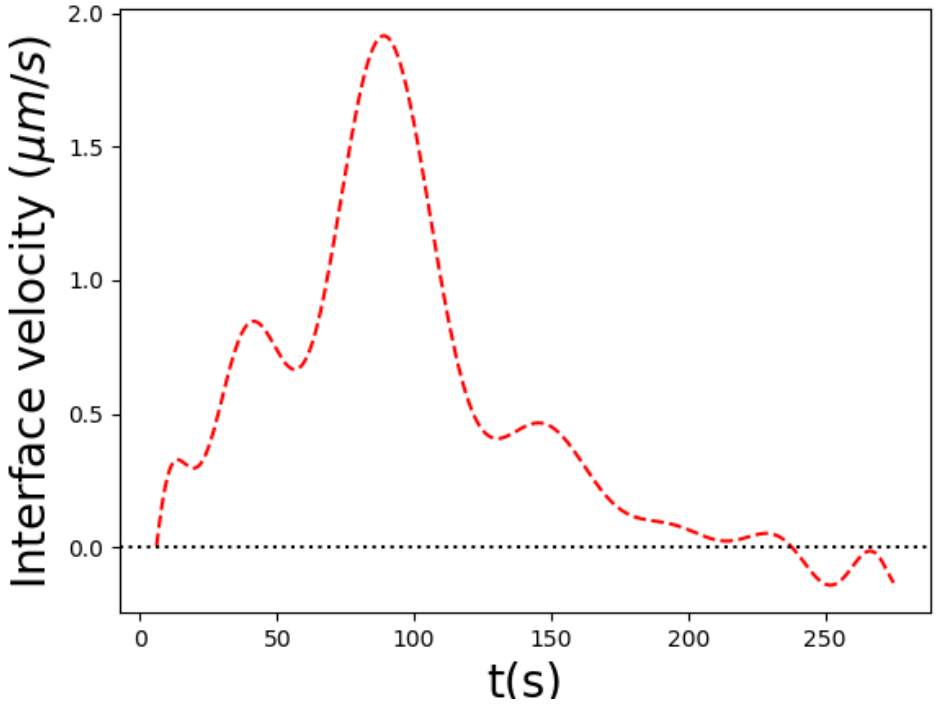

Figure 1.17 – Interface velocity as function of time.

The velocity peaks when the sample reaches 1000 ℃, and then, as more Au is dissolved, less driving force is available, causing the interface velocity to slow down. A small resolidification is observed at around 240 secondes, indicated by the negative value of the velocity.
This sample was examined post-mortem using a Scanning Electron Microscope (SEM). The post-mortem Au-Ag micrography is shown in figure 1.18. Two concentric circles can be noticed in the Ag sample. The inner circle, with a measured diameter of 3 mm, corresponds to the initial Ag sample size, and the outer circle represents the dissolved thickness. The dissolved thickness is given by the difference between the outer and inner circle, and is found to be 173 µm.
The dissolved thickness was determined using the subtraction method by measuring the thickness of the white ring shown in figure 1.15, and was found to be equal to 170 µm, which agrees surprisingly well with the SEM measurement.

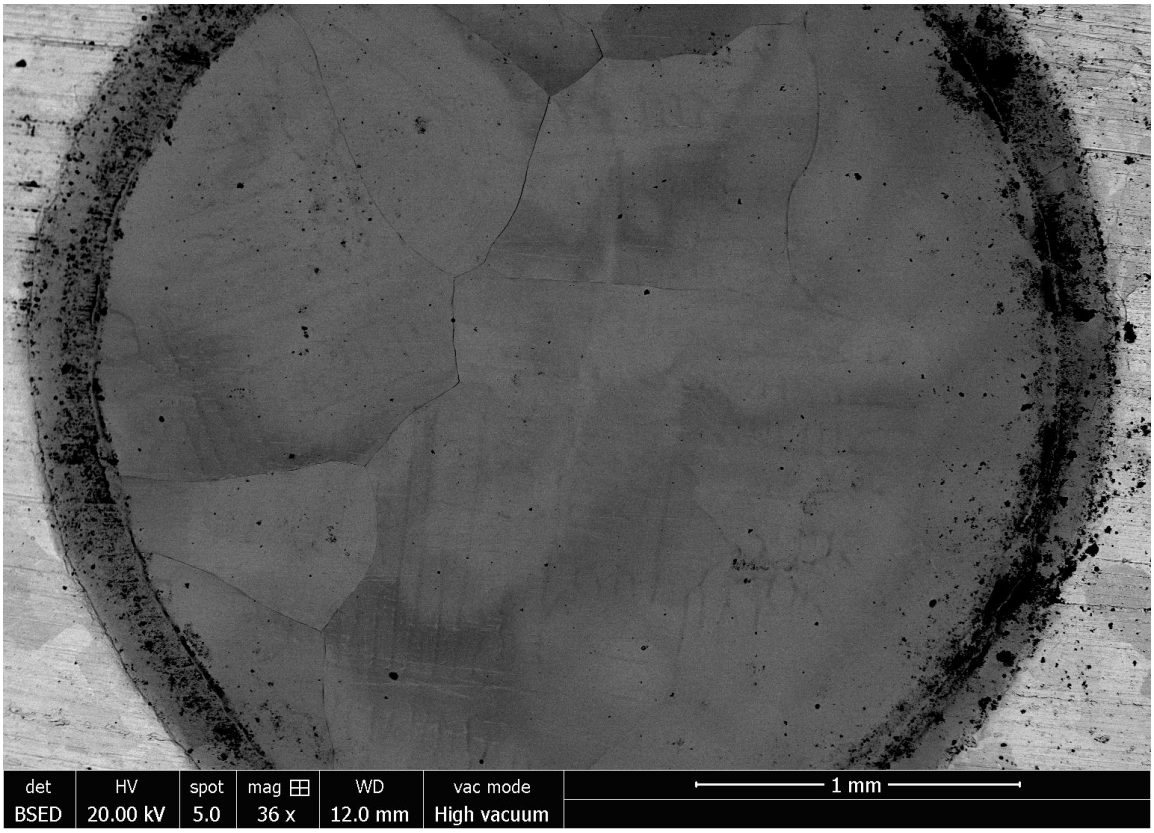

Figure 1.18 – Backscattered eletrons image of a post-mortem Au-Ag sample: The central region, formerly liquid Ag, appears darker, while the surrounding pure gold material exhibits a brighter appearance. The two distinct ring-shaped interfaces represent the thickness of material dissolved.

1.6.2 Interface composition evolution

Few assumptions regarding the parameters involved in equation 1.7 were made to calculate the concentration. The gray-levels are considered constant with respect to temperature, as temperature changes during the heating stage did not result in a noticeable change in gray-level values. The thickness of the Ag sample is also assumed to be constant before and after melting, and during the whole dissolution process.
The density of the solid phase is estimated using the following equation [27]:

$$\rho^s(T_{exp}) = \rho^s(25\,^\circ\mathrm{C})\,[1 - 3\alpha\,(T_{exp} - 25)] \tag{1.9}$$

α being the linear thermal expansion coefficient at 25 ℃. The liquid density is given by:

$$\rho^l(T_{exp}) = \rho_M - \eta\,(T_M - T_{exp}) \tag{1.10}$$

where ρ_M is the density at the melting temperature T_M, and η is the volumetric thermal expansion of the liquid phase. The values of densities and thermal expansion coefficients at 1000 ℃ were taken from [28, 29] and are reported in table 1.1.

The X-ray source being polychromatic, the only way to extract the mass absorption coefficient of a given phase is by measuring the gray-level intensity of a known composition,

El.	η ($\mathrm{g\,cm^{-3}\,K^{-1}}$)	$\alpha \times 10^{-6}$ ($\mathrm{K^{-1}}$)	$\rho^s(25℃)$ ($\mathrm{g\,cm^{-3}}$)	$\rho^l(T_M)$ ($\mathrm{g\,cm^{-3}}$)	$\rho^s(1000\,°C)$ ($\mathrm{g\,cm^{-3}}$)	$\rho^l(1000\,°C)$ ($\mathrm{g\,cm^{-3}}$)
Ag	-9.78×10^{-4}	18.9	10.5	9.32	10.31	9.28
Au	-12.7×10^{-4}	14.2	19.32	17.2	18.51	17.28

Table 1.1 – Values of volumetric thermal expansions, thermal expansion coefficients, and densities of Ag and Au [28, 29].

then using Beer-Lambert's equation to calculate the specific mass absorption. The value of μ_m is assumed to be solely related to the wavelength passing across the material. $\mu^s_{m,\mathrm{Au}}$ is the easiest to extract since the gray-level intensity at 1000 °C can be measured directly from the images, and the sample composition is known. $\mu^l_{m,\mathrm{Ag}}$ is calculated by measuring the gray-level intensity directly on the Ag melt. Initially, right after melting, the liquid Ag is at pure state $x_{\mathrm{Ag}} = 1$ and $x_{\mathrm{Au}} = 1 - x_{\mathrm{Ag}} = 0$, equation 1.7 becomes:

$$I^l = I_0 \exp\left(-\mu^l_{m,\mathrm{Ag}}\,\rho^l_{\mathrm{Ag}}\,d\right) \tag{1.11}$$

The value of I_0 can be determined by measuring the gray-level of the detector after removing the sample. d is taken as 50 µm and is assumed to be constant. Knowing all the parameters, $\mu^l_{m,Ag}$ can easily be estimated:

$$\mu^l_{m,\mathrm{Ag}} = -\frac{1}{\rho^l_{\mathrm{Ag}}\,d}\ln\left(I/I_0\right) \tag{1.12}$$

$\mu^s_{m,Au}$ is calculated in the same manner. However, equation 1.7 is valid for a single phase, and in order to calculate the concentration in the liquid phase, both $\mu^l_{m,\mathrm{Ag}}$ and $\mu^l_{m,\mathrm{Au}}$ are required (respectively $\mu^s_{m,\mathrm{Ag}}$ and $\mu^s_{m,\mathrm{Au}}$ for the solid phase). The value of $\mu^l_{m,Au}$ is unknown since it requires measuring liquid Au gray intensity. To circumvent this issue, the ratio $\mu^l_{m,\mathrm{Ag}}/\mu^s_{m,\mathrm{Ag}}$ was calculated from equation 1.7 using the intensities around the melting point at 961 °C before and after the melting of Ag:

$$\frac{\mu^l_{m,\mathrm{Ag}}}{\mu^s_{m,\mathrm{Ag}}} = \frac{\ln(I_l/I_0)}{\ln(I_s/I_0)} \times \frac{\rho^s_{\mathrm{Ag}}}{\rho^l_{\mathrm{Ag}}} \tag{1.13}$$

At 960 °C the measured parameters are $\rho^s_{\mathrm{Ag}} = 9.943\,\mathrm{g\,cm^{-3}}$, $\rho^l_{\mathrm{Ag}} = 9.296\,\mathrm{g\,mL^{-1}}$, $d = 50\,\mu\mathrm{m}$, $I_0 = 214.745$, $I_s = 82.252$, and $I_l = 84.065$. The intensity ratio in equation (1.13) is calculated as:

$$\frac{\ln(I_l/I_0)}{\ln(I_s/I_0)} = 0.98 \tag{1.14}$$

The change in intensity before and after phase transformation is negligible and can therefore be disregarded in the ratio 1.13. The mass absorption coefficient is found to be inversely proportional to the density ratio. As a first approximation, it can be considered that:

$$\frac{\mu^l_{m,\mathrm{Ag}}}{\mu^s_{m,\mathrm{Ag}}} \approx \frac{\rho^s_{\mathrm{Ag}}}{\rho^l_{\mathrm{Ag}}} \tag{1.15}$$

El.	μ_m^l ($cm^2\,g^{-1}$)	μ_m^s ($cm^2\,g^{-1}$)	I_0	$\rho^s(1000\,°C)$ ($g\,cm^{-3}$)	$\rho^l(1000\,°C)$ ($g\,cm^{-3}$)
Ag	7.961	7.166	214.745	10.31	9.28
Au	11.153	10.412	214.745	18.51	17.28

Table 1.2 – Values of mass absorption coefficients and densities at 1000 °C *of Ag and Au.*

Both μ^s_{Ag} and μ^l_{Au} can then be calculated from the densities at 1000 °C. All the parameters for calculating and plotting the concentration profile are therefore known, and given in Table 1.2.

Plots of Ag concentration profiles with respect to position are shown in figure 1.19 for two different times, 80 and 300s. The red dashed lines represent the equilibrium solidus and liquidus. The vertical blue span and horizontal orange span respectively represent the interfacial region (deduced from the image analysis) and its corresponding concentration range. While the associated uncertainty seems quite large, the differences between equilibrium and measured values are also large enough to be considered as significant.

On the left side of concentration profiles for the two times, near the zero position, lies liquid Ag with an Ag concentration approaching 90%. It is actually close to 100% farther in the liquid, which has not been captured here due to the interface tracking approach described previously. At positions further along the horizontal axis is solid Au with an Ag concentration close to but not 0. This gives another hint on the uncertainty associated with the conversion of greyscale values into concentration, on the order of a few wt%. On the profile captured at 80 seconds, the concentration values near the zero position are above the equilibrium concentrations marked by the red dashed lines, with a liquidus of 65.5 wt% Ag and a solidus of 64.5 wt% Ag, as derived from the Ag-Au phase diagram. The interface is located somewhere between 220 µm and 258 µm. The first thing to note is that the liquid and solid phase in the interfacial region are significantly out-of-equilibrium. Both the solid and liquid phase concentrations are located in the one-phase domain of the solid beneath the solidus value, reproducing thus the same behaviour reported in the Cu-Ni solutal melting experiment by Deillon et al. The peak discernible at 300 µm stems from a small local gray-level variation of unknown origin (but most probably a local thickness variation) and is not representative of diffusion or Ag content.

The concentration profile in the lower graph is plotted at 300 s, at the end of the experiment. The liquid concentration between 0 and 120 µm is closer to the equilibrium value, but still has not reached equilibrium. The liquid phase expanded at the expense of the solid Au, with the solid-liquid interface now located between 270 µm and 315 µm. As with the first profile, the concentration near the interface remains strongly out-of-equilibrium. The interface stopped its motion after 160 s, giving enough time for the dissolved Au to diffuse into the liquid phase and bring the liquid far from the interface slightly closer to equilibrium. However, the liquid in the interfacial region, which is usually expected to be at equilibrium state, remains far from the liquidus and is closer to the solid composition of pure Au. This liquid region, characterized by a concentration beneath the liquidus and solidus values, extends approximately over 140 µm. This suggests that, the dissolved Au remained confined in the interfacial region during the whole process of solutal melting.

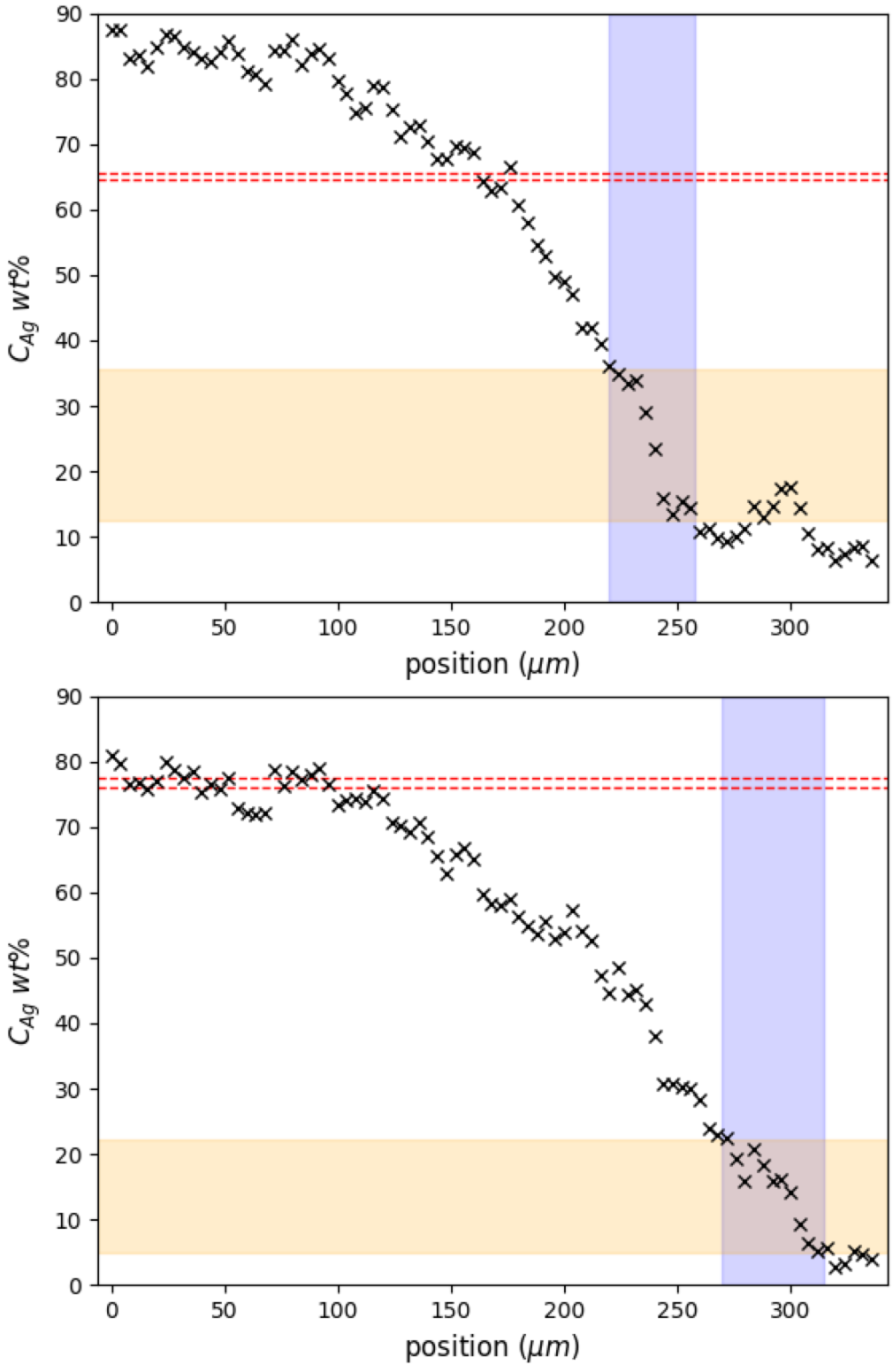

Figure 1.19 – Concentration profiles in the vicinity of the solid-liquid Au-Ag interface at: 80s after the beginning of solutal melting (upper image), 300s towards the end of solutal melting (lower image). The red dashed lines represent the liquidus (upper line) and solidus (lower line) composition. The blue span represent the interface region and the orange span correspond to the associated interface compositions.

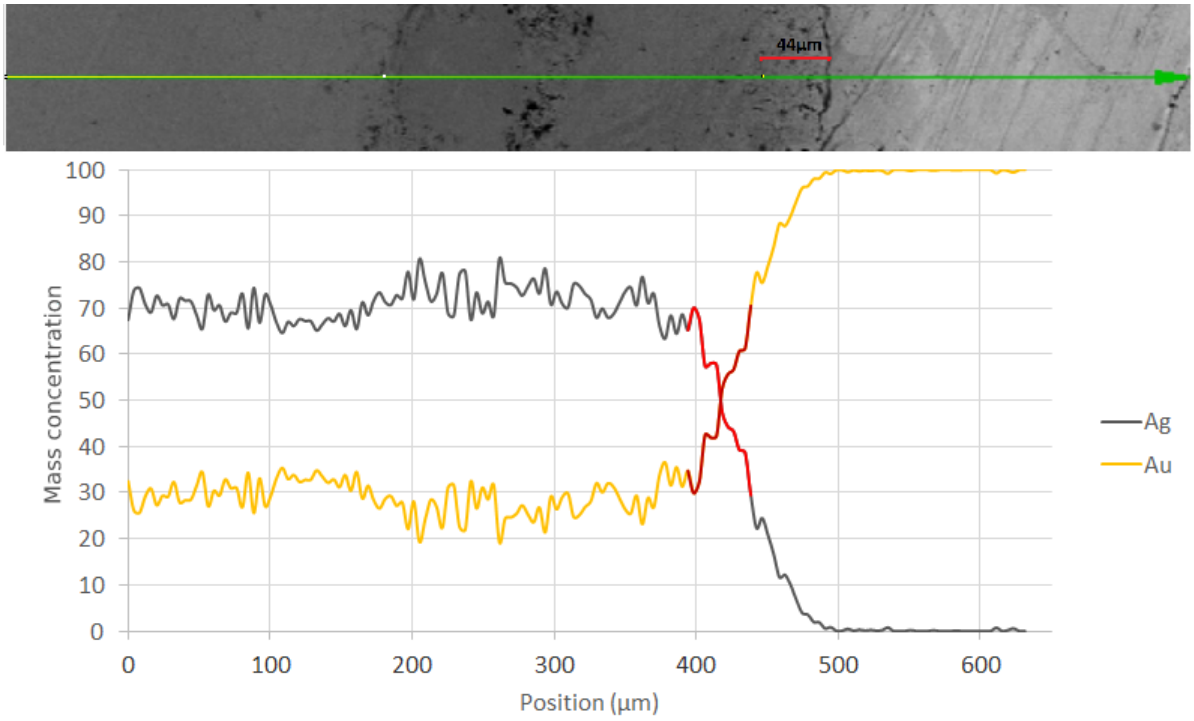

Figure 1.20 – Post-mortem concentration profile at Au-Ag interfacial region: the top image shows the microstructure and the green arrow where the profile was measured.

In order to compare the values obtained with in-situ measurements as well as to get more data, post-mortem concentration profiles using EDX presented in figure 1.20 were characterized at different interfacial regions. It has to be kept in mind that the area that was liquid during in-situ experiment has experienced solidification - with associated microstructure formation and microsegregations. The profiles revealed that the solidified Ag has an average composition of 70 wt% Ag in the entire solidified liquid area, above the liquidus composition value of 65.5 wt% Ag at 1000 ℃. This finding is consistent with observations made for the Cu-Ni system, where both the interface and the bulk solidified liquid were found in a non-equilibrium state. Note that the cooling from 1000 ℃ to solidus temperature was achieved in nearly 1 minute, and equilibrium might have shifted during this step. However, this still does not explain the measured concentration values in the liquid area, particularly at the interfacial region.

The diffuse nature of the interface concentration profile extends roughly over the same distance as measured with X-ray radiography. In the figure, the red segment in the micrograph positioned at the interface with its tip at the solid Au front, corresponds to the red portion in the concentration curve and reveals that the interface is at non-equilibrium concentration. The profile also indicates that the Au rich solid phase is at non-zero concentration at the interfacial region and diffusion towards the solid phase might have occured due to the fact that the concentration gradient starting from the interface position (given by the tip of the red portion of the curve) extends over 50 to 60 µm inside the solid Au before reaching 100 wt% Au.

The same conclusion was drawn from figure 1.21 when measuring at a different region

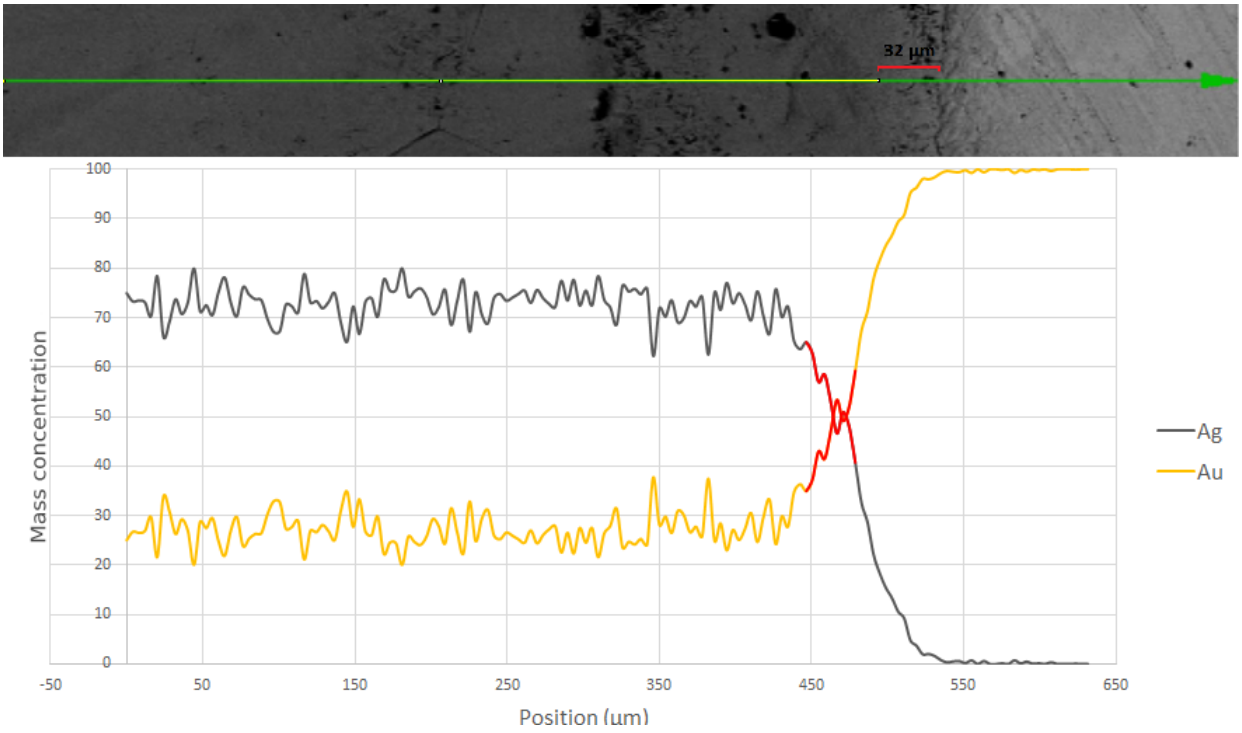

Figure 1.21 – Post-mortem concentration profile at Au-Ag interfacial region in a different area than figure 1.20 : again, the top image shows the microstructure and the green arrow where the profile was measured.

of the interface. The average concentration in the entire solidified liquid is lower than the liquidus value at 1000 ℃, and the interface exhibits a significant deviation from equilibrium. All the concentration profiles measured show the same solidified liquid concentration, and diffusion profiles in the solid phase.

The in-situ concentration profile measured at the five-minute mark of the solutal melting process is superimposed with the post-mortem measurement shown in Figure 1.22. The experiment involved a cooling phase from 1000 ℃ to room temperature, spanning approximately two hours, with a crucial minute where the liquid was actively cooling down before reaching the solidus temperature and solidifying. It's reasonable to expect minor diffusion during this interval, as is evident in the concentration gradients near what used to be the interface prior to solidification. Nevertheless, the in-situ and post-mortem concentration profiles show remarkably similar values, lending credence to the in-situ methodology employed for monitoring concentration profiles using gray-level values. This convergence in the data underscores the validity of using gray-level values as a reliable tool for real-time concentration tracking.

Figure 1.23 shows again a concentration profile obtained post-mortem by EDS measurements. It displays two distinct slopes in the concentration profile, which suggests a sudden change in diffusive properties. This change may indicate the presence of an interface where the diffusion coefficient shifts when transitioning between phases, with a much steeper gradient in the solid phase on the right side due to lower diffusion. The solid phase concentration profile was reproduced using simple 1-D diffusion equation for a semi-infinite media given

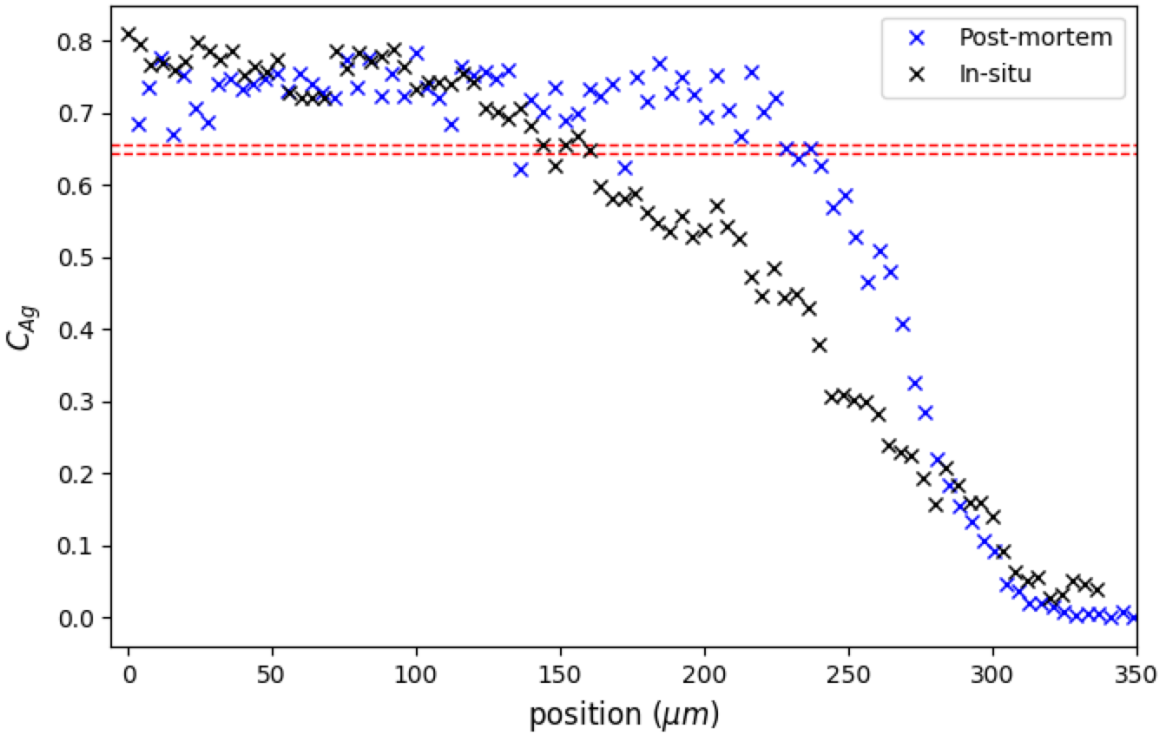

Figure 1.22 – Comparison of post-mortem concentration profile (depicted in blue) and in-situ profile at the five-minute mark (depicted in black). The red dashed lines illustrate the positions of the solidus and liquidus.

by:

$$\frac{c - c_1}{c_0 - c_1} = \text{erf}\left(\frac{x}{2\sqrt{Dt}}\right) \tag{1.16}$$

with c_0 the initial concentration, c_1 the interface concentration maintained constant.
The initial concentration of the Au is $c_0 = 0$, and the interface concentration is chosen to best reproduces the profile. The diffusion coefficient of Ag in solid Au is calculated at 1000 °C from [30] using Arrhenius equation:

$$D_{Ag} = D_0 \exp\left(-\frac{E_A}{RT}\right) \tag{1.17}$$

where the constant $D_0 = 0.072\ \text{m}^2\,\text{s}^{-1}$, the activation energy $E_A = 40.20\ \text{kcal}\,\text{mol}^{-1}$. The Ag diffusion coefficient in the solid phase is estimated to be $D = 9.769\,10^{-13}\ \text{m}^2\,\text{s}^{-1}$. The duration was set to $t = 300s$ because, as shown in figure 1.16, dissolution slows down significantly around 300 s. After this point, trans-interface diffusion occurs for the remainder of the experiment, lasting another 300s. The interface concentration for the solid phase that best fits the curve was found to be $C_S = 46wt\%$ Ag (see figure 1.24). The solid interface is thus substantially lower than the solidus composition, which confirms the observations made from the gray-level concentration profiles where the solid is far from equilibrium throughout the entire experiment.

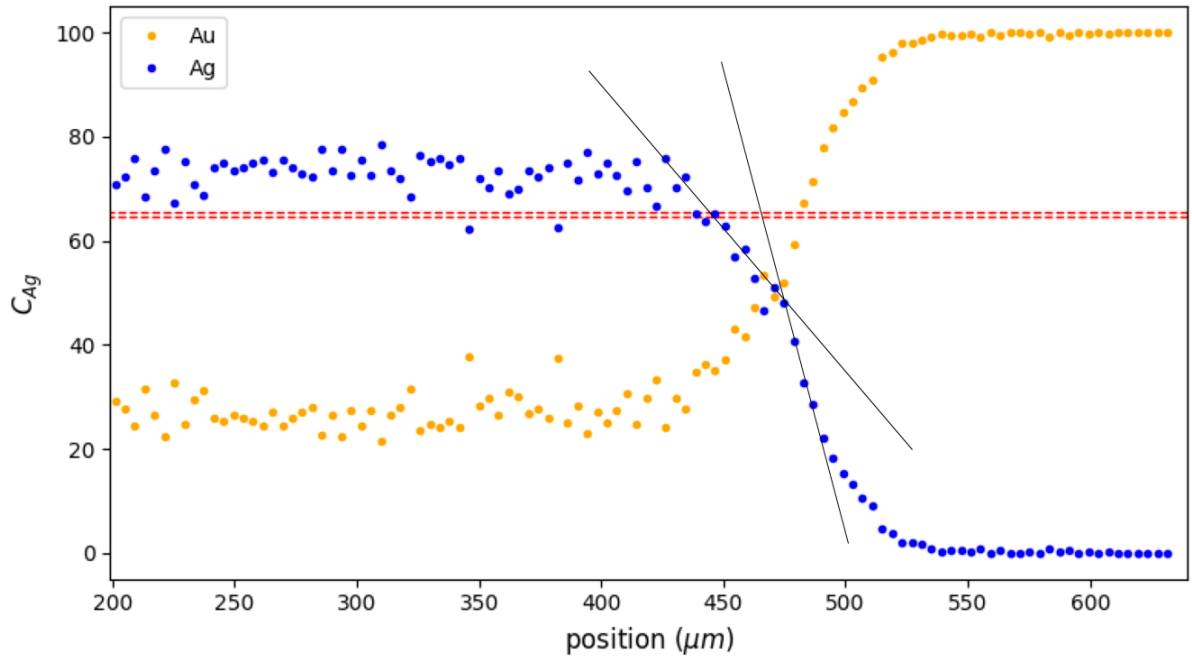

Figure 1.23 – Post-mortem concentration profile at Au-Ag interfacial region showing two distinct slopes at the interface.

On the other hand, accurately reproducing the concentration profile on the liquid side was not possible due to the fact that solidification has modified too deeply the concentration profile in post-mortem. If using the in-situ measurement and trying to apply the same analysis as in the solid phase, liquid diffusion is too rapid to allow the establishment of a gradient, and a flat concentration profile is obtained when using the liquid diffusion coefficient ($D = 2.837\,10^{-9}$ $m^2\,s^{-1}$ [31, 32]). Solid state diffusion after solidification was also dismissed since it requires times that far exceed the duration accorded for the experiment and cooling step to obtain a reasonable fit.

However, in order to have some insights into the liquid concentration, the theoretical maximum dissolved thickness can be used. Mass balance calculation similar to equation 1.2 can be employed to deduce the dissolved thickness when knowing the bulk composition change and assuming zero solid diffusion. Equation 1.2 is:

$$\Delta r = r_0 \left(\sqrt{\rho_l^0 / (\rho_l^f c_l^f)} - 1 \right) \tag{1.18}$$

With ρ_l^f and c_l^f the density and concentration of the saturated liquid - i.e. the equilibrium concentration. With the density values taken from table 1.2 assumed to vary linearly with concentration, and the equilibrium liquidus concentration of 65.5 wt% Ag, and an initial radius of 1.5 mm, a theoretical value of 127 µm is found at 1000 ℃ for the Au-Ag system. The local dissolved thickness measured from the SEM image in figure 1.21 was found to be 173 µm, which is exactly equal to the one found from figure1.18 by measuring the diameter difference. However, the dissolved thickness measured from a restricted area of the interface taken from figure 1.20 was found to be between 242 µm and 279 µm, depending on which

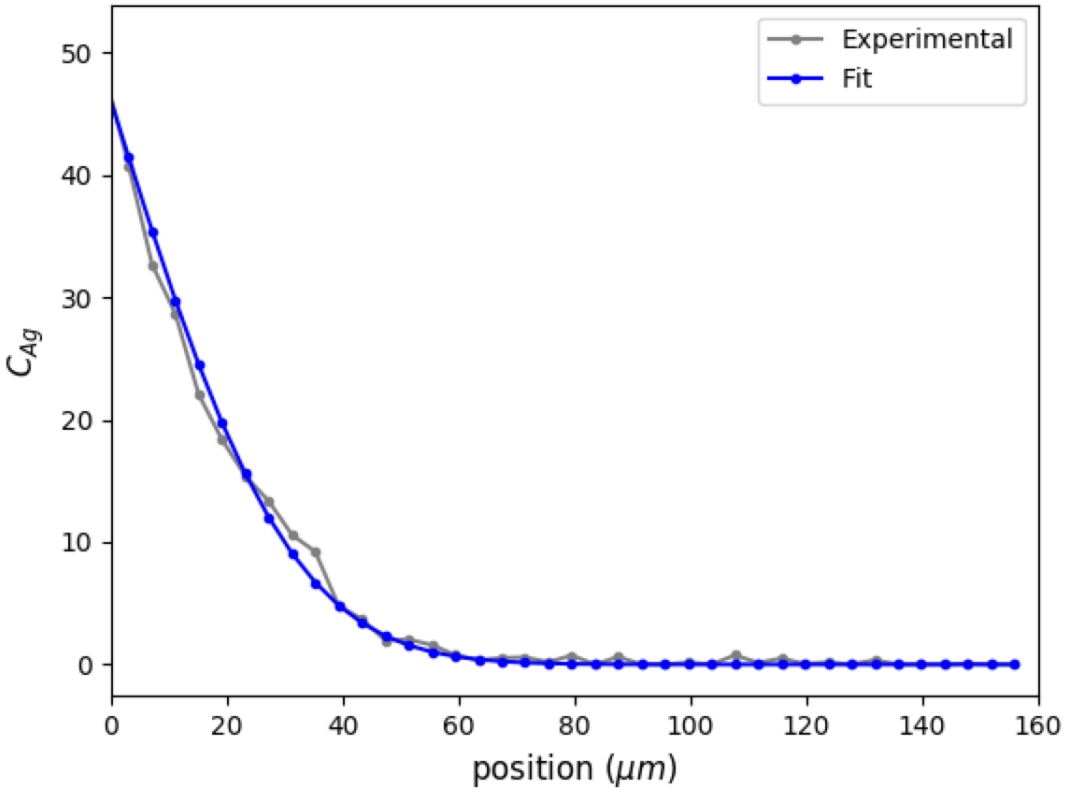

Figure 1.24 – Post-mortem concentration profile at Au-Ag solid region with the 0 position corresponding the interface position.

portion it was measured from and where the limit was set since the interface is not perfectly circular. The minimum value of 173 µm will be kept for the discussion as it was obtained from two different methods (SEM and image substraction), having in mind that it could be larger. It is important to note that an uncertainty of 10 °C on the temperature (inducing a modification of the liquid concentration) would lead to a change of calculated thickness of $\approx$ 10µm. As for the Ag disk initial diameter, a error of 100 µm on measurement of the diameter would induce an change $<$ 5 µm on the calculated thickness. It has to be mentioned that such gap or overlapping of the Ag foil would have been seen on X-Ray images such as in figure 1.11. Again this result is comparable as the one obtained by Deillon et al. [4], with an experimental dissolved thickness which is larger than the theoretical one assuming the saturated liquid is at equilibrium. In the present case, the difference is however less pronounced with a difference of 25% between experiment and calculated while it was greater than 50% for the study of Deillon et al., indicating that some convection could have amplified the phenomena.

Reaching a calculated value of dissolved thickness of 170 µm would require the saturated liquid to have an average concentration $c_l^f = 60$ wt.% Ag. While it does not provide information on the composition at the interface, this result indicates as for the solid concentration at the interface that the liquid composition is substantially lower than the solidus composition, and by far in the single phase domain of the equilibrium phase diagram.

1.7 Conclusion

The investigation of solutal melting behavior in the Ag-Au system has successfully identified similarities with the Cu-Ni system previously studied by Deillon et al. [4]. A remarkable element of the comparison between these two studies is that the results obtained are similar with completely different experimental systems and setups.

In this work, an innovative X-ray radiography technique was used to study the solutal melting process with the Au-Ag system. The novel X-ray radiography technique, in particular, has resolved convection issues and enabled a more precise investigation of solutal melting. As a powerful tool for future studies, it facilitates real-time monitoring of concentration profile evolution and the study of solutal melting across various alloy systems. The data analysis was conducted using image analysis, interface tracking, and composition determination to understand the solutal melting behavior.

The dissolution process in both systems followed three key steps: a steady increase in velocity due to temperature increase, diffusion-controlled dissolution with decreasing velocity, and resolidification during the holding period. The measured interfacial velocities in both systems were of the same order of magnitude, and both exhibited out-of-equilibrium conditions at the solid-liquid interface, with concentration values deviating from their respective equilibrium states. Concentration profiles obtained from in-situ experiments and post-mortem EDX measurements revealed the non-equilibrium state of both the interface and the bulk solidified liquid. In particular, we have shown that the solid composition close to the interface was around 46 wt% Ag (64.5 wt% Ag at equilibrium), and the liquid composition was below 60 wt% Ag (65.5 wt% Ag at equilibrium). These observations emphasize the need to consider such deviations when studying solutal melting processes. The surprising results obtained on the Cu-Ni system by Deillon et al. [4] were reproduced here for the Au-Ag system, with an experimental set-up which overcomes convection.

Overall, this investigation has made significant contributions to the understanding of solutal melting behavior in binary systems such as Ag-Au and Cu-Ni, providing valuable insights into the complex, non-equilibrium processes governing solutal melting. Further investigations with improved experimental designs and methodologies can help validate and expand upon these findings, leading to a more comprehensive understanding of solutal melting in various alloy systems. There is indeed room for improvement in other aspects of the experimental design, such as improved sample preparation and enhanced resolution techniques like synchrotron-based experiments, which could offer more accurate interfacial position and composition measurements.

CHAPTER 2

Thermodynamic model

The distinction between the solidification of metal alloys and solutal melting processes, in terms of achieving local thermodynamic equilibrium at the solid-liquid interface, remains a puzzling topic. Indeed, while the former appears to attain equilibrium very fast, the latter does not, highlighting an asymmetry that necessitates a comprehensive exploration of the governing dynamics of these processes. The objective of this chapter is dedicated to such an exploration using a sharp interface thermodynamic model proposed long time ago, and rediscovered several times.
In diffusion-controlled phase transformations, the local conditions at the interface significantly modulate the kinetics of the transformation. Consequently, this chapter provides an overview of the prevalent models employed to delineate these conditions. The goal is to pave the way for a more detailed comprehension of the observed asymmetry between solidification and dissolution processes.

The chapter begins with an introduction to the concept of thermodynamic equilibrium and its significance within the context of solid-liquid interfaces. The discourse expands to encompass out-of-equilibrium thermodynamics, a core component of the chapter, which provides the necessary theoretical background for understanding the observed phenomena. Hillert model for solute trapping and solutal melting is then discussed in depth, elucidating its implications and limitations.
The culmination of this chapter is the introduction of a novel thermodynamic model, designed to predict the kinetics of diffusive phase transformations. This innovative model, while firmly grounded in the fundamental principles of thermodynamics, integrates novel perspectives on the effects of solutal melting on the local conditions at the solid-liquid interface. Importantly, it demonstrates the ability to reproduce some of the behaviors observed in the experimental results detailed in the previous chapter.

2.1 Local equilibrium

When the diffusion-controlled phase transformations proceed under normal conditions (casting for solidification, high temperature precipitation for solid state phase transformations...), one can reasonably consider that the interfaces are at local equilibrium. In the case of binary alloys, the concentrations at the interface are given by the phase diagram, while in multicomponent alloys, the local equilibrium tie-line, called operative in the dedicated literature [33], still lies on the two-phase field boundaries in the phase diagram but is selected from the interfacial solute balance.

In the case of a binary alloy, all that is required is to impose the usual equilibrium conditions obtained by Gibbs energy minimization [34] at fixed pressure and temperature. In the context of a two-phase system with α and β phases, the Gibbs energy minimization method under the constraint of fixed global composition leads to the equality of the chemical potentials for each component A and B between α and β:

$$\mu_{\mathrm{A}}^{\alpha} = \mu_{\mathrm{A}}^{\beta} \tag{2.1}$$

$$\mu_{\mathrm{B}}^{\alpha} = \mu_{\mathrm{B}}^{\beta} \tag{2.2}$$

where the chemical potentials are defined as follows:

$$\mu_i^{\phi} = \left.\frac{\partial G}{\partial n_i^{\phi}}\right|_{p,T,n_{j\neq i}^{\phi}} \tag{2.3}$$

with $i \in \{\mathrm{A},\mathrm{B}\}$ and $\phi \in \{\alpha,\beta\}$, and where n_i^{ϕ} is the number of moles of the element i in the phase ϕ.
In the case where the molar Gibbs energy G_m^{ϕ} of phase ϕ depends on the concentration $c_i^{\phi} = n_i^{\phi} / \sum_j n_j^{\phi}$, it is more convenient to express the chemical potentials in the following way:

$$\mu_{\mathrm{A}}^{\phi} = G_m^{\phi} - c_{\mathrm{B}} \frac{\partial G_m^{\phi}}{\partial c_{\mathrm{B}}} \tag{2.4}$$

$$\mu_{\mathrm{B}}^{\phi} = G_m^{\phi} + (1 - c_{\mathrm{B}}) \frac{\partial G_m^{\phi}}{\partial c_{\mathrm{B}}} \tag{2.5}$$

The expressions in equations (2.4) and (2.5) are sufficient to graphically determine the thermodynamic equilibrium between the two phases in a binary alloy at fixed temperature and pressure. The equilibrium is represented when the molar Gibbs energy curves of two distinct phases are linked by a shared tangent, as illustrated in figure 2.1. The equilibrium concentrations can then be graphically extracted at the tangent points of each curve. Any departure from this equilibrium state will manifest as separate tangents for each coexisting phase's respective energy curve, which can then be contrasted with the common tangent. This visual representation offers an intuitive means to discern and understand the state of equilibrium in binary alloy systems.

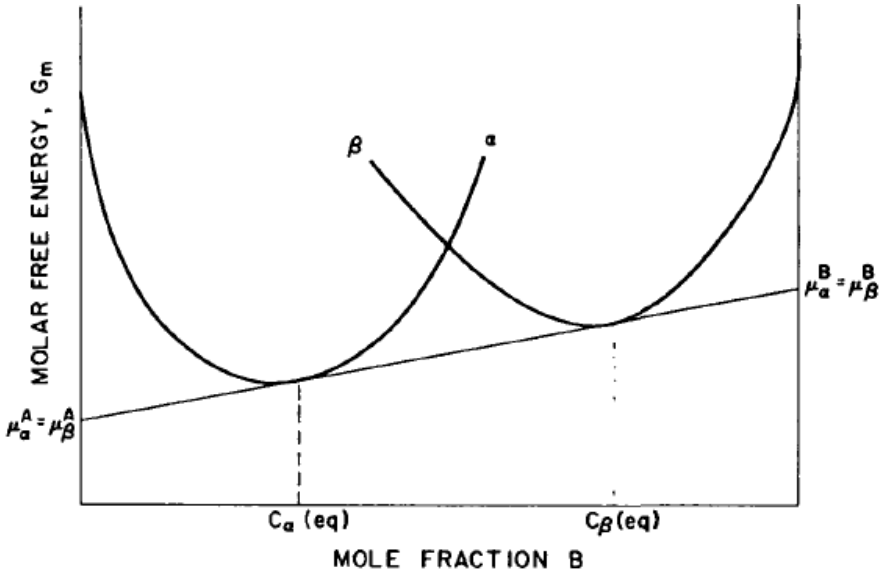

Figure 2.1 – Graphical construct for determining the equilibrium between phases α and β in a binary alloy at constant pressure and temperature.

2.2 Classical irreversible thermodynamics

In contrast to the local equilibrium conditions discussed previously, which focuses on static or quasi-static processes, classical irreversible thermodynamics acknowledges the presence of driving forces and fluxes that lead to changes in the system state. The driving forces can arise from factors such as temperature gradients, concentration gradients, or external influences, which bring the system away from its equilibrium state. Using classical irreversible thermodynamics [35, 36], one can explore the dynamic interplay between thermodynamic forces and kinetic processes, leading to the emergence of new phases, the evolution of microstructures, and the change of the material properties.

Rapid solidification, in contrast to solutal melting, has long been the topic of several studies since the precursor work of Baker and Cahn [37] (see, for example [38, 39]). To explain the dependence of interface concentrations on solidification rate, numerous models have been proposed that rely predominantly on a thermodynamic description of the interface, as opposed to atomic scale descriptions that do not depend on average mesoscopic quantities [40]. Within the realm of thermodynamic models, two major approaches stand out, as Hillert elucidated in his comprehensive review [41], which also inspired the thermodynamic model presented later in this chapter.
The first approach considers that the interface possesses a certain width, spanning a few atomic layers, as might suggest the analysis of atomic-scale simulations [40, 42] or observations of related interfaces at the solid state. Assuming homogeneous and constant properties of the interface within that width, a Gibbs energy description can be attributed to the interface that can be represented by an independent curve in the same $G_m(c)$ diagram as in figure 2.1. If these properties vary continuously in a thick interface, the description falls into phase field models that takes into account a variety of out-of-equilibrium phenomena (see [43]).

The second approach, more prevalent in the literature, considers the interface as a surface that separates two phases, usually referred to as "sharp"interface. This approach simplifies the description of some interfaces, such as solid-liquid, which are less likely to be influenced by segregation of impurities or elastic deformations. Thus, it eliminates the necessity of complex interfaces while still delivering relevant and realistic outcomes. This approach forms the foundation for the two thermodynamic models to be introduced and analysed in the ensuing sections; the first one proposed by Hillert and the second inspired by the work of Lesoult. The baseline formulations of thermodynamics of irreversible processes, from which both models were derived, will be detailed in the forthcoming sections.

2.2.1 Entropy production rate

The derivation proposed by Callen [44] (see also Onsager [6] and Prigogine [35]) is followed. The entropy of a system $S(X_0, X_1, \dots)$ is a homogeneous first order function of the extensive parameters X_i. Differentiating the entropy $S(X_0, X_1, \dots)$ with respect to time gives:

$$\frac{dS}{dt} = \sum_i \frac{\partial S}{\partial X_i} \frac{dX_i}{dt} \tag{2.6}$$

Equivalently, it can be expressed as:

$$\dot{S} = \sum_i \mathscr{F}_i \frac{dX_i}{dt} \tag{2.7}$$

As suggested by Callen [44], by analogy with (2.7) it seems reasonable to consider that the entropy current densities are:

$$j_s = \sum_i \mathscr{F}_i \, j_i \tag{2.8}$$

where j_i is the flux density of the extensive quantity X_i and $\mathscr{F}_i = \partial S / \partial X_i$ its associated intensive parameter, that plays the role of a driving force for the flux.
In local form, the balance of entropy per unit volume reads

$$\dot{s}_{\text{irr}} = \frac{\partial s}{\partial t} + \nabla \cdot j_s \geq 0 \tag{2.9}$$

where the rate of entropy production $\dot{s}_{\text{irr}}$ is the sum of the local variation and of the entropy entering or leaving the region per unit of volume j_s.
Considering the local version of (2.6):

$$\frac{\partial s}{\partial t} = \sum_i \mathscr{F}_i \frac{\partial x_i}{\partial t} \tag{2.10}$$

Taking the divergence of (2.8):

$$\nabla \cdot j_s = \nabla \cdot \left(\sum_i \mathscr{F}_i \, j_i \right) = \sum_i \nabla \mathscr{F}_i \cdot j_i + \sum_i \mathscr{F}_i \nabla \cdot j_i \tag{2.11}$$

Then, substituting (2.10) and (2.11) into (2.9) gives:

$$\dot{s}_{\text{irr}} = \sum_i \mathscr{F}_i \frac{\partial x_i}{\partial t} + \sum_i \nabla \mathscr{F}_i \cdot j_i + \sum_i \mathscr{F}_i \nabla \cdot j_i \geq 0 \tag{2.12}$$

Assuming that the extensive parameters are conserved, their balance equations are:

$$\frac{\partial x_i}{\partial t} + \nabla \cdot j_i = 0 \tag{2.13}$$

Using (2.13) into (2.12), the following is obtained:

$$\dot{s}_{\text{irr}} = \sum_i \nabla \mathscr{F}_i \cdot j_i \geq 0 \tag{2.14}$$

Thus, the entropy production rate for continuous systems corresponds to the product of the gradient of *entropy-representation* intensive parameters and their associated flux. The expression of the entropy production vanishes at equilibrium state when there are no thermodynamic forces available. It is important to note that the entropy production is always positive, thereby conditioning the directionality of the associated fluxes.
When the entropy production rate is positive, it implies that the system is undergoing irreversible processes [36] or is out of equilibrium. The sign of the fluxes, on the other hand, depends on the specific system and on the thermodynamic forces acting upon it. The fluxes can be positive or negative, indicating the direction of the flow or transport of certain quantities (such as mass, energy, or particles) within the system. The sign of the fluxes is directly related to the driving forces present in the system.

2.2.2 Linear constitutive laws

For purely *resistive* systems, each of the local fluxes are assumed to depend on all the instantaneous local thermodynamic forces of the system. Considering that equilibrium requires the fluxes in the entropy production (2.14) to vanish in the absence of thermodynamic forces, the expression of these fluxes can then be expanded as [44]:

$$j_i = \sum_j L_{ij} \mathscr{F}_j + \sum_j \sum_k L_{ijk} \mathscr{F}_j \mathscr{F}_k + \dots \tag{2.15}$$

where $L_{ij} = \frac{\partial j_i}{\partial \mathscr{F}_j}$ and $L_{ijk} = \frac{\partial^2 j_i}{\partial \mathscr{F}_j \delta \mathscr{F}_k}$.

The L_{ij} parameters are called kinetic parameters and are function of the local intensives parameters. For small deviations from equilibrium, where the thermodynamic forces are small enough that all the quadratic and higher order terms in (2.15) can be neglected, equation (2.15) simplifies to:

$$j_i = \sum_j L_{ij} \mathscr{F}_j \tag{2.16}$$

This equation lays the groundwork for irreversible thermodynamics of linearized processes and will be a critical component in the formulation of the models below.

2.2.3 Solute fluxes in binary systems

The case of mass transport at the interface between a liquid and solid phase in a binary mixture composed of two species A and B will be considered, where temperature variations across the interface are negligible along with the hydrodynamic and elastic phenomena. According to equation (2.14), the entropy production rate at the interface is given by [5]:

$$T\,\dot{s}_{\mathrm{irr}} = I_{\mathrm{A}}\left(\mu_{\mathrm{A}}^{s} - \mu_{\mathrm{A}}^{l}\right) + I_{\mathrm{B}}\left(\mu_{\mathrm{B}}^{s} - \mu_{\mathrm{B}}^{l}\right) \tag{2.17}$$

where all quantities are at the interface, with T the temperature, μ_i^{ϕ} the chemical potential of species i in phase $\phi \in l,s$, and I_i the flux density of $i \in \mathrm{A},\mathrm{B}$. In analogy with equation (2.14), I_i is identified as the local flux density and $\Delta\mu_i = \mu_i^s - \mu_i^l$ the associated thermodynamic force.

Considering that the linear regime is a good first approximation even for highly out-of equilibrium processes, the fluxes are linear functions of the thermodynamic forces [45]:

$$I_{\mathrm{A}} = L_{\mathrm{AA}}\,\Delta\mu_{\mathrm{A}} + L_{\mathrm{AB}}\,\Delta\mu_{\mathrm{B}} \tag{2.18}$$

$$I_{\mathrm{B}} = L_{\mathrm{BA}}\,\Delta\mu_{\mathrm{A}} + L_{\mathrm{BB}}\,\Delta\mu_{\mathrm{B}} \tag{2.19}$$

where I_i are the same independent fluxes intervening in the entropy production (2.17), and $\Delta\mu_i = \mu_i^s - \mu_i^l$. L_{ij} are called phenomenological coefficients, kinetic parameters or Onsager mobilities.

Introducing the expression of the local fluxes I_i in the entropy production rate (2.17), quadratic forms of the thermodynamic forces are obtained:

$$T\,\dot{s}_{\mathrm{irr}} = \sum_{ij} \Delta\mu_i\, L_{ij}\, \Delta\mu_j \tag{2.20}$$

In order to ensure a positive entropy production $\dot{s}_{\mathrm{irr}} \geq 0$ in accordance with the second principle of thermodynamics, the kinetic coefficients matrix must be positive definite. This implies that all the diagonal elements of the matrix are positive (meaning that diffusion of an element i in presence of some gradient of i only takes place only in the direction of decreasing chemical potential), whereas the off-diagonal elements must satisfy a condition of the form:

$$L_{\mathrm{AA}} L_{\mathrm{BB}} \geq \frac{1}{4}\left(L_{\mathrm{AB}} + L_{\mathrm{BA}}\right)^2 \tag{2.21}$$

Moreover, from considerations of statistical thermodynamics, Onsager establishes a reciprocity relation between the cross terms, resulting in the following conditions for the kinetic parameters [6]:

$$L_{ii} \geq 0 \tag{2.22}$$

$$L_{\mathrm{AB}} = L_{\mathrm{BA}} \tag{2.23}$$

$$L_{\mathrm{AA}} \times L_{\mathrm{BB}} \geq L_{\mathrm{AB}}^2 \tag{2.24}$$

From equations (2.18) and (2.19) and using mass balance equations, it is possible to determine the time evolution of all local thermodynamic state variables at the interface.

2.3 Hillert model

Baker and Cahn [46] have developed a sharp interface model grounded in irreversible thermodynamics, with special emphasis on solidification. They explored the precipitation of a solid phase, denoted as α, from a supersaturated liquid with a given composition x^l. Using a tangent-to-tangent construct in the Gibbs energy plot, they have defined the range of thermodynamically possible interface concentrations in the solid, given by the area bordered by the vertical lines stretching from x_1^α to x_3^α in figure 2.2. The concentration in the solid that would give the higher driving force corresponds to x_2^α

Upon solidification, a liquid layer at concentration x^l is assumed to transform into a solid layer at concentration x^s by adjusting its composition by diffusion in the liquid phase while considering that diffusion in the solid phase is negligible (x stands for the molar fraction of species B). The Gibbs energy will decrease by ΔG_{tot} (counted positively by convention) during the whole process:

$$\Delta G_{\text{tot}} = (1-x^s)\left(\mu_{\text{A}}^l - \mu_{\text{A}}^s\right) + x^s\left(\mu_{\text{B}}^l - \mu_{\text{B}}^s\right) \tag{2.25}$$

In fact, Baker and Cahn's model is quite similar to what Hillert [47] has introduced early for trying to unify the description of the different transformations observed in Fe-C steels, from diffusion-controlled to martensitic. He described the transformation by assuming two independent processes: the first one involving a diffusionless transformation by simple interface migration; the second one allowing the solute to migrate back into the parent phase by some so-called trans-interface diffusion. Hillert later reformulated equation (2.25) as follows [41]:

$$\Delta G_{\text{tot}} = (1-x^l)\left(\mu_{\text{A}}^l - \mu_{\text{A}}^s\right) + x^l\left(\mu_{\text{B}}^l - \mu_{\text{B}}^s\right) + (x^l - x^s)\left(\mu_{\text{A}}^l - \mu_{\text{A}}^s - \mu_{\text{B}}^l + \mu_{\text{B}}^s\right) \tag{2.26}$$

The first two terms and the last term in the above equation are identified as:

$$\Delta G^{\text{m}} = (1-x^l)\left(\mu_{\text{A}}^l - \mu_{\text{A}}^s\right) + x^l\left(\mu_{\text{B}}^l - \mu_{\text{B}}^s\right) \tag{2.27}$$

$$\Delta G^{\text{t}} = (x^l - x^s)\left(\mu_{\text{A}}^l - \mu_{\text{A}}^s - \mu_{\text{B}}^l + \mu_{\text{B}}^s\right) \tag{2.28}$$

ΔG^{m} is called the interface migration driving force which is used to overcome the resistance to interface displacement at constant concentration, such as friction and pressure stemming from interfacial energy. ΔG^{t} is the change in Gibbs energy following the diffusion of elements A and B across the interface to adjust the composition from x^l to x^s by diffusing back the quantity $(x^l - x^s)$ of solute element.

The combination of the two processes is illustrated by the molar Gibbs energy construct in the diagram in figure 2.3. The total driving force for solidification is given by the tangent-to-curve representation, which is the distance, at position x^α, between the curve of the solid α phase and the tangent line to the liquid curve at concentration x^l. ΔG^{m} is defined graphically by taking the tangent to the curve of solid α at concentration x^α, and plotting its parallel at position x^l on the liquid curve. ΔG^{m} is then given by the distance from this parallel (represented by the dashed line) to the tangent at the liquid curve at x^α. Finally, ΔG^{t} is deduced by subtracting ΔG^{m} from ΔG_{tot}, as illustrated in figure 2.3.

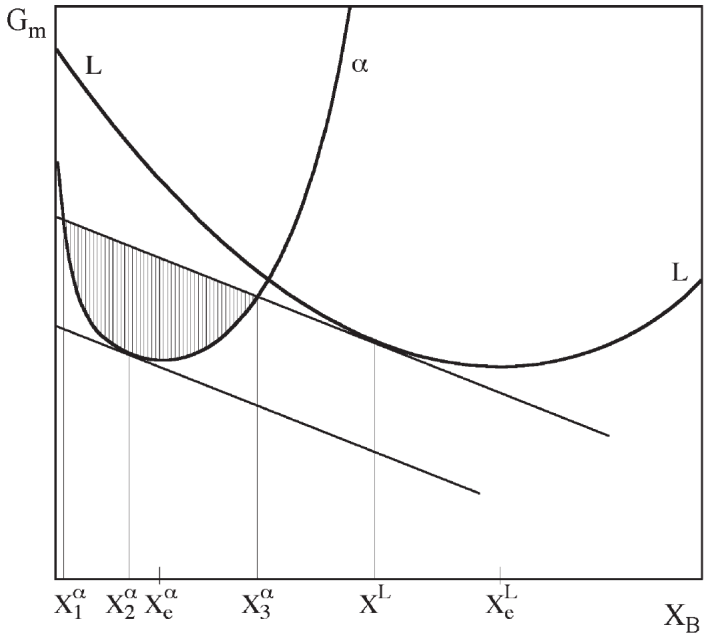

Figure 2.2 – Molar Gibbs energy diagram giving the possible concentration range in solid α precipitating from some liquid at composition x^l [48].

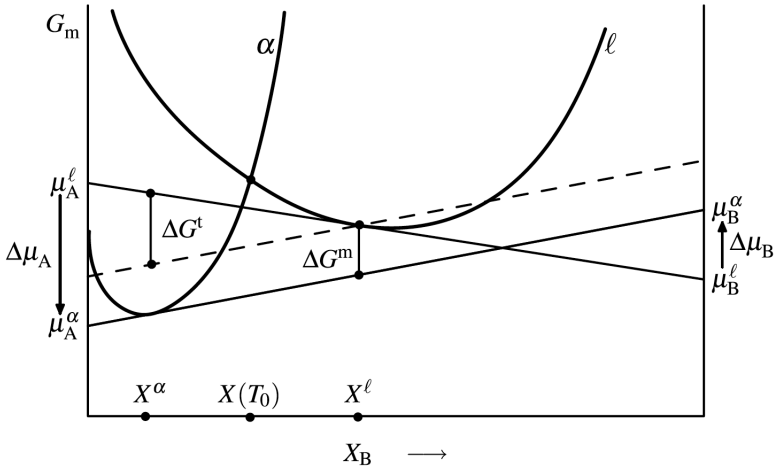

Figure 2.3 – Gibbs energy diagram showing the decomposition of the driving force into the migration and trans-interface diffusion contributions [49].

The flux of atoms incorporated in the solid that causes the interface to migrate with a velocity v is given by [41]:

$$I^{\mathrm{m}} = \frac{v}{v_m} = I_{\mathrm{A}} + I_{\mathrm{B}} \tag{2.29}$$

where v is the interface velocity, v_m is the molar volume which is assumed to be equal and constant in both phases for the sake of simplicity. I_{A} and I_{B} are the fluxes of the individual species, coupled to the differences in their chemical potentials between the two phases via equation (2.18) and (2.19).

A and B atoms exchange across the interface to regulate the concentration in both phases via

the trans-interface diffusion, assumed to be independent of the driving force for the migration process, at the following rate:

$$I^{\mathrm{t}} = (x^l - x^s)\, I^{\mathrm{m}} = (x^l - x^s)\, \frac{v}{v_m} = j^l - j^s \tag{2.30}$$

where j^l and j^s are the diffusion current densities inside the liquid and solid phases respectively. The last equality in (2.30) is the usual solute balance at a moving interface exhibiting solute partitioning.
The solute atoms that are not incorporated in the solid layer at the interface, are evacuated by diffusion inside both phases. The trans-interface diffusion flux I^{t} is thus the difference between the fluxes in the two adjacent phases. In the case of steady-state growth where there is no gradient in the solid phase, I^{t} is equal to the flux in the liquid bulk j^l at the interface.

The driving forces for migration are usually considered to feature a linear dependency on its corresponding flux, assuming that higher order terms have a negligible influence on the kinetic of the system:

$$I^{\mathrm{m}} = \frac{M}{v_m} \Delta G^{\mathrm{m}} \tag{2.31}$$

where M is the interface mobility.
Buchmann and Rettenmayr [49, 50, 51] have proposed to relate the mobility to the maximum crystallisation velocity v_0, usually assumed to be of the order of magnitude of the sound velocity in metals,

$$M = \frac{v_0}{RT} \tag{2.32}$$

The driving force for exchanging A and B across the interface is independent of the migration process and is given by the difference $\Delta(\mu_A - \mu_B)$. Using (2.28) the trans-interface diffusion is given by:

$$I^{\mathrm{t}} = \frac{1}{v_m} L \Delta\left(\mu_{\mathrm{A}} - \mu_{\mathrm{B}}\right) = \frac{1}{v_m} L \frac{\Delta G^{\mathrm{t}}}{x^l - x^s} \tag{2.33}$$

with L a kinetic coefficient, defined in [49, 50] as:

$$L = \frac{v_D}{RT} \tag{2.34}$$

where v_D is the diffusion velocity given by the ratio of the interdiffusion coefficient D_i inside the interface and the interface width a,

$$v_D = \frac{D_i}{a} \tag{2.35}$$

Combining (2.29) with (2.31), and (2.30) with (2.33) gives the solid/liquid interface velocity with respect to the driving forces:

$$v = v_m I^{\mathrm{m}} = M \Delta G^{\mathrm{m}} \tag{2.36}$$

$$v = \frac{v_m}{x^l - x^s} I^{\mathrm{t}} = L \frac{\Delta G^{\mathrm{t}}}{(x^l - x^s)^2} \tag{2.37}$$

Injecting the expressions of the driving forces ΔG^{m} and ΔG^{t} in (2.36) and (2.37) gives the final system of equations to solve:

$$v = M\left[(1-x^l)\,\Delta\mu_{\mathrm{A}} + x^l\,\Delta\mu_{\mathrm{B}}\right] \tag{2.38}$$

$$v = L\,\frac{\Delta\mu_{\mathrm{A}} - \Delta\mu_{\mathrm{B}}}{x^l - x^s} \tag{2.39}$$

This system of equations can be solved for a given velocity and kinetic parameters M and L to get the concentrations (x^l, x^s) at the interface.

Specific constructs of the driving force can be performed depending on the values of the pair concentrations (x^l, x^s). Two extreme cases are illustrated in figure 2.4 for the case of melting ($\mathrm{S} \rightarrow \mathrm{L}$).
The first case corresponds to two tangents that are parallel. Therefore, the totality of the driving force is dissipated through interface migration and the interface velocity is maximum. Although there is some trans-interface diffusion to adjust the partitioning between the solid and liquid, the process does not consume any driving force due to the compensation of one chemical potential jump by the other one ($\Delta\mu_{\mathrm{A}} = \Delta\mu_{\mathrm{B}}$).
The second scenario is having the tangent of the liquid G-curve intersecting the solid G-curve at the solid concentration x^s. Here, the entirety of the driving force is consumed by solute redistribution, rendering $\Delta G^{\mathrm{m}} = 0$, which in turn leads to an infinitely slow velocity.
Interestingly, in both these extreme cases where ΔG^{m} or ΔG^{t} are null, the velocity does not mirror this zero value, as (2.38) or (2.38) might suggest. Trans-interface and migration fluxes subsist, but they do not require any energy expenditure in one or the other case.

Hillert graphical interpretation of the driving force in the context of solidification, as detailed in [41], is not without shortcomings. In particular, it does not remain valid throughout the spectrum of potential solid concentrations.
In fact, examining a case where the solidified concentration lies between x_1^α and x_2^α, as depicted in figure 2.2, it becomes apparent that the graphical construct becomes untenable because it would require $\Delta G^{\mathrm{t}} < 0$ when $\Delta G^{\mathrm{m}} > 0$. Hillert model does not address this particular case, suggesting that some of the model's underpinning assumptions may not apply to such scenarios. This gap underscores the need for further exploration and refinement of the model to accommodate a broader range of solid concentrations.

In his work, Cahn [52] elucidates the scenario in which an infinitesimal quantity of a material with composition x^i is transferred from a phase with composition x^l to another phase with composition x^s. Under such circumstances, the modification in Gibbs energy, as represented by equation (2.25), is revised accordingly:

$$\Delta G_{\mathrm{tot}} = (1-x^i)\left(\mu_{\mathrm{A}}^l - \mu_{\mathrm{A}}^s\right) + x^i\left(\mu_{\mathrm{B}}^l - \mu_{\mathrm{B}}^s\right) \tag{2.40}$$

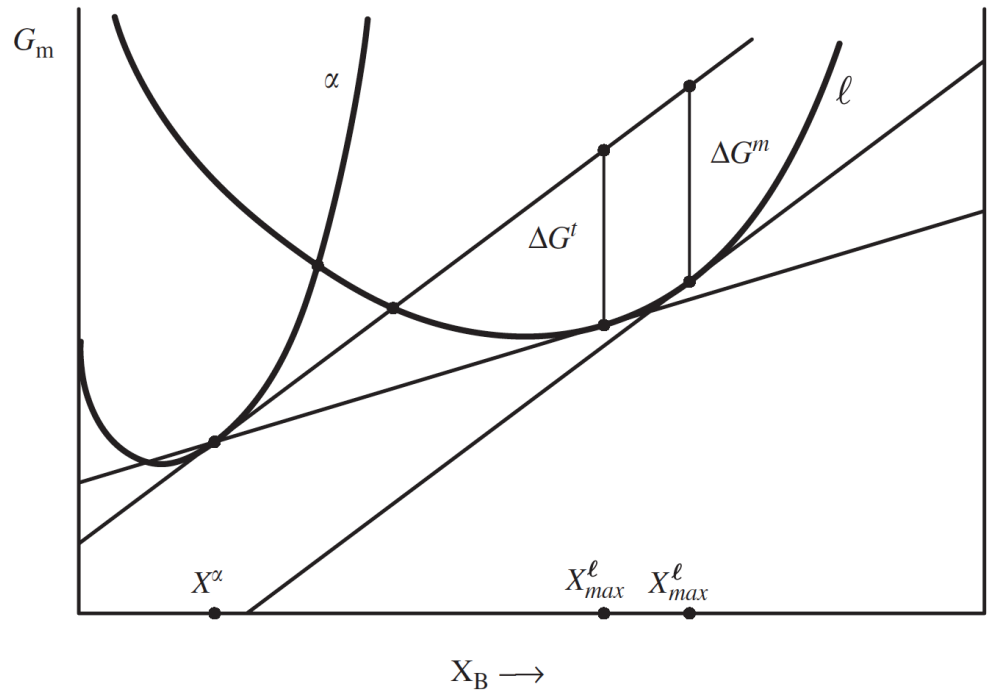

Figure 2.4 – Schematic diagram of two extreme cases of melting where all the driving force is dissipated by either migration or trans-interface diffusion [50].

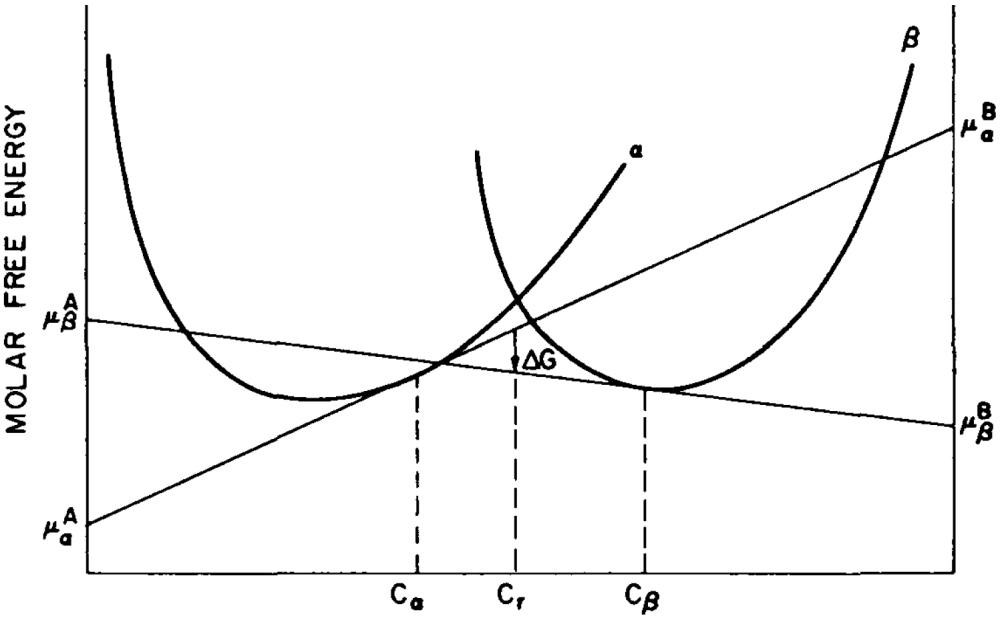

Figure 2.5 – Schematic diagram for obtaining the free energy change when transferring material of composition C_r from a phase α at concentration C_α to β at concentration C_β [52].

The tangent-to-curve principle in Hillert model evolves into a tangent-to-tangent rule (refer to Figure 2.5) when x^i does not align with the precipitated phase, and into a curve-to-curve rule when the transformation is diffusionless.

Until now, it has been assumed that during solidification, the composition change from x^l to x^s was mainly driven by diffusion in the liquid phase, and that the diffusion flux in the solid was zero such that the solid precipitated with a constant composition. Negligible flux in the solid can be due to either very slow diffusion or vanishing concentration gradients. In this case, the interface composition x^i was considered equal to the solid composition x^s. However, this simplification does not hold for non-steady-state transformations (or when a gradient is present in the product phase), such as melting, as both the parent and the product phases can alter the interface composition through diffusion ($j_s \neq 0$) [7].

Consequently, the driving force for melting is adjusted to account for the intermediate composition x^i as follows [7, 48] (be aware that now $\Delta G_{\text{tot}} > 0$ for melting):

$$\Delta G_{\text{tot}} = (1-x^s)\left(\mu^s_{\text{A}} - \mu^l_{\text{A}}\right) + x^s\left(\mu^s_{\text{B}} - \mu^l_{\text{B}}\right) + (x^s - x^i)\left(\mu^s_{\text{A}} - \mu^l_{\text{A}} - \mu^s_{\text{B}} + \mu^l_{\text{B}}\right) \tag{2.41}$$

The quantity $x^s - x^i$ is determined, considering the solute balance, as function of the ratio between the fluxes in the two adjacent phases [53, 48]:

$$x^s - x^i = \frac{x^s - x^l}{1 - j^l/j^s} \tag{2.42}$$

As inferred from equation (2.42), if diffusion in the growing phase (liquid in this context) is neglected, x^i becomes the concentration of the growing phase. Hence, the transferred quantity x^i is function of the concentration at the interface and the fluxes of both phases [51]:

$$x^i = \frac{x^s\, j^l - x^l\, j^s}{j^l - j^s} \tag{2.43}$$

Now, the driving force for migration is dependent on the interfacial concentration x^s of solid, while the driving force for trans-interface diffusion depends on both x^s and x^i:

$$\Delta G^{\text{m}} = (1-x^s)\left(\mu^s_{\text{A}} - \mu^l_{\text{A}}\right) + x^s\left(\mu^s_{\text{B}} - \mu^l_{\text{B}}\right) \tag{2.44}$$

$$\Delta G^{\text{t}} = (x^s - x^i)\left(\mu^s_{\text{A}} - \mu^l_{\text{A}} - \mu^s_{\text{B}} + \mu^l_{\text{B}}\right) \tag{2.45}$$

Unfortunately, the new expressions of migration and trans-interface fluxes were not explicitly laid out in Rettenmayr papers. To establish the relationship between the fluxes and driving forces, one could follow the same procedure or assumptions that were used to derive the linear dependence of interfacial fluxes on their corresponding driving forces (Eqs. (2.18) and (2.19)). Starting from equation (2.17), the entropy production rate can be written as a function of the migration and trans-interface fluxes and driving forces, and from there, the expressions for the fluxes can be deduced:

$$\begin{aligned} T\,\dot{s}_{\text{irr}} &= I_A\,\Delta\mu_{\text{A}} + I_B\,\Delta\mu_{\text{B}} \\ &= \left[(1-x^s)\,v + j^s_{\text{B}}\right]\Delta\mu_{\text{A}} + \left[x^s\,v - j^s_{\text{B}}\right]\Delta\mu_{\text{B}} \\ &= v\left[x^s\,\Delta\mu_{\text{B}} + (1-x^s)\,\Delta\mu_{\text{A}}\right] + j^s_B\left(\Delta\mu_{\text{A}} - \Delta\mu_{\text{B}}\right) \end{aligned} \tag{2.46}$$

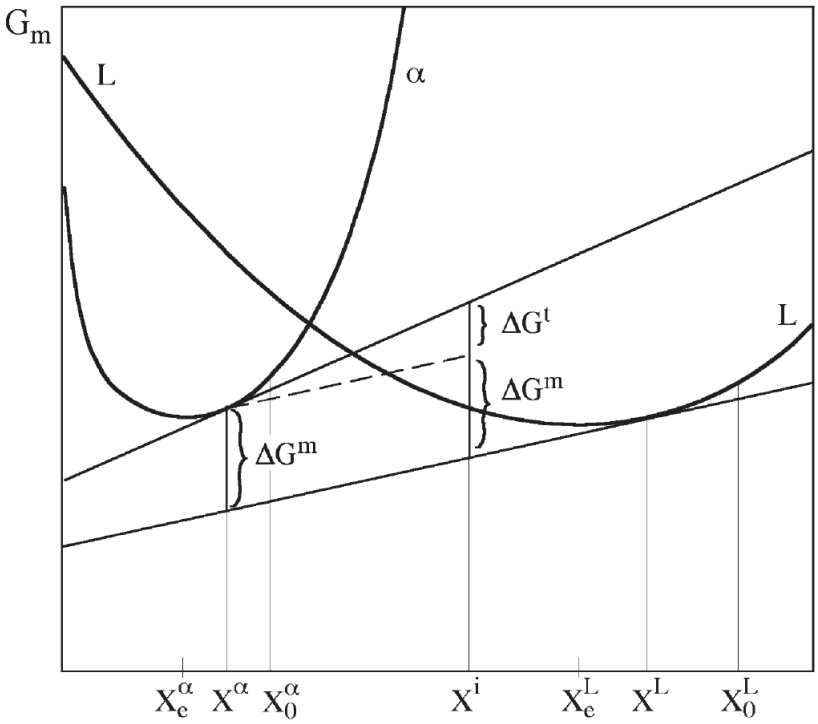

Figure 2.6 – Qualitative representation of a transferred layer of composition X^i to the liquid phase L [48].

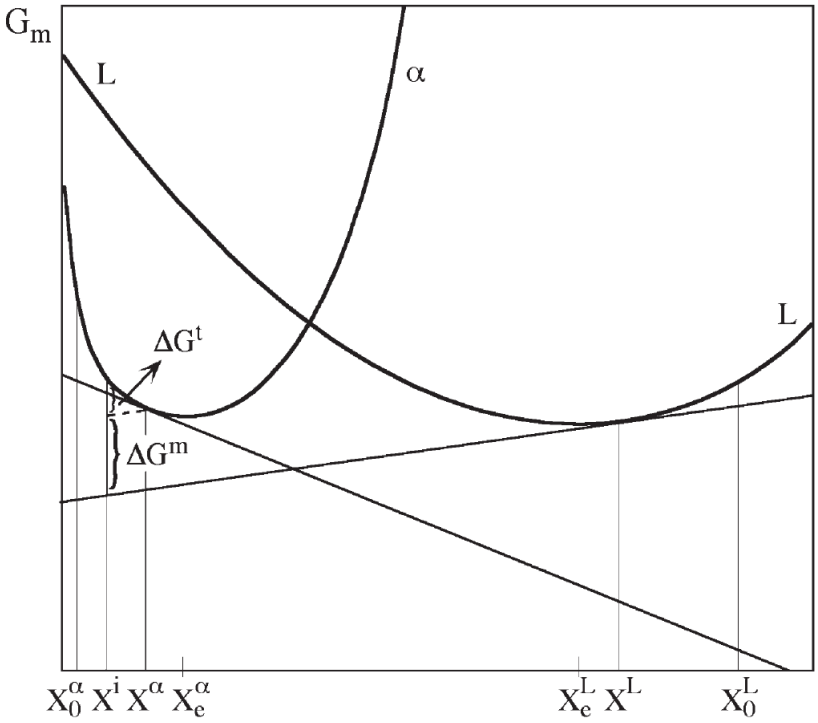

Figure 2.7 – Representation of solutal melting as presented by Hillert and Rettenmayr in [48], where concentrations of both phases lie in their respective one-phase field, X^α and X^L. As opposed to solidification, Hillert decomposition is thus constructed at an intermediate concentration X^i of the parent phase rather than the growing phase.

Now, $\Delta\mu = \mu^s - \mu^l$, as opposed to solidification. Moreover, in (2.46) $x^s\Delta\mu_\mathrm{B} + (1-x^s)\Delta\mu_\mathrm{A}$ is the driving force for migration as defined in equation (2.27) associated to the migration flux which is the velocity v. Consequently, j_B^s and $\Delta\mu_A - \Delta\mu_B$ can be identified as the trans-interface flux and driving force respectively.
In the formalism of irreversible thermodynamics, the fluxes depend linearly on the driving forces:

$$I^\mathrm{m} = v = M\left[x^s\Delta\mu_\mathrm{B} + (1-x^s)\Delta\mu_\mathrm{A}\right] \tag{2.47}$$

$$I^\mathrm{t} = j_\mathrm{B}^s = L\left(\Delta\mu_\mathrm{A} - \Delta\mu_\mathrm{B}\right) \tag{2.48}$$

which are the same equations defined earlier in (2.31) and (2.33).
The trans-interface flux is then given by:

$$I^\mathrm{t} = j^s = v\left(x^s - x^l\right) + j^l = vx^s - \left(vx^l - j^l\right) = vx^s - I_\mathrm{B} \tag{2.49}$$

The interface velocity v is given by the mass balance equation:

$$v = \frac{j_\mathrm{B}^l - j_\mathrm{B}^s}{x^l - x^s} \tag{2.50}$$

so that substituting this expression into the interfacial flux of B atoms I_B yields:

$$I_\mathrm{B} = vx^l - j^l = x^s v - j_\mathrm{B}^s = \frac{x^s}{x^l - x^s}\left(j_\mathrm{B}^l - j_\mathrm{B}^s\right) - j_\mathrm{B}^s = \frac{x^s j_\mathrm{B}^l - x^l j_\mathrm{B}^s}{x^l - x^s} \tag{2.51}$$

From the definition of x^i in (2.43), the following expression is obtained:

$$I_\mathrm{B} = vx^i \tag{2.52}$$

Substituting equation (2.52) into (2.49) gives:

$$I^\mathrm{t} = vx^s - vx^i = v\left(x^s - x^i\right) = I^\mathrm{m}\left(x^s - x^i\right) \tag{2.53}$$

Finally, the system of equation that relates the interface velocity to the interfacial concentrations in the case of melting can be obtained by combining (2.53) with (2.48) and (2.47):

$$v = M\left[x^s\Delta\mu_\mathrm{B} + (1-x^s)\Delta\mu_\mathrm{A}\right] \tag{2.54}$$

$$v = \frac{I^\mathrm{t}}{x^s - x^i} = L\frac{\Delta\mu_\mathrm{A} - \Delta\mu_\mathrm{B}}{x^s - x^i} \tag{2.55}$$

Contrary to the simplified scenario of solidification presented in Hillert model, where diffusion in the solid phase is overlooked, the present context requires consideration of diffusion in both adjoining phases in order to accurately determine the concentration of the transferred solute quantity, x^i.

2.3.1 Results and discussion

To investigate the outcomes of the Hillert model, the Cu-Ni system studied by Deillon et al. [4] for solidification was considered. For that purpose, the CalPhaD expressions and data of the Gibbs energies of solid and liquid phases were taken from [54]. The resulting phase diagram is illustrated in figure 2.8, where the liquidus is plotted in red and the solidus in black. The melting temperatures for copper and nickel are $T_m(\mathrm{Cu}) = 1086\,°\mathrm{C}$ and $T_m(\mathrm{Ni}) = 1455\,°\mathrm{C}$ respectively.

The Gibbs energy curves at $T = 1115\,°\mathrm{C}$ are plotted in Figure 2.9. The dashed line represents the common tangent intersecting both G-curves at the equilibrium concentrations, $x^s_{\mathrm{eq}} = 0.907$ for the solid phase and $x^l_{\mathrm{eq}} = 0.930$ for the liquid phase, close to the pure Cu border.

The parameters entering M and L, as given by equations (2.32) and (2.34), were drawn from the study by Buchmann and Rettenmayr [50], which was applied to the Cu-Ni system: values $v_0 = 1000\,\mathrm{m/s}$ and the interface width $a = 0.6\,\mathrm{nm}$ were taken. To emphasize the non-equilibrium interfacial behavior for illustrative purposes, it was assumed that the diffusion coefficient at the interface D_i is the interdiffusion coefficient in solid. The parameters of the Arrhenius law were sourced from [55] ($D^0_s = 1.4 \times 10^{-4}\ \mathrm{m^2/s}$ and $Q = 228.2\,\mathrm{kJ/mol}$) which gives at $1115\,°\mathrm{C}$ $D_s = 3.614 \times 10^{-13}\ \mathrm{m^2\,s^{-1}}$.

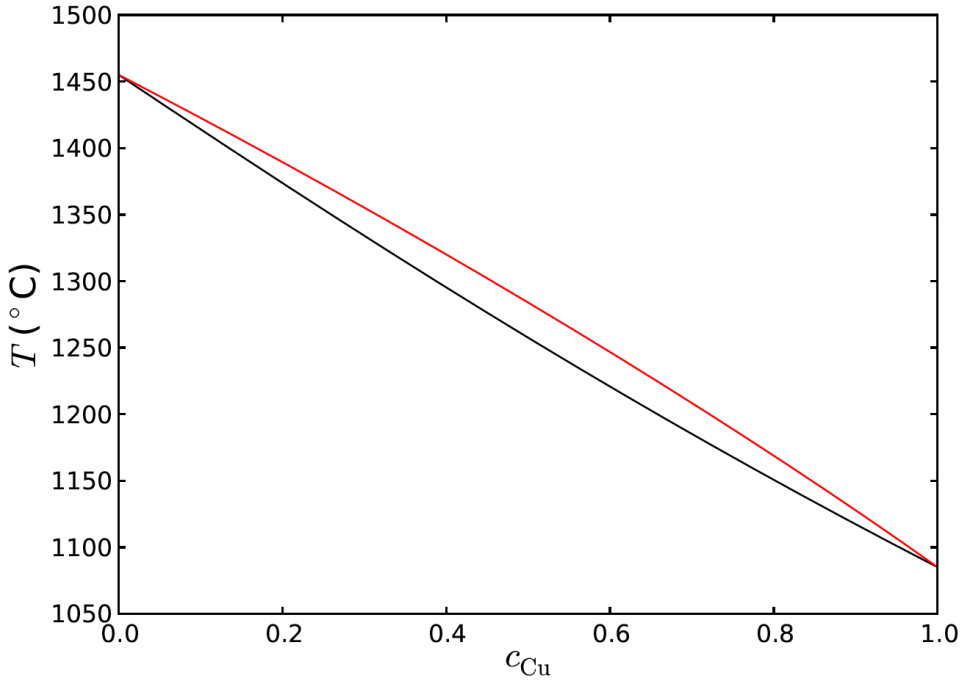

Figure 2.8 – Cu-Ni diagram as calculated from the CalPhad expressions and data in [54].

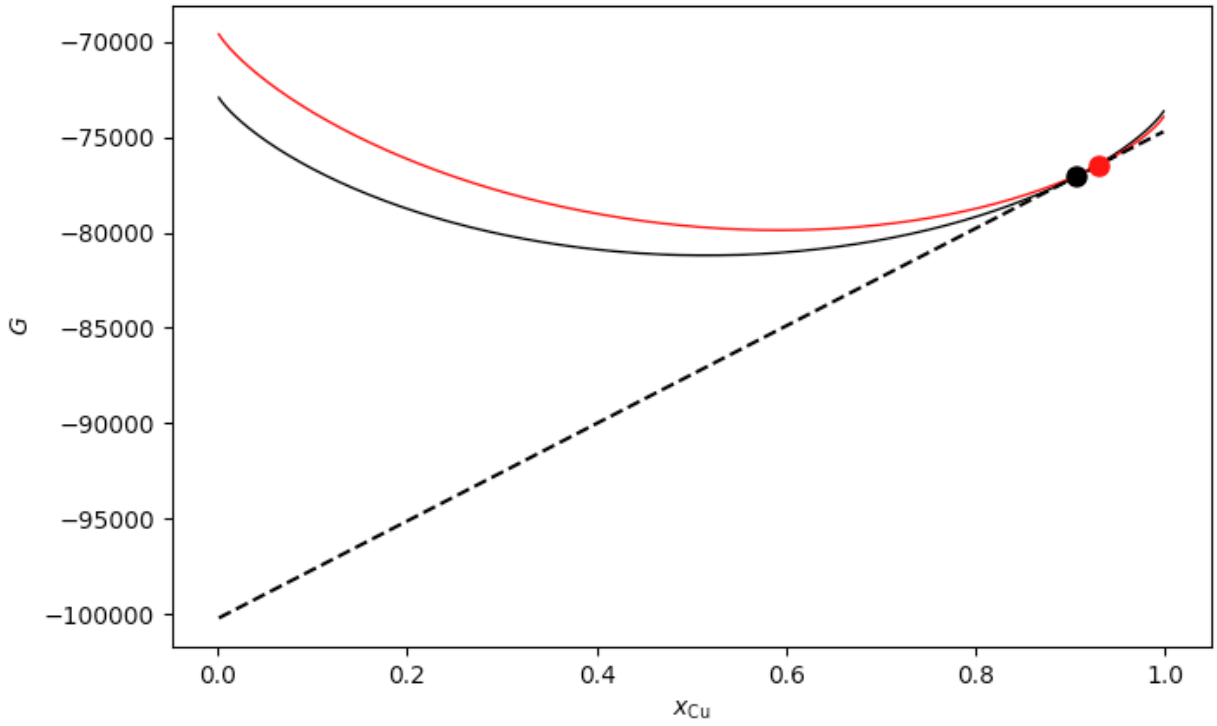

Figure 2.9 – Gibbs energy curves (in $\mathrm{J\,mol^{-1}}$*) of liquid (red) and solid (black) in the Cu–Ni system at* $T = 1115\,^{\circ}\mathrm{C}$*. The red and black points are the liquidus and solidus concentrations respectively.*

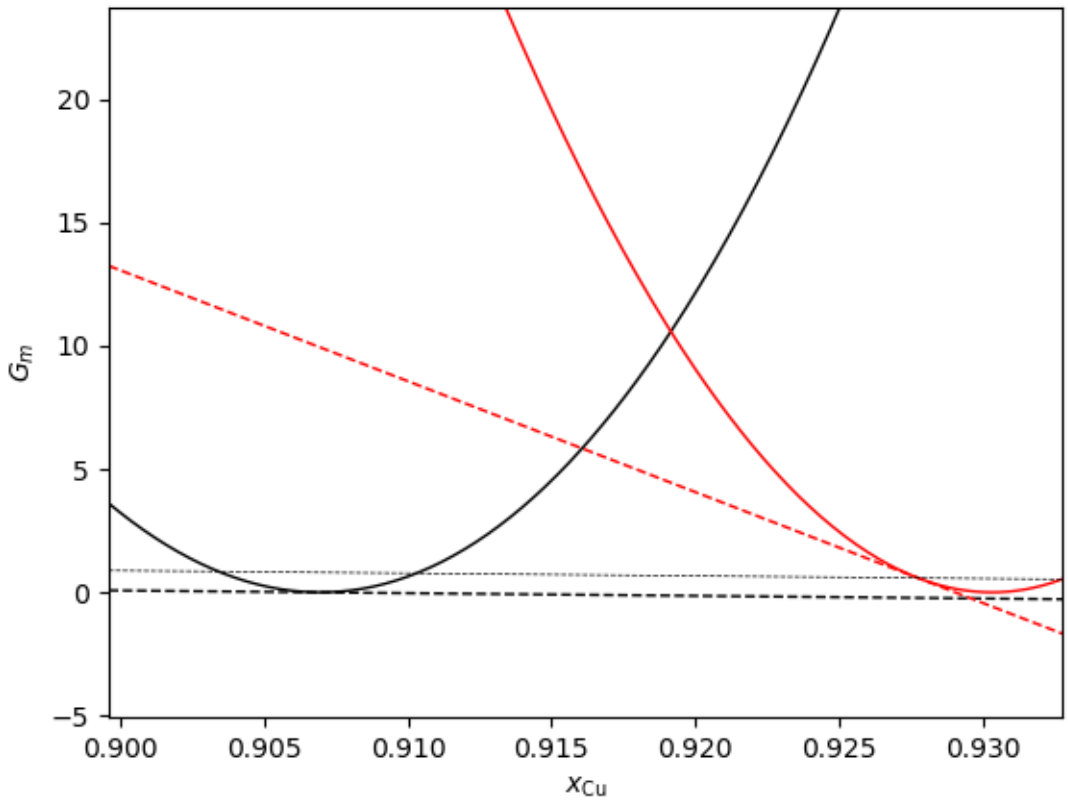

Figure 2.10 – Hillert construct of the driving force for solidification at $v = 0.7\,\mu\mathrm{m/s}$ *in the binary Cu-Ni system at* $T = 1115\,^{\circ}\mathrm{C}$*. The curves are* $G_m 60 x\, dG_m/dx(x^s)$ *(in* $\mathrm{J\,mol^{-1}}$*).*

For a specified velocity, the system of equations (2.38) and (2.39) can be solved using the `fsolve` function from the Scipy library. The resulting Hillert construct is illustrated in figure 2.10 for a fixed velocity $v = 0.7\,\mu\mathrm{m/s}$, and the following values of the mobilities: $M = 8.66 \times 10^{-2}\ \mathrm{mol\,J^{-1}\,m\,s^{-1}}$ and $L = 5.22 \times 10^{-8}\ \mathrm{mol\,J^{-1}\,m\,s^{-1}}$. To make reading of the construct easier, the tangent line to the solid G curve has been subtracted from the Gibbs energies, i.e., the curves are $G_m - x\,dG_m/dx(x^s)$, where the slope is evaluated at the concentration in the solid x^s. Therefore, the tangent to the G curve of solid is the thick black horizontal dashed line. The thin horizontal black dashed line is the parallel line passing through the tangent point to the liquid G curve. The distance between both horizontal lines is the driving force for migration ΔG^{m}. In the present example, this contribution is small with respect to the driving force for trans-interface diffusion ΔG^{t}.

The evolution of the interfacial concentrations as a function of the imposed interface velocity is shown in figure 2.11. Concentrations start at the equilibrium ones at $v = 0$. Rapidly, the concentrations of both phases deviate from equilibrium inside the two-phase domain, as interface velocity increases: the concentrations of both sides of the interface get closer to each other and the solute partitioning decreases drastically ($x^s/x^l \to 1$). For $v \geq 0.1\,\mathrm{m/s}$, x^s and x^l are very close and evolve jointly, decreasing progressively with increasing velocity. When the interface velocity exceeds about $3.8\,\mathrm{m/s}$, the concentrations of solid and liquid are almost the same and fall outside the two-phase domain to penetrate into the solid phase field (Figure 2.11 bottom). It is worth stressing that this can be achieved for very large interface velocities, on the order of $1\,\mathrm{m/s}$, for the selected parameters and for the particular system investigated.

If qualitatively somehow similar trends are reported by Buchmann and Rettenmayr [50], such as the non-monotonic evolution of the interfacial concentrations with v, these authors seem not to have achieved the high velocity regime where the solid and liquid concentrations penetrate into the one-phase field. This is likely to be due to the differences in the Gibbs energies associated with our different binary alloys.

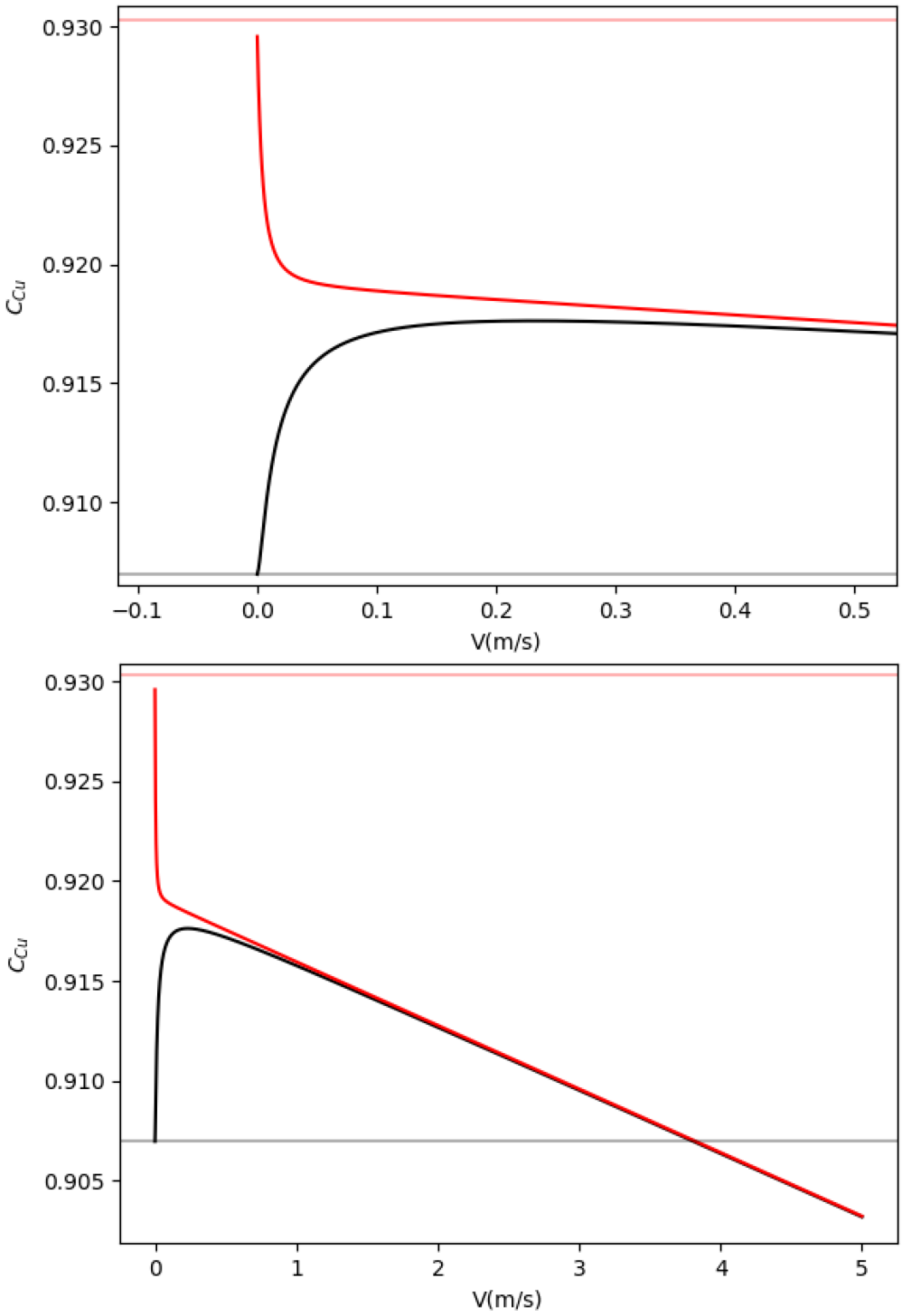

Figure 2.11 – Solid and liquid concentrations in Cu as function of the interface velocity (top: zoom in the lowest velocities range) for $M = 8.66 \times 10^{-2}\ \mathrm{mol\,J^{-1}\,m\,s^{-1}}$ *and* $L = 5.2195 \times 10^{-8}\ \mathrm{mol\,J^{-1}\,m\,s^{-1}}$. *The two horizontal lines represent the equilibrium compositions.*

The evolutions of the concentrations with respect to the kinetic parameters M and L are plotted in figures 2.13 and 2.12 for a fixed interface velocity ($v = 0.7\,\mu\mathrm{m\,s^{-1}}$). Given a fixed velocity, according to equations (2.38) and (2.39), small values of L (respectively, M) imply a high diffusion driving force ΔG^{t} (respectively migration driving force ΔG^{m}).

In the case illustrated in figure 2.12, when L is very large, ΔG^{t} tends to zero. According to the definition of ΔG^{t} in (2.28), it implies that $\Delta\mu_{\mathrm{A}} - \Delta\mu_{\mathrm{B}} \to 0$, meaning that both G-curve tangents become parallel. For reasonable values of M (i.e. excluding the extreme case where $\Delta G^{\mathrm{m}} \to \infty$), the concentrations tend towards the equilibrium values where both curves share the same tangent. On the other hand, small values of L imply that ΔG^{t} is large, indicating that the tangents are non parallel and the concentrations can only deviate from equilibrium: very small L favors non partitioning transformations because the process of atom redistribution across the interface is too slow.

In the second case illustrated in figure 2.13, when M is large, the interface migration driving force ΔG^{m} is small, and the concentrations approach equilibrium. Here, the liquid concentration lies in the two phase domain, which corresponds to the construct shown in figure 2.4 for the case of melting, where $\Delta G^{\mathrm{m}} = 0$ and the entire driving force is dissipated through trans-interface diffusion (at the largest x^{l}_{max}). On the contrary, small values of M lead to very large values of ΔG^{m} that is expended on friction and surface energy, with ΔG^{m} is largest when both concentrations lie in the solid one-phase domain.

In figure 2.13 and 2.12 it is worth noting that L and M influence the evolution of the interfacial concentrations in very different ways. L influences mainly partitioning, as expected from usual solute drag theory (e.g. [56]): as trans-interface diffusion becomes slower with small L, the two concentrations tend to collapse in the middle of the equilibrium two-phase field toward the T_O line (given by the intersection of the G curves). On the contrary, mobility M for interface migration significantly impacts the solid and liquid concentrations in a different way. When small, the interface migration is the limiting process and the interfacial concentrations strongly deviate from equilibrium into the one-phase domain of solid. For the particular system and velocity selected, it seems that the order of magnitude of M should be smaller than L to influence significantly the interfacial concentrations.

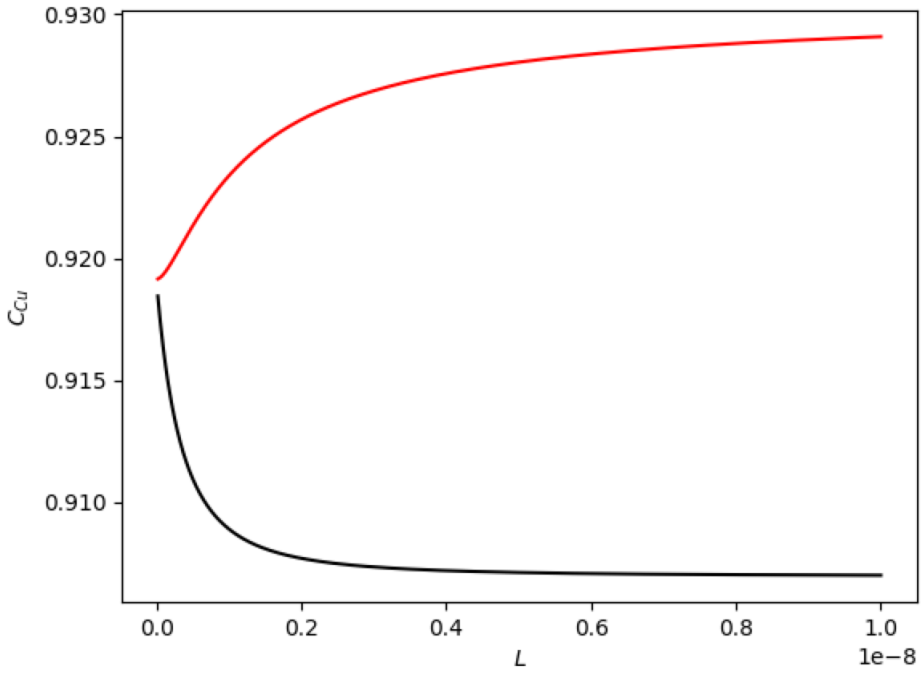

Figure 2.12 – Dependency of the solid and liquid concentrations in Cu with mobility L (in $\mathrm{mol\,J^{-1}\,m\,s^{-1}}$*) at* $v = 10^{-3}\ \mu\mathrm{m\,s^{-1}}$ *and* $M = v_0/(RT) = 8.66 \times 10^{-2}\ \mathrm{mol\,J^{-1}\,m\,s^{-1}}$.

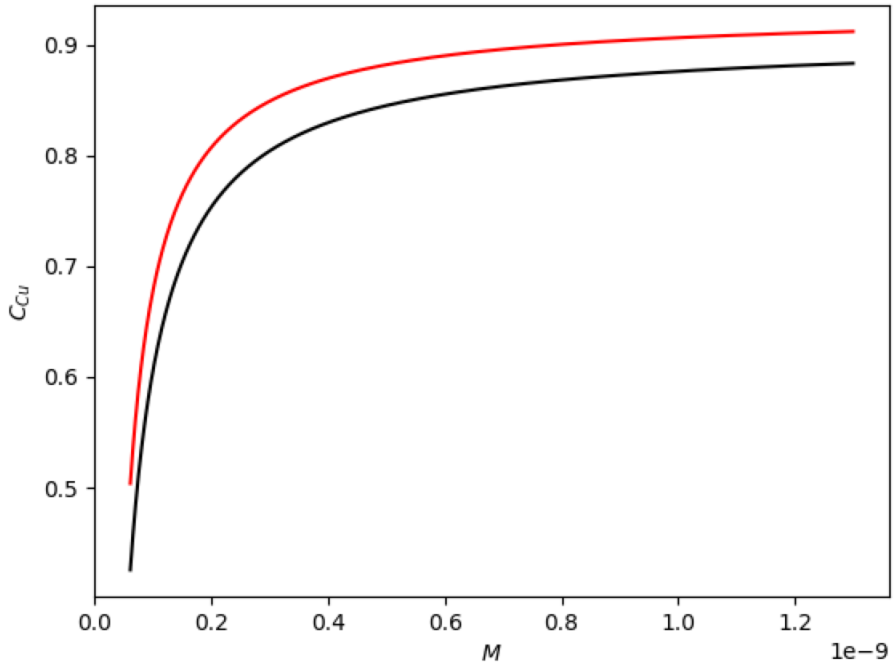

Figure 2.13 – Dependency of the solid and liquid concentrations in Cu with mobility M (in $\mathrm{mol\,J^{-1}\,m\,s^{-1}}$*) at* $v = 10^{-7}\mu\mathrm{m\,s^{-1}}$ *and* $L = D_i/(aRT) = 5.2195 \times 10^{-8}\ \mathrm{mol\,J^{-1}\,m\,s^{-1}}$.

These two effects can be observed directly on the concentration versus velocity curves. Taking the curve in figure 2.11 as a reference, an increase in M results in the interface concentrations remaining within the two-phase domain as shown in figure 2.14. When increasing the L parameter, the concentration partitioning is amplified, as illustrated in figure 2.15. Thus, M determines the domain in which interface concentrations lie, while L governs the concentration partitioning between the solid and liquid phases.

This model predicts interfacial compositions based on instantaneous velocity and the values of the kinetic parameters L and M. However, the model validity has not been really supported by experimental results, and the practical use of such arbitrary driving force decomposition remains unclear*. The direction of transformation must be known beforehand, precluding the model ability to predict the type of transformation (i.e. melting or solidification). Furthermore, considering that migration and redistribution of solute as two independent processes does not offer better insights into the processes occurring at the interface. In particular, as will be discussed at the end of this chapter, this choice is arbitrary and restrict the interfacial behaviors that can be described.

*with this respect, it is interesting to note that Hillert himself has recognize the arbitrariness of such a decomposition in [41].

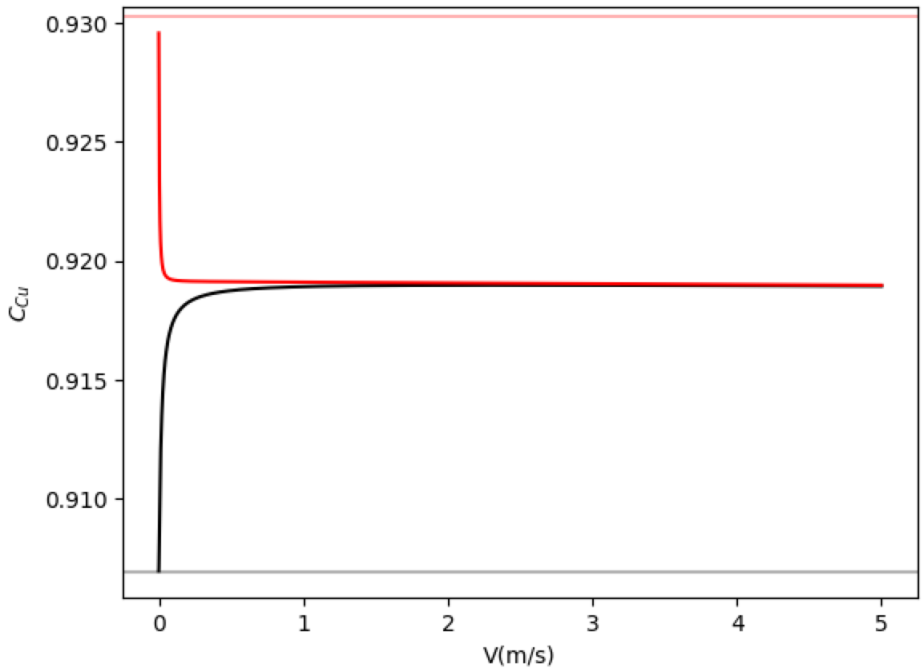

Figure 2.14 – Solid and liquid concentrations in Cu as function of the interface velocity for $L = 5.22 \times 10^{-8}\,\mathrm{mol\,m\,s^{-1}\,J^{-1}}$ *and* $M = 3.47\,\mathrm{mol\,m\,s^{-1}\,J^{-1}}$*, 40 times larger than in the reference case in figure 2.11.*

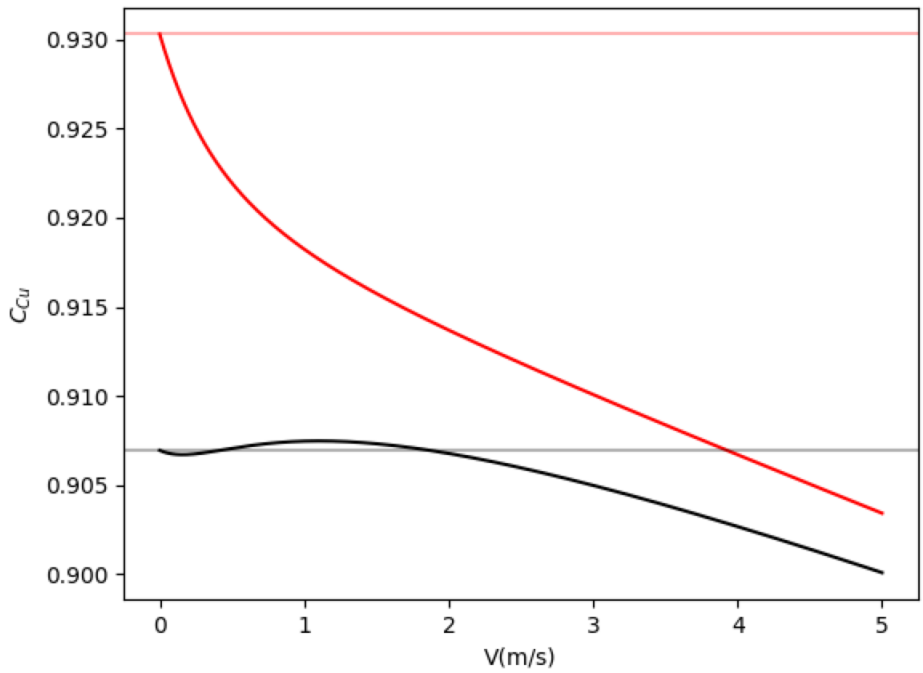

Figure 2.15 – Solid and liquid concentrations in Cu as function of the interface velocity for $M = 0.0866\,\mathrm{mol\,m\,J^{-1}\,s^{-1}}$ *and* $L = 5.22 \times 10^{-6}\,\mathrm{mol\,m\,J^{-1}\,s^{-1}}$*, 100 times higher than in the reference case in figure 2.11.*

2.4 Lesoult model

A new approach for handling non-equilibrium interfaces is proposed, which does not rely on Hillert arbitrary decomposition of the driving force into two independent processes. The downside of Hillert model is the requirement for knowing beforehand the direction of the transformation (S $\rightarrow$ L or L $\rightarrow$ S), which determines the system to be solved. The model proposed here does not impose this prior knowledge. Instead, it allows the system to evolve freely from its initial conditions, compliant with the second law of thermodynamics.

Picking up from Lesoult calculations in [57] with simplified notations and assumptions, e.g. equal molar volumes between solid and liquid, the interfacial fluxes of A and B are redefined as:

$$I_{\mathrm{A}} = \left[(1-c^s)\,\mathbf{v}^s + \mathbf{j}^s_{\mathrm{A}}\right]\cdot\mathbf{n}^s = -\left[(1-c^l)\,\mathbf{v}^l + \mathbf{j}^l_{\mathrm{A}}\right]\cdot\mathbf{n}^l \tag{2.56}$$

$$I_{\mathrm{B}} = \left[c^s\,\mathbf{v}^s + \mathbf{j}^s_{\mathrm{B}}\right]\cdot\mathbf{n}^s = -\left[c^l\,\mathbf{v}^l + \mathbf{j}^l_{\mathrm{B}}\right]\cdot\mathbf{n}^l \tag{2.57}$$

where $\mathbf{n}^s = -\mathbf{n}^l$ are the unit vectors normal to the interface, pointing respectively into the solid and the liquid, and where $\mathbf{v}^\phi$ is the mean velocity of atoms (A and B) in phase ϕ The following convention is adopted: $v = \mathbf{v}^s\cdot\mathbf{n}^s = -\mathbf{v}^l\cdot\mathbf{n}^l$ ($v>0$ for solidification). To differentiate the Lesoult model from the Hillert one, the solute molar fractions of B is denoted as c rather than x (concentration of A is $1-c$).

From the postulate of linearity of fluxes with the driving forces (chemical potentials) in equation (2.18) and (2.19):

$$(1-c^s)\,v + \mathbf{j}^s_{\mathrm{A}}\cdot\mathbf{n}^s = L_{\mathrm{AA}}\,\Delta\mu_{\mathrm{A}} + L_{\mathrm{AB}}\,\Delta\mu_{\mathrm{B}} \tag{2.58}$$

$$c^l\,v - \mathbf{J}^l_{\mathrm{B}}\cdot\mathbf{n}^l = L_{\mathrm{BA}}\,\Delta\mu_{\mathrm{A}} + L_{\mathrm{BB}}\,\Delta\mu_{\mathrm{B}} \tag{2.59}$$

$$(c^l - c^s)\,v = \left(\mathbf{j}^l_{\mathrm{B}} - \mathbf{j}^s_{\mathrm{B}}\right)\cdot\mathbf{n}^l \tag{2.60}$$

Equation (2.60) is the solute balance. When vacancies in the solid are neglected, it is found that $\mathbf{j}^s_{\mathrm{A}} = -\mathbf{J}^s_{\mathrm{B}}$ and:

$$(1-c^s)\,v + \mathbf{j}^s_{\mathrm{B}}\cdot\mathbf{n}^l = L_{\mathrm{AA}}\,\Delta\mu_{\mathrm{A}} + L_{\mathrm{AB}}\,\Delta\mu_{\mathrm{B}} \tag{2.61}$$

$$c^s\,v - \mathbf{j}^s_{\mathrm{B}}\cdot\mathbf{n}^l = L_{\mathrm{BA}}\,\Delta\mu_{\mathrm{A}} + L_{\mathrm{BB}}\,\Delta\mu_{\mathrm{B}} \tag{2.62}$$

$$(c^l - c^s)\,v = \left(\mathbf{j}^l_{\mathrm{B}} - \mathbf{j}^s_{\mathrm{B}}\right)\cdot\mathbf{n}^l \tag{2.63}$$

where $\Delta\mu = \mu^l - \mu^s$ whatever the direction of the transformation (contrary to Hillert model where the conventions must be changed).

Next, simple expressions of the jumps in the chemical potentials are sought to be substituted into equations (2.61) and (2.62).

For simplicity, the interaction terms in the CalPhaD description of the Gibbs energies have been neglected, assuming that the solid and liquid phases can be described reasonably well by ideal solutions. Hence:

$$\mu_i^\phi = \mu_i^{\phi 0} + RT\ln\left(c_i^\phi\right) \tag{2.64}$$

for $i\in\{\mathrm{A},\mathrm{B}\}$ and $\phi\in\{l,s\}$, and where $\mu_i^{\phi 0}$ is the chemical potential of reference.

At equilibrium, all chemical potentials between coexisting phases are equal so that:

$$\mu_i^{l0} + RT\ln\left(c_i^{l\,\mathrm{eq}}\right) = \mu_i^{s0} + RT\ln\left(c_i^{s\,\mathrm{eq}}\right) \tag{2.65}$$

$$\mu_i^{l0} - \mu_i^{s0} = RT\ln\left(c_i^{s\,\mathrm{eq}}/c_i^{l\,\mathrm{eq}}\right) = RT\ln\left(k_i^{\mathrm{eq}}\right) \tag{2.66}$$

with $c^{\phi\,\mathrm{eq}}$ the equilibrium concentration of phase ϕ, and $k_i^{\mathrm{eq}} = c_i^{s\,\mathrm{eq}}/c_i^{l\,\mathrm{eq}}$ the equilibrium partition coefficient.
The final expression of the jump in chemical potential is derived. For any couple of concentrations (c_i^s, c_i^l), one has:

$$\Delta\mu_i = RT \ln\left(k_i^{\mathrm{eq}} c_i^l / c_i^s\right) \tag{2.67}$$

The next step consists in assessing the fluxes in the bulk in equations (2.61)-(2.63). With ideal solutions, the expressions of the fluxes in terms of the gradient of chemical potentials reduce simply to the 1st Fick's law. Introducing characteristic diffusion lengths δ^ϕ to express the concentration gradients, the following is obtained:

$$J_{\mathrm{B}}^\phi = -D_{\mathrm{B}}^\phi \frac{c^\phi - \langle c^\phi \rangle}{\delta^\phi} \tag{2.68}$$

where $\langle c^\phi \rangle$ is the concentration in phase ϕ away from the interface.

Finally, the kinetic coefficients L_{ij} can be related to some kind of interfacial diffusion coefficients $D_{ij}^\star$ characterizing the atom transfer at the interface with units easier to interpret:

$$L_{ij} = \frac{D_{ij}^\star}{aRT} \tag{2.69}$$

where a is the interface width.

Using the definitions in equations (2.68) and (2.69), and normalizing (2.61) and (2.62) by the rate of diffusion of B atoms in the liquid $D_{\mathrm{B}}^l/\delta^l$ gives the final system of equations to solve:

$$(1-c^s)\,\mathrm{Pe} + \gamma\left(\langle c^s\rangle - c^s\right) = \alpha\,\Delta\tilde{\mu}_{\mathrm{A}} + \varepsilon\,\Delta\tilde{\mu}_{\mathrm{B}} \tag{2.70}$$

$$c^s\,\mathrm{Pe} - \gamma\left(\langle c^s\rangle - c^s\right) = \varepsilon\,\Delta\tilde{\mu}_{\mathrm{A}} + \beta\,\Delta\tilde{\mu}_{\mathrm{B}} \tag{2.71}$$

$$(c^l - c^s)\,\mathrm{Pe} = \left(c^l - \langle c^l\rangle\right) + \gamma\left(c^s - \langle c^s\rangle\right) \tag{2.72}$$

where $\mathrm{Pe} = v\delta^l/D_{\mathrm{B}}^L$ is the Péclet number and $\Delta\tilde{\mu}_i = \ln\left(k_i^{\mathrm{eq}} c_i^l/c_i^s\right)$ is the non-dimensional chemical potential jumps of species i. α, β and ε are the non-dimensional interfacial kinetic coefficients, defined as follows:

$$\alpha = \frac{D_{\mathrm{AA}}^\star}{D_{\mathrm{B}}^l}\,\delta_l' \tag{2.73}$$

$$\beta = \frac{D_{\mathrm{BB}}^\star}{D_{\mathrm{B}}^l}\,\delta_l' \tag{2.74}$$

$$\varepsilon = \frac{D_{\mathrm{AB}}^\star}{D_{\mathrm{B}}^l}\,\delta_l' \tag{2.75}$$

where $\delta_l' = \delta_l/a$ is the non-dimensional diffusion length in bulk liquid. The last non-dimensional parameter is the ratio between the characteristic diffusion times in solid and liquid:

$$\gamma = \frac{D_{\mathrm{B}}^s}{\delta_s}\,\frac{\delta_l}{D_{\mathrm{B}}^l} \tag{2.76}$$

2.4.1 Implementation and parameters

Rather than finding the zero of the full nonlinear system, the interfacial solute balance (2.72) is inserted into (2.71) and (2.70). The resulting system of 2 nonlinear equations with the 2 unknowns (c^s, c^l) is then solved using a minimization method with the `fmin` function from the `scipy.optimize module`. For that purpose, the squares of equations (2.71) and (2.70) are summed, and the global minimum is searched by mapping the entire (c^s, c^l) space with some specified grid as initial guess for the Nelder-Mead simplex method called by `fmin`. Since the kinetic parameters are unknown due to the difficulty of measuring $D^\star_{ij}$ (or L_{ij}), the problem is simplified by assuming that α, β, and ε are simple functions of the interfacial concentrations. These parameters are also assumed to vary with a quantity $\alpha^\star$ that mimics time evolution since they are all proportional to δ_l (see equations (2.73)–(2.75)) that can be reasonably assumed to vary as $\sqrt{t}$:

$$\alpha = \alpha^\star f(c^l, c^s) \tag{2.77}$$

$$\beta = \alpha^\star g(c^l, c^s) \tag{2.78}$$

$$\varepsilon = \lambda \sqrt{\alpha\beta} \tag{2.79}$$

with $\lambda \leq 1$ to fulfill the condition (2.24) of positive definiteness of interfacial mobilities.

Different concentration dependencies can be considered. Unlike the usual assumption for solid-liquid interfaces where diffusion depends solely on the liquid side, here, for solutal melting, a simple linear dependency on solid concentration is considered:

$$f(c^l, c^s) = 1 - c^s \tag{2.80}$$

$$g(c^l, c^s) = c^s \tag{2.81}$$

With these functions ε varies as $\sqrt{c^s(1-c^s)}$.

2.4.2 Results and discussion

Figure 2.16 represents a qualitative time evolution (i.e. versus $\alpha^\star \propto \delta'_l \propto \sqrt{t}$ in logarithmic scale) of the interfacial concentration of Cu in liquid in red and in solid in black. The dotted lines represent the equilibrium concentrations. Analogously to solutal melting experiment of [4], the Cu-Ni system is chosen with $T = 1115\,°\text{C}$, and the initial concentrations of solid and liquid are $c^l = 1$ and $c^s = 0$ respectively. Three values of λ have been tested: 0, 0.5 and 1 from light to dark color. γ, accounting for the asymmetrical diffusion time scale between solid and liquid and is set to 0.2.

The negative value of the Péclet number in figure 2.17 indicates that a dissolution process is predicted. The liquid starts from a pure composition. During the first transient stage ($\alpha^\star \leq 0.02$), $|\text{Pe}|$ decreases linearly with $\alpha^\star$ and the liquid concentration drops below the solidus concentration, while the solid remains pure Ni. In a second stage, for $\alpha^\star \in [0.02; 4]$ the amplitude of the Péclet number decreases faster and tends to 0. The liquid concentration remains around 85% of Cu (with a very small increase). Solid concentration continues to increase but is still below 75% of Cu.

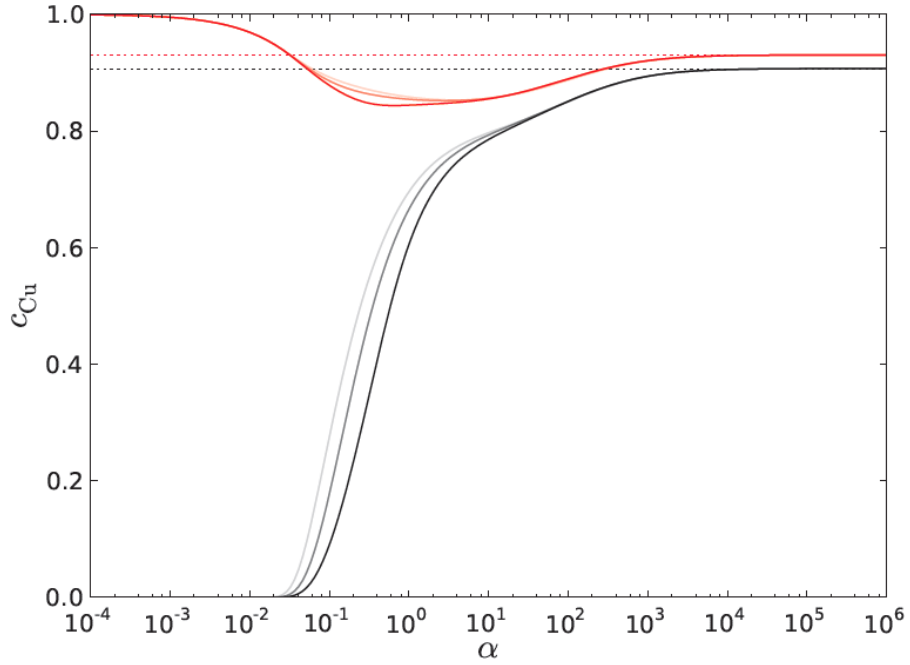

Figure 2.16 – Concentration of Cu in liquid (red) and in solid (black) as function of the non-dimensional parameter $\alpha^\star$ varying as $\sqrt{t}$. The lightest curve corresponds to no cross-mobility $\lambda = 0$, while the darkest corresponds to the largest possible cross-mobility $\lambda = 1$ (Eq. 2.79).

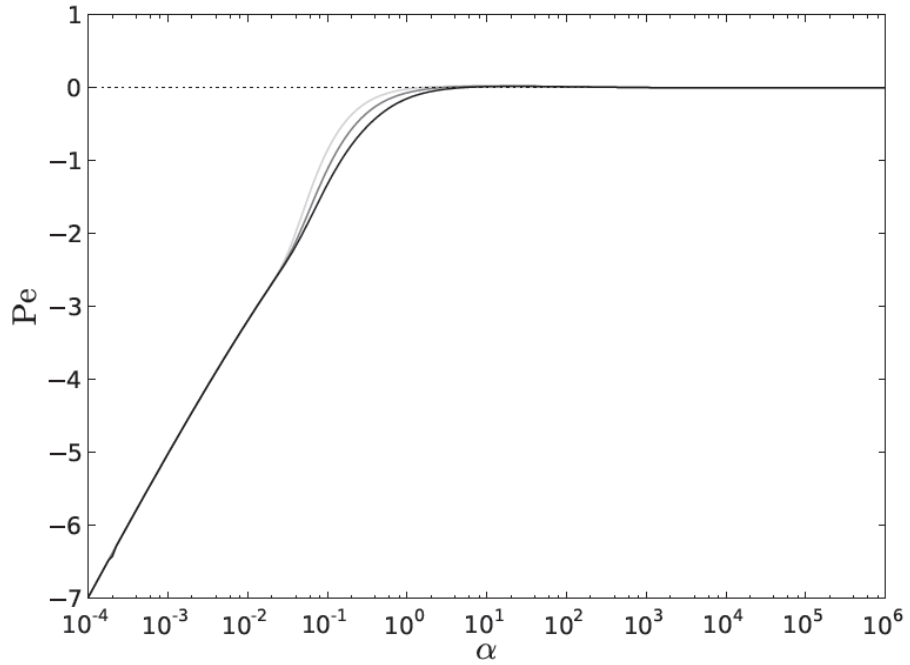

Figure 2.17 – Péclet number as function of the non-dimensional parameter $\alpha^\star$. The lightest curve corresponds to no cross-mobility $\lambda = 0$, while the darkest corresponds to the largest possible cross-mobility $\lambda = 1$ (Eq. 2.79).

In a third stage, the interface velocity is very small and tends very slowly to 0 (not visible in figure 2.17). Interfacial concentrations also increase slowly together and achieve their equilibrium values for $\alpha^\star > 4000$. For $\alpha^\star > 3$, Pe becomes slightly positive (not visible on the scale of Figure 2.17), indicating that the system solidifies back. It is worth noting that such a phenomenon has been observed at the end of solutal melting experiments in both Cu-Ni and Au-Ag systems [4].
These calculations would suggest that the solutal melting experiments where both solid and liquid interface concentrations are located in the one-phase domain would correspond to the second transient stage for $\alpha^\star \in [0.02;4]$. Considering the definition of this nondimensional parameter

$$\alpha^\star = \frac{D^\star_{\mathrm{NiNi}}}{D^l_{\mathrm{Cu}}} \times \frac{\delta_l}{a}$$

and assuming that $\delta_l = \sqrt{D^l_{\mathrm{Cu}} t}$, the following expression for $D^\star_{\mathrm{NiNi}}$ can be provided::

$$D^\star_{\mathrm{NiNi}} = a\,\alpha^\star \sqrt{\frac{D^l_{\mathrm{Cu}}}{t}} \tag{2.82}$$

It must be stressed that $\alpha^\star \propto \sqrt{t}$ for $D^\star_{\mathrm{NiNi}}$ to be constant. Moreover, β is set to scale directly as $\alpha^\star$ (Eq. (2.78)) so that the estimation of $D^\star_{\mathrm{NiNi}}$ holds also for $D^\star_{\mathrm{CuCu}}$ if one neglect the dependencies with respect to concentrations. Considering that

- the kinetics at $t \approx 30\,\mathrm{s}$ in figure 1.5 would correspond to $\alpha^\star = 0.2$,
- the order of magnitude found in the literature for the intrinsic diffusivity of Ni in Ni-Cu liquid around 1100 °C is $D^l_{\mathrm{Cu}} \approx 10^{-9}\ \mathrm{m^2\,s^{-1}}$, e.g. [58],
- the interface width is about $a = 0.6\,\mathrm{nm}$,

An interfacial diffusion coefficient $D^\star_{\mathrm{NiNi}}$ of approximately $6.93 \times 10^{-16}\ \mathrm{m^2\,s^{-1}}$ was obtained (corresponding to $L_{\mathrm{NiNi}} \approx 10^{-10}\ \mathrm{mol\,m\,J^{-1}\,s^{-1}} \approx 9.66 \times 10^{-5}\ \mathrm{Å\,eV^{-1}\,ns^{-1}}$), which is three orders of magnitude lower than the intrinsic diffusivity of Cu in Cu-Ni solid around 1100 °C [59, 60]. Nonetheless, using the definition of the Péclet number which takes a value around -0.5 for $\alpha^\star \approx 0.2$, considering the very low value of $D^\star_{\mathrm{NiNi}}$ gives a dissolution rate of about $-2.88\,\mathrm{\mu m\,s^{-1}}$, in agreement with the experiments of [4] (Fig. 1.5).
If one considers that $\alpha^\star \approx 0.2$ corresponds to much shorter times, such as 100 ns (the typical time reached in our molecular dynamics simulations in §3), the interfacial diffusivity is still two orders of magnitude (around $10^{-11}\ \mathrm{m^2\,s^{-1}}$) lower than that of a liquid (and the dissolution rate much too large, of the order of $5\,\mathrm{cm\,s^{-1}}$).
Finally, the three different curves in Figures 2.16 and 2.17 show that the cross-term ε delays the process only slightly and does not drastically change the picture.

The same calculations were repeated for different dependencies of the mobilities with the concentration, with results presented in Figures 2.18 and 2.19. The lightest curve depends only on c^l, as Lesoult suggested [57],

$$\begin{aligned} f(c^s, c^l) &= 1 - c^l \\ g(c^s, c^l) &= c^l \end{aligned} \tag{2.83}$$

while the darkest depends solely on c^s.

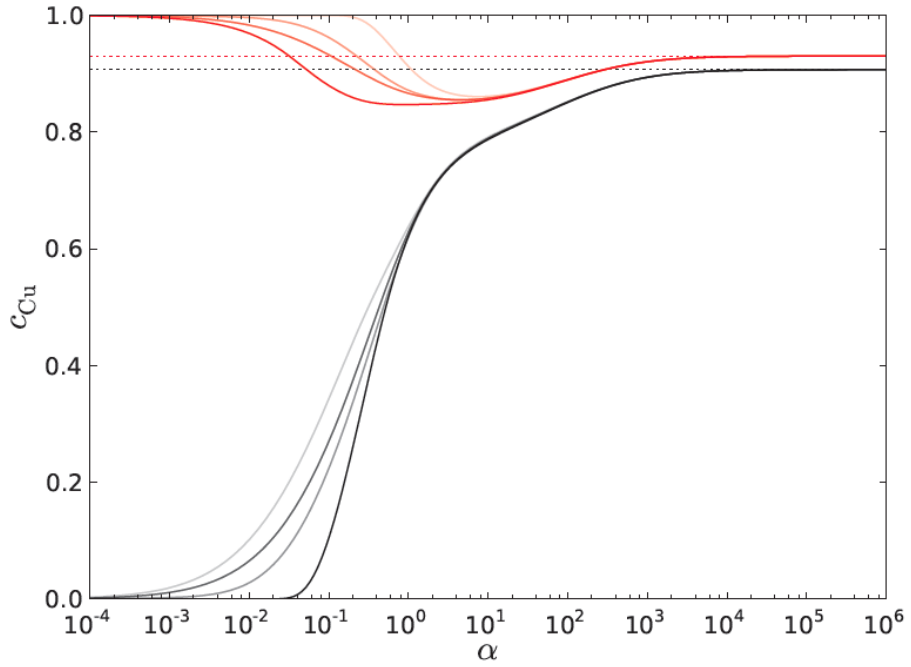

Figure 2.18 – Evolution of the interfacial concentrations for different dependencies of the mobilities with concentrations: on c^l (clearest), c^s (darkest), arithmetic Eqs. (2.84) and geometric averages Eqs. (2.85) (intermediate transparencies).

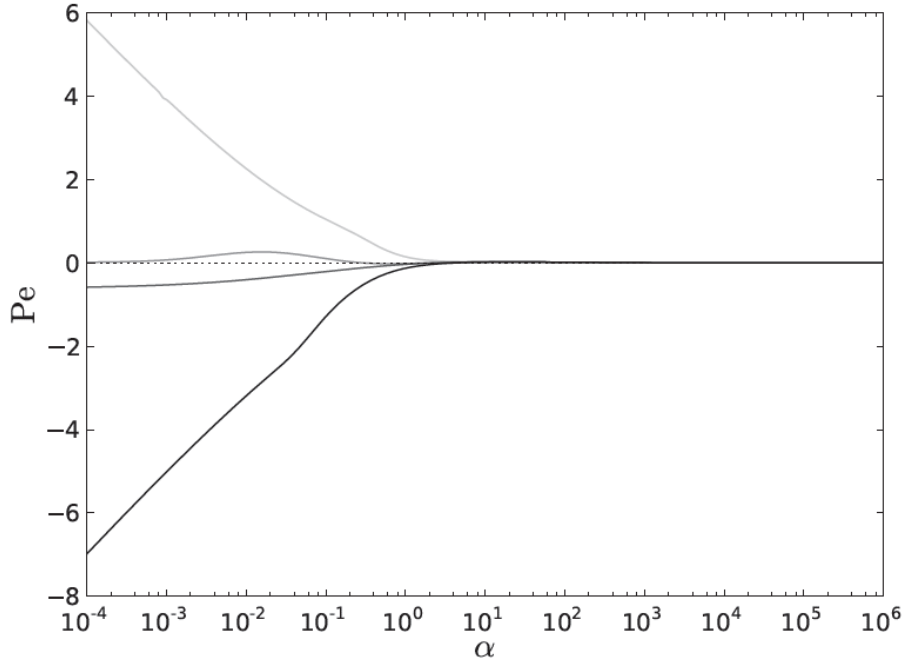

Figure 2.19 – Evolution of the Péclet number for different dependencies of the mobilities with concentrations: on c^l (clearest), c^s (darkest), arithmetic Eqs. (2.84) and geometric averages Eqs. (2.85) (intermediate transparencies).

The remaining curves rely on different averages, such as arithmetic:

$$\begin{aligned} f(c^s, c^l) &= 1 - \frac{c^s + c^l}{2} \\ g(c^s, c^l) &= \frac{c^s + c^l}{2} \end{aligned} \tag{2.84}$$

or quadratic:

$$\begin{aligned} f(c^s, c^l) &= \sqrt{(1-c^s)(1-c^l)} \\ g(c^s, c^l) &= \sqrt{c^s c^l} \end{aligned} \tag{2.85}$$

While the evolutions of the concentration profiles remain similar (c^s seems to extend slightly the non-equilibrium regime), the differences emerged in the Péclet number. Indeed, when the mobilities depend on c^s, Ni dissolves in Cu (Pe < 0) as previously; on the contrary, when the mobilities depend on c^l, one observes only solidification (Pe > 0), in complete contradiction to the experiments. Taking into account two different averages, Eqs. (2.84) and (2.85) between c^s and c^l slow down the entire process with Pe remaining moderate. Still, the direction of the transformation, whether dissolution or solidification, differs and depends on the weight attributed to either solid and liquid. Thus, the concentration dependence of the mobilities is critical in determining the direction of transformation.

Finally, the influence of the ratio γ between the diffusion rate of Cu in solid $D^s_{\mathrm{Cu}}/\delta_s$ and in liquid $D^l_{\mathrm{Cu}}/\delta_l$ was investigated. For that purpose, calculations with different values of $\gamma \in \{0.1; 0.25; 0.3; 0.5; 1\}$[†] was performed. The evolutions of the concentrations and Péclet are plotted in Figures 2.20 and 2.21 respectively, the largest γ the darkest. It is clear that changing γ has a strong influence on the process. The largest γ (i.e. when Cu diffuses rapidly in Ni solid) the longest the non-equilibrium regime: the liquid concentration at the interface dives more deeply in the solid phase field for a longer duration, and the solid concentration only starts to increase for $\alpha^\star > 0.2$. On the contrary, for the lowest γ, the behavior is very different. Indeed, the liquid concentration remains in the liquid phase field and the solid concentration increases rapidly ($\alpha^\star \leq 0.1$) to penetrate also in the liquid phase field. It seems that there is a critical ratio (in between $\gamma = 0.1$ and the reference case at $\gamma = 0.2$) above which the two interfacial concentrations dive into the solid one phase field. The evolution of the Péclet number is relatively unaffected: All values cause the process to start with a fast dissolution stage (Pe < 0). Nonetheless, the smaller γ leads to a faster decay of the dissolution rate (almost finished for $\alpha^\star > 0.1$), and for $\gamma = 1$ a larger overshoot of Pe in the solidification domain is observed. These results suggest that bulk diffusion in both phases significantly influences the shape of the concentration profile at the interface.

[†]The reference case discussed previously was for $\gamma = 0.2$

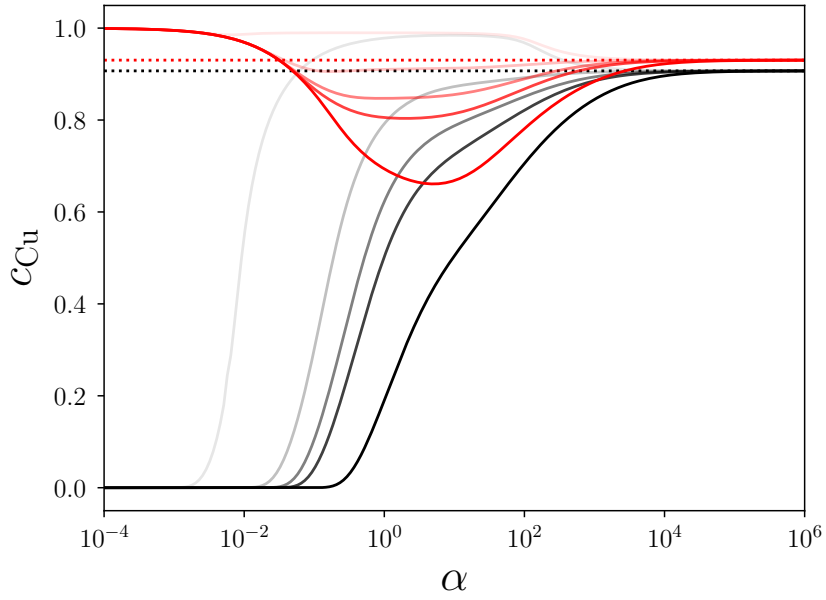

Figure 2.20 – Influence of $\gamma \in \{0.1; 0.25; 0.3; 0.4; 1\}$ *(lightest to darkest) on the evolution of the interfacial concentrations.*

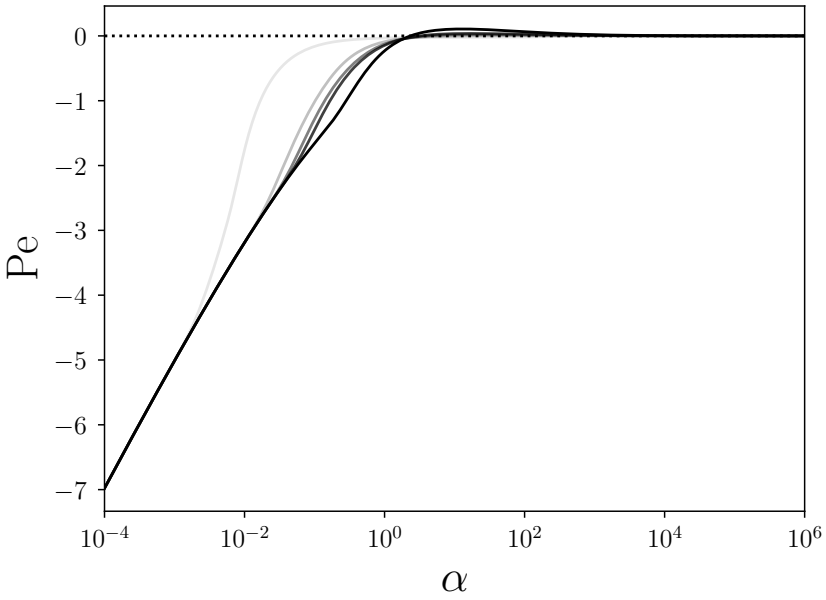

Figure 2.21 – Influence of $\gamma \in \{0.1; 0.25; 0.3; 0.4; 1\}$ *(lightest to darkest) on the evolution of the Péclet number.*

Although the predictions of Lesoult model shown above seem appealing, it has been found that the interfacial diffusivities should be much smaller than their bulk counterparts to comply with the experiments [4]. Therefore, the case of solidification using the values of the reference case of solutal melting has been examined. It must be emphasized again that the equations to solve remain the same regardless of the direction of the transformation, contrary to the Hillert and Rettenmayr formulation.

Similar to the reference solutal melting calculation, $\alpha = \alpha^\star, f(c^s, c^l)$ and $\beta = \alpha^\star, g(c^s, c^l)$ have been considered. A significant off-diagonal term with $\lambda = 0.9$ has been selected, and a small ratio $\gamma = 0.1$ has been chosen. The initial concentrations of Cu c^s and c^l were set at their equilibrium values at 1150 °C, which is higher than the holding temperature of 1115 °C. According to the phase diagram in Fig. 2.8, c^s and c^l starts at values below the solidus, as shown also in Figure 2.22 where the horizontal dashed lines define the boundaries of the two phase field. As expected, this initial condition induces the solidification of the system, as clearly shown by the positive values of the Péclet number in Figure 2.23. During the entire process ($\alpha^\star \leq 10^4$), the interfacial concentrations are out of equilibrium. They are starting to increase towards their equilibrium values around $\alpha^\star \approx 10^2$. Using the same values of interfacial diffusivities/mobilities as those found to agree with solutal melting experiments, the interface would remain out of equilibrium for more than 7.5×10^6 s. This is obviously not the usual time scales for the initial transient regime in solidification processes. If one considers that this time scale should be smaller than 0.1 s (which gives solidification rates $\mathcal{O}(1\,\mu\mathrm{m\,s^{-1}})$), one obtains $D^\star_{\mathrm{NiNi}} = 6 \times 10^{-12}$ $\mathrm{m^2\,s^{-1}}$, four orders of magnitude larger than for solutal melting. The reason for the discrepancy has remained puzzling, and no arguments have been found that can reconcile the parameters compliant with solutal melting on the one hand and solidification on the other hand.

Surprisingly, neither the concentration profiles nor the Péclet number is affected by the concentration dependence of the kinetic parameters in the case of solidification. Unlike the configuration that leads to solutal melting, Pe in this configuration remains unchanged for all the functions mentioned previously $f(c^s, c^l)$ and $g(c^s, c^l)$. The controlling parameter is γ, which represents the ratio of the diffusion coefficients of solid and liquid. A high value of γ indicates a more significant diffusion in the solid phase, delaying the transformation, while a low γ value suggests greater diffusion in the growing phase, leading to an accelerated transformation.

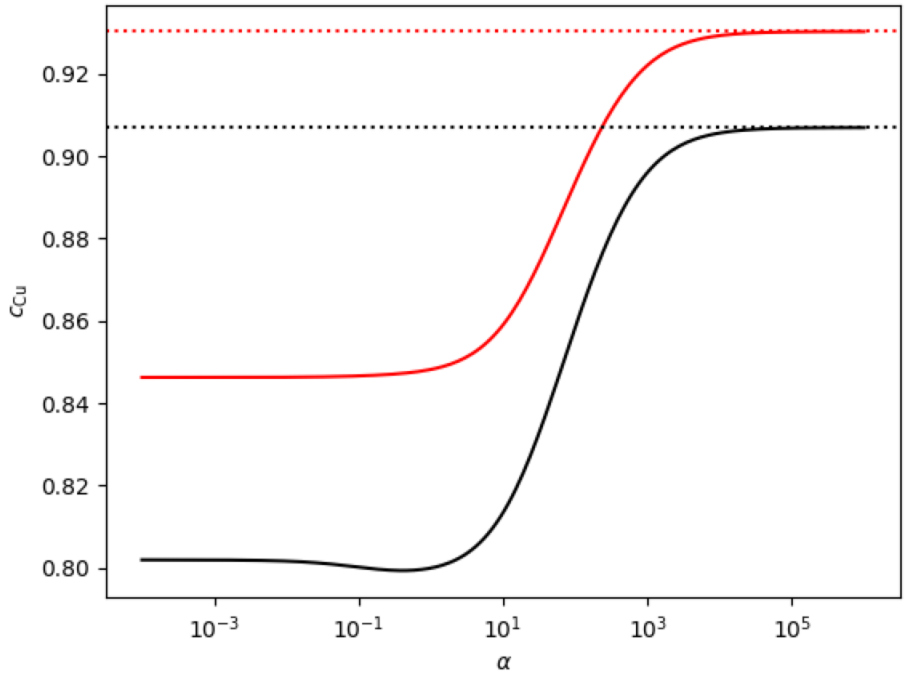

Figure 2.22 – Evolution of the solid and liquid concentrations at the interface during solidification.

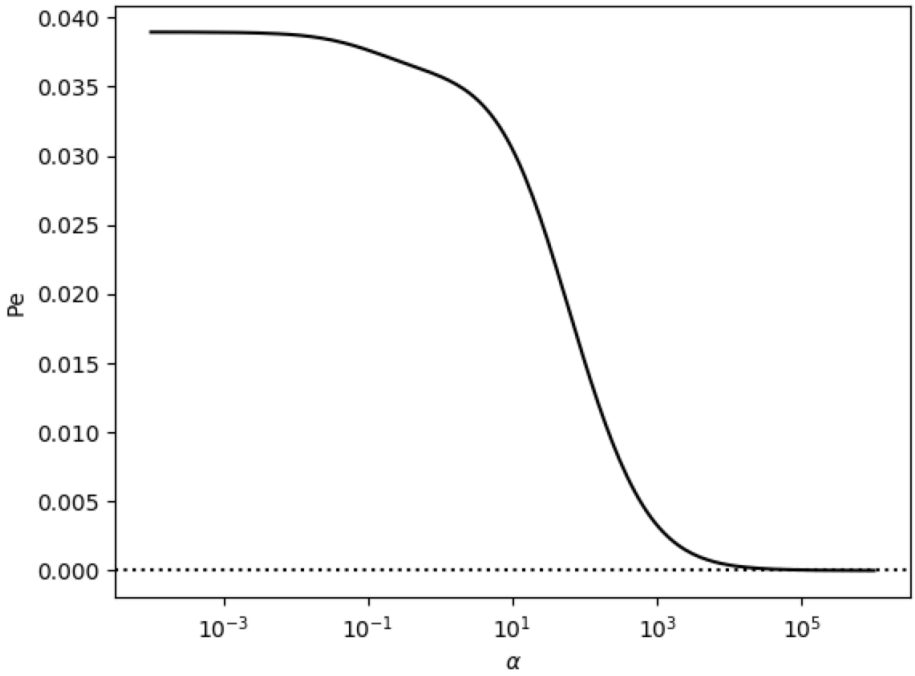

Figure 2.23 – Pe evolution of solid and liquid phase during solidification.

2.5 Mapping Hillert and Lesoult formulations

Although the use of the Lesoult model was motivated by the flaws and unnecessary assumptions of the Hillert model, it is shown in this last section that an equivalence between them can be established.
Starting from the same assumptions, the entropy production rate is written as:

$$T\,\dot{s}_{\text{irr}} = I^{\text{m}}\,\mathscr{A}^{\text{m}} + I^{\text{t}}\mathscr{A}^{\text{t}} = I_{\text{A}}\Delta\mu_{\text{A}} + I_{\text{B}}\Delta\mu_{\text{B}} \geq 0 \tag{2.86}$$

where the affinities $\mathscr{A}^{\text{t}}$ and $\mathscr{A}^{\text{m}}$ have been introduced, associated to the migration and trans-interface fluxes I^{m} and I^{t} respectively.
As stated in equation 2.46, the entropy production rate can be expressed in terms of liquid fluxes and concentrations as follows:

$$T\,\dot{s}_{\text{irr}} = I^{\text{m}}\,\mathscr{A}^{\text{m}} + I^{\text{t}}\mathscr{A}^{\text{t}} = v\left[x^{l}\Delta\mu_{\text{B}} + (1-x^{l})\Delta\mu_{\text{A}}\right] + j^{l}_{\text{B}}\left(\Delta\mu_{\text{A}} - \Delta\mu_{\text{B}}\right) \tag{2.87}$$

By simple analogy, and using (2.57) and (2.87), the following equations are found:

$$\begin{aligned} I^{\text{m}} = v &= I_{\text{A}} + I_{\text{B}} \\ I^{\text{t}} = j^{l}_{\text{B}} &= -I_{\text{B}} + x^{l}_{\text{B}}\,v = x^{l}\,I_{\text{A}} - (1-x^{l})\,I_{\text{B}} \end{aligned} \tag{2.88}$$

In (2.87), the affinities associated with migration and trans-interface diffusion can be identified:

$$\begin{aligned} \mathscr{A}^{\text{m}} &= x^{l}\,\Delta\mu_{\text{B}} + (1-x^{l})\,\Delta\mu_{\text{A}} \\ \mathscr{A}^{\text{t}} &= \Delta\mu_{\text{A}} - \Delta\mu_{\text{B}} \end{aligned} \tag{2.89}$$

In Hillert model, the affinities are related to the Gibbs energies as follows: $\mathscr{A}^{\text{m}} = \Delta G^{\text{m}}$ and $\mathscr{A}^{\text{t}} = \Delta G^{\text{t}}/(x^{l} - x^{s})$.
Using (2.88) and (2.89), the reciprocal expressions of the flux and driving forces for each species can be obtained:

$$I_{\text{A}} = (1-x^{l})\,I^{\text{m}} + I^{\text{t}} \tag{2.90}$$

$$I_{\text{B}} = x^{l}\,I^{\text{m}} - I^{\text{t}} \tag{2.91}$$

$$\Delta\mu_{\text{A}} = \mathscr{A}^{\text{m}} + x^{l}\,\mathscr{A}^{\text{t}} \tag{2.92}$$

$$\Delta\mu_{\text{B}} = \mathscr{A}^{\text{m}} - (1-x^{l})\,\mathscr{A}^{\text{t}} \tag{2.93}$$

Now, the general expressions relating the flux and forces for the migration and trans-interface diffusion processes is introduced:

$$I^{\text{m}} = L_{\text{mm}}\,\mathscr{A}^{\text{m}} + L_{\text{mt}}\,\mathscr{A}^{\text{t}} \tag{2.94}$$

$$I^{\text{t}} = L_{\text{tm}}\,\mathscr{A}^{\text{m}} + L_{\text{tt}}\,\mathscr{A}^{\text{t}} \tag{2.95}$$

These equations are the same as equations (2.36) and (2.37) defined by Hillert, with the only difference in the cross terms not being neglected in the present case.
The Onsager conditions on the kinetic parameters impose the following constraints:

$$L_{\text{mt}} = L_{\text{tm}} \tag{2.96}$$

$$L_{\text{mm}},\, L_{\text{tt}} \geq 0 \tag{2.97}$$

$$L_{\text{mm}} \times L_{\text{tt}} \geq L^{2}_{\text{mt}} \tag{2.98}$$

By combining the expressions (2.88), (2.18) and (2.19), the migration flux can be written as follows:

$$I^{\mathrm{m}} = I_{\mathrm{A}} + I_{\mathrm{B}} = (L_{\mathrm{AA}} + L_{\mathrm{BA}})\,\Delta\mu_{\mathrm{A}} + (L_{\mathrm{BB}} + L_{\mathrm{AB}})\,\Delta\mu_{\mathrm{B}} \tag{2.99}$$

The chemical potentials can be replaced by their expressions (2.90) and (2.91) with respect to the affinities :

$$I^{\mathrm{m}} = \left[L_{\mathrm{AA}} + 2L_{\mathrm{BA}} + L_{\mathrm{BB}}\right] \mathscr{A}^{\mathrm{m}} + \left[x^l L_{\mathrm{AA}} - (1-2x^l)L_{\mathrm{AB}} - (1-x^l)L_{\mathrm{BB}}\right] \mathscr{A}^{\mathrm{t}} \tag{2.100}$$

Using the same procedure for the trans-interface flux, the following expression is obtained:

$$\begin{aligned} I^{\mathrm{t}} = &\left[x^l L_{\mathrm{AA}} - (1-2x^l)L_{\mathrm{AB}} - (1-x^l)L_{\mathrm{BB}}\right] \mathscr{A}^{\mathrm{m}} \\ &+ \left[(x^l)^2 L_{\mathrm{AA}} - 2x^l(1-x^l)L_{\mathrm{AB}} - (1-x^l)^2 L_{\mathrm{BB}}\right] \mathscr{A}^{\mathrm{t}} \end{aligned} \tag{2.101}$$

Thus, by simple analogy, the relation between the kinetic parameters of both models is found:

$$\begin{aligned} L_{\mathrm{mm}} &= L_{\mathrm{AA}} + 2L_{\mathrm{BA}} + L_{\mathrm{BB}} \\ L_{\mathrm{tt}} &= (x^l)^2 L_{\mathrm{AA}} - 2x^l(1-x^l) L_{\mathrm{AB}} - (1-x^l)^2 L_{\mathrm{BB}} \\ L_{\mathrm{mt}} &= x^l L_{\mathrm{AA}} - (1-2x^l) L_{\mathrm{AB}} - (1-x^l) L_{\mathrm{BB}} \end{aligned} \tag{2.102}$$

The reciprocal formulation is given as follows:

$$\begin{aligned} L_{\mathrm{AA}} &= (1-x^l)^2 L_{\mathrm{mm}} + 2(1-x^l) L_{\mathrm{mt}} + L_{\mathrm{tt}} \\ L_{\mathrm{BB}} &= (x^l)^2 L_{\mathrm{mm}} - 2x^l L_{\mathrm{mt}} - L_{\mathrm{tt}} \\ L_{\mathrm{AB}} &= x^l(1-x^l) L_{\mathrm{mm}} - (1-2x^l) L_{\mathrm{mt}} - L_{\mathrm{tt}} \end{aligned} \tag{2.103}$$

Upon revisiting Hillert model (Eqs. (2.36) and (2.37)), the fluxes are replaced with their respective definitions provided in equations (2.94) and (2.95):

$$v = I^{\mathrm{m}} = L_{\mathrm{mm}} \mathscr{A}^{\mathrm{m}} + L_{\mathrm{mt}} \mathscr{A}^{\mathrm{t}} \tag{2.104}$$

$$v = \frac{I^{\mathrm{t}}}{x^l - x^s} = \frac{1}{x^l - x^s}\left(L_{\mathrm{mt}} \mathscr{A}^{\mathrm{m}} + L_{\mathrm{tt}} \mathscr{A}^{\mathrm{t}}\right) \tag{2.105}$$

Hillert model can now be expressed as a function of the kinetic parameters from Lesoult model, and it has been checked that solving equations (2.104) and (2.105) yields the same result as the Lesoult initial formulation. It is worth emphasizing that Hillert original equations, as defined in [41], emerge when the cross terms $L_{\mathrm{mt}} = L_{\mathrm{tm}}$ are neglected.

2.6 Conclusion

This investigation has shed light on the dynamic mechanisms underpinning phase transformations in metal alloys, highlighting the importance of accurate thermodynamic modeling. The work has demonstrated the shortcomings of existing models such as the Hillert one, which, despite providing a valuable framework for understanding phase transformations, presents limitations, as it does not fully account for all possible scenarios, especially when the solidified concentration falls within a certain range. The assumption that the interface composition equals the solid composition is challenged in cases of nonsteady-state transformations, requiring a revision of the Gibbs energy decomposition and the equations involving the model depending on the direction of the transformation. The model's practical application is thus somewhat limited due to its requirement for prior knowledge of the transformation direction, which restricts its predictive capabilities. Moreover, the decomposition of the driving force into two independent processes seems also very restrictive

In response to the limitations of the Hillert model, the Lesoult model has been used as a more flexible alternative. The strength of this model lies in its approach to manage non-equilibrium interfaces. Notably, it does not require a predefined direction of transformation, offering a more unified view of interface migration during phase transformations. The model has reproduced qualitatively the peculiar behavior observed in solutal melting experiments in both Cu-Ni and Au-Ag systems, where the interface concentrations seem to penetrate into the solid phase field.
Moreover, the crucial role of the kinetic parameters, also known as Onsager parameters, in these models has been highlighted. These parameters, which dictate the relationship between fluxes and driving forces in irreversible thermodynamic processes, are key to a comprehensive understanding of phase transformations. Interestingly, the analysis has confirmed the equivalence between Hillert and Lesoult models, providing a deeper understanding of how kinetic parameters influence these models. In particular, this has shed light on the unnecessary removal of kinetic cross terms in the dominant use of Hillert model.
Yet, the accuracy and predictive capabilities of these models hinge on the precise estimation of the kinetic parameters. Indeed, a crude estimate of these parameters suggests that very small mobilities would be necessary for recovering the experimental time scales, in contradiction with the predictions of solidification.

To address these issues, the upcoming investigation will use molecular dynamics simulations to estimate these parameters and subsequently feed them into the thermodynamic model.

CHAPTER 3

Molecular dynamics

3.1 Molecular dynamics overview

The concept of molecular dynamics (MD) as a numerical simulation method was first proposed in the late 1950s by Alder and Wainwright, who studied the phase transition of a hard-sphere system which relies on perfect elastic collisions of particles [61]. Later, in 1964, Rahman made a significant stride forward by using MD with continuous potential (Lennard-Jones) to simulate liquid argon, and calculated physical properties such as the coefficient of self-diffusion, which were found to agree well with experimental measurements [62]. Rahman's work became widely known for integrating the equations of motion with the finite difference method, which involved a step-by-step integration process to approximate molecular trajectories.

In a typical MD simulation, the trajectories of atoms and molecules are determined by numerically solving Newton's equations of motion for a system of interacting particles. The forces between all pairs of atoms are calculated from a well-defined set of interaction potentials, and then each atom is moved accordingly. The prerequisites for these simulations include an ergodicity of positions and velocities of the atoms in the system and a description of the interatomic potentials or molecular mechanics force fields for calculating each particle's forces and potential energies. Once the forces and the atom masses are known, their accelerations can be computed. The positions, velocities, and accelerations are enough to determine the time evolution of the system. By knowing the state of the system, all the other information such as temperature, pressure and potential/kinetic energies can be calculated using statistical analysis functions at specified intervals for accessing information, such as for instance, interfacial interactions or detailed information about individual atoms, which are usually inaccessible in real experiments.

However, although very attractive because it accounts for the discrete nature of matter, MD simulations have limitations. They cannot realistically portray macro scale bodies due to

constraints on size and time scales. Despite there being no upper limit on both time and length scales, simulating bulk matter on relevant time scale is difficult because of computational capacity limitations. Periodic boundary conditions (PBCs) try to circumvent this issue by simulating bulk matter through replicating the simulation cell throughout space, forming an infinite lattice by translation in all three Cartesian directions. Each particle that leaves or enters the simulation cell on one side, an image of the particle enters or leaves through the opposite side. This property leads to conservation of the number of particles, energies, and momentums, and removes surface effects. Nonetheless, PBC do not alleviate the problem of time scale that is achievable with the current computational resources.

3.1.1 Verlet algorithm

The computation of new positions and velocities of particles in MD simulations relies on solving numerically Newton's second law of motion:

$$m_i a_i = F_i \tag{3.1}$$

$$m_i \frac{\partial^2 r_i}{\partial t^2} = -\frac{\partial U}{\partial r_i} \tag{3.2}$$

Where F_i is the resulting force applied to atom i, m_i and a_i its mass and acceleration, r_i its position at time t and U the potential energy function.
The most commonly used integration scheme for the equation of motion is the Velocity-Verlet method 3.2. It calculates the position at $t+\Delta t$ using the position, velocity, and acceleration at time t:

$$r(t+\Delta t) = r(t) + v(t)\Delta t + \frac{1}{2}a(t)(\Delta t)^2 \tag{3.3}$$

With the position $r(t+\Delta t)$ known, the new forces acting on the particle and hence the acceleration at $a(t+\Delta t)$ can be calculated. The new velocity is calculated in two steps, first at half the time step $t+\frac{1}{2}\Delta t$ then at $t+\Delta t$:

$$v(t+\frac{1}{2}\Delta t) = v(t) + \frac{1}{2}\Delta t\, a(t) \tag{3.4}$$

$$v(t+\Delta t) = v(t+\frac{1}{2}\Delta t) + \frac{1}{2}\Delta t\, a(t+\Delta t) \tag{3.5}$$

Knowing the position, velocity and acceleration is sufficient to describe the configuration of the system at time $t+\Delta t$, and to compute the next configuration through repeating the same process.

3.1.2 Ensembles in molecular dynamics

Ensuring MD simulations consistency with experimental data of real systems requires an accurate representation of the governing thermodynamic properties. MD make use of various statistical mechanical ensembles with fixed microscopic parameters that corresponds to the thermodynamic independent variables (extensive and intensive parameters) derived from the fundamental equations of thermodynamics. A statistical ensemble is an abstraction that considers all the virtual copies of a system, each of which is accessible to the real system

with equal probability. A thermodynamic ensemble is a statistical ensemble in statistical equilibrium, which strives to derive the properties and interactions between the particles that constitute the system, bridging the gap between macroscopic properties and microscopic behavior.
MD simulations may be run in a number of different thermodynamic ensembles depending on the purpose of the study. Different macroscopic constraints lead to different types of ensembles with particular statistical characteristics. In the following sections, a rapid overview of the main ensembles used in MD simulations is given.

Microcanonical ensemble (NVE)

The *microcanonical ensemble* is the default ensemble that is usually employed in MD to simulate a purely dynamical behavior with no external influence by merely solving Newton's equation of motion, as described earlier. This ensemble mimics a completely isolated system where the number of particles (N), the system volume and the total energy are conserved. The system cannot exchange heat with the exterior, which is why it is usually used to simulate adiabatic processes where only exchange of potential and kinetic energy is allowed within the system, while the total sum of these energies being conserved.

Canonical ensemble (NVT)

The *canonical ensemble* describes a system in thermal equilibrium with a large heat bath at a fixed temperature. Unlike the microcanonical ensemble, the energy of the system is not precisely known, but the temperature (T), the volume, and the number of particles are specified. Experiments usually control the temperature instead of the energy, making the canonical ensemble typically favored over the microcanonical ensemble when measuring physical properties. The temperature control is achieved by applying a thermostat that modifies the Newtonian MD scheme by modulating the kinetic energies and forces acting on a particle. Several thermostats are available for this purpose, this includes velocity rescaling, Berendsen thermostat [63], Nosé-Hoover thermostat [64][65], Andersen thermostat [66] and Langevin dynamics [67]. Despite the fact that all the mentioned thermostats succeed in maintaining temperature control, not all of them lead to a behavior that corresponds to a real ensemble. For instance, the velocity scaling technique adjusts the instantaneous temperature by scaling all velocities. This method sets the system at the specified temperature, but does not allow proper temperature fluctuations and doesn't correspond to any ensemble. Thus, not every thermostat is valid when it comes to simulating a proper canonical ensemble behavior, and depending on the investigated physical properties, choosing the correct thermostating method becomes crucial.
The most popular thermostats for mimicking a canonical distribution are the Langevin, Andersen, and Nosé-Hoover. Generally, thermostats are grouped in two categories: stochastic thermostats and deterministic thermostats. Berendsen and Langevin, for instance, are stochastic thermostats because some randomness is involved in generating the appropriate velocities to maintain the set temperature. In the case of Andersen, to mimic particle collision with a heat bath, some particles are randomly selected with a given probability; then random velocities are attributed to these particles according to the Maxwell-Boltzmann distribution of velocities, which results in a velocity consistent with the desired temperature since

the temperature is related to the average kinetic energy via the equation:

$$E_c = \left\langle \frac{3}{2} N k_B T \right\rangle \tag{3.6}$$

where k_B is the Boltzmann constant, and the brackets $\langle \cdot \rangle$ denote the thermodynamic expectation value in the equilibrium state.

The kinetic energy of the selected particles propagates to the surrounding particles, and the process is refreshed at a given frequency as the system starts to deviate from the set temperature. The Langevin thermostat modifies the force acting on a particle by adding a frictional or drag term in addition to a random force representing some thermal motion generated using the Wiener process in random number theory. Both Andersen and Langevin lead to canonical distribution, but the fact that momentum transfer is lost during the process of temperature control allows a particle to have a completely different velocity from one time step to another. This implies that some of the measured kinetic parameters, such as diffusion coefficients, are erroneous, which is why, depending on the investigated physical parameters, not every thermostat is viable.
Nosé-Hoover on the other hand is a deterministic and time-reversible thermostat and most popular for canonical sampling. It is based on the extended Lagrangian formalism, meaning that it does not deal with random forces or velocities, which makes it ideal for simulating diffusion coefficients. The basic idea is to include a non-Newtonian term to the force by introducing a fictitious dynamical variable, symbolizing friction, to maintain the total kinetic energy constant [68]:

$$\frac{d\mathbf{v}_a}{dt} = \frac{\mathbf{F}_a}{m} - \zeta(t)\,\mathbf{v}_a \quad \forall a \tag{3.7}$$

$$\frac{d\zeta}{dt} = \frac{1}{Q}\left[\sum_a m_a |\mathbf{v}_a|^2 - (N+1)\,k_b T\right] \tag{3.8}$$

where ζ is the thermodynamic friction coefficient, and Q determines the coupling strength of the thermostat usually regarded as "mass".
The Nosé-Hoover method shares similarities with the Berendsen approach, but has an integral feedback in rescaling the velocity by knowing the derivative of ζ instead of a direct feedback, as seen in Berendsen. The gradual increase in the ζ value initiates a growing heat flow, leading to a smooth temperature increase / decrease, which allows for kinetic energy fluctuations.
The selection of the correct coupling factor Q is crucial as it dictates the rate at which the thermostat rescales the temperature. It is important to note that the more a system is subjected to external interferences, the less realistically it behaves. An inappropriate choice of the coupling parameter could result in a non-canonical distribution.
Finally, the coupling should be small enough to facilitate thermal fluctuations and maintain a proper canonical distribution. However, too small a coupling may prevent the system from returning to equilibrium and may induce exaggerated temperature fluctuations around the equilibrium value. Thus, balancing is the key to ensure accurate and reliable results.

Isothermal-Isobaric ensemble (NPT)

In the isothermal-isobaric ensemble, both the temperature T and the pressure p are fixed. The NPT ensemble is much closer to laboratory conditions since the majority of chemical reactions are carried out under controlled temperature and pressure. NPT is also valuable for estimating the Gibbs free energies and coexistence curves in mixed phase systems. Just like for the case of the canonical ensemble, temperature control is performed using the same thermostats presented earlier, with an additional feature to exert control over the pressure of the system by means of a barostat.
The barostat modifies the system pressure by rescaling the volume of the simulation box, and consequently the positions of the atoms, so that it matches the target pressure value. In molecular dynamics, the pressure is obtained using the virial equation, which connects the pressure with volume and forces acting on the particles [69]:

$$p = \frac{Nk_bT}{V} + \frac{1}{dV}\left\langle \sum \mathbf{r}_{ij} \cdot \mathbf{F}_{ij} \right\rangle \tag{3.9}$$

with d the dimension of the system. Here, the first term, related to the kinetic energy, describes the pressure of an ideal gas. The second term, called virial, is related to the potential energy and relies on the sum over all pairs of particles i and j of the forces between them times their distance.
The most common barostats include Berendsen, Andersen, Nosé-Hoover, Martyna-Tuckerman-Tibias-Klein (MTTK), Langevin piston, and Parrinello-Rahman barostats. Careful considerations are necessary when combining a barostat with various thermostats. Depending on the goals, certain combinations may not be suitable. The Berendsen thermostat for example is very efficient in equilibrating the system. However, due to low pressure fluctuation, this barostat fails to correctly sample the isothermal-isobaric statistical ensemble.
The Parrinello-Rahman barostat, MTTK barostat, and the Nosé-Hoover barostat are all based on the Andersen barostat, which includes an additional degree of freedom analogous to a piston. This piston is endowed with a fictitious mass that represents the strength of the coupling, which adjusts the simulation cell volume to balance internal and external pressure. Strong coupling delays the equilibration process and leads to lower fluctuations in properties, because the system can only equilibrate by relaxing to different configurations. In contrast, weak coupling offers poor control but faster system equilibration. Depending on the pressure tensor, the shape of the simulation box may also change. Thus, the choice of barostat and the appropriate coupling strength must align with the simulation objectives.

Grand-canonical ensemble (μVT)

In the grand-canonical ensemble, both the energy and particle number are allowed to change. Instead, the temperature and chemical potential are specified. This ensemble emulates an open system in thermal and chemical equilibrium with a reservoir, with which energy and particle exchange is possible. μVT can be viewed as an ensemble of canonical ensembles with different particle numbers N. The weighted sum over N of these canonical ensembles constitutes the grand-canonical ensemble. This ensemble is particularly useful when simulating systems with fixed shapes but the energy and particle number can fluctuate, such as adsorption phenomena or electrons in a conductor.

Isoenthalpic–isobaric ensemble (NPH)

The Isoenthalpic–Isobaric Ensemble, analogous to the Microcanonical Ensemble (NVE), introduces the volume as a degree of freedom. Thus, the system's enthalpy, given by $H = E + pV$, remains constant while the pressure is maintained fixed without any temperature control. This ensemble is especially practical for systems involving phase transitions in solids.

While the ensembles presented are commonly employed in MD simulations, other variants may be utilized depending on specific applications such as the NST ensemble, which stands for constant particles, constant temperature, and constant stress. The NST ensemble is an extension of the NPT ensemble, useful for studying stress-strain relationships. Another example is the semi-grand canonical ensemble, which is similar to the grand canonical ensemble, where the chemical potential; volume and temperature are fixed. The difference lies on the fact that the number of particles is also a fixed quantity, but the composition of the system is allowed to change.

3.1.3 EAM potential

The dynamical evolution of a system hinges on the forces acting on each of its particles. These forces are derived from the potential energy, calculated from interatomic potential functions describing the particle interactions. It is crucial to note that only interactions within a defined cut-off distance are calculated. Interactions beyond this range are either disregarded due to their negligible contribution or approximated via continuum or reciprocal space method, depending on the nature of the interaction. Therefore, the predicted properties of the system are only as good as the accuracy of the underlying interatomic potential.
The Embedded Atom Method (EAM) is a semiempirical approach widely used to calculate the total energy of metal and metal alloy interactions. EAM has its roots in the density functional theory, which expresses the energy of a system by a functional of its electronic density. The EAM gives an approximation of this functional by assuming that the potential energy of a particle is on one part determined by a contribution from a pair potential and that the other part is determined by the electron density of the host system in which the particle is placed (embedded).
The particle or atom energy in the embedded atom method proposed by Daw and Baskes [70] is given by:

$$E_i = \frac{1}{2}\sum_j \phi(r_{ij}) + F(\overline{\rho_i}) \tag{3.10}$$

with

$$\overline{\rho_i} = \sum_j \rho(r_{ij}) \tag{3.11}$$

where r_{ij} is the distance between atom i and j, ϕ is the pair potential function, $\rho(r)$ is the electronic density as function of the distance from the atom, $\overline{\rho_i}$ is the electronic density of the host system with atom i removed, and $F(\overline{\rho})$ is the embedding function that represents the energy required to place the atom i into the electron cloud. The sum over j of the neighboring atoms for calculating $\rho(r_{ij})$ and $\phi(r_{ij})$ are limited by the range of the cutoff distance.

The total energy of a system of N particles is thus:

$$E_{tot} = \sum_{i}^{N} E_i \tag{3.12}$$

For a pure element system, three functions must be specified: the pair-wise interaction ϕ, the electronic density contribution function ρ, and the embedding function F. For an alloy consisting of more than one type of atom, equation 3.10 is rewritten as:

$$E_i = \frac{1}{2} \sum_{j} \phi_{t_i t_j}(r_{ij}) + F_i(\overline{\rho_i}) \tag{3.13}$$

where t_i defines the type of atom. Thus, for a binary alloy A-B, seven functions are required to calculate the EAM energy: three pairwise interactions ($\phi_{\mathrm{AA}}(r)$, $\phi_{\mathrm{AB}}(r)$, $\phi_{\mathrm{BB}}(r)$), two electron cloud contribution functions ($\rho_{\mathrm{A}}(r)$, $\rho_{\mathrm{B}}(r)$), two embedding functions ($F_{\mathrm{A}}(\overline{\rho})$, $F_{\mathrm{A}}(\overline{\rho})$).

3.2 Structure identification methods

3.2.1 Available methods

A wide variety of structure analysis methods have been developed to classify local atomic arrangements in large-scale atomistic simulations of solids. These methods assign distinctive colors to particles based on user-specified criteria for visualization purposes, to define the boundaries between distinct phases, map the contours of the interfaces, or to quantify the occurrence of different crystalline phases and defects in a simulation. The core purpose of these methods is to analyze the local environment of each atom or particle and allocate a local structural type that closely resembles an idealized one (HCP, BCC, FCC, etc.) by gauging the degree of fit.

The first method is the energy filtering, which uses the potential energy of an atom as a criterion to decide whether it forms a perfect lattice with its neighbors by comparing it to a threshold value. Atoms with higher energy, indicating a crystal defect, are considered if they exceed the threshold that usually corresponds to that of a perfect lattice, while those with lower values are deemed crystalline. The second method uses a centrosymmetry parameter [71] that quantifies the local loss of centrosymmetry at an atomic site of a given lattice, distinguishing the structure apart from other structures like crystal defect where the local bond symmetry is broken. The third method is the bond order analysis, where near neighbor bonds of a central atom are projected onto a unit sphere. Local bond order parameters, known as Steinhardt order parameters [72], are defined based the projected vectors, which take characteristic values for each crystal structure.

The three aforementioned methods assess the similarity of a specific atomic arrangement to a particular reference structure. However, there are other more sophisticated techniques that allow to uniquely identify and assign a structure type to each atom in the system among the available reference structures based on a discrete signature that is calculated from the atom positions.

Common neighbor analysis

Referred to as CNA [73], this method computes a characteristic signature from the topology of bonds connecting surrounding neighbor atoms to the central one.Two atoms are deemed neighbors or bonded if they fall within a cutoff radius. A set of three indices are computed in order to assign the local structure of the atom: the number of neighbors common to the central atom and its bonded neighbor, the number of bonds between these common neighbors, the number of bonds in the longest continuous chain of bonds connecting the common neighbors. These indices are computed for each neighbor bonds of the central atom, yielding a set of indices triplets which are then compared with a set of reference signatures to assign a structural type to the central atom.

Bond angle analysis

This method [74] was developed to distinguish fcc, hcp, bcc, and other relatively close-packed structures. The bond angle cosines formed by bond vectors of the central atom and its neighbors (the number of neighbors is determined by a cutoff radius, proportional to the average distance of the six nearest neighbors) are measured to obtain an eight-bin histogram that is then further evaluated using a set of heuristic decision rules to determine the most likely structure type.

Voronoi analysis

This approach utilizes a geometric method [75] based on an analysis of the shapes of the Voronoi polyhedron enclosing an atom , which reflects the characteristic arrangement of near neighbors, thereby enabling the structure to be characterized. The Voronoi polyhedron is defined as a minimal polyhedron with planar faces that bisect at right angles the lines joining an atom to its neighbors. The number of faces corresponds to the geometric coordination number of the atom of interest, which is further used as a compact signature by enumerating the number of polygonal facets having three, four, and so on vertices, yielding a vector of four integers which identifies the structure type.

Adaptive common neighbor analysis

The a-CNA is a simple extension of the standard CNA method, adding the ability to analyze multi-phase systems. In multi-phase systems, determining a global cutoff radius that suits all phases is not straightforward, leading to the need for an individualized cutoff radius for each atom, taking into account the reference structure it corresponds to. Firstly, the neighbors are generated for all contemplated reference structures, based on their maximum requirement, and then sorted by distance. To verify whether the local coordination structure matches a certain structure, the neighbor list is reduced to the number relevant to this particular structure. The mean distance of these closest neighbors results in a local cut-off radius that is atom-specific and utilized only for matching with the reference structure. This is then used to ascertain the bonding between the nearest neighbors and compute the usual CNA signature. If the signature fails to align with the chosen structure, the algorithm rewinds the process, testing the subsequent candidate structure.

Neighbor distance analysis

In order to determine which structure a given atom belongs to, its nearest-neighbor vectors are first identified and arranged on the basis of their distance from the central atom. This is compared to a benchmark coordination structure characterized by the list of bond vectors, which is also ordered similarly. Factors such as thermal displacements or elastic distortions of the crystal might interfere with matching the actual neighbor bonds with their counterparts in the reference pattern, resulting in bond length perturbations. In that regard, a local hydrostatic scale factor that links the lattice constant of the reference structure to that of the actual crystal is computed. This factor depends on various elements, including hydrostatic stress, temperature, and chemical composition. Alongside $\delta_{\max}$, defined as the maximum admissible displacement of an atom from its equilibrium position specified by the user, it facilitates a one-to-one mapping between the reference vectors and the actual neighbor vectors to determine the type of structure. Further discussion of the method can be found in [76].

Many other computational analysis methods have been developed, spanning from simple local order parameter (LOP) [77] that differentiate crystalline from liquid phases, to enhanced versions of existing methods such as interval CNA (i-CNA) [78], and even more complex ones like 3D-CNN [79], which utilize machine learning techniques for automated analysis of atomic configurations in MD simulations. Most common techniques try to match a local structure to an idealized counterpart based on the degree of fit. The PTM method, available in the Ovito visualization software, is chosen for characterizing the Cu-Ni solid-liquid due to its simplicity, robustness, high temperature accuracy, and computational effectiveness. This method is detailed in the subsequent subsection.

3.2.2 Polyhedral Template Matching method

The polyhedral template matching (PTM) method was developed to overcome the various challenges encountered in the previously mentioned methods. The Common Neighbor Analysis (CNA) often contains inherent errors due to difficulties in identifying a universally applicable cutoff parameter in systems with multiple phases, and it can introduce noise in the analysis due to thermal vibrations and fluctuations in local density. A-CNA is able to automatically pick a cutoff distance individually for each atom. Although it is the most popular method at present, but just like CNA, it still suffers from noise introduced by thermal vibrations, causing bonds to be broken or formed. This was noted by Fukuya and Shibuta [79] during the identification of solid and liquid atoms. They found that many atoms in solid area were incorrectly assigned as liquid due to significant thermal vibration at the melting point using a-CNA. In contrast, PTM performed better at correctly identifying the structure, given it was designed specifically to handle the issue of thermal vibrations. Similarly, Ueno and Shibuta [80] demonstrated a comparison between a-CNA and PTM for detecting the BCC configuration in a solid-liquid system of pure Fe at the melting point. Due to thermal vibrations, only 55% of the atoms were assigned as BCC in the solid region compared to 92% using PTM. These findings show that PTM is reliable even at high temperatures near the melting point, and it yields results comparable to more advanced techniques such as 3D-CNN [79], albeit at a significantly lower computational cost. One limitation of PTM is the necessity for a suitable root-mean-square deviation (RMSD) cutoff parameter, which must be manually

Structure	Neighbours required
SC	6
FCC	12
HCP	12
ICO	12
BCC	14

Figure 3.1 – Convex hulls of the nearest neighbors of five different structures. The table shows the number of neighbor atoms required for each structure [81].

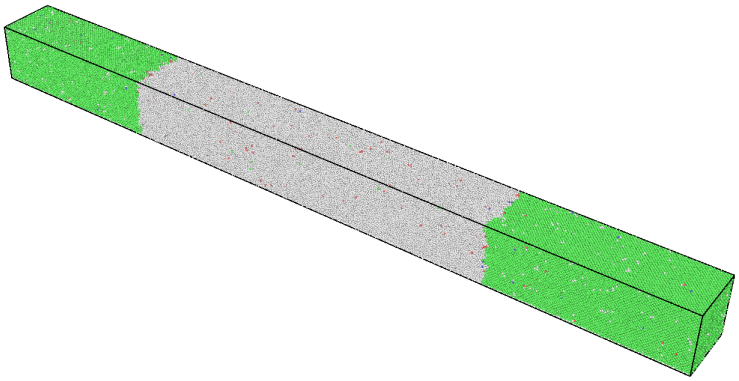

Figure 3.2 – Structure detection using Polyhedral Template Matching method (PTM).

established via trial and error for each system.

Although the Voronoi method is more robust to thermal vibrations compared to a-CNA, it has been rarely utilized for simulations of crystalline materials because of the challenge of differentiating between highly symmetric crystalline packings such as FCC and HCP structures. PTM adopts a similar approach to Voronoi, where the convex hull formed by the set of neighboring atoms serves to characterize the local structure around an atom. This convex hull is then represented in a planar graph form, which is used to classify the structure [81]. PTM considers a fixed number of neighboring atoms around the central atom, making it less sensitive to thermal fluctuations since it does not rely on the concept of bonds between these atoms. Given a set of reference templates corresponding to the positions of well-known structures (the convex hulls of such structures are shown in Figure 3.1), the template that best matches an atom and its neighbors, thus defining its structure, is the one that minimizes the RMSD.

The chosen RMSD cutoff parameter for the PTM in the current Cu-Ni system is set to 0.155, consistent with the parameter used by Ueno and Shibuta in [80]. The PTM method is imple-

mented in OVITO software, which also facilitates the visualization of the atomic structure as demonstrated in Figure 3.2. The gray atoms correspond to the liquid phase, while the green atoms represent the solid FCC structure. Examining this structure facilitates the identification and tracking of the boundaries between these phases, allowing the extraction of interface shape, observing structural changes, or isolating a specific phase to reduce computational costs during data processing.

3.3 Melting temperature

3.3.1 Melting temperature determination methods

Numerous methodologies have been developed to efficiently determine melting temperatures using MD simulations. The melting point and solidus-liquidus temperatures in the MD simulation tend to deviate from the experimental value, mainly due to the difficulty of relating directly the interatomic potentials to the properties [80]. Phillpot et al. [82] characterized two types of melting in their MD calculations for silicon. The first is thermal melting, a heterogeneous process initiated from a surface or interface, which relies on the free energies of the two phases. The melting temperature is reduced in this case because the interface can reduce the nucleation energy barrier between the solid and liquid phases. The second type, mechanical melting, is a homogeneous process instigated by elastic or phonon instability, independent of temperature, usually occurring when a perfect crystal in a periodic cell undergoes melting. It seems inappropriate to heat up a crystalline bulk phase in a simulation box with periodic boundary conditions and hope that the melting temperature coincides with the jump in energy or volume, or when disorder/diffusion is observed, which is why the interpretation of the melting point in the MD simulation is complex.

There are multiple strategies for computing melting points (T_m) using MD simulations. The Lindemann criterion proposes that melting occurs when the thermal vibration of atoms becomes so intense that adjacent atoms collide, reaching the limit of stability, typically identified when the Mean Squared Displacement (MSD) surpasses a certain threshold. The thermodynamic integration method [83, 84] calculates the Gibbs free energies for both the solid and liquid phases as functions of temperature or pressure. The melting temperature at a specific pressure is determined by the intersection of these two curves.
Another approach for determining the melting point is to continuously heat or cool a solid or liquid phase, and take note of the temperature at which a volume jump is observed, indicative of a phase transformation. The barrier of free energy to the formation of a solid–liquid interface in perfect crystalline solids leads to some hysteresis, caused by superheating of the solid in simulations of melting, and supercooling of the liquid in simulations of freezing. During melting, the volume of the system changes abruptly when heated to a temperature $T_+ > T_m$. In solidification, the homologous crystallization temperature T_- is lower than T_m when cooling from a liquid to a crystalline structure. To assess the melting point, the hysteresis method is established [83, 84, 85]: $T_m = T_+ + T_- - \sqrt{T_+ T_-}$
The melting point can be lowered by introducing a heterogeneous interface or a defect, thereby reducing the nucleation free energy barrier between solid and liquid. This gives rise to the defect-induced melting and the two-phase co-existence methods in determining T_m. The melting point using the defect induced melting method is determined through NPT

simulations as a function of temperature and void count. The voids are introduced by removing particles from the solid structure, which then form solid–liquid interfaces by creating localized pockets of liquid-like structures near the voids. Increasing the proportion of voids reduces T_m by lowering or even eliminating the energy barrier for a sufficient proportion, where T_m hits a plateau extending over a limited proportion of voids, typically about 5–10% of the total number of particles [83]. The distribution of voids in the simulation cell does not affect the melting-point predictions.
The two-phase co-existence method is selected for calculating T_m due to its simplicity and relative precision. There are several ways for achieving equilibrium with this method. The first approach uses the NPT or NVT ensembles at different temperatures in the solid-liquid configuration. For both cases, if the set temperature is different from T_m, the system melts or solidifies completely with sufficient run time. The stress anisotropy problem may occur using the NVT ensemble due to the high interfacial contact stress between the solid and liquid phases [85]. T_m can also be found by monitoring the solid-liquid interface velocity as function of temperature and extrapolating to the temperature corresponding to zero motion [86]. Another approach is relaxing the solid-liquid system using the NVE [77] or NPH ensemble [87, 88, 89, 90]. Working with an NPH ensemble avoids the stress anisotropy problem when using a constant volume with the NVE ensemble, since the components of the stress tensor can be adjusted to match the set pressure.

3.3.2 Melting temperature using the NPH ensemble

For all our MD calculations, we have used the EAM potential of [91] for the Ni-Cu system. To check its relevance for our investigations, we first estimated how well its predictions are in terms of the melting temperature of the pure elements. When these calculations are carried out, we also identify the best methods for determining these temperatures.

The procedure was initiated with a solid-liquid coexisting structure of pure Cu. The structure was equilibrated at varying temperatures ranging from 1200 K to 1300 K at 0 pressure, then the thermostat was turned off to allow the system to relax in a NPH ensemble for a duration of 1 ns. Since the system can evolve without temperature control, if the initial temperature is lower than T_m, solidification occurs along with a release of latent heat, causing the system temperature to rise until it reaches the melting point, at which the interface stops moving. Conversely, if the system temperature is higher than T_m, melting occurs, and the temperature decreases due to latent heat absorption. Figure 3.3 illustrates both scenarios, with starting temperature either lower or higher than T_m. The temperature at which the system stabilizes is interpreted as the melting point for the given EAM potential. The melting point for Cu was found to be $T_m \approx 1278.9$ K, which closely aligns with the reported melting point $T_m = 1278$ K in [91].

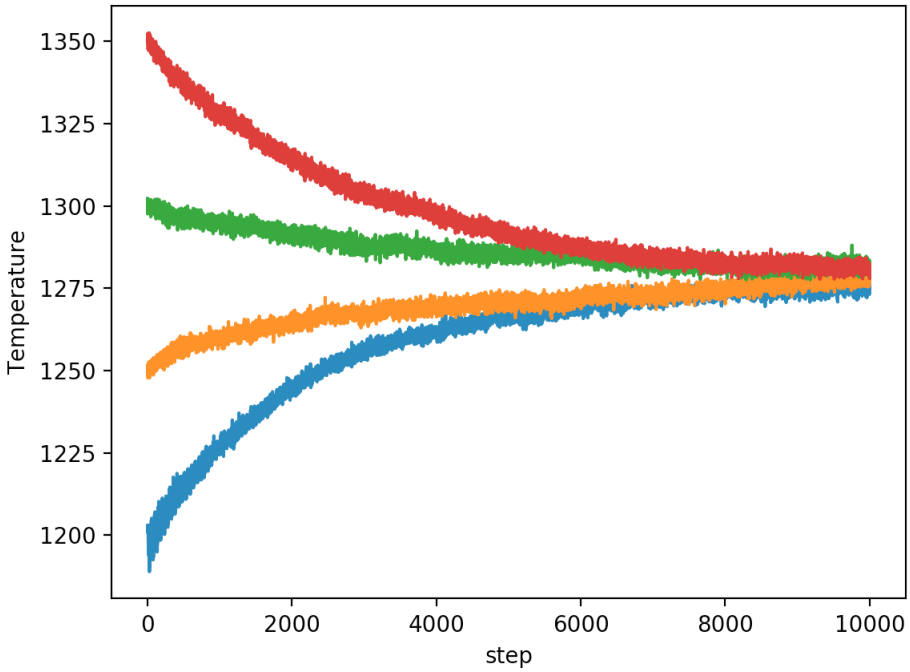

Figure 3.3 – Temperature evolution towards the melting temperature of Pure Cu using the NPH ensemble starting from different initial temperatures.

3.4 Equilibrium concentrations

3.4.1 Methodologies

Determining the solidus and liquidus temperatures of binary systems is a little more involved. Therefore, several methods have been tested to estimate the equilibrium concentrations at the given simulation temperature. One such method is a variant of the previously described moving interface method, called the compositional moving interface (CMI) [92]. In the CMI method, the solid and liquid have different compositions, and equilibrium is determined when the solid and liquid phases coexist. The procedure for calculating the liquidus composition for a binary alloy A-B is summarized below:

1. A pure liquid structure of the end member A is created at a temperature T_i, chosen between the melting temperatures of both end members $T_m^{\mathrm{A}} < T_i < T_m^{\mathrm{B}}$.
2. A solid structure of a test composition x_i of the A-B mixture is prepared in a separate simulation at the same temperature T_i.
3. Both structures are assembled in a single solid-liquid simulation supercell and the MD simulation is conducted. The liquid consumes the solid and the entire structure melts in this given energy system where T_i is higher than the liquidus temperature.
4. The procedure is repeated by lowering T_i until the limit where both phases coexist, meaning that the system is now in the two phase regime.

To calculate the solidus point, the inverse process is applied. This process involves raising the temperature T_i of the system, where the solid is now the pure end member B and the

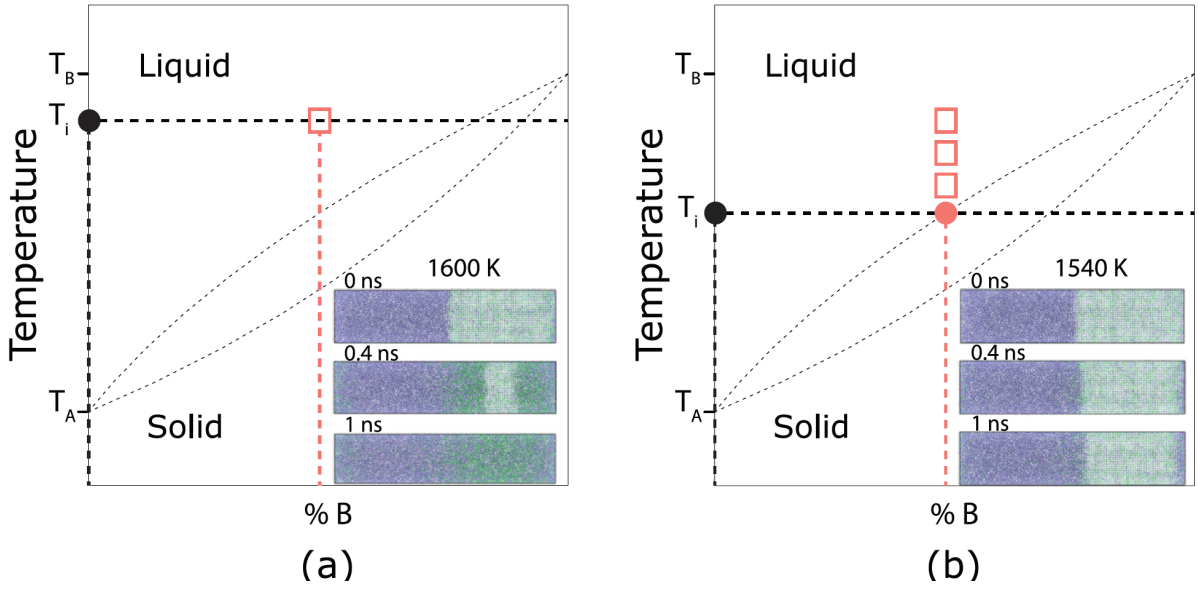

Figure 3.4 – Illustration of the CMI method on a Cu–Ni type binary system. The temperature/composition where both liquid and solid can coexist is marked by a filled pink circle signifying that liquidus has been reached [92].

liquid is a composition mixture x_i. The system undergoes solidification until an equilibrium temperature T_i is reached where both phases coexist. However, this method led to a liquidus composition of 25% Ni and a solidus composition of 24% Ni. These results are erroneous since the solidus composition cannot be lower than the liquidus according to the Cu-Ni phase diagram.

The second approach used to calculate the equilibrium involves the semi-grand canonical Monte Carlo (SGCMC) [90, 89]. The semi-grand canonical ensemble is used for mixtures, where the number of atoms or particles is fixed but the composition or atoms types are allowed to interchange. This method aims to determine the Gibbs free energy curves of each phase, then extract the solidus and liquidus compositions defined by the contact points of the common tangent line. We have conducted SGCMC simulation using the atom/swap technique in LAMMPS. The process begins with a $20 \times 20 \times 20$ Å^3 structure, which is equilibrated at 1400 K for 10 ps with the NPT ensemble. An equilibrium concentration is obtained by imposing a given chemical potential difference $\Delta\mu = \mu_{\mathrm{Ni}} - \mu_{\mathrm{Cu}}$ between the two kinds of atoms for the case of a binary system using SGCMC. The imposed chemical potentials vary from 0.72 to 0.98 eV per atom with a step of 0.02 eV per atom.
The $\Delta\mu$ vs Ni concentration curve for a given phase ϕ is fitted with a sub-regular solution model [93]:

$$\Delta\mu^{\phi} = k_b T \ln\left(\frac{1-c^{\phi}_{\mathrm{Cu}}}{c^{\phi}_{\mathrm{Cu}}}\right) + \sum_{i=0}^{p} A_i \left(c^{\phi}_{\mathrm{Cu}}\right)^i \tag{3.14}$$

where c_{Cu} the Cu concentration, A_i the polynomial coefficients to be fitted ($p = 5$) in order to

obtain the Gibbs free energy (per atom) of a given phase ϕ:

$$G^{\phi}(c_{\mathrm{Cu}}) - \mu_{\mathrm{Ni}}^{\phi 0}(T) = k_b T \left[c_{\mathrm{Cu}} \ln(c_{\mathrm{Cu}}) + (1 - c_{\mathrm{Cu}}) \ln(1 - c_{\mathrm{Cu}}) \right] + \sum_{i=0}^{p} \frac{A_i}{i+1} c_{\mathrm{Cu}}^{i+1} \tag{3.15}$$

where $\mu_{\mathrm{Ni}}^{\phi 0}$ is the chemical potential of reference of pure Ni.
Nevertheless, challenges were encountered in implementing this method. First, it proved difficult to replicate the precise $\Delta\mu$ versus concentration values reported in the study by Ueno and Shibuta [90] for the Cr-Fe system using the SGCMC atom/swap technique in LAMMPS. Additionally, a crucial limitation of the SGCMC method is its focus on a single phase, disregarding the dynamics of the heterointerface. As a more efficient alternative exists for calculating the concentration profile without the drawbacks and intricacies of the atom/swap method, it was deemed unsuitable for determining the solidus and liquidus. However, the method will demonstrate its utility in a subsequent section for extracting the chemical potential (§3.7.2).

3.4.2 Solute partitioning method

The solidus and liquidus composition can directly be estimated with the solute partitioning method [94], by monitoring the evolution of solute composition at the solid–liquid interface during the solidification process. A solid structure of size $21 \times 21 \times 100$ Å, with a uniform concentration of 27% Ni along the longest direction z is prepared with the NPT ensemble for 15 ps at 1400 K (1127 °C). The concentration of 27% was chosen because it resides within

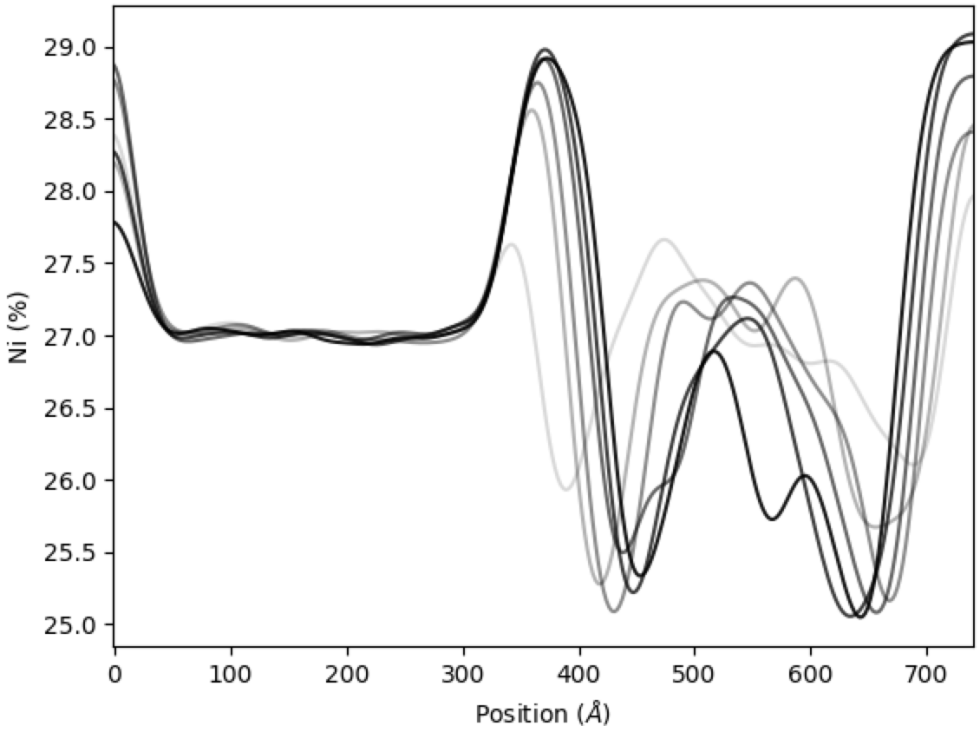

Figure 3.5 – Evolution of the Ni concentration profiles and appearance of solute partitioning at the interface during solidification.

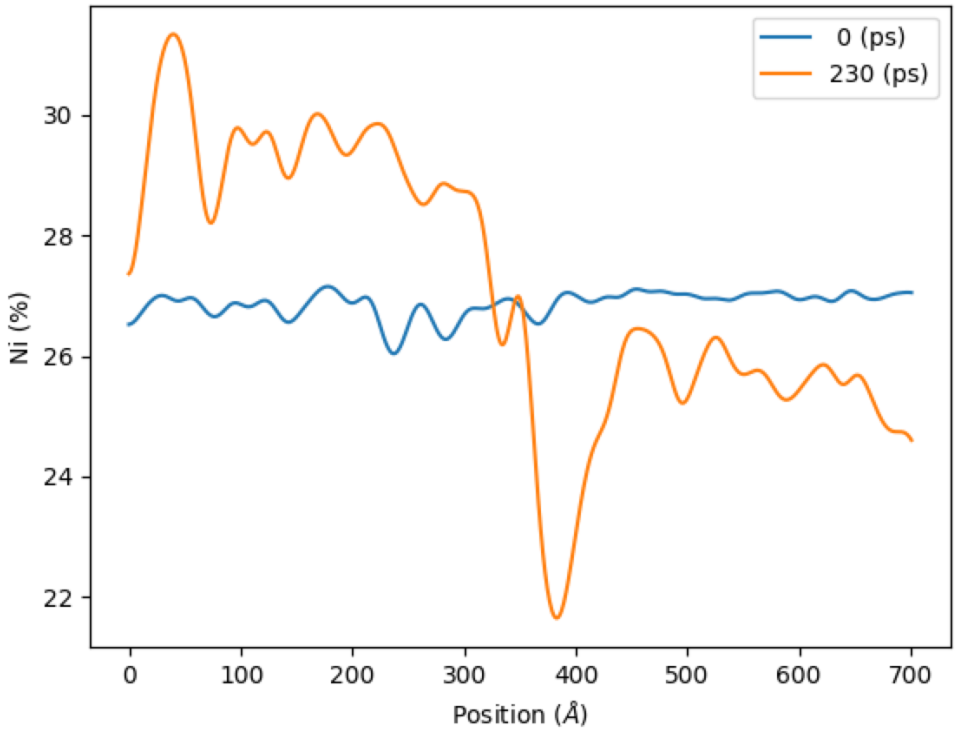

Figure 3.6 – Solute partitioning using the atom/swap technique.

the two phase domain, where both solid and liquid coexist. The liquid is prepared by first heating a duplicate of the previous solid structure at 5000 K for 1 ps with the NVT ensemble in order to break the structure, followed by an equilibration step with the NPT ensemble at 1400 K for 10 ps. Both structures are assembled in a single simulation. After an energy minimization step, the solid-liquid structure is allowed to relax with the NPT ensemble at 1400 K for 30 ns.

Since both solid and liquid have the same composition of 27%, the initial concentration profile is flat. As solidification proceeds, the newly solidified region exhibits a higher solute concentration, whereas the liquid region at the interface is depleted. Therefore, solute partitioning is observed at both interfaces as shown in Figure 3.5. The different lines represent plots of the concentration profiles at different and evenly spaced intervals of the solidification process, going from lighter to darker lines[‡]. As solidification carries on, the Ni content in both solid and liquid phases at the interfacial region converges and stabilizes at some equilibrium values. These are interpreted as the solidus and liquidus compositions. The solidus and liquidus compositions at 1400 K are estimated to be 29% and 25%, respectively.

Solute partitioning can also be achieved using the atom/swap technique in LAMMPS. Unlike the SGMC, the atom/swap routine does not change the overall composition. Instead, it swaps atoms of one type with atoms of another type according to a Monte Carlo probability at a specified temperature. The temperature is utilized in the Metropolis criterion to dictate

[‡]The post-treatment for estimating the concentrations does not handle properly the periodic boundary conditions, but without any consequence on the quantification of partitioning at the interface. This comment applies also to the post-treatment of the atom/swap technique in Figure 3.6.

swap probabilities, and a two-phase system with thermodynamically correct partitioning is achieved after sufficient swap attempts. The atom/swap technique was executed on a solid-liquid simulation cell similar to the previous one, with 27% initial Ni composition. Five atom swapping was attempted for every atom at each time step, for a total of 230 000 time steps. The resulting concentration profile is shown in Figure 3.6. Solute partitioning is observed at the interface with concentrations more or less close to the ones measured in Figure 3.5. However, the correct equilibrium concentrations are harder to read from such profile as compared to the previous method, and a much longer run time is required in order to obtain a somewhat cleaner concentration profile to extract the solidus and liquidus temperatures. Despite the atom/swap method contributions, the initial method, which is based on running an MD simulation, remains the superior approach. This is due to the method ability to generate clearer profiles and incorporate the system dynamics introduced by the presence of an interface, in comparison to a Monte-Carlo simulation.

3.5 Diffusion coefficients

3.5.1 Calculation methods

The self diffusivities (tracer in the case of alloys) are typically evaluated using two methods derived from MD trajectories. The first is the Einstein equation, which associates the diffusion coefficient with the long-term behavior of the mean-square displacement (MSD) per atom. The diffusion coefficient corresponding to a given bin located at position x is determined from the limiting slope of the MSD vs time plot via the following equation:

$$D(x) = \frac{1}{2d} \lim_{t\to\infty} \frac{d}{dt} \left\langle \left| r_j(t) - r_j(0) \right|^2 \right\rangle_x \tag{3.16}$$

where d is the system dimensionality, $r_j(t)$ is the position of particle j at time t inside the bin centered at x, and the term in brackets is the ensemble averaged MSD given by:

$$\left\langle \left| r_j(t) - r_j(0) \right|^2 \right\rangle_x = \frac{1}{N} \sum_{i=1}^{N} \left| r_j(t) - r_j(0) \right|^2 \tag{3.17}$$

The second method relies on the formulation of the auto-correlation function of the velocity, defined as [40]:

$$Z(t) = \frac{1}{d} \left\langle \mathbf{u}_j(t) \cdot \mathbf{u}_j(0) \right\rangle \tag{3.18}$$

where $\mathbf{u}_j$ is the velocity vector of atom j.
The diffusion coefficient is then calculated by integrating $Z(t)$ over time, according to the Green-Kubo relation:

$$D = \int_0^\infty Z(t)\, dt \tag{3.19}$$

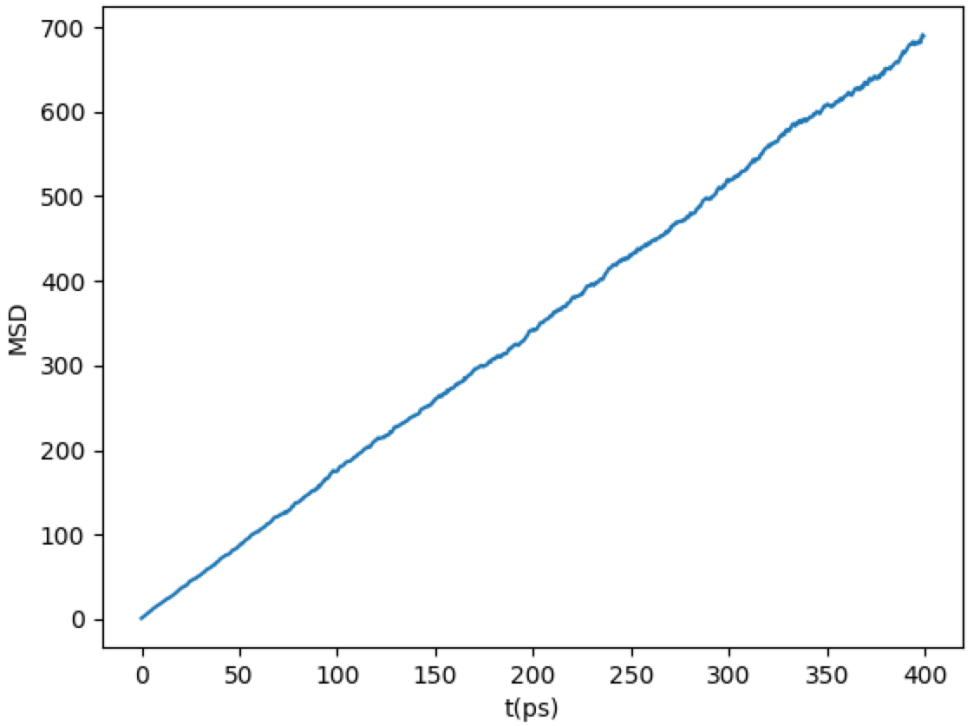

Figure 3.7 – MSD of Ni atoms in a homogeneous box of 15% Ni content.

3.5.2 Homogeneous liquid box against two-phase box

The presence of a solid-liquid interface changes the dynamics of diffusion and breaks the symmetry of the liquid by introducing anisotropy of the diffusion coefficient. The MSD method for estimating the diffusivities is most effective for homogeneous systems where the diffusion behavior of each element does not depend on time and location within the simulation cell (in the steady state regime). Studies usually calculate the self diffusivities as function of the position normal to the interface, going from the solid layers towards the liquid bulk [77, 95]. The diffusivities for the solid layers are generally negligible. Starting from the solid-liquid interface, the diffusivity monotonically increases to the liquid bulk value over a few Å from the interface.

Figure 3.7 shows the shape of the MSD of Ni atoms in a homogeneous Cu-Ni liquid with 15% Ni content, considering 4 Å bins. Figure 3.8 shows plots of several MSDs at different positions from the interface inside the liquid phase during solutal melting. The plots are distanced equally by 2 Å which corresponds to the period of the density peaks of the two-phase Cu-Ni system at 1400 K. The first point to note is that, unlike in the homogeneous case, diffusion in a two-phase system depends on the position relative to the interface, which hinders the motion of the atoms in its vicinity. The presence of vacancies left by the diffusing solid atoms towards the liquid phase and the layering of the liquid at the interface causes the MSD to increase gradually the further away from the solid layers. Because the interface is abrupt, it is also possible that measuring the MSD in a position where some of the atoms belong to the solid phase and others to the liquid phase would lead to an averaged MSD that spreads over the interface width, causing the MSD to increase as the proportion of the liquid

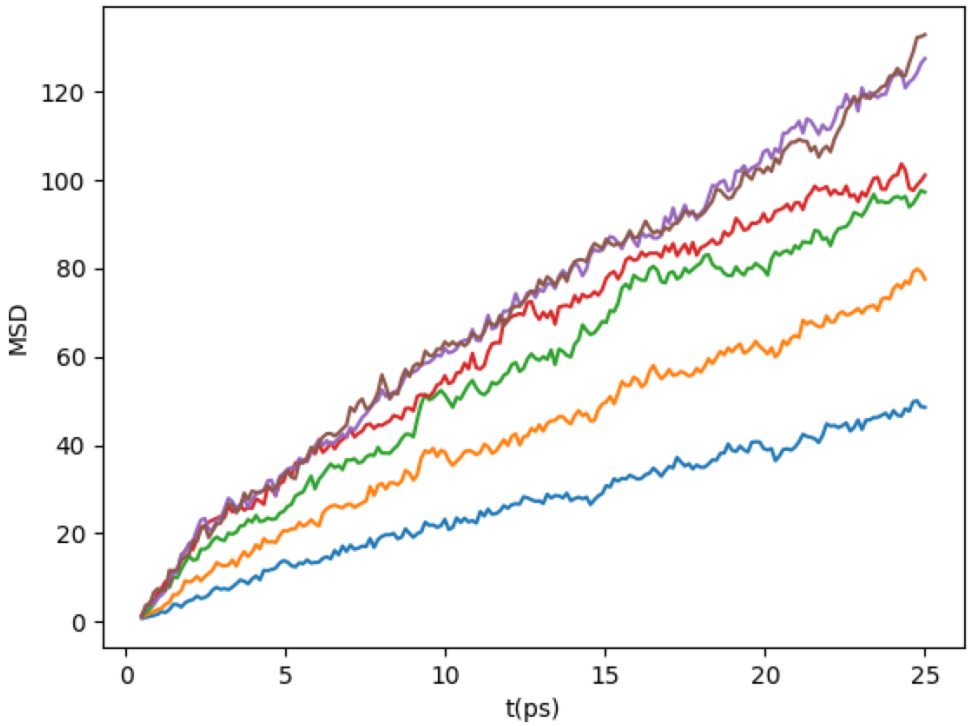

Figure 3.8 – MSD of Ni atoms in a Cu-Ni simulation box with coexisting solid and liquid at different position from the interface in the liquid.

increases until it reaches the bulk value.
Another factor that adds up and affects the MSD slope is the presence of a concentration gradient at the interface during the solutal melting of two asymmetrical materials. Self diffusivities of Ni in Cu-Ni liquid alloys with a size of $15 \times 15 \times 15\,\text{Å}^3$ with different Ni content were measured at 1400 K in the following alloys:

- for 5 % Ni, $D_{\text{Ni}} = 3.22 \times 10^{-5}\ \text{cm}^2\,\text{s}^{-1}$
- for 15 % Ni, $D_{\text{Ni}} = 3.07 \times 10^{-5}\ \text{cm}^2\,\text{s}^{-1}$
- for 30 % Ni, $D_{\text{Ni}} = 2.85 \times 10^{-5}\ \text{cm}^2\,\text{s}^{-1}$
- for 40 % Ni, $D_{\text{Ni}} = 2.76 \times 10^{-5}\ \text{cm}^2\,\text{s}^{-1}$.

The self diffusivity of Ni decreases slightly with increasing Ni concentration. There are several other factors that influence the value of D in MD, such as pressure tensors, choice of thermostat etc. The most subtle and least understood is the effect of the shape and size of the simulation box due to periodic boundary conditions, which will be discussed in details later on.

In the presence of an interface, the diffusivity varies from one region to another, necessitating careful consideration of the position of the atoms relative to the region of interest. If the MSD becomes linear at times long enough for the particles to leave the region of interest, the measured diffusivity would be averaged over all regions. Additionally, for such nonuniform systems, the free diffusion equation, from which the Einstein relation is derived, will no longer hold. According to Liu, Harder and Berne [96], the Smoluchowski equation should be

used near the interface. They propose a method for determining the diffusivity tensor for confined fluids or systems containing interfaces using a dual simulation technique. The gist of the method is to perform MD simulation with virtual absorbing boundaries around the region of interest and to perform a sequence of Langevin dynamics with different values of friction coefficient which is related to the diffusivity in the direction perpendicular to the interface. The optimal value for the diffusivity is selected based on the friction coefficient that yields the closest match between the survival probability obtained from Langevin dynamics and that obtained from MD simulation.

3.6 Solutal melting

3.6.1 Simulation setup

The solutal melting process necessitates an out-of-equilibrium solid-liquid interface at a set temperature. In this regard, a solid-liquid simulation box is prepared by having a pure Ni solid structure in contact with a pure Cu slab at liquid state. To characterize dynamic aspects, such as interface displacement and diffusivities, along the normal direction of the interface, a quasi-2D structure containing approximately 400 000 atoms is selected as the first reference simulation. This choice is inspired by the work of Ueno and Shibuta [80][79].

A Ni FCC crystal of 105 216 atoms ($225.3 \times 482.2 \times 10.5\,\text{Å}^3$) is prepared at $T = 1400\,\text{K}$ with the canonical ensemble (NVT) for 15 ps. The liquid structure is prepared by annealing an FCC crystal of 196 608 Cu atoms ($483.5 \times 483.5 \times 11.3\,\text{Å}^3$) at $T = 5000\,\text{K}$ for 1 ps to ensure complete melting of the structure. After the melting process, the structure is equilibrated at $T = 1400\,\text{K}$ under 0 bar with the isothermal-isobaric ensemble (NPT) for a duration of 10 ps. This step enables volume expansion. Finally, both the Ni solid and Cu liquid slabs are connected along the $[001]$ direction, creating an assembly where the liquid is sandwiched between two solid slabs. The composite structure undergoes an energy minimization process to alleviate issues related to unexpected atom proximity at the interface. This process is allowed to proceed for a maximum of 100 time steps, after which an ordered structure emerges on the liquid side, in the vicinity of the interface.
Following the relaxation of the structure, a simulation is initiated using the NPT ensemble under 0 bar and at 1400 K. This simulation runs for a duration of 100 ns with a time step of 1 fs. The timescales for thermostating and barostating are set at 0.1 and 1 ps, respectively. The utilization of the NPT ensemble allows volume adjustments during the dissolution process, which results in a minor volume increase as the structure undergoes melting.

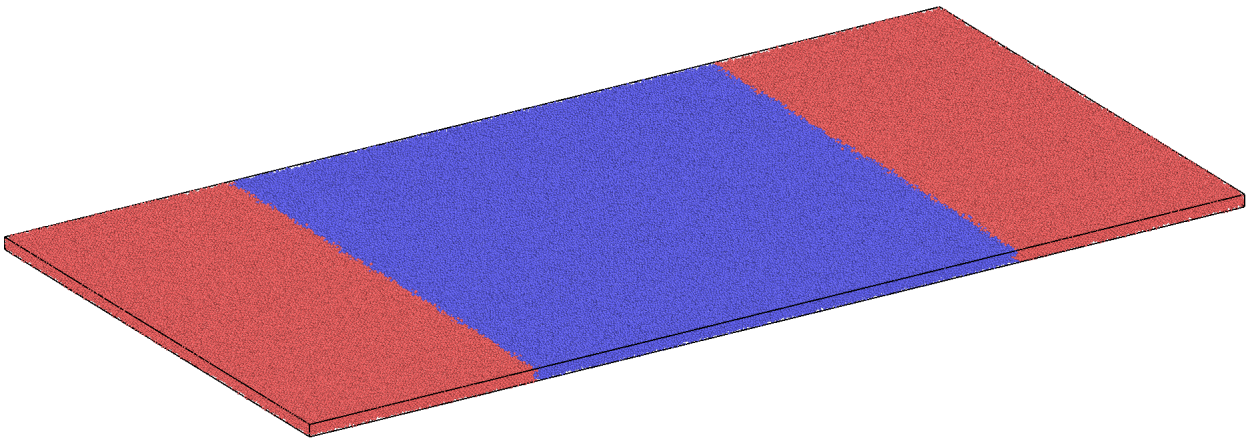

Figure 3.9 – Quasi-two-dimensional solid-liquid system of pure Ni FCC crystal connected to the liquid by a (001) *plane.*

3.6.2 Results

3.6.2.1 Reference simulation

Density profile

The local density is calculated by partitioning the simulation cell into uniformly sized slices or bins, aligned parallel to the interface. The fine-scale density profile of an atom i is given by [95, 97, 98]:

$$p_i(x) = \frac{\langle N_i \rangle_x}{A_{yz}\,\Delta x} \tag{3.20}$$

with $\Delta x = 0.045\,\text{Å}$ the bin thickness, A_{yz} the surface of yz planes, and $\langle N_i \rangle_x$ denotes the number of atoms i inside the bin centered at x.
Figure 3.10 shows the fine-scale density profile in the vicinity of the interface. The density profile demonstrates periodic oscillations of peaks, which are indicative of the long-range crystalline order aligned with the atomic planes. As the profile crosses the interfacial region, there is a noticeable decay in the crystalline density oscillations, a result of the loss of ordered structure in the liquid phase. The persistence of the periodic structure beyond the solid is attributed to the layering of the liquid in contact with the solid, as demonstrated by the oscillation visible in the density profile of the liquid phase, where the liquid inherits the solid structure on a few atomic layers [98, 77].
This effect has also been observed in experimental studies [99], where they found that the layering is related to density variations in the liquid perpendicular to the solid-liquid inter-

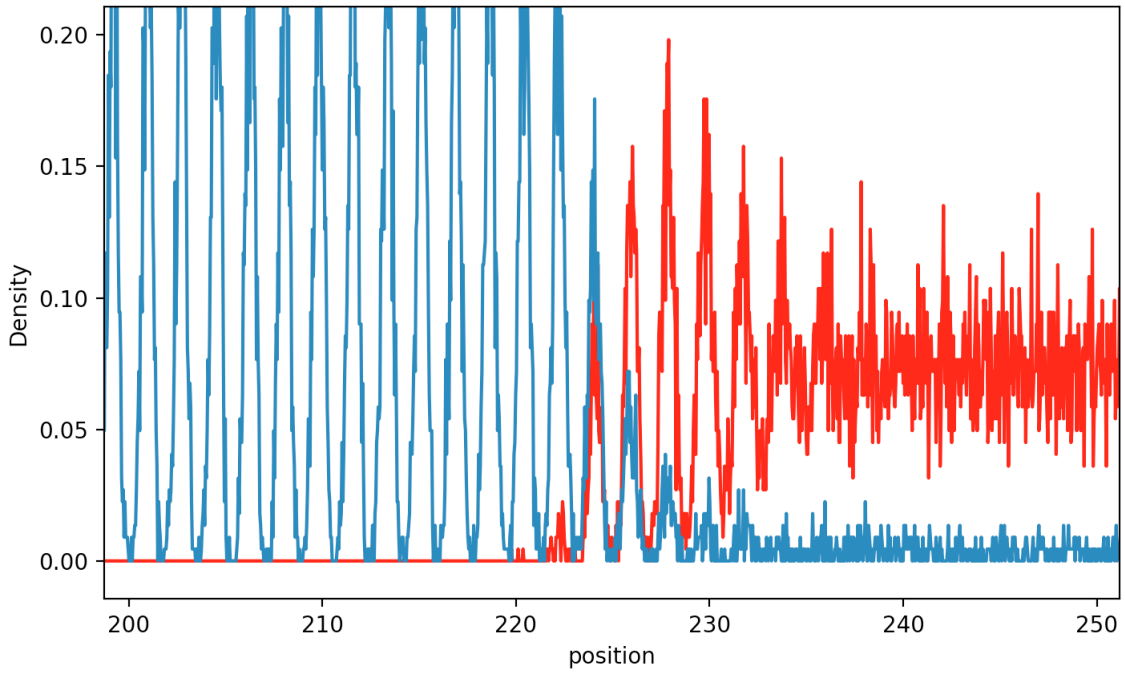

Figure 3.10 – Density profile of Ni (blue) and Cu (red) along the x direction in the vicinity of the interface.

face. When the bulk periodicity of the crystalline phase is close to the mean nearest-neighbor distance of the bulk liquid, the periodicity of the ordered liquid layers mimics the periodicity of the bulk crystal. However, when the crystalline periodicity is significantly larger than the mean nearest-neighbor distance in the bulk liquid, the distance between liquid layers reduces to the nearest-neighbor distance of the bulk liquid.
The Figure also shows that there is close to no diffusion of Cu in the solid phase except on the very first atomic layer of the solid, where a very small peak of Cu is observed. The overlapping of the density peaks of Ni and Cu near the interface means that some of Ni atoms have been substituted by Cu atoms, leading to a decrease of the Ni density peak.
A noticeable enlargement of density peaks on the liquid side and expansion of interlayer distances can be observed. This phenomenon has been reported in [77] for the Cu-Ni system using a different EAM potential [100]. They found that the interlayer distances in the liquid side depend on the orientation of the underlying solid, where a significant expansion is noted for the $[100]$ direction, while remaining the same as those in the bulk solid for the (110) and (111) interfaces. This phenomenon has also been reported in other systems such as aluminum [101] and hard-sphere systems [102]. However, it is essential to note that not all systems exhibit this behavior, exemplified by the Cu-Al system [98].

Interface position

Several methods exist for determining the interface position, and in this context, three have been implemented. Each method yielded similar results for the position of the interface.
The first one relies on determining the interfacial excess of any thermodynamic quantity by defining a Gibbs dividing surface that separates solid from liquid. Assuming zero interfacial excess of Ni atoms, the position of the dividing surface can be determined by solving the equation:

$$\Gamma_{\mathrm{Ni}} = \frac{N_{\mathrm{Ni}}}{A_{yz}} - L^s \rho^s_{\mathrm{Ni}} - (L - L^s)\,\rho^l_{\mathrm{Ni}} = 0 \tag{3.21}$$

N_{Ni} is the total number of Ni atoms, L is the total length of the simulation box along the x direction, L^s the length of the solid slab along x, ρ^s_{Ni} and ρ^l_{Ni} the density of Ni in the solid and liquid respectively.
The interface position is then given by [95]:

$$L^s = \frac{(N_{\mathrm{Ni}}/A_{yz} - L\rho^l_{\mathrm{Ni}})}{\rho^s_{\mathrm{Ni}} - \rho^l_{\mathrm{Ni}}} \tag{3.22}$$

One limitation arises with this method due to the need for updating the solid and liquid lengths as the dissolution proceeds. Otherwise, the measured interface position would deviate from the real position.

The second method consists of determining the local structure of the atoms using the PTM method. The position of the interface is determined by extracting the position of the jump in the structure distribution at 50%.

The final method employed is the most practical and easy to implement, as it simply involves applying a Gaussian filter to the density profiles and identifying the inflection point, which corresponds to the position of the interface.

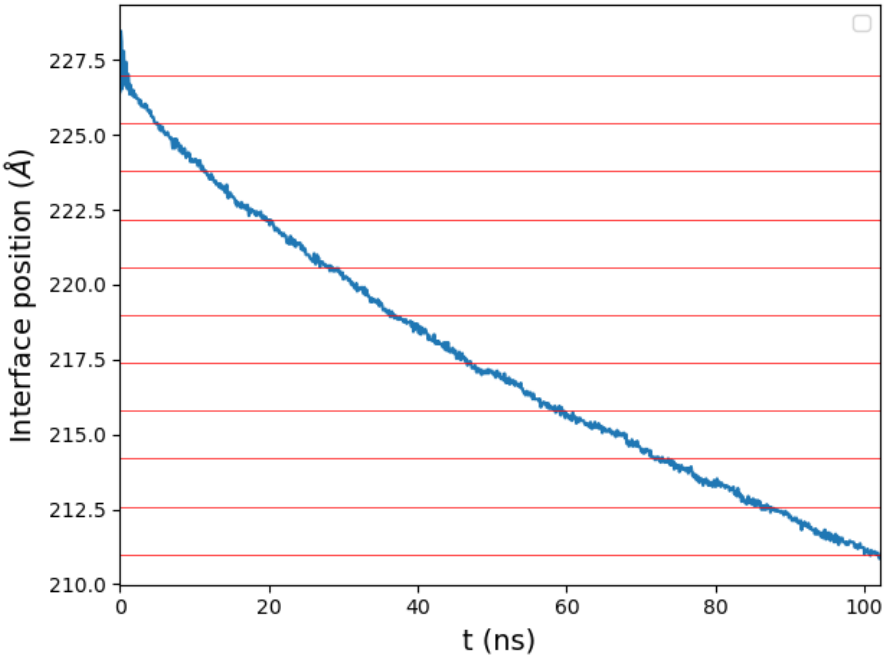

Figure 3.11 – Interface position vs. time: the red horizontal lines represent the spacing between adjacent atomic planes.

Several other methodologies have been developed to determine the position of the interface, but have not been tested in the present work. One such method, typically used for face-centered cubic (FCC) structures, which parallels the PTM method, involves assigning each atom a solid-liquid order parameter ϕ [103]. This is done by calculating the deviation of a neighboring atom from the ideal FCC positions of the crystal in the given orientation ($\mathbf{r}_{\text{fcc}}$). The summation of the deviations over the 12 nearest neighbors, $\phi = \frac{1}{2}\sum_i |\mathbf{r}_i - \mathbf{r}_{\text{fcc}}|^2$, serves as an order parameter assigned to the central atom. The value $\phi = 0.7$ was chosen in [103] to locate the interface where ϕ undergoes a significant change.

Interface velocity

The interface velocity can be determined by the slope of the time evolution curve of the interface position (Figure 3.11), which is fitted using a 3rd order polynomial function:

$$x^\star = 226 - 0.2147\,t + 1.1065 \times 10^{-3}\,t^2 - 3.5167 \times 10^{-6}\,t^3 \tag{3.23}$$

with $x^\star$ in Å and t in ns.
The highest velocity values are measured at the beginning of the melting process ($\approx 2\,\text{cm}\,\text{s}^{-1}$) when the interface is strongly out of equilibrium. As the concentration on the liquid side increases as a result of solid phase dissolution, there is a corresponding decrease in the interface velocity. The observed velocities are significantly higher than those found in experimental studies, which are typically of the order of µm. Due to the limitations of molecular dynamics (MD) simulations, which include constraints on time scales and system sizes, it is currently impossible to achieve the temporal overlap required for precise quantitative comparisons with

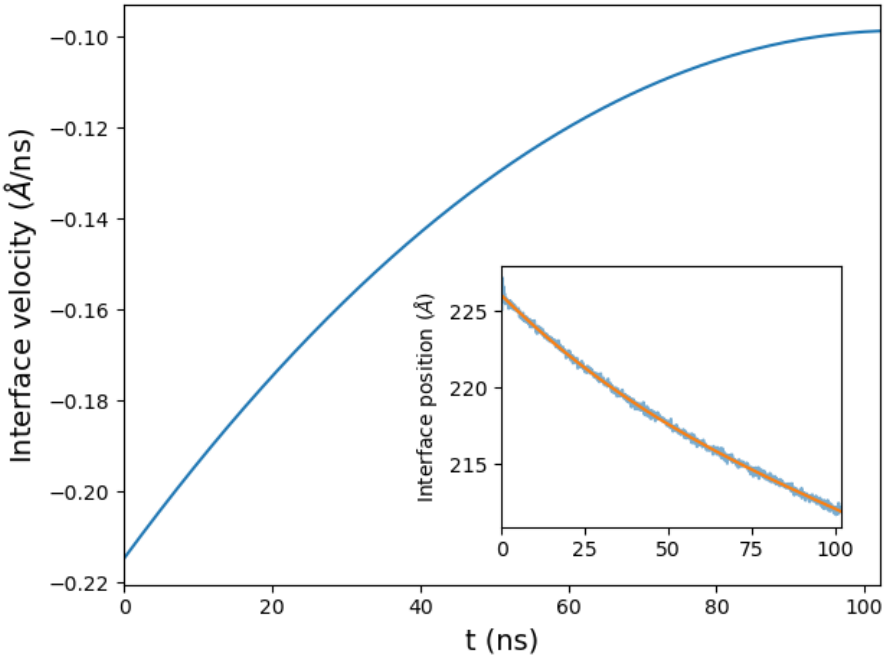

Figure 3.12 – Interface velocity during solutal melting.

experiments. Small MD simulation systems have concentration gradients at the interface that far exceed those of a real system, where the diffuse interface spans a few nm. This discrepancy may account for the substantially higher velocities measured by MD.
Although the values of the velocity ($\mathcal{O}(2000)$ $\mu m\,s^{-1}$) are three order of magnitude larger than the measurements of Deillon et al. [4] ($\mathcal{O}(2)$ $\mu m\,s^{-1}$), it is worth stressing that they are significantly lower compared to the reported velocities in thermal solidification and melting of pure elements. In these cases, the velocities can reach values ranging from a few dozen to several hundred $m\,s^{-1}$ [40, 86, 42, 104, 105]. At first sight, this difference could appear as surprising when the deviations from equilibrium of our interface were compared with those obtained during rapid solidification. But, as already mentioned and discussed in §2, the asymmetry of situations between solutal melting and solidification is likely to rely on the role played by diffusion in the solid phase, which is the slowest process setting the typical time scale of the interface motion.

Concentration profiles

The concentration profiles are determined in a manner similar to the density profiles. This involves dividing the simulation box into equal slices along the x-direction and then counting the number of atoms of a given type in each slice, normalized by the total number of atoms in that slice.
Figure 3.13 shows the concentration profiles at different times during solutal melting after smoothing the curves using a gaussian filter. Throughout the entire simulation, the interface concentrations are far from the equilibrium values, represented by the red dashed lines (solidus 29%, liquidus 25%). The solid side concentration remains at 100% Ni, given the lack

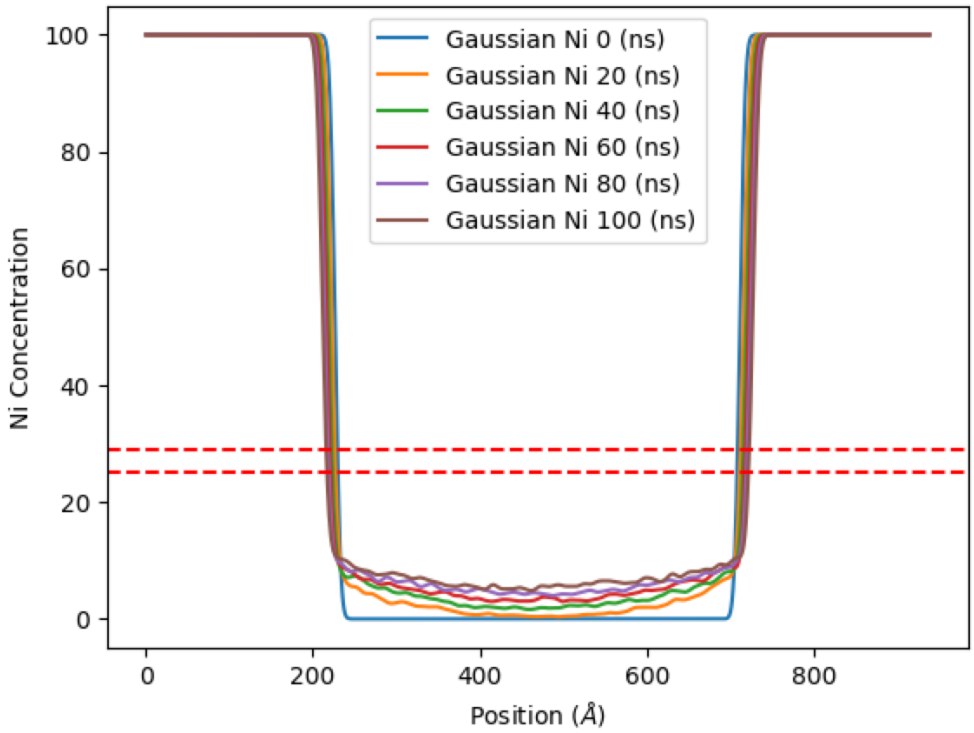

Figure 3.13 – Evolution of concentration profiles of Ni during solutal melting.

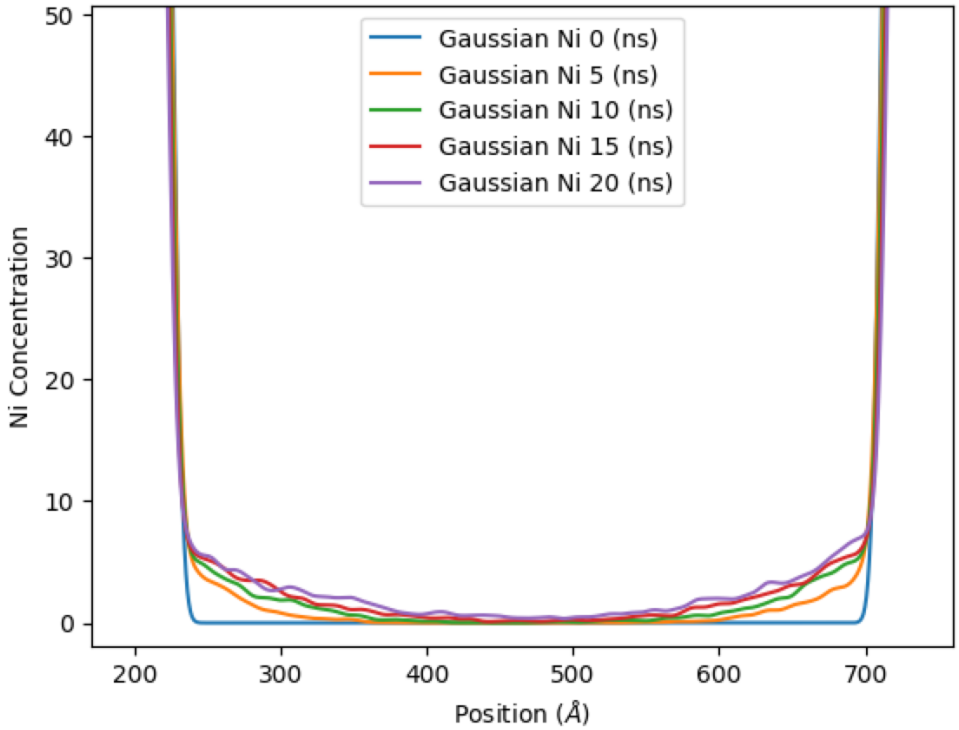

Figure 3.14 – Evolution of the concentration profiles of Ni during the first 20 ns *of solutal melting.*

of diffusion on this side, as observed in the density profile in Figure 3.10. The liquid concentration, on the other hand, increases quickly in the vicinity of the interface during the first 5 ns as shown in Figure 3.14. Then, it slowly increases as it reaches values close to 10%, and the interfacial concentration increases by roughly 1% each 20 ns. After 20 ns, the Ni atoms start to reach the central zone of the liquid region: the two interfaces start to interact and the concentration gradients between the interfacial region and the center gradually decrease.

3.6.3 Influence of size and shape of the simulation box

This section examines the impact of the size and shape of the simulation box on the interfacial velocities. Four simulation boxes, as depicted in Figure 3.15, are selected for this purpose:

- the first is a quasi-2D box with 400 000 atoms,
- the second possesses the same atom count and x-axis length as the first but features a square interface section,
- the third also maintains the same x-axis length and square interface section but is needle-shaped with 24 000 atoms,
- and the final box houses a broad square interface with 1.4 million atoms.

Comparison of the plotted interface positions across all cases in Figure 3.16 reveals distinct interface displacements for each, suggesting a correlation between the system size and the interface velocity. The larger the simulation box (in terms of the number of atoms), the faster the interface migration.
The shape of the simulation box also appears to affect the velocity of the interface, as evidenced by the differences between the blue and orange curves. Although the two boxes share the same number of atoms, the two boxes demonstrate distinct velocities owing to their differing shapes. These differences in interface velocities are very likely related to the differences in diffusivities across the simulation boxes. Previous research has indicated that the strong dependence of the diffusivities on the size of the simulation box for both pure and multicomponent mixtures is a consequence of the periodic boundary conditions, which has been shown to slow down the diffusivity for cubic isotropic boxes [106]. The long-range nature of hydrodynamic interactions of particles or molecules with their own periodic images introduces finite-size effects, leading to erroneous measurements of dynamical properties, such as self diffusivities [107, 108, 106, 109, 110, 111, 112], activity coefficients [113], thermal and ionic conductivities [114] [115]. Whereas properties such as the viscosity seem to be unaffected by the system size [109, 116, 117].

One could consider performing simulations without periodic boundary conditions to avoid the finite-size effects by introducing hard walls, for instance. However, such a modification does not only remove these effects but would also add other unwanted effects such as fluid-wall interactions, which are less controlled and understood. The finite-size effect can only be eliminated by having a sufficiently large system, which is computationally not feasible. Even the most advanced computational systems capable of handling systems with millions or even billions of atoms cannot directly simulate the behavior of systems as large as experimental samples. This limitation necessitates the use of periodic boundary conditions

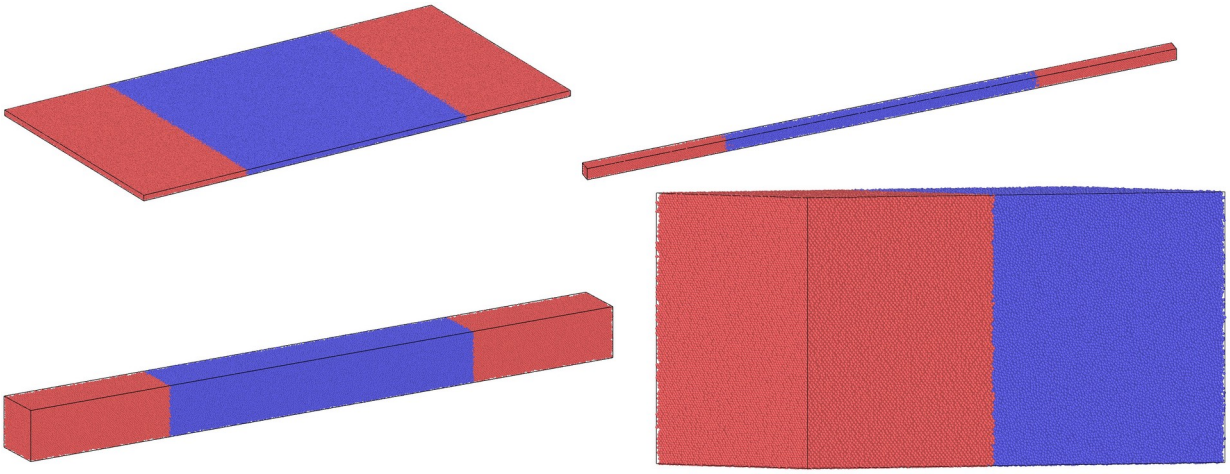

Figure 3.15 – Solid-liquid Cu-Ni simulation boxes of different sizes and shapes.

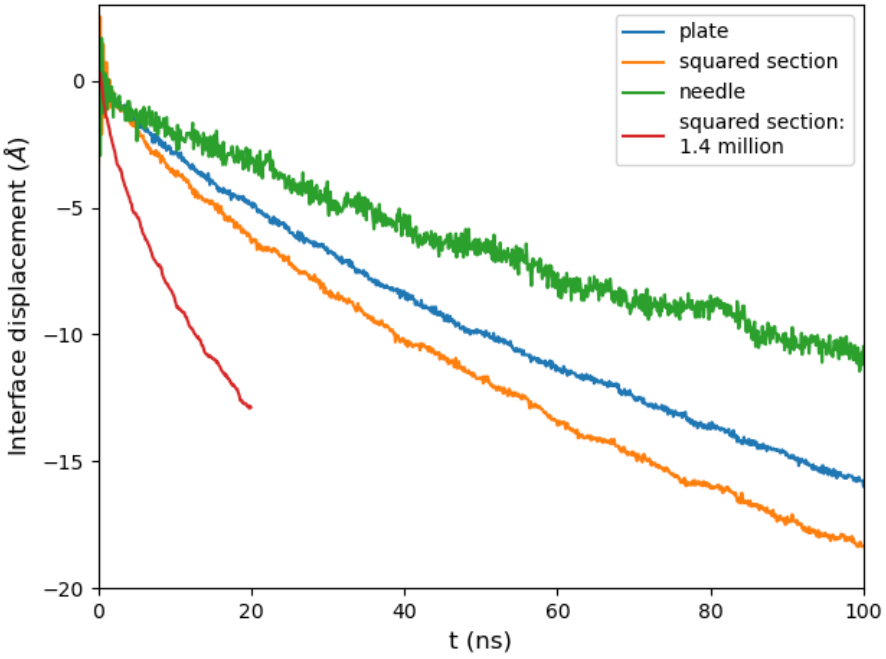

Figure 3.16 – Dependence of the interface velocity with the size of the simulation box.

in calculations. Mitigating these effects is typically achieved by employing relatively large system sizes, a large cutoff radius in interaction potentials, or applying analytical corrections for the parameters of interest.

The MSD is often used to estimate diffusivities. It is also widely used to estimate the melting temperatures of materials using Lindemann criterion which states that the system melts when the MSD exceeds a given fraction of the average particles distance. Robbins et al. [118] used the MSD to study the effect of a finite-size system on thermal fluctuations and

its impact on melting temperatures T_m for solid structures. They found that MSD increases with increasing number of atoms N and scales as $N^{-1/3}$ in FCC structures (although the opposite was observed in the BCC structure, suggesting that this correlation depends on the interaction potentials). For small N, the structure could be easily superheated above T_m, but as N increases, the MSD increases and the structure becomes unstable and melts. This observation implies that it is essential to correct diffusivities computed from MD simulations due to finite-size effects and the fact that the number of particles used in typical MD simulations is in orders of magnitude lower than in the thermodynamic limit.
Dünweg and Kremer [106] studied the brownian motion of a polymer chain in solvent. They found that the long range of the hydrodynamic interaction induces a large effect of finite box size on the diffusivities of both the chain and solvent particles as they interact with an infinite number of periodic images. The finite-size corrections were found to be inversely proportional to the linear box dimensions. Yeh and Hummer [109] also made the same observation for water system, where the diffusion coefficients increase strongly as the system size increases, and finite-size analytical corrections scaling as $N^{-1/3}$.
For a cubic MD box denoted by a linear size L, the self diffusivity D^{∞}_{self} in an infinite system is obtained by a correction scaling as $1/L$ as demonstrated first by Dünweg and Kremer and confirmed later on by Yeh and Hummer:

$$D^{\infty}_{\text{self}} = D^{\text{MD}}_{\text{self}} + \frac{k_b T \xi}{6\pi\eta L} \tag{3.24}$$

with $D^{\text{MD}}_{\text{self}}$ calculated from MD, T the temperature, η the shear viscosity computed in MD simulations, and $\xi = 2.84$ for a cubic lattice.
If viscosity is not known, the apparent self diffusivities $D^{\text{MD}}_{\text{self}}$ can be calculated for different system sizes. D^{∞}_{self} can then be estimated from the intercept of a linear fit of $D^{\text{MD}}_{\text{self}}$ with respect to $1/L$, which corresponds to an extrapolation to infinite system size. For a spherical particle of radius R relatively large ($R > L/2$), an additional correction may be incorporated into equation 3.24 to consider the particle size in a cubic simulation cell [109]:

$$D^{\infty}_{\text{self}} = D^{\text{MD}}_{\text{self}} + \frac{k_b T}{6\pi\eta L}\left(\xi - \frac{4\pi R^2}{3L^2}\right) \tag{3.25}$$

For multicomponent mixtures, it is shown that the diagonal elements of the diffusivity matrix depend on the system size following equation 3.24, while the off diagonal elements do not depend on the system size [112]. For rectangular anisotropic boxes, the diffusivity along the shorter dimension D_x is always higher than that along the longer dimension D_z [119, 120, 121, 122].
A. Botan et al. [121] studied the asymmetry of diffusivities by taking an elongated simulation cell with equal side lengths ($L_x = L_y \neq L_z$). They observed the evolution of the components of the diffusivity tensor D_x, D_y and D_z for fixed values of $L_x = L_y$ as a function of the perpendicular dimension L_z. They found that while the x and y components were equal, D_x and D_y differed from D_z, reflecting the symmetry of the simulation cell. In particular, they observed that D_x, D_y, and D_z did not adhere to the simple scaling outlined by equation 3.24 for the isotropic case. The components could decrease or increase, either simultaneously or in opposite directions, depending on the size and aspect ratio. They could even exceed the value of D^{∞}_{self} for an infinite system, whereas hydrodynamic effects can only reduce the diffusivity

for the isotropic case.
Kikugawa et al. [120] also examined the effect of system size and shape on diffusion by choosing rod-shaped rectangular boxes with fixed side lengths ($L_x = L_y = 10.94$) and varying the length in the z direction L_z (ranging from 10.95 for cubic to 54.71). This is only possible by increasing the number of atoms along that direction, ranging from 1000 to 5000 atoms. Their findings suggested that as the number of atoms increased, D_x and D_y increased more or less linearly with increasing L_z, while diffusion in the z direction did not exhibit any visible change. Moreover, in systems over 3000 atoms, D_x and D_y exceeded D^{∞}_{self} predicted by equation 3.24.

In the context of anisotropic simulation boxes, the correction becomes dependent on direction. Vögele and Hummer [123] were able to provide explicit corrections based on hydrodynamic theory to the diagonal components of the diffusivity tensor for the case of elongated and flat boxes with similar shapes to the ones presented in Figure 3.15.
For rectangular elongated boxes $L_x = L_y \ll L_z$, they arrived to similar conclusions as Kikugawa et al. The diffusivity components normal to the long axis, $D_{xx} = D_{yy}$, increase linearly with the increasing box asymmetry L_z/L_x, while the diffusivity correction in the z direction of the long axis has no diverging component and scales almost similarly as the isotropic case:

$$D_{xx} = D_{yy} \approx D^{\infty} + \frac{k_b T}{6\pi\eta\, L_x}\left(\frac{\pi}{2}\frac{L_z}{L_x} - \chi_{xx}\right) \tag{3.26}$$

$$D_{zz} \approx D^{\infty} - \frac{k_b T}{6\pi\eta\, L_x}\,\chi_{zz} \tag{3.27}$$

where the coefficients χ_{xx} and χ_{zz} are determined by numerical fits.
For flat rectangular simulation boxes, $L_x = L_y \gg L_z$, the diffusivity in all directions increases logarithmically with the ratio of width to height, and both the in-plane ($D_{xx} = D_{yy}$) and the out-of-plane diffusion coefficients (D_{zz}) are predicted to diverge with increasing asymmetry L_x/L_z:

$$D_{xx} = D_{yy} \approx D^{\infty} + \frac{k_b T}{6\pi\eta\, L_z}\left(\frac{3}{2}\ln\left(\frac{L_x}{L_z}\right) - \xi_{xx}\right) \tag{3.28}$$

$$D_{zz} \approx D^{\infty} + \frac{k_b T}{6\pi\eta\, L_z}\left(3\ln\left(\frac{L_x}{L_z}\right) - \xi_{zz}\right) \tag{3.29}$$

where the coefficients ξ_{xx} and ξ_{zz} are also determined by numerical fits.
Inspection of the above equations reveals that the hydrodynamic theory predicts that all diagonal components (except D_{zz} in elongated boxes (eq.3.27)) diverge as $L_z \to \infty$ for elongated boxes and $L_x \to \infty$ for flat boxes.
Vögele and Hummer also noted that the linear divergence of $D^{\text{MD}}_{\text{self}}$ in elongated boxes, the logarithmic divergence for flat boxes, and the convergence of $1/L$ in cubic boxes all reflect a close analogy to electrostatics. In 1D, 2D, and 3D systems, Coulomb interactions depend linearly, logarithmically, and inversely on distance, respectively. According to the authors, for the elongated and flat systems, the periodic replicates of particles can be seen as forming infinite sheets and lines that move "collectively".

The above phenomenological descriptions, derived from hydrodynamic theory, appear to manifest themselves in the solid-liquid interfaces as demonstrated in Figure 3.11. Both the system shape and size influence the interface velocities and, subsequently, the diffusivities. Figure 3.17 represents concentration profiles of the four simulation cells taken at the same time t. Figure 3.18 presents the concentrations for the same interface displacement. In both illustrations, larger simulation boxes produce more pronounced concentration gradients leading to a higher interfacial velocity with the increasing number of atoms.
For the needle and square section boxes, where there is only an increase in the xy surface (interface surface), the square section exhibits a higher interface velocity and concentration gradient. At a first approximation, this can be seen as increased diffusivity, which seems to be consistent with equation 3.27 for elongated boxes. A similar observation is made for the simulation box with 1.4 million atoms, which displays an even higher velocity and concentration gradient due to the large side length L_x, thus increasing the diffusivity in the z direction as per equation 3.27.
Regarding the square section and the quasi-2D boxes, no specific conclusion can be drawn on why the square section exhibits higher interface velocity, except that modifying the interface shape by changing the L_x/L_y ratio affects diffusion in the normal direction. The most notable change in diffusion dynamics would occur in the direction of the shorter side of the quasi-2D cell.

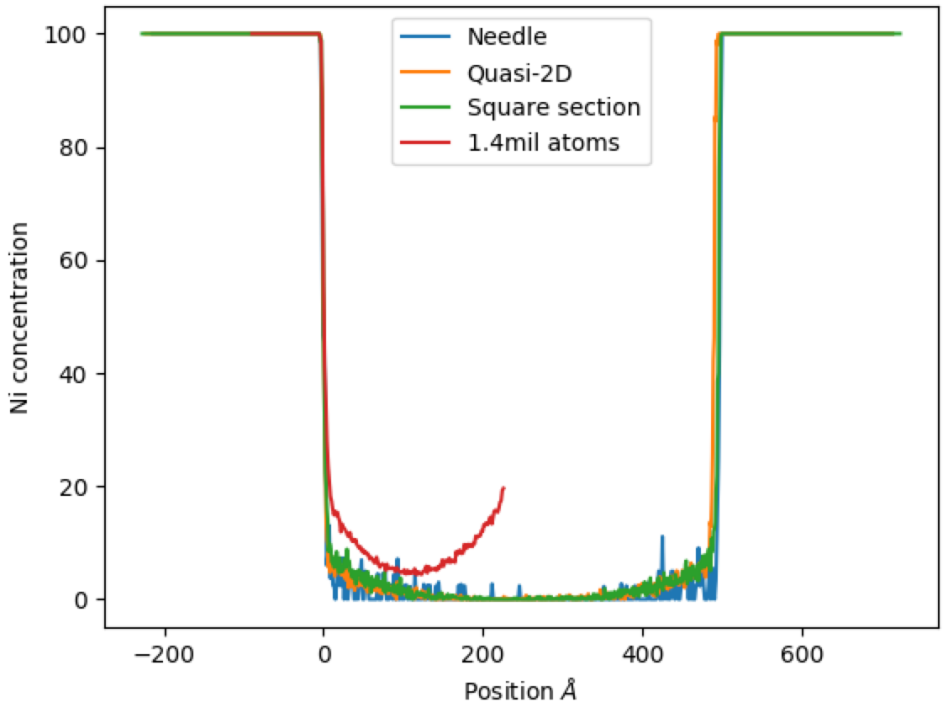

Figure 3.17 – Concentration profiles taken at the same instant for simulation boxes of different sizes and shapes.

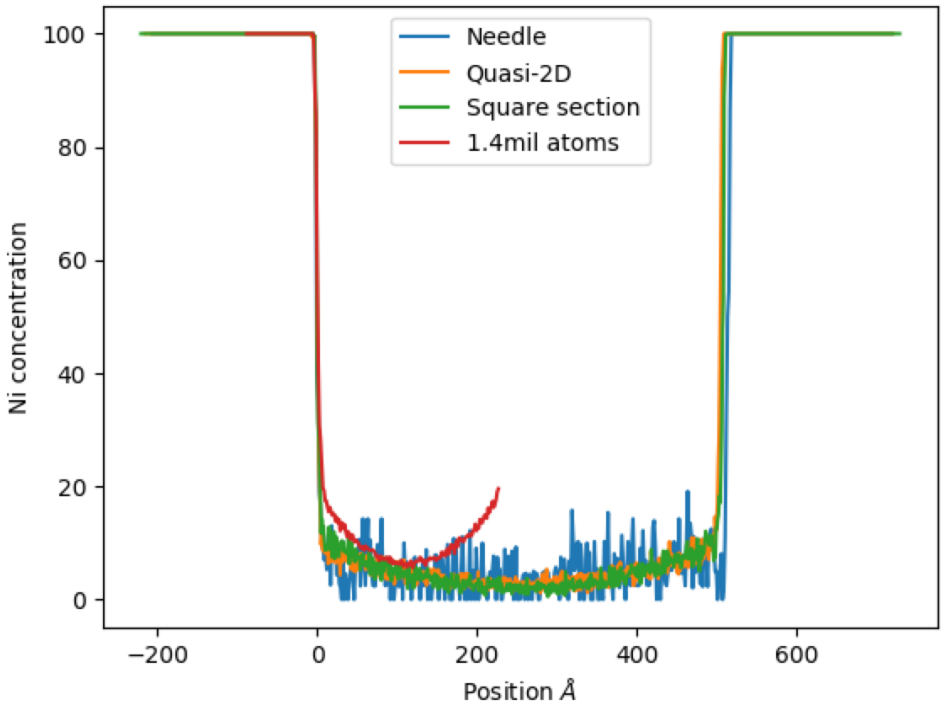

Figure 3.18 – Concentration profiles taken at the same displacement of the interface for simulation boxes of different sizes and shapes.

3.6.4 Dissolution process in the vicinity of the interface

A closer examination of the solid-liquid interface, which provides insight into the dissolution process, was conducted by capturing several snapshots of the *xy* plane at a specific instant during the dissolution process. Snapshots correspond to the positions at the center of the peaks on the density profiles in the interface region, as represented in Figure 3.19.

These snapshots were extracted from the simulation box containing 1.4 million atoms depicted in Figure 3.15, given its extensive *xy* surface area. In the upper images, green indicates atoms in a solid structure, while blue signifies atoms in a disordered or liquid structure. The lower images use color coding based on particle type, with blue and red corresponding to Cu and Ni atoms, respectively. The snapshots are situated at layers where a transition from the solid to liquid phase can be observed. On the right side, the atoms are predominantly in an ordered configuration, and this order is gradually lost as the bulk liquid is approached on the left side.
The first image corresponds to a fraction of 75% solid structure. Going further on the right side, the layers are 100% solid. But as has been illustrated previously from the concentration and density profiles (Fig. 3.10), there is no diffusion in the solid phase, which implies that all the atoms are Ni atoms only. In the first image, the structure is primarily solid (25% liquid)

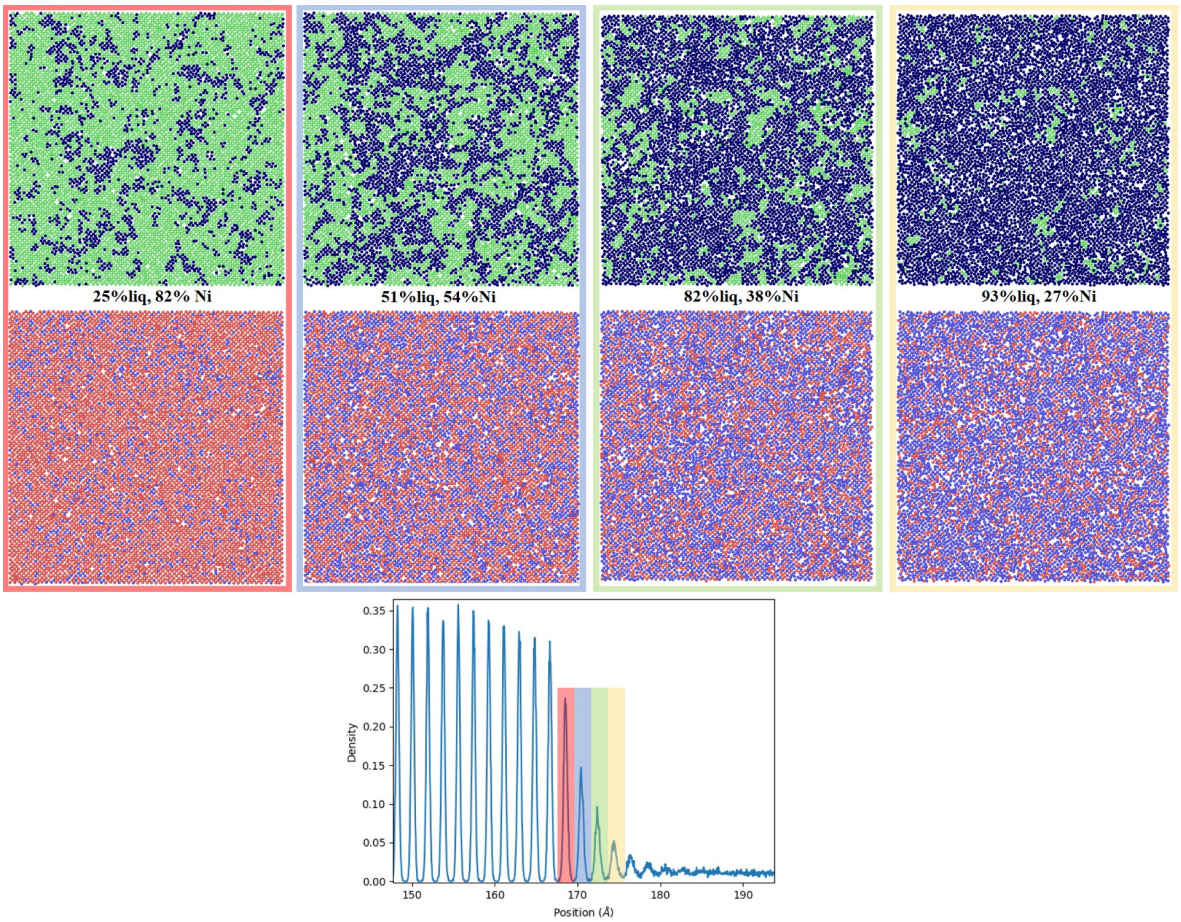

Figure 3.19 – Snapshots of atomic planes at different positions in the vicinity of the interface.

and some of the free sites vacated by outgoing Ni atoms are occupied by Cu atoms, adopting a local fcc arrangement. The same behavior was observed on the Ni-Al system [124], where Al atoms (from pure liquid Al) occupied the vacancies created by the outgoing Ni atoms. In the second image, the structure is half solid and half liquid. This position can be considered as the interface position, since the same criterion was used to determine the interface position using the PTM method, defined by having 50% solid and 50% liquid. The concentration of Ni at this position is still far from the equilibrium values (25% solidus, 29% liquidus). The same observation is made for the third image, with a 82% liquid fraction and 38% Ni content. The atoms start losing their local organization gradually as the in-plane Cu content increases by substitution of Ni atoms, until the in-plane concentration hits a value where the solid structure is no longer stable and melts completely.

A noteworthy observation is that the profiles are almost stationary in the frame moving with the migrating interface, on the time scale investigated, except at the interface boundary on the liquid side. In that case, it is almost equivalent to analyze the behavior of the interface with respect to position or to time. Hence, selecting a specific instant t during simulation and examining snapshots at different positions is equivalent to fixing the position in a solid layer near the interface and observing how it evolves over time as the interface passes through this solid layer, causing it to melt. The same procedure was applied to the square section box containing 400 000 atoms, as shown in Figure 3.15. Since the displacement of the interface is slower compared to the bigger simulation cell, the snapshot of the interface at 50% solid and 50% liquid revealed that the concentration of Ni was between the solidus and the liquidus value, suggesting that the interface could be at or close to equilibrium due to the lower interface velocity.

3.7 From Molecular Dynamics to Lesoult Model

Having provided an overview of the MD facet of solid-liquid interfaces, this chapter proceeds to the final segment of this study: combining the MD simulation results with Lesoult thermodynamic model. This integration involves utilizing kinetic and thermodynamic parameters derived from the MD simulations at the interface and incorporating these parameters into the Lesoult thermodynamic model. Subsequently, predictions are made based on the model regarding Onsager parameters and the resulting concentration profiles.

3.7.1 Interfacial concentrations

The evolution of the interfacial concentration on the liquid side is determined from the concentration profiles. To achieve accurate results, ten successive concentration profiles, captured at very close temporal intervals, are selected such that their concentration values exhibit minimal differences. The profiles are smoothed by applying a Gaussian filter and the resulting smoothed profiles are then averaged to obtain the mean concentration profile. This method helps to remove some of the fluctuations and helps to identify the general trend of concentration over a short time frame. The final result of this process is demonstrated in Figure 3.20.

The interfacial concentration on the liquid side is identified at the position where the concentration profile exhibits a drastic increase in the interfacial region. This point can be pinpointed by calculating the gradient of the concentration profile and then selecting the position at which the absolute value of the gradient begins to rapidly increase at the interface. The aforementioned procedure is reiterated for multiple points within the 0 to 100 ns range, enabling the extraction of the liquid concentration at the interface as a function of time.

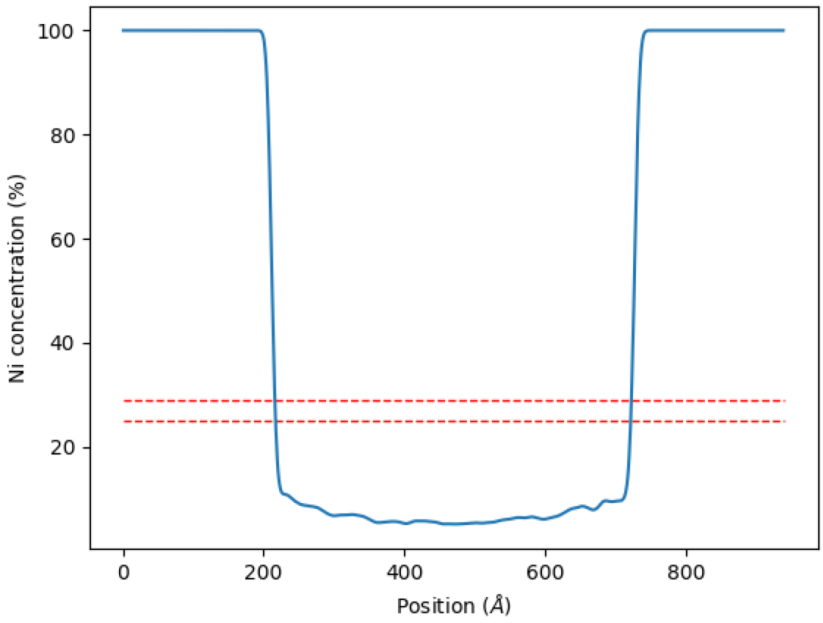

Figure 3.20 – Concentration profile of Ni from the Gaussian filtered concentration snapshot at 100 ns.

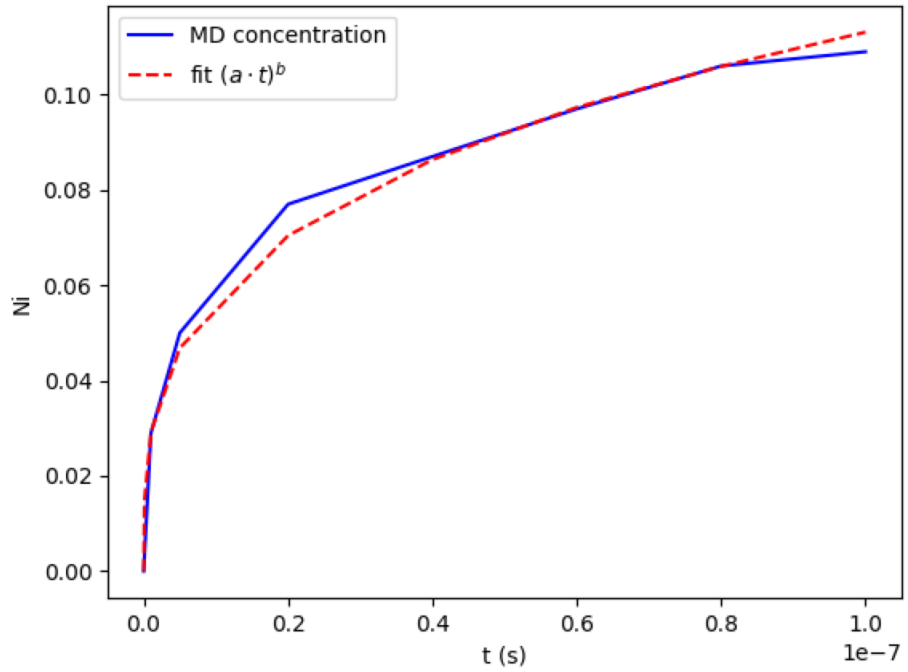

Figure 3.21 – Time evolution of the concentration at the interface on the liquid side during solutal melting.

Subsequently, the derived profile is fitted using a simple power law $(at)^b$ with $a = 6097\,\mathrm{s}^{-1}$ and $b = 0.3$. This fitting will be used subsequently in the thermodynamic model to describe the evolution of concentration over time as presented in Figure 3.21.

3.7.2 Chemical potentials

The most efficient technique to determine the chemical potential as a function of the solute concentration is thermodynamic integration using the atom/swap method. This method simulates a semi-grand canonical ensemble SGCMC behavior, as elucidated in a previous section on equilibrium concentration determination. By incorporating the insights from Ueno and Shibuta [90], the atom/swap method provides a means to estimate the chemical potential using equation (3.14), and the Gibbs energy curve can be obtained using equation (3.15).
A chemical potential difference is imposed. The composition of the structure starts to change to accommodate the difference in chemical potential imposed between the first and second element $\Delta\mu = \mu_{\mathrm{Ni}} - \mu_{\mathrm{Cu}}$. Monte Carlo swaps are attempted 5000 times every 1000 calculation steps. MD simulation is conducted simultaneously using the NPT ensemble to relax the structure, so that the volume accommodates to the newly obtained composition. After sufficient run time (in this case, 30 ps), the concentration stabilizes at a certain value. This concentration value is then recorded for the specific chemical potential difference.
The procedure is repeated by varying the imposed chemical potential differences, which enables the generation of a plot showing the chemical potential difference as a function of the concentration. The resulting curves for both the solid phase and the liquid phase are illustrated in Figure 3.22.

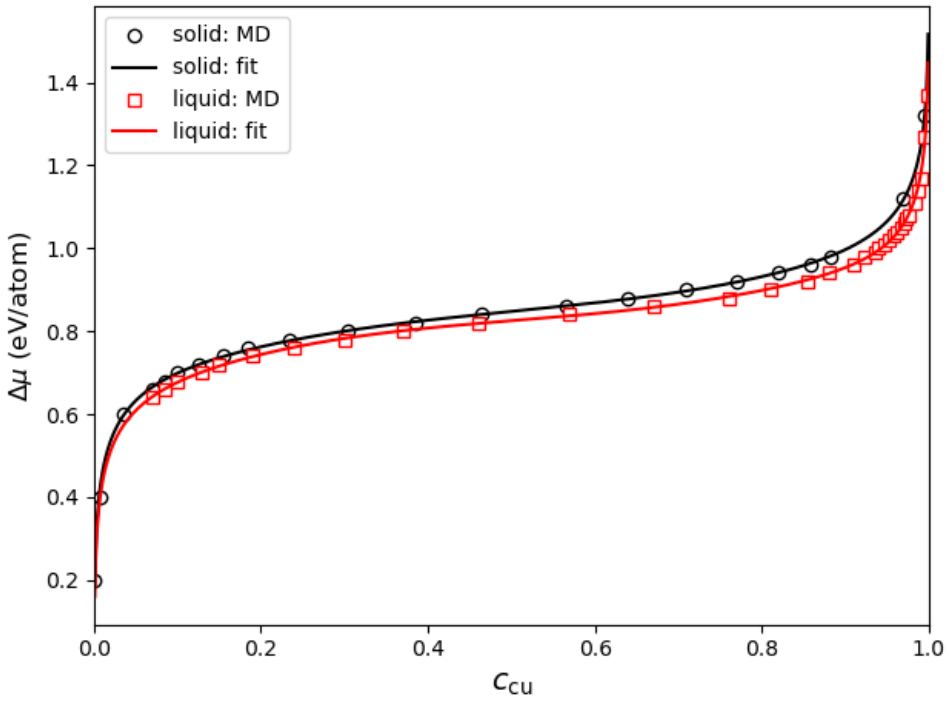

Figure 3.22 – Chemical potential difference between Ni and Cu for the liquid (red) and solid (black) phases.

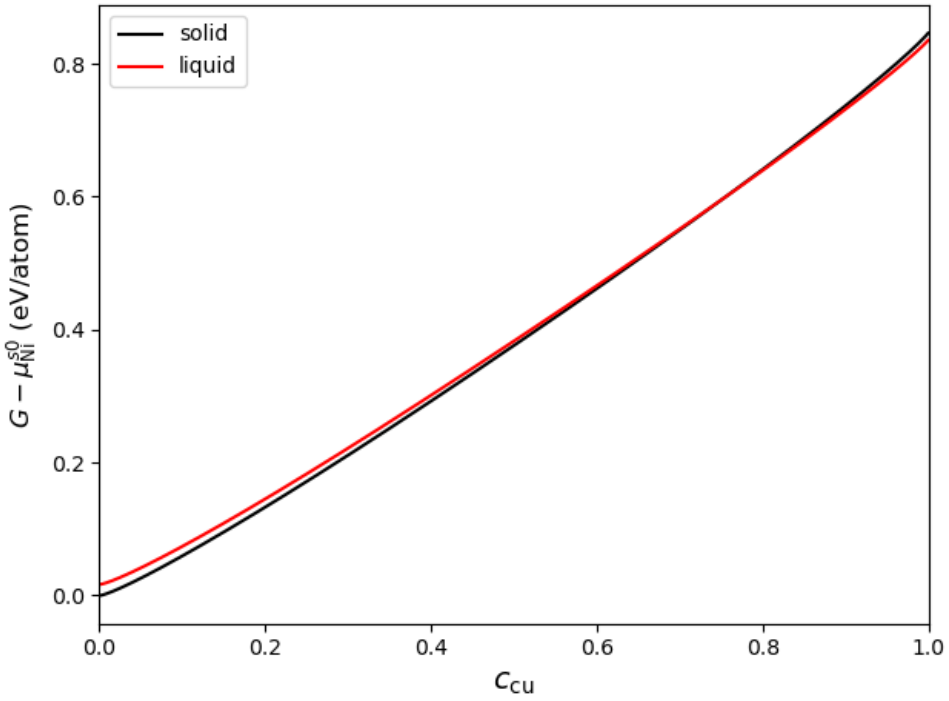

Figure 3.23 – Gibbs free energies of solid and liquid obtained after integration of the Δμ in Fig. 3.22 and adjustment of μ_{Ni}^{l0}.

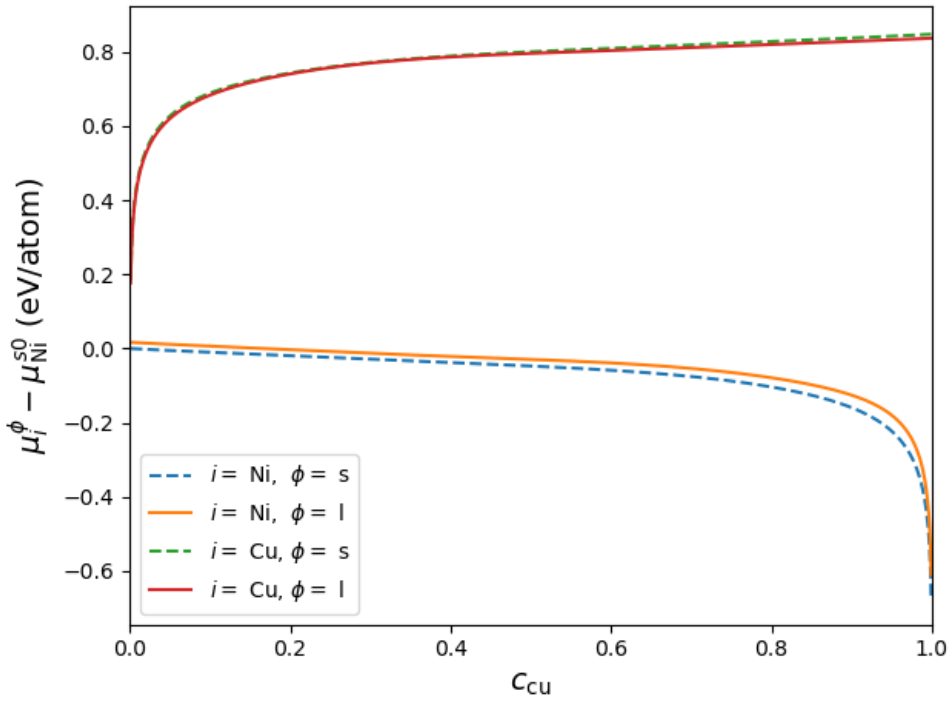

Figure 3.24 – Chemical potentials of Cu and Ni in solid and liquid with respect to concentration in Cu.

power i	0	1	2	3	4	5
liquid	0.994	-0.72	2.53	-6.33	7.06	-2.93
solid	1.019	-0.716	2.11	-4.65	4.79	-1.87

Table 3.1 – Polynomial coefficients describing the excess contributions to the chemical potential differences between Ni and Cu in each phase (Fig. 3.22).

The obtained chemical potential curves are then fitted using equation (3.14), Tab. 3.1. The fitted parameters are used to calculate the integral of this equation, which equates to the Gibbs energy up to some integration constant (e.g. the chemical potential of pure Ni), as given by equation (3.15). It is sufficient to determine one constant, considering the other as a reference (e.g. $\mu_{Ni}^{s0} = 0$). For that purpose, the best value of $\mu_{Ni^{l0}}$ (corresponding to shifting vertically the G curve of liquid with respect to the G curve of solid) that gives the common tangent with the equilibrium concentrations the closest to the experimental phase diagram at 1115 °C was sought. It was found that with $\mu_{Ni}^{s0} = 1.672 \times 10^{-2}$ eV/atom, the equilibrium concentrations are $c_{Cu}^{s} = 0.707$ and $c_{Cu}^{l} = 0.794$ ($c_{Ni}^{s} = 0.293$ and $c_{Ni}^{l} = 0.206$). It can be seen that the concentration of liquid is 4.4% lower than what was found at 1127 °C with the solute partitioning method in §3.4.2. The resulting Gibbs energy curves for the solid and liquid phases are plotted as a function of the Cu concentration in Figure 3.23.

The chemical potentials of Cu and Ni in each phases can be obtained as a function of the concentration in Cu, using their definitions:

$$\mu_i = G + \left(\delta_{ij} - c_j\right) \frac{\partial G}{\partial c_j} c_j \tag{3.30}$$

with δ_{ij} the Kronecker function.
They are plotted in Figure 3.24, and will be used subsequently to feed Lesoult model.

3.7.3 Moving interface model

Next, the 1D numerical resolution of the moving boundary problem controlled by solute diffusion in the liquid have been implemented, aiming to accurately simulate the progression of the interface considering the interface concentrations obtained from the MD simulations (Fig. 3.21) as input.
On the basis of the results of the MD simulations, diffusion of Cu in solid can be neglected such that the solid is considered to be pure Ni. Hence, Fick law is solved only in liquid:

$$\frac{\partial c}{\partial t} = D \frac{\partial^2 c}{\partial x^2} \tag{3.31}$$

where c is the concentration of Ni in liquid, and where it has been assumed that the intrinsic diffusivity of Ni in liquid D is constant in the range of variation of Ni observed in the MD simulations.

The diffusion equation is supplied with the following boundary conditions.

- First, on the right side at $x = L$ (with L the system size) in the middle of liquid, Neumann with zero flux is imposed to account for the symmetry of the problem: $\partial c/\partial x|_{x=L} = 0$.
- At the interface $x = x^\star(t)$, the interfacial solute balance reads (solid is for $x < x^\star$):

$$\left(1 - c^{l\star}\right) \frac{dx^\star}{dt} = D \left.\frac{\partial c}{\partial x}\right|^\star \tag{3.32}$$

  where $\star$ denotes quantities estimated at the interface. Concentration $c^{l\star}$ and velocity $dx^\star/dt$ are taken from the MD simulations, figures 3.21 and 3.12 respectively.

Equations (3.31) and (3.32) are discretized in time with a first order implicit Euler scheme. Then, to ensure solute conservation, they are discretized in space according to the finite volume method with fluxes computed at the sides of the control volume (surrounding a given grid node, see Figure 3.25) with first order approximations:

$$\mathbf{J}_{i+1/2} \cdot \mathbf{e}_x = -D \left.\frac{\partial c}{\partial x}\right|_{i+1/2} \approx S_{i+1/2} D \frac{c_{i+1} - c_i}{\Delta x} \tag{3.33}$$

for the right side of volume i with surface $S_{i+1/2}$, and where Δx is the distance between two neighboring volumes.
At each time step, the resulting linear system is inverted using Thomas algorithm (or TDMA for tri-diagonal matrix); and the position of the interface is updated according to equation (3.12). Although the interface is rarely located in the center of the control volumes, the volume j where the interface is located is classified as interfacial and receives a particular treatment.

- There is no flux on its left side ($\mathbf{J}_{j-1/2} = 0$), assuming that diffusion of Cu in solid (pure Ni) is not operative on the time scale of MD simulations.
- The concentration c_j is set equal to $c^{l\star}$ given by MD (using its fit by a simple power law, see §3.7.1). Hence, the expression (3.33) becomes

$$\mathbf{J}_{j+1/2} \cdot \mathbf{e}_x \approx S_{j+1/2} D \frac{c_{j+1} - c^{l\star}}{\Delta x} \tag{3.34}$$

  keeping the distance between the grid nodes Δx rather than using $x_{j+1} - x^\star$ for simplicity.
- The status (and treatment) of the control volumes is changed when the interface moves from one volume to its neighbor.
- Using the balance equation (3.32) at the interface is easier than if the Lesoult model had to be solved at each time step to determine the interfacial concentrations and the velocity.

The initial length of the liquid zone is 25.2 nm, and the size of the control volumes (or the distance between neighboring nodes) corresponds to the lattice parameter of solid Cu, $\approx$ 3.6 Å. As such, the total number of control volumes in the liquid is 70. Additionally, a small number of solid layers are taken into consideration, equivalent at least to the number of layers that transition to the liquid phase during the total time considered.
The first attempts have been made considering the impurity diffusion coefficients found in §3.5.2. It appears that the values around 3×10^{-5} cm^2 s^{-1} give too fast dissolution rates with respect to the MD simulations. As shown in Figures 3.25 and 3.26, the best value has been found to be slightly smaller, i.e. 2.3×10^{-5} cm^2 s^{-1}. The small difference may be due to

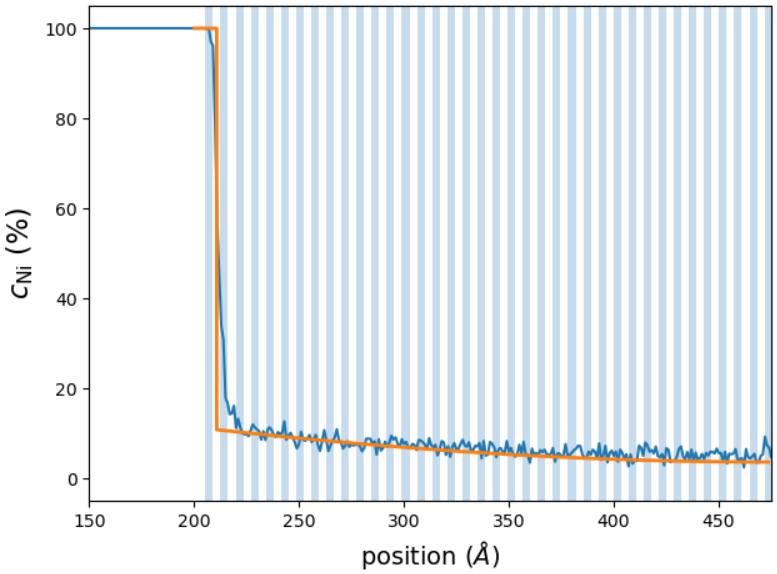

Figure 3.25 – Profiles of Ni in liquid after 100 ns*: 1D finite volume (orange) and MD (blue). Control volumes are represented as white and blue vertical slabs.*

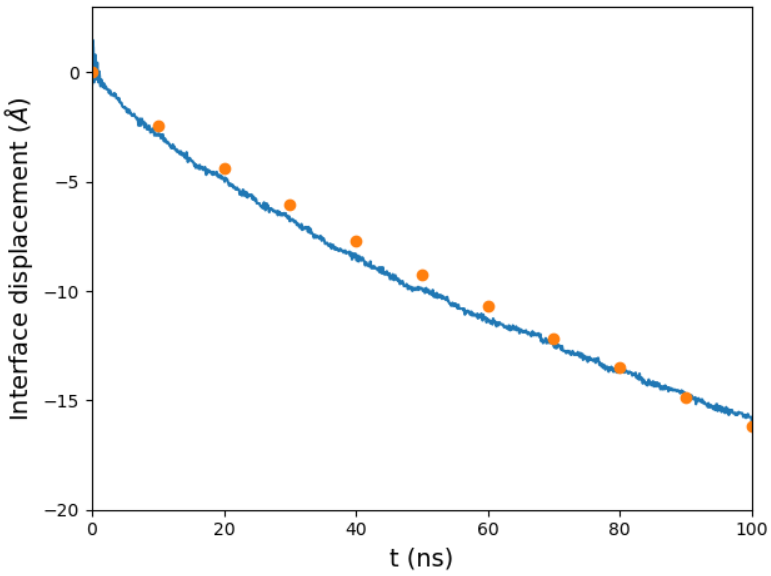

Figure 3.26 – Interface displacement during the dissolution process: MD (blue) vs. 1D diffusion model (orange).

differences in the shapes and sizes of the simulation box, or to the fact that D in (3.31) is the intrinsic diffusivity that contains a thermodynamic factor $(\partial\mu/\partial c)$. Finally, as expected with the moderate variations of the concentration of Ni in the liquid, considering a constant diffusivity seems to be valid.

As already mentioned, the agreement between the 1D diffusion calculations and the MD simulations is particularly appealing: the profiles are in very good agreement (Fig. 3.25) as well as the interface displacement (Fig. 3.26). This adds further support to our estimation of the interfacial concentration in the liquid in §3.7.1.

The next step involves estimating all the quantities that enter the interfacial equations in Lesoult model. Extracting the density of flux of Ni in the liquid at the interface $\mathbf{J}_{\mathrm{Ni}} \cdot \mathbf{e}_x$ is straightforward. As shown in Fig. 3.27 (blue dots), it features small oscillations that can be explained by its linear approximation using Δx (the gradient of concentration is successively underestimated and overestimated when $x^\star > x_j$ and $x^\star < x_j$). Nevertheless, the flux density can be fitted very well by $K/\sqrt{t}$ with $K = \sqrt{D/2}\,c^{l\star}$. Considering the approximate expression in Lesoult model (Eq. (2.68)), our fit amounts to choose $\langle c^l \rangle \approx 0$ and $\delta = \sqrt{2Dt}$, which is consistent with the diffusion length in a 1D problem (it is worth noting that [125] came to a similar conclusion in the Ni-Al system).

Finally, to compute the evolution of the chemical potential jumps $\Delta\mu_{\mathrm{Cu}}$ and $\Delta\mu_{\mathrm{Ni}}$, one can first insert the evolution of the interfacial concentration in the liquid $c^{l\star}$ in the expressions of the chemical potentials (Fig. 3.24). However, some value $c^{s\star} < 1$ must be assumed to avoid the divergence of the chemical potential of Cu in the solid. A parametric study has shown that $c^{s\star}_{\mathrm{Cu}} = 10^{-4}$ ensures that the solutions seem physically consistent and that the solutions do not change drastically for larger concentrations of Cu.

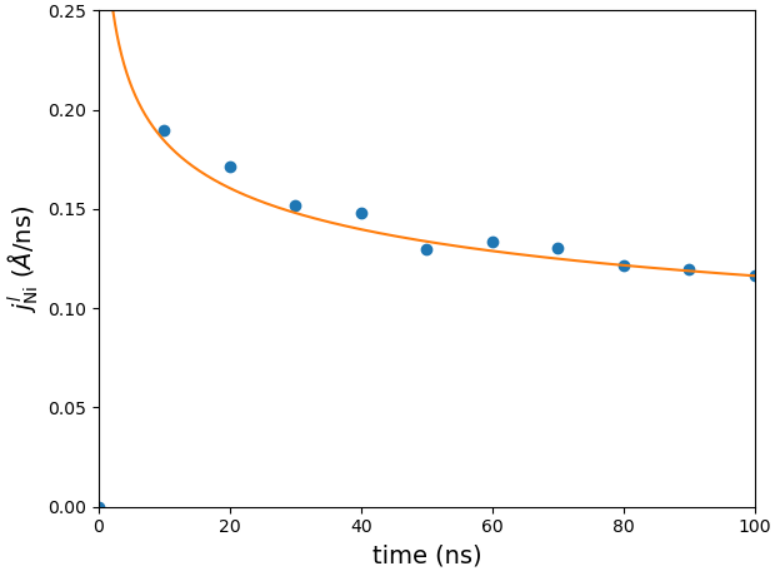

Figure 3.27 – Density of flux of Ni entering the liquid at the interface: 1D diffusion model (blue) fitted with a law scaling as $1/\sqrt{t}$ (orange).

3.7.4 Interfacial Onsager mobilities

Let us recall the equations of the interfacial fluxes of Lesoult model (Eqs (2.56)-(2.59)), specialized for the Cu-Ni system (A = Cu and B = Ni), and expressed in terms of the quantities extracted from the MD simulations (i.e. with $\mathbf{J}^l_{\mathrm{Ni}}$):

$$(1-c^l_{\mathrm{Ni}})v + \mathbf{J}^l_{\mathrm{Ni}} \cdot \mathbf{e}_x = L_{\mathrm{CuCu}}\,\Delta\mu_{\mathrm{Cu}} + L_{\mathrm{CuNi}}\,\Delta\mu_{\mathrm{Ni}} \tag{3.35}$$

$$c^l_{\mathrm{Ni}}v - \mathbf{J}^l_{\mathrm{Ni}} \cdot \mathbf{e}_x = L_{\mathrm{NiCu}}\,\Delta\mu_{\mathrm{Cu}} + L_{\mathrm{NiNi}}\,\Delta\mu_{\mathrm{Ni}} \tag{3.36}$$

All the terms in the above equations having been extracted from the MD simulations, the Onsager mobilities can be obtained by solving the system. However, it is worth noting that the system contains two equations but three unknowns (L_{NiNi}, L_{CuCu}, and $L_{\mathrm{NiCu}} = L_{\mathrm{CuNi}}$). As previously discussed in §2.2.3, to ensure positive entropy production, the matrix of mobilities must be defined as positive so that the equations remain consistent with the second principle of thermodynamics, see Eq. (2.24).
To reduce the number of unknown parameters, two limit cases have been considered.

- First, the cross terms are neglected, i.e. $L_{\mathrm{NiCu}} = 0$.
- Second, the cross terms were assumed to take their upper bound value, i.e. $(L_{\mathrm{NiCu}})^2 = L_{\mathrm{NiNi}}\,L_{\mathrm{CuCu}}$.

In the first case, the system reduces to:

$$L_{\mathrm{CuCu}} = \frac{I_{\mathrm{Cu}}}{\Delta\mu_{\mathrm{Cu}}} \tag{3.37}$$

$$L_{\mathrm{NiNi}} = \frac{I_{\mathrm{Ni}}}{\Delta\mu_{\mathrm{Ni}}} \tag{3.38}$$

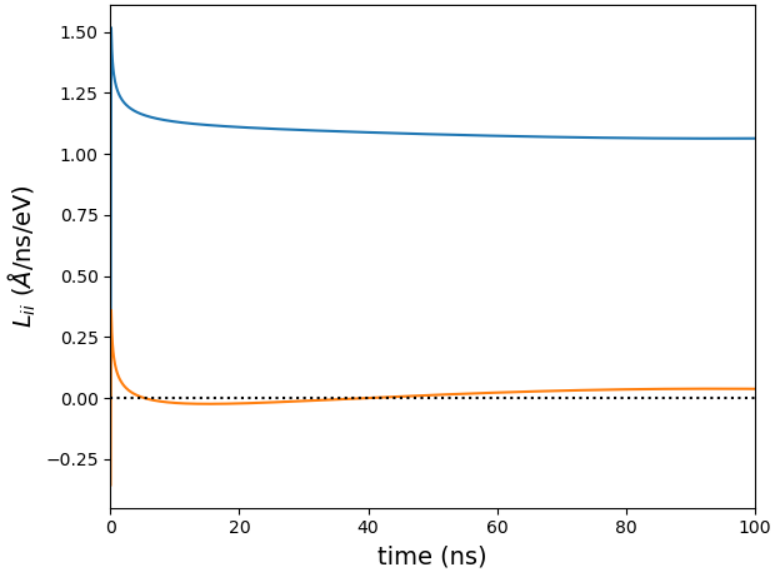

Figure 3.28 – Interfacial Onsager mobilities L_{NiNi} (blue) and L_{CuCu} (orange), neglecting the cross terms.

where the interfacial fluxes are:

$$I_{\mathrm{Cu}} = (1 - c^{l}_{\mathrm{Ni}})v + \mathbf{J}^{l}_{\mathrm{Ni}} \cdot \mathbf{e}_x \tag{3.39}$$

$$I_{\mathrm{Ni}} = c^{l}_{\mathrm{Ni}}v - \mathbf{J}^{l}_{\mathrm{Ni}} \cdot \mathbf{e}_x \tag{3.40}$$

The result is shown in Figure 3.28. The Onsager conditions stipulate that both L_{CuCu} and L_{NiNi} must be positive. However, it is found that while L_{NiNi} is positive, L_{CuCu} exhibits negative values. This surprising result suggests that the role of the cross-terms in the model is more significant than initially anticipated (in particular in §2.4). Hence, it is inferred that these cross terms should not be ignored in the study of such processes, despite our partial conclusion that the cross terms did not play a significant role in the Lesoult model (Figs. 2.16 and 2.17). The reason for this discrepancy may lie in our choice of equivalent diagonal interfacial mobilities for Ni and Cu.

In the second case, it is also possible to express explicitly the Onsager coefficients as follows:

$$\begin{aligned} L_{\mathrm{CuCu}} &= \frac{(I_{\mathrm{Cu}})^2}{P} \\ L_{\mathrm{NiNi}} &= \frac{(I_{\mathrm{Ni}})^2}{P} \end{aligned} \tag{3.41}$$

with $P = I_{\mathrm{Cu}}\Delta\mu_{\mathrm{Cu}} + I_{\mathrm{Ni}}\Delta\mu_{\mathrm{Ni}}$

The resulting curves are depicted in Figure 3.29: both L_{NiNi} and L_{CuCu} remain positive at any time. Additionally, these kinetic parameters do not retain a constant value but exhibit evolution as the dissolution process unfolds. This dynamic behavior of the kinetic parameters suggests a complex interplay of factors that may influence the dissolution process. At first

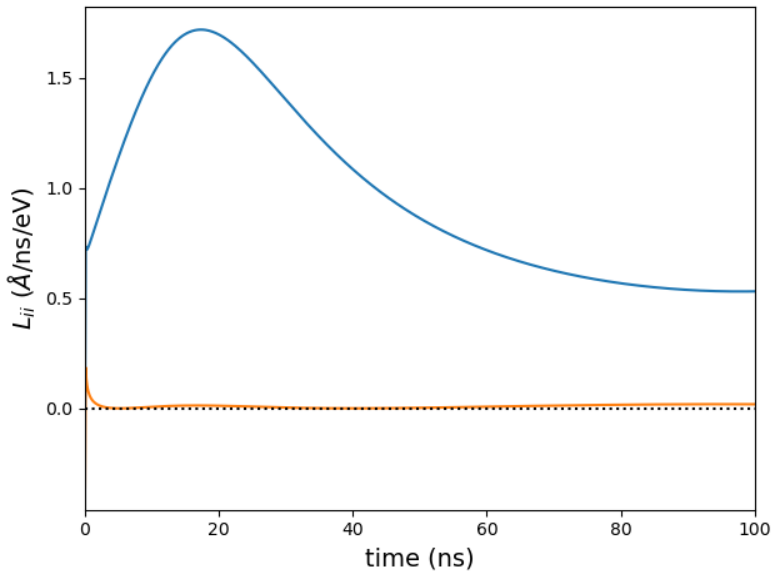

Figure 3.29 – Interfacial Onsager mobilities L_{NiNi} (blue) and L_{CuCu} (orange) accounting for the upper bound of the cross terms.

sight, it seems that the mobilities would depend on the concentration in a nonmonotonic way. But a rapid analysis of the expressions (3.41) shows that the shape of the evolutions depends much on the different contributions entering the interfacial fluxes I_{NiNi} and I_{CuCu}, as well as how accurately the chemical potential jumps are evaluated. To illustrate this point, the two contributions to I_{CuCu} have been plotted in Figure 3.30: when the contribution of the interface movement is obviously negative for dissolution ($c_{\mathrm{Cu}} v < 0$), it is balanced with the diffusion flux within the liquid, which is positive ($\mathbf{J}_{\mathrm{Ni}} \cdot \mathbf{e}_x = -\mathbf{J}_{\mathrm{Cu}} \cdot \mathbf{e}_x > 0$). Both are decreasing in absolute value, so that the sum can change sign depending on their respective relaxation times (they both must tend to zero at $t \to \infty$). Although our extraction of these terms from MD using the 1D model has been as accurate as possible, it appears that slight modifications of the fits can change the balance to remove the incursion of I_{Cu} in the negative region. If the evolution curves are sensitive to our extraction procedure, the order of magnitude of the mobilities is much less sensitive to it, from a preliminary parametric study (due to time limitations, this study could not be pursued to cover the full spectrum of values of the different parameters entering the Lesoult model).

Considering the order of magnitude of the interfacial mobilities (averaged over 100 ns), the following results were obtained:

- $L_{\mathrm{NiNi}} \approx 1.1\,\text{Å}\,\text{ns}^{-1}\,\text{eV}^{-1}$, or $1.2 \times 10^{-6}\,\text{mmol}\,\text{J}^{-1}\,\text{s}^{-1}$,
- $L_{\mathrm{CuCu}} \approx 9.1 \times 10^{-3}\,\text{Å}\,\text{ns}^{-1}\,\text{eV}^{-1}$, or $9.4 \times 10^{-9}\,\text{mmol}\,\text{J}^{-1}\,\text{s}^{-1}$.
- $L_{\mathrm{NiCu}} \approx 0.1\,\text{Å}\,\text{ns}^{-1}\,\text{eV}^{-1}$, or $7.2 \times 10^{-13}\,\text{mmol}\,\text{J}^{-1}\,\text{s}^{-1}$.

It is worth noting that the cross-term L_{NiCu} is significant with respect to mobility L_{CuCu}. One can compute the equivalent interfacial diffusivities using Eq. (2.69) that are easier to compare with the bulk diffusivities:

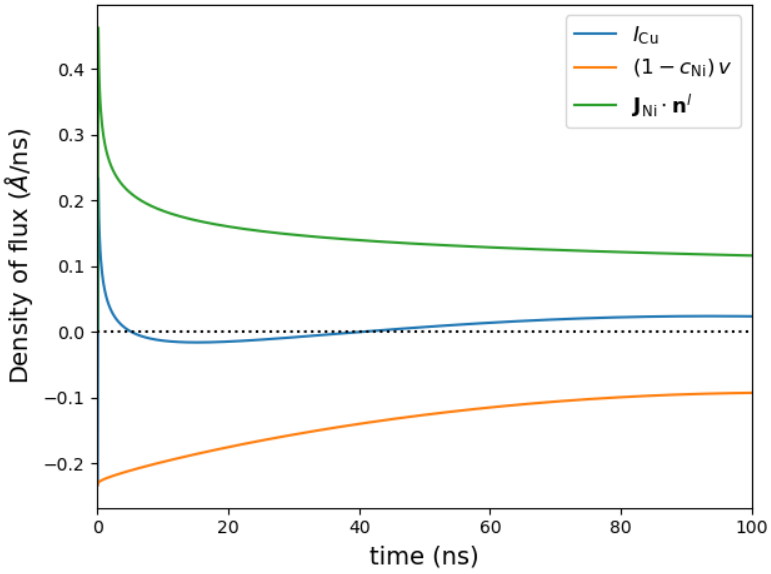

Figure 3.30 – Contributions to the interfacial flux of Cu, Eq. (3.39).

- $D^{\star}_{\mathrm{NiNi}} \approx 8 \times 10^{-12}\ \mathrm{m^2\,s^{-1}}$,
- $D^{\star}_{\mathrm{CuCu}} \approx 6.5 \times 10^{-14}\ \mathrm{m^2\,s^{-1}}$,
- $D^{\star}_{\mathrm{NiCu}} \approx 7.25 \times 10^{-13}\ \mathrm{m^2\,s^{-1}}$.

Let us compare these values with preliminary estimations with the Lesoult model in §2.4. For solutal melting, based on the time scale deduced from the experiments of Deillon et al. [4], it was found that $D^{\star}_{\mathrm{NiNi}}$ should be about $8 \times 10^{-16}\ \mathrm{m^2\,s^{-1}}$, i.e. 4 orders of magnitude smaller than with MD. If L_{CuCu} is considered, the ratio decreases to 2 orders of magnitude.
This discrepancy could have been anticipated with the time evolution of the interfacial concentration in Ni in liquid predicted by MD (Fig. 3.21). Indeed, $c^{l\star}_{\mathrm{Ni}} \approx 0.1$ ($c^{l\star}_{\mathrm{Cu}} \approx 0.9$) would correspond to $\alpha \approx 0.02$ in the calculations of §2.4.2 (Fig. 2.16). Hence, using Eq. (2.82) with $t = 100\,\mathrm{ns}$ gives $D^{\star}_{\mathrm{NiNi}} \approx 2 \times 10^{-12}\ \mathrm{m^2\,s^{-1}}$, of the same order as the values obtained above. However, computing the velocity using the value of the corresponding Péclet number ($\mathrm{Pe} \approx -2$) gives $v \approx -30\,\mathrm{cm\,s^{-1}}$ a dissolution rate that is far too large.
The last mismatch between the concentration and dissolution rate when considering MD and the Lesoult curves in Figs. 2.16 and 2.17 gives a clue on what may be the origin of the disagreement. First, the calculations with the Lesoult model were performed considering interfacial (diagonal) mobilities for Ni and Cu of the same order of magnitude (equal when not accounting for any dependence on the concentrations), when the ratio obtained by MD is two orders of magnitude, with $D^{\star}_{\mathrm{CuCu}}$ significantly small (and much smaller than the diffusivity in bulk liquid). Second, in line with the first point, it has been shown in §2.4.2 that diffusion of Cu in solid Ni can significantly change the evolution of the interfacial concentrations (Fig. 2.20). Although it is not obvious why diffusion of Cu in bulk solid should be of comparable to diffusion in bulk liquid, one must question the relevance of the parameters used in the preliminary calculations with Lesoult model. To conclude, the present results do not invalidate Lesoult model, but point out the necessity to handle in a more comprehensive and systematic way the different contributions to the dissolution process.

3.8 Conclusion

Molecular dynamics (MD) simulations successfully replicated solutal melting, revealing challenges in accurately determining quantities characterizing the S/L equilibrium, and beyond, in monitoring their evolutions during solutal melting. Different techniques, found in the literature, have been used and tested such as the two-phase coexistence method combined with the NPH ensemble, the solute partitioning method and thermodynamic integration to find the equilibrium concentrations and chemical potentials; and the Polyhedral Template Matching (PTM) method for finding efficiently the solid-liquid interface. Crucially, we have demonstrated the significant impact of the simulation system size and shape on the results, especially in terms of the interface velocities and concentration profiles during solutal melting. A direct correlation was established between the system size in terms of the number of atoms and the interface velocity, emphasizing the dependence of interfacial motion on diffusion in the liquid. A thorough literature review has suggested that diffusion in the liquid is modified by the shape and size of the simulation box.
The dissolution process at the interface was also highlighted, where it was shown that the dissolution of a solid layer happens gradually. The vacancies left by outgoing Ni are occupied by Cu atoms and adopt the local structure. As the Cu content starts to increase, the solid layer starts to lose its ordered structure and melts away. Nevertheless, we have not been able to correlate these observations with any particular process that would explain fast or slow effective transfer of atoms across the solid/liquid interface.

The emphasis was placed on the extraction of pivotal kinetic and thermodynamic parameters, which will be incorporated into the Lesoult thermokinetic model. For that purpose, we have implemented a 1D moving boundary model in which interface migration is controlled by diffusion in the bulk liquid. Feeding this model with the interfacial concentrations measured in the MD simulations, we have been able to recover the dissolution rate of the MD simulation, and to extract the flux of Ni in the liquid at the interface. Knowing all quantities entering the expressions of the interfacial fluxes in Lesoult model, we have determined the evolution of the interfacial mobilities on the time scale of the MD simulations. Unfortunately, the values obtained by such an analysis do not agree with the preliminary estimated in §2.4. We suspect some strong assumptions on the parameters in the preliminary predictions of the Lesoult model to be the cause of the disagreement. In particular, the role of the ratio between the diagonal interfacial mobilities and of the diffusivity in bulk solid is worth to be further investigated.

Despite this quite negative conclusion, we believe that the methodology implemented in this chapter is worth following to gain new understanding of the puzzling experiments of solutal melting.

General conclusion

The present work provides an exploration into the intricacies of solutal melting, using different tools at different scales, such as dedicated experiments, thermo-kinetic modeling, and Molecular Dynamics simulations. It delves into the interfacial mechanisms driving this complex process, particularly within Ag-Au and Cu-Ni alloy systems.

One of the salient revelations is the inherent asymmetry between solidification and melting. The conventional belief of viewing melting as the inverse of solidification is questioned. Observations from solutal melting experiments indicate that, unlike solidification, where the solid forms at equilibrium concentration by rejecting excess solute into liquid, melting exhibits unique characteristics. In the process of melting, the interface remains out-of-equilibrium throughout, in relation with a slow diffusion in the solid. The consequence of this phenomenon is that the excess solute diffusing into the first few layers of the solid phase cannot be diffused quickly enough into the deeper layers. As a result, as the liquid front continues to advance, these layers undergo further melting, maintaining the solid-liquid interface in a perpetually out-of-equilibrium state.

To capture this out-of-equilibrium behavior, a novel thermodynamic model was proposed based on the original work of Lesoult. This model demonstrated its proficiency in predicting interface concentrations, mirroring qualitatively the conditions observed in the experiments. This modeling approach, an alternative to Hillert model commonly used for diffusion-controlled transformations, brings a new perspective on non-equilibrium interfaces. This model distinctly deviates from traditional frameworks by not mandating a predefined direction of transformation, thereby offering a dynamic perspective on phase transformations.

Molecular Dynamics (MD) simulations emerged as a crucial tool in this research, affording another dimension to the study of solutal melting. These simulations were instrumental in successfully replicating the process of solutal melting at the atomic scale, thereby contributing significantly to the robustness of the study. During this endeavor, the research encountered numerous challenges, all of which provided opportunities for continuous refinement of the MD methodology for our particular topics. Among these challenges were the identification and application of accurate methods for calculating equilibrium concentrations and chemical potentials, for establishing the position of the interface, and for handling unexpected phe-

nomena that emerged during the simulation process. Of these, the effect of the liquid phase layering in proximity to the interface, along with the impact of the size and shape of the simulation cell on key kinetic parameters, was particularly notable. Delving deeper into the interfacial behavior, the research provided substantial insights into the dissolution process that occurs at the interface. This unveiled the sequential nature of the transformation of the solid layer. As Ni atoms vacated their positions, these vacancies were subsequently occupied by Cu atoms, which adapted to the local atomic structure. As the concentration of Cu increased, the solid layer progressively lost its ordered structure, resulting in melting.
Next, the MD simulations have been analyzed by means of a 1D model where the migration of the interface is controlled by diffusion in bulk liquid. Feeding this model with the time evolution of the interfacial concentration measured in the MD simulations, we have been able to reproduce the dissolution rate, and to extract the flux of Ni in the liquid at the interface. Having all the quantities entering Lesoult model, we have been able to quantify the interfacial mobility matrix, assuming either that the cross terms vanish or that they are taking their upper bound values. As a major outcome, we have found that the cross-terms are necessary to ensure that the mobility for Cu be positive. When comparing the values from MD, they seem not to agree with the preliminary estimates using Lesoult model fitted on the experimental time scale. Hence, explaining quantitatively the solutal melting experiments remains an open challenge.

Our work presents ambitious prospects to reconcile experimental measurements, preliminary results from the thermo-kinetic model by Lesoult, and molecular dynamics simulations.

First and foremost, we can consider conducting additional experiments to substantiate the results. This involves, on the one hand, the Ni-Cu system, for which it is possible to perform calculations at the atomic scale using empirical interatomic potentials, and on the other hand, the Au-Ag system. For this purpose, X-ray radiography experiments at the synchrotron facility could be performed to achieve better time and spatial resolutions. To this end, we would need to revisit the principle of the thin-film setup to avoid convection-related artifacts and enhance it to eliminate thickness variations. Prolonged holding followed by quenching would also be necessary to measure diffusion profiles in the solid and determine diffusivities in this phase. Finally, it may be conceivable to carry out experiments at different temperatures to alter the dominant species in the liquid at the interface and observe the consequences on the process and its kinetics.

Next, revisiting the Lesoult thermo-kinetic model would require coupling it with a 1D diffusion model to overcome rough estimates of volume diffusion terms. It would also be valuable to incorporate solid-state diffusion and the chemical potentials obtained through thermodynamic integration to be as closely aligned as possible with molecular dynamics (MD) calculations. This would enable us to rerun calculations using mobilities extracted from MD, particularly accounting for their strong contrasts. Finally, it appears crucial to extensively investigate the significance of cross-mobilities.

Lastly, it might be worthwhile to repeat the analysis of MD calculations to extract interfacial mobilities for the other systems explored in this study and understand how interfacial mobilities depend on effective volume diffusivities. The use of Ab initio molecular dynamics simulations on the Ag-Au potential to corroborate MD results on the Cu-Ni system and compare them to experiments conducted within the scope of this thesis would also present an interesting prospect.

Bibliography

[1] PC Collins, DA Brice, P Samimi, I Ghamarian, and HL Fraser. Microstructural control of additively manufactured metallic materials. *Annual Review of Materials Research*, 46:63–91, 2016.

[2] Lisa Kaden, Gabor Matthäus, Tobias Ullsperger, Hannes Engelhardt, Markus Rettenmayr, Andreas Tünnermann, and Stefan Nolte. Selective laser melting of copper using ultrashort laser pulses. *Applied Physics A*, 123:1–6, 2017.

[3] B Dutta and M Rettenmayr. An experimental investigation on the kinetics of solute driven remelting. *Metallurgical and Materials Transactions A*, 31(11):2713–2720, 2000.

[4] Léa Deillon, Julien Zollinger, Dominique Daloz, Miha Založnik, and Hervé Combeau. In-situ observations of solutal melting using laser scanning confocal microscopy: The Cu/Ni model system. *Materials characterization*, 97:125–131, 2014.

[5] B Caroli, C Caroli, and B Roulet. Non-equilibrium thermodynamics of the solidification problem. *Journal of Crystal Growth*, 66(3):575–585, 1984.

[6] Lars Onsager. Reciprocal relations in irreversible processes. i. *Physical review*, 37(4):405, 1931.

[7] M Rettenmayr. Melting and remelting phenomena. *International Materials Reviews*, 54(1):1–17, 2009.

[8] Markus Rettenmayr. Solidification and melting processes—one of the fundamental asymmetries in nature. *Transactions of the Indian Institute of Metals*, 62(4):265–268, 2009.

[9] M Rettenmayr. Reply: Discussion on local equilibrium at solid/liquid interfaces during melting, by M. Hillert and J. Agren Scripta Materialia, 2002; 46: 455. *Scripta Materialia*, 48(3):315–319, 2003.

[10] Edward F Emley. Continuous casting of aluminium. *International Metals Reviews*, 21(1):75–115, 1976.

[11] M Schwarz, A Karma, K Eckler, and DM Herlach. Physical mechanism of grain refinement in solidification of undercooled melts. *Physical Review Letters*, 73(10):1380, 1994.

[12] RH Mathiesen, L Arnberg, P Bleuet, and A Somogyi. Crystal fragmentation and columnar-to-equiaxed transitions in Al-Cu studied by synchrotron X-ray video microscopy. *Metallurgical and Materials Transactions A*, 37(8):2515–2524, 2006.

[13] MC Schneider, JP Gu, C Beckermann, WJ Boettinger, and UR Kattner. Modeling of micro- and macrosegregation and freckle formation in single-crystal nickel-base superalloy directional solidification. *Metallurgical and Materials Transactions A*, 28:1517, 1997.

[14] Hideyuki Yasuda, Itsuo Ohnaka, Koichi Kawasaki, Akira Sugiyama, Tetsutaro Ohmichi, Jun Iwane, and Keiji Umetani. Direct observation of stray crystal formation in unidirectional solidification of Sn–Bi alloy by X-ray imaging. *Journal of Crystal Growth*, 262(1-4):645–652, 2004.

[15] Markus Rettenmayr, Oliver Warkentin, and Hans Eckart Exner. Deviations from equilibrium at remelting solid/liquid interfaces. *International Journal of Materials Research*, 88(8):617–619, 1997.

[16] M Rettenmayr, O Warkentin, M Rappaz, and HE Exner. Simulation of solutal remelting. *Acta Materialia*, 49(13):2499–2510, 2001.

[17] Ernst Gamsjäger, Jiri Svoboda, Franz Dieter Fischer, and Markus Rettenmayr. Kinetics of solute driven melting and solidification. *Acta Materialia*, 55(8):2599–2607, 2007.

[18] Mats Hillert and John Ågren. Discussion on local equilibrium at solid/liquid interfaces during melting. *Scripta Materialia*, 46(6):455–457, 2002.

[19] Fang Dacheng and A Hellawell. The surface morphology of crystals melting under solutions of different densities. *Journal of Crystal Growth*, 92(3-4):364–370, 1988.

[20] G Rajesh, M Arivanandhan, H Morii, T Aoki, T Koyama, Y Momose, A Tanaka, T Ozawa, Yuko Inatomi, and Yasuhiro Hayakawa. In-situ observations of dissolution process of GaSb into InSb melt by X-ray penetration method. *Journal of Crystal Growth*, 312(19):2677–2682, 2010.

[21] Philip Nash. Phase diagrams of binary nickel alloys. *ASM International(USA), 1991,*, page 394, 1991.

[22] H Okamoto and TB Massalski. The Ag-Au (silver-gold) system. *Bulletin of Alloy Phase Diagrams*, 4(1):30–38, 1983.

[23] Stefan Klein, Dirk Braeuer, Maike Becker, Alexander Knipstein, Sebastian Meckel, Elke Sondermann, and Florian Kargl. X-rise-a multifunctional x-ray radiography device for parabolic flights and laboratory use. *International Journal of Microgravity Science and Application*, 33(4):330405, 2016.

[24] Maike Becker, C Dreißigacker, Stefan Klein, and Florian Kargl. Near-isothermal furnace for in situ and real time X-ray radiography solidification experiments. *Review of Scientific Instruments*, 86(6):063904, 2015.

[25] ImageJ Auto Threshold. https://imagej.net/plugins/auto-threshold.

[26] Maike Becker, Stefan Klein, and Florian Kargl. In-situ solute measurements with a laboratory polychromatic microfocus X-ray source during equiaxed solidification of an Al-Ge alloy. *Scripta Materialia*, 124:34–37, 2016.

[27] Adeline Buffet. *Etude in situ, par combinaison de techniques d'imagerie synchrotron (radiographie X/topographie X), de la formation de la microstructure de solidification d'alliages métalliques*. PhD thesis, Université Joseph-Fourier-Grenoble I, 2008.

[28] David R Lide. CRC handbook of chemistry and physics, 88th edition., 2008.

[29] Jürgen Brillo, Ivan Egry, and Ivan Ho. Density and thermal expansion of liquid Ag–Cu and Ag–Au alloys. *International journal of thermophysics*, 27(2):494–506, 2006.

[30] WC Mallard, AB Gardner, Ralph F Bass, and LM Slifkin. Self-diffusion in silver-gold solid solutions. *Physical Review*, 129(2):617, 1963.

[31] JI Akhter, E Ahmed, and M Ahmad. Study of diffusion coefficients in liquid noble metals. *Materials chemistry and physics*, 93(2-3):504–507, 2005.

[32] Nikolay Dubinin. Self-diffusion in liquid copper, silver, and gold. *Metals*, 10(12):1651, 2020.

[33] DE Coates. Diffusion-controlled precipitate growth in ternary systems I. *Metallurgical Transactions*, 3(5):1203–1212, 1972.

[34] YS Teh and GP Rangaiah. A study of equation-solving and Gibbs free energy minimization methods for phase equilibrium calculations. *Chemical Engineering Research and Design*, 80(7):745–759, 2002.

[35] Ilya Prigogine. *Introduction à la Thermodynamique des Processus Irréversibles*. Dunod, 1968.

[36] Sybren Ruurds De Groot and Peter Mazur. *Non-equilibrium thermodynamics*. Courier Corporation, 2013.

[37] John W Cahn, W Craig Carter, and William C Johnson. *The selected works of John W. Cahn*. Wiley-TMS, 1998.

[38] Michael J Aziz. Model for solute redistribution during rapid solidification. *Journal of Applied Physics*, 53(2):1158–1168, 1982.

[39] Harith Humadi, JJ Hoyt, and Nikolas Provatas. Microscopic treatment of solute trapping and drag. *Physical Review E*, 93(1):010801, 2016.

[40] JJ Hoyt, B Sadigh, M Asta, and SM Foiles. Kinetic phase field parameters for the Cu–Ni system derived from atomistic computations. *Acta Materialia*, 47(11):3181–3187, 1999.

[41] Mats Hillert. Solute drag, solute trapping and diffusional dissipation of Gibbs energy. *Acta Materialia*, 47(18):4481–4505, 1999.

[42] JJ Hoyt, Mark Asta, and Alain Karma. Atomistic simulation methods for computing the kinetic coefficient in solid-liquid systems. *Interface Science*, 10(2):181–189, 2002.

[43] Adam A Wheeler, William J Boettinger, and Geoffrey B McFadden. Phase-field model of solute trapping during solidification. *Physical Review E*, 47(3):1893, 1993.

[44] Herbert B Callen. *Thermodynamics and an introduction to thermostatistics*. John Wiley & Sons, New York, 1985.

[45] B Caroli, C Caroli, and B Roulet. Interface kinetics and solidification of alloys: a discussion of some phenomenological models. *Acta Metallurgica*, 34(9):1867–1877, 1986.

[46] JC Baker and JW Cahn. Solidification, american society for metals. *Metals Park, OH*, 23, 1971.

[47] M Hillert. The growth of ferrite, bainite and martensite. *Report, Swedish Inst. Metal Res. Stockholm*, pages 113–58, 1960.

[48] M Hillert and M Rettenmayr. Deviation from local equilibrium at migrating phase interfaces. *Acta Materialia*, 51(10):2803–2809, 2003.

[49] M Buchmann and M Rettenmayr. Rapid solidification theory revisited–a consistent model based on a sharp interface. *Scripta Materialia*, 57(2):169–172, 2007.

[50] M Buchmann and M Rettenmayr. Numerical study of steady state melting of a binary alloy. *Journal of Crystal Growth*, 310(21):4623–4627, 2008.

[51] M Buchmann and M Rettenmayr. Non-equilibrium transients during solidification – A numerical study. *Scripta Materialia*, 58(2):106–109, 2008.

[52] W Craig Carter and William C Johnson. *The selected works of John W. Cahn*. John Wiley & Sons, 2013.

[53] Markus Rettenmayr. Solidification and melting processes—one of the fundamental asymmetries in nature. *Transactions of the Indian Institute of Metals*, 62(4):265–268, 2009.

[54] Sabine an Mey. Thermodynamic re-evaluation of the Cu-Ni system. *Calphad*, 16(3):255–260, 1992.

[55] CJ Smithells, WF Gale, and TC Totemeier. Smithells Metals Reference Book, 2004.

[56] M.J. Aziz. Non-equilibrium interface kinetics during rapid solidification: Theory and experiment. *Materials Science and Engineering*, 98:369–372, 1988.

[57] Gérard Lesoult. *Thermodynamique des matériaux: de l'élaboration des matériaux à la genèse des microstructures*, volume 5. PPUR Presses polytechniques, 2010.

[58] H. Cheng, Lü Y.J., and Chen M. Interdiffusion in liquid Al–Cu and Ni–Cu alloys. *The Journal of Chemical Physics*, 131:044502, 2009.

[59] Iijima Y., Hirano K., and Kikuchi M. Determination of intrinsic diffusion coefficients in a wide concentration range of a Cu-Ni couple by the multiple markers method. *Transactions of the Japan Institute of Metals*, 23(1):19–23, 1982.

[60] J. Wang, H.S. Liu, L.B. Liu, and Z.P. Jin. Assessment of diffusion mobilities in fcc Cu–Ni alloys. *Calphad*, 32(1):94–100, 2008.

[61] Berni Julian Alder and Thomas Everett Wainwright. Phase transition for a hard sphere system. *The Journal of chemical physics*, 27(5):1208–1209, 1957.

[62] Aneesur Rahman. Correlations in the motion of atoms in liquid argon. *Physical review*, 136(2A):A405, 1964.

[63] Herman JC Berendsen, JPM van Postma, Wilfred F van Gunsteren, ARHJ DiNola, and Jan R Haak. Molecular dynamics with coupling to an external bath. *The Journal of chemical physics*, 81(8):3684–3690, 1984.

[64] Denis J Evans and Brad Lee Holian. The Nosé–Hoover thermostat. *The Journal of chemical physics*, 83(8):4069–4074, 1985.

[65] Glenn J Martyna, Michael L Klein, and Mark Tuckerman. Nosé–Hoover chains: The canonical ensemble via continuous dynamics. *The Journal of chemical physics*, 97(4):2635–2643, 1992.

[66] E Weinan and Dong Li. The andersen thermostat in molecular dynamics. *Communications on pure and applied mathematics*, 61(1):96–136, 2008.

[67] Tamar Schlick. Similarity and diversity in chemical design. In *Molecular Modeling and Simulation*, pages 463–496. Springer, 2002.

[68] William G Hoover. Canonical dynamics: Equilibrium phase-space distributions. *Physical review A*, 31(3):1695, 1985.

[69] Enrique de Miguel and George Jackson. The nature of the calculation of the pressure in molecular simulations of continuous models from volume perturbations. *The Journal of chemical physics*, 125(16):164109, 2006.

[70] Murray S Daw and Michael I Baskes. Embedded-atom method: Derivation and application to impurities, surfaces, and other defects in metals. *Physical Review B*, 29(12):6443, 1984.

[71] Cynthia L Kelchner, SJ Plimpton, and JC Hamilton. Dislocation nucleation and defect structure during surface indentation. *Physical review B*, 58(17):11085, 1998.

[72] Paul J Steinhardt, David R Nelson, and Marco Ronchetti. Bond-orientational order in liquids and glasses. *Physical Review B*, 28(2):784, 1983.

[73] Daniel Faken and Hannes Jónsson. Systematic analysis of local atomic structure combined with 3D computer graphics. *Computational Materials Science*, 2(2):279–286, 1994.

[74] GJ Ackland and AP Jones. Applications of local crystal structure measures in experiment and simulation. *Physical Review B*, 73(5):054104, 2006.

[75] Georges Voronoi. Nouvelles applications des paramètres continus à la théorie des formes quadratiques. deuxième mémoire. recherches sur les parallélloèdres primitifs. *Journal für die reine und angewandte Mathematik (Crelles Journal)*, 1908(134):198–287, 1908.

[76] Alexander Stukowski. Structure identification methods for atomistic simulations of crystalline materials. *Modelling and Simulation in Materials Science and Engineering*, 20(4):045021, 2012.

[77] C Qi, JF Li, B Xu, LT Kong, and S Zhao. Atomistic characterization of solid-liquid interfaces in the Cu-Ni binary alloy system. *Computational Materials Science*, 125:72–81, 2016.

[78] Peter M Larsen. Revisiting the Common Neighbour Analysis and the Centrosymmetry Parameter. *arXiv preprint arXiv:2003.08879*, 2020.

[79] Teppei Fukuya and Yasushi Shibuta. Machine learning approach to automated analysis of atomic configuration of molecular dynamics simulation. *Computational Materials Science*, 184:109880, 2020.

[80] Kensho Ueno and Yasushi Shibuta. Composition dependence of solid-liquid interfacial energy of Fe-Cr binary alloy from molecular dynamics simulations. *Computational Materials Science*, 167:1–7, 2019.

[81] Peter Mahler Larsen, Søren Schmidt, and Jakob Schiøtz. Robust structural identification via polyhedral template matching. *Modelling and Simulation in Materials Science and Engineering*, 24(5):055007, 2016.

[82] Simon R Phillpot, Sidney Yip, and Dieter Wolf. How do crystals melt? computer simulations demonstrate the interplay between thermodynamics and kinetics during the melting process. *Computers in physics*, 3(6):20–31, 1989.

[83] Saman Alavi and Donald L Thompson. Simulations of melting of polyatomic solids and nanoparticles. *Molecular Simulation*, 32(12-13):999–1015, 2006.

[84] JH Los and RJM Pellenq. Determination of the bulk melting temperature of nickel using Monte Carlo simulations: Inaccuracy of extrapolation from cluster melting temperatures. *Physical Review B*, 81(6):064112, 2010.

[85] YangChun Zou, ShiKai Xiang, and ChengDa Dai. Investigation on the efficiency and accuracy of methods for calculating melting temperature by molecular dynamics simulation. *Computational Materials Science*, 171:109156, 2020.

[86] JJ Hoyt and Mark Asta. Atomistic computation of liquid diffusivity, solid-liquid interfacial free energy, and kinetic coefficient in Au and Ag. *Physical Review B*, 65(21):214106, 2002.

[87] Yasushi Shibuta and Toshio Suzuki. Melting and nucleation of iron nanoparticles: A molecular dynamics study. *Chemical Physics Letters*, 445(4-6):265–270, 2007.

[88] Yasushi Shibuta, Shinya Takamoto, and Toshio Suzuki. A molecular dynamics study of the energy and structure of the symmetric tilt boundary of iron. *ISIJ international*, 48(11):1582–1591, 2008.

[89] Yasushi Shibuta. Estimation of thermodynamic and interfacial parameters of metallic materials by molecular dynamics simulations. *Materials Transactions*, page ME201712, 2019.

[90] Kensho Ueno and Yasushi Shibuta. Semi-grand canonical Monte Carlo simulation for derivation of thermodynamic properties of binary alloy. In *IOP Conference Series: Materials Science and Engineering*, volume 529, page 012037. IOP Publishing, 2019.

[91] Berk Onat and Sondan Durukanoğlu. An optimized interatomic potential for Cu–Ni alloys with the embedded-atom method. *Journal of Physics: Condensed Matter*, 26(3):035404, 2013.

[92] COT Galvin, RW Grimes, and PA Burr. A molecular dynamics method to identify the liquidus and solidus in a binary phase diagram. *Computational Materials Science*, 186:110016, 2021.

[93] H Ramalingam, M Asta, A Van de Walle, and JJ Hoyt. Atomic-scale simulation study of equilibrium solute adsorption at alloy solid-liquid interfaces. *Interface Science*, 10(2-3):149–158, 2002.

[94] Kensho Ueno and Yasushi Shibuta. Solute partition at solid-liquid interface of binary alloy from molecular dynamics simulation. *Materialia*, 4:553–557, 2018.

[95] J Pablo Palafox-Hernandez, Brian B Laird, and Mark Asta. Atomistic characterization of the Cu–Pb solid–liquid interface. *Acta Materialia*, 59(8):3137–3144, 2011.

[96] Pu Liu, Edward Harder, and BJ Berne. On the calculation of diffusion coefficients in confined fluids and interfaces with an application to the liquid-vapor interface of water. *The Journal of Physical Chemistry B*, 108(21):6595–6602, 2004.

[97] Xianglai Gan, Shifang Xiao, Huiqiu Deng, Xuegui Sun, Xiaofan Li, and Wangyu Hu. Atomistic simulations of the Fe (001)–Li solid–liquid interface. *Fusion Engineering and Design*, 89(12):2894–2901, 2014.

[98] Pascale Geysermans, D Gorse, and V Pontikis. Molecular dynamics study of the solid–liquid interface. *The Journal of Chemical Physics*, 113(15):6382–6389, 2000.

[99] Maria Gandman, Yaron Kauffmann, Christoph T Koch, and Wayne D Kaplan. Direct quantification of ordering at a solid-liquid interface using aberration corrected transmission electron microscopy. *Physical review letters*, 110(8):086106, 2013.

[100] SM Foiles. Calculation of the surface segregation of Ni-Cu alloys with the use of the embedded-atom method. *Physical Review B*, 32(12):7685, 1985.

[101] Adham Hashibon, Joan Adler, Michael W Finnis, and Wayne D Kaplan. Atomistic study of structural correlations at a liquid–solid interface. *Computational materials science*, 24(4):443–452, 2002.

[102] Ruslan L Davidchack and Brian B Laird. Simulation of the hard-sphere crystal–melt interface. *The Journal of chemical physics*, 108(22):9452–9462, 1998.

[103] JJ Hoyt, Mark Asta, and Alain Karma. Method for computing the anisotropy of the solid-liquid interfacial free energy. *Physical review letters*, 86(24):5530, 2001.

[104] A Salhoumi and PK Galenko. Analysis of interface kinetics: solutions of the gibbs-thomson-type equation and of the kinetic rate theory. In *IOP Conference Series: Materials Science and Engineering*, volume 192, page 012014. IOP Publishing, 2017.

[105] DY Sun, M Asta, and JJ Hoyt. Kinetic coefficient of Ni solid-liquid interfaces from molecular-dynamics simulations. *Physical Review B*, 69(2):024108, 2004.

[106] Burkhard Dünweg and Kurt Kremer. Molecular dynamics simulation of a polymer chain in solution. *The Journal of Chemical Physics*, 99(9):6983–6997, 1993.

[107] Max Linke, Jürgen Köfinger, and Gerhard Hummer. Rotational diffusion depends on box size in molecular dynamics simulations. *The journal of physical chemistry letters*, 9(11):2874–2878, 2018.

[108] Alper T Celebi, Seyed Hossein Jamali, André Bardow, Thijs JH Vlugt, and Othonas A Moultos. Finite-size effects of diffusion coefficients computed from molecular dynamics: a review of what we have learned so far. *Molecular Simulation*, 47(10-11):831–845, 2021.

[109] In-Chul Yeh and Gerhard Hummer. System-size dependence of diffusion coefficients and viscosities from molecular dynamics simulations with periodic boundary conditions. *The Journal of Physical Chemistry B*, 108(40):15873–15879, 2004.

[110] David M Heyes, MJ Cass, Jack G Powles, and WAB Evans. Self-diffusion coefficient of the hard-sphere fluid: System size dependence and empirical correlations. *The Journal of Physical Chemistry B*, 111(6):1455–1464, 2007.

[111] Pauline Simonnin, Benoit Noetinger, Carlos Nieto-Draghi, Virginie Marry, and Benjamin Rotenberg. Diffusion under confinement: Hydrodynamic finite-size effects in simulation. *Journal of chemical theory and computation*, 13(6):2881–2889, 2017.

[112] Seyed Hossein Jamali, André Bardow, Thijs JH Vlugt, and Othonas A Moultos. Generalized form for finite-size corrections in mutual diffusion coefficients of multicomponent mixtures obtained from equilibrium molecular dynamics simulation. *Journal of Chemical Theory and Computation*, 16(6):3799–3806, 2020.

[113] Jeffrey M Young and Athanassios Z Panagiotopoulos. System-size dependence of electrolyte activity coefficients in molecular simulations. *The Journal of Physical Chemistry B*, 122(13):3330–3338, 2018.

[114] Daniel P Sellan, Eric S Landry, JE Turney, Alan JH McGaughey, and Cristina H Amon. Size effects in molecular dynamics thermal conductivity predictions. *Physical Review B*, 81(21):214305, 2010.

[115] Matthew J Klenk and Wei Lai. Finite-size effects on the molecular dynamics simulation of fast-ion conductors: A case study of lithium garnet oxide $Li_7La_3Zr_2O_{12}$. *Solid State Ionics*, 289:143–149, 2016.

[116] Seyed Hossein Jamali, Remco Hartkamp, Christos Bardas, Jakob Söhl, Thijs JH Vlugt, and Othonas A Moultos. Shear viscosity computed from the finite-size effects of self-diffusivity in equilibrium molecular dynamics. *Journal of chemical theory and computation*, 14(11):5959–5968, 2018.

[117] Kang-Sahn Kim, Changho Kim, George Em Karniadakis, Eok Kyun Lee, and John J Kozak. Density-dependent finite system-size effects in equilibrium molecular dynamics estimation of shear viscosity: Hydrodynamic and configurational study. *The Journal of chemical physics*, 151(10):104101, 2019.

[118] Mark O Robbins, Gary S Grest, and Kurt Kremer. Effect of finite system size on thermal fluctuations: Implications for melting. *Physical Review B*, 42(9):5579, 1990.

[119] Dmitri Rozmanov and Peter G Kusalik. Transport coefficients of the TIP4P-2005 water model. *The Journal of chemical physics*, 136(4):044507, 2012.

[120] Gota Kikugawa, Shotaro Ando, Jo Suzuki, Yoichi Naruke, Takeo Nakano, and Taku Ohara. Effect of the computational domain size and shape on the self-diffusion coefficient in a Lennard-Jones liquid. *The Journal of Chemical Physics*, 142(2):024503, 2015.

[121] Alexandru Botan, Virginie Marry, and Benjamin Rotenberg. Diffusion in bulk liquids: finite-size effects in anisotropic systems. *Molecular Physics*, 113(17-18):2674–2679, 2015.

[122] Xiaofeng Yang, Hui Zhang, Lei Li, and Xiangfei Ji. Corrections of the periodic boundary conditions with rectangular simulation boxes on the diffusion coefficient, general aspects. *Molecular Simulation*, 43(17):1423–1429, 2017.

[123] Martin Vögele and Gerhard Hummer. Divergent diffusion coefficients in simulations of fluids and lipid membranes. *The Journal of Physical Chemistry B*, 120(33):8722–8732, 2016.

[124] F Baras, V Turlo, and O Politano. Dissolution at interfaces in layered solid-liquid thin films: a key step in joining process. *Journal of Materials Engineering and Performance*, 25(8):3270–3274, 2016.

[125] V Turlo, O Politano, and F Baras. Dissolution process at solid/liquid interface in nanometric metallic multilayers: Molecular dynamics simulations versus diffusion modeling. *Acta Materialia*, 99:363–372, 2015.